

AD-769 063

**IN-FLIGHT STABILIZATION OF EXTERNALLY
SLUNG HELICOPTER LOADS**

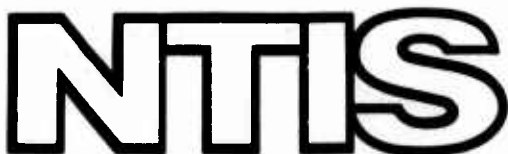
Northrop Corporation

Prepared for:

**Army Air Mobility Research and Development
Laboratory**

May 1973

DISTRIBUTED BY:



**National Technical Information Service
U. S. DEPARTMENT OF COMMERCE
5285 Port Royal Road, Springfield Va. 22151**

DISCLAIMERS

The findings in this report are not to be construed as an official Department of the Army position unless so designated by other authorized documents.

When Government drawings, specifications, or other data are used for any purpose other than in connection with a definitely related Government procurement operation, the U.S. Government thereby incurs no responsibility nor any obligation whatsoever; and the fact that the Government may have formulated, furnished, or in any way supplied the said drawings, specifications, or other data is not to be regarded by implication or otherwise as in any manner licensing the holder or any other person or corporation, or conveying any rights or permission, to manufacture, use, or sell any patented invention that may in any way be related thereto.

Trade names cited in this report do not constitute an official endorsement or approval of the use of such commercial hardware or software.

DISPOSITION INSTRUCTIONS

Destroy this report when no longer needed. Do not return it to the originator.

1015
500
EXAMINER: WOOD
JUSTIFICATION: *[Redacted]*

BY: *[Redacted]*

DISTRIBUTION/COMPLIABILITY CODES
Dist. *[Redacted]* Ref ID: *[Redacted]*

<i>A</i>		
----------	--	--

ia/

UNCLASSIFIED

Security Classification

AD-769063

DOCUMENT CONTROL DATA - R & D

(Security classification of title, body of abstract and indexing annotation must be entered when the overall report is classified)

1. ORIGINATING ACTIVITY (Corporate author) Northrop Corporation, Electronics Division 2301 West 120th Street Hawthorne, California 90250	2a. REPORT SECURITY CLASSIFICATION UNCLASSIFIED
	2b. GROUP

3. REPORT TITLE

IN-FLIGHT STABILIZATION OF EXTERNALLY SLUNG HELICOPTER LOADS

4. DESCRIPTIVE NOTES (Type of report and inclusive dates)

Final Report (25 June 1970 to 17 January 1972)

5. AUTHOR(S) (First name, middle initial, last name)

David T. Liu

6. REPORT DATE May 1973	7a. TOTAL NO. OF PAGES 252 237	7b. NO. OF REPS 9
7. CONTRACT OR GRANT NO. DAAJ02-70-C-0067	8a. ORIGINATOR'S REPORT NUMBER(S) USAAMRDL Technical Report 73-5	
8. PROJECT NO. 1F162203A435	8b. OTHER REPORT NO(S) (Any other numbers that may be assigned this report) NORT 72-39	
9.		
10. DISTRIBUTION STATEMENT		

Approved for public release; distribution unlimited.

11. SUPPLEMENTARY NOTES	12. SPONSORING MILITARY ACTIVITY Eustis Directorate, U. S. Army Air Mobility Research and Development Laboratory, Fort Eustis, Virginia
-------------------------	--

13. ABSTRACT

The purpose of this study has been to select the best technical approaches for stabilizing a wide spectrum of externally slung helicopter loads at forward speeds up to 150 knots equivalent airspeed (KIAS). This effort has been accomplished in a two-phase program. Phase I was designed to identify and characterize typical sling loads, to establish their aerodynamic and dynamic characteristics, to gain physical understanding of helicopter/sling-load coupling dynamics, and to develop design approaches for stabilizing devices together with criteria and methodology for cost-effectiveness analysis. Phase II was devoted to the performance of a trade-off study of load stabilization systems, the formulation of preliminary design concepts for the most effective load stabilization approaches, and an evaluation of candidate stabilization systems utilizing a moving-base flight simulator. Several technical approaches were found to satisfy the 150-knot criterion for carrying specific loads. These included two-point suspension systems, the use of drag chutes, mechanical stabilization systems which show considerable promise, aerodynamic load stabilization with rate sensors and a beam with control surfaces secured to the load, display systems for monitoring load position, and electronic stabilization systems providing rate and acceleration inputs to the helicopter's stability augmentation system (SAS). The last approach is favored. The electronic stabilization system, although complex in implementation, is versatile. Overall system stability is very sensitive to varying flight configurations and conditions. For each specific flight configuration and condition, the optimized load stabilization system is extremely effective. Practical implementation of the proposed concept and a complete evaluation with respect to the promising mechanical stabilization approaches require further study.

Reproduced by

NATIONAL TECHNICAL
INFORMATION SERVICE

U S Department of Commerce
Springfield VA 22151

DD FORM 1 NOV 1973 1473
REPLACES DD FORM 1473, 1 JAN 64, WHICH IS
OBSOLETE FOR ARMY USE.

1b

UNCLASSIFIED

Security Classification

UNCLASSIFIED
Security Classification

14. KEY WORDS	LINK A		LINK B		LINK C	
	ROLE	WT	ROLE	WT	ROLE	WT
Helicopter						
Sling Load						
Helicopter/Sling-Load						
Load Stabilization						
Suspension Systems						
Mechanical Stabilization Systems						
Electronic Stabilization Systems						
Stability Augmentation System						
Rate Sensors						
Display Systems						

iC

UNCLASSIFIED

Security Classification



DEPARTMENT OF THE ARMY
U. S. ARMY AIR MOBILITY RESEARCH & DEVELOPMENT LABORATORY
EUSTIS DIRECTORATE
FORT EUSTIS, VIRGINIA 23604

This report was prepared by the Northrop Corporation, Electronics Division, as a requirement of Contract DAAJ02-70-C-0067. It documents a program to investigate the effect of aerodynamic instabilities on externally slung helicopter loads at speeds up to 150 knots, and to advance the technology and means by which cargo may be transported externally at this speed.

The objective of this contractual effort was to develop preliminary design concepts for stabilization devices and/or systems that are responsive to the 150-knot speed requirement. Northrop's large-amplitude moving-base simulator was used to demonstrate the problem and the effectiveness of proposed solutions.

This Directorate generally concurs in the conclusions drawn by the contractor; however, final selection of an in-flight stabilization system or concept, applicable to a particular Army helicopter, will depend on many other considerations not included in the scope of this investigation.

The technical monitor for this contract was Mr. Richard E. Lane of the Military Operations Technology Division.

IC

Project 1F162203A435
Contract DAAJ02-70-C-0067
USAAMRDL Technical Report 73-5
May 1973

IN-FLIGHT STABILIZATION OF EXTERNALLY SLUNG HELICOPTER LOADS

Final Report

By

David T. Liu

Prepared by

Northrop Corporation
Electronics Division
Hawthorne, California

for

EUSTIS DIRECTORATE
U.S. ARMY AIR MOBILITY RESEARCH AND DEVELOPMENT LABORATORY
FORT EUSTIS, VIRGINIA

Approved for public release;
distribution unlimited.

ABSTRACT

The purpose of this study was to select the best technical approaches for stabilizing a wide spectrum of externally slung helicopter loads at forward speeds up to 150 knots equivalent air speed (KEAS).

This effort was accomplished in a two-phase program. Phase I was designed to identify and characterize typical sling loads, to establish their aerodynamic and dynamic characteristics, to gain physical understanding of helicopter/sling-load coupling dynamics, and to develop design approaches for stabilizing devices together with criteria and methodology for cost-effectiveness analysis. Phase II was devoted to the performance of a trade-off study of load stabilization systems, the formulation of preliminary design concepts for the most effective load stabilization approaches, and an evaluation of candidate stabilization systems using a moving-base flight simulator.

Several technical approaches were found to satisfy the 150-knot criterion for carrying specific loads. These included two-point suspension systems, the use of drag chutes, mechanical stabilization systems which show considerable promise, aerodynamic load stabilization with rate sensors and a beam with control surfaces secured to the load, display systems for monitoring load position, and electronic stabilization systems providing rate and acceleration inputs to the helicopter's stability augmentation system (SAS). The last approach is favored.

The electronic stabilization system, although complex in implementation, is versatile. Overall system stability is very sensitive to varying flight configurations and conditions. For each specific flight configuration and condition, the optimized load stabilization system is extremely effective. Practical implementation of the proposed concept and a complete evaluation with respect to the promising mechanical stabilization approaches require further study.

TABLE OF CONTENTS

<u>Section</u>	<u>Page</u>
ABSTRACT	iii
LIST OF ILLUSTRATIONS	viii
LIST OF TABLES	xii
LIST OF SYMBOLS	xiii
INTRODUCTION	1
1.0 IDENTIFICATION AND CATEGORIZATION OF HELICOPTER SLING LOADS .	2
1.1 Initial Identification	2
1.2 Final Load Selection	3
2.0 LOAD ANALYSES	5
2.1 Currently Available Body of Data	5
2.2 Determination of Critical Loads and Carrying Speed Limitation	5
2.3 Loads for Initial Studies	5
2.4 Simplified Mathematical Models for Initial Studies	6
2.5 Method of Obtaining Sling-Load Aerodynamics	6
2.6 Limitations of Method	6
2.7 Analysis of Cargo Containers	7
2.8 Discussion of Errors in Analytical Data	14
2.9 Analyses of Other Sling Loads	17
2.10 Sources of Aerodynamic Characteristics Used in the Dynamic Analysis of Various Sling Loads	17
3.0 PILOT INTERVIEWS	19
3.1 Single-Point Suspension	19
3.2 Two-Point Suspension	21
3.3 Four-Point Suspension	22
4.0 DERIVATION OF EQUATIONS OF MOTION FOR COMBINED HELICOPTER AND SLING LOAD WITH LOAD AERODYNAMICS	23
4.1 Formulation of Simplified Mathematical Models for Dynamic Analysis	23
4.2 Stability Analysis of Pendulum/Yaw Oscillation Mode of Load With Drag Chute	30
4.3 Analytical Investigation of Coupled Helicopter and Sling-Load Dynamics	33
4.4 Optimal Control Analysis	36
4.5 Helicopter Flight Simulation	42
4.6 Flight Simulation of Helicopter/Sling-Load Dynamics	42
5.0 AERODYNAMIC EFFECTS OF FLOW FIELD ON THE SLING LOAD IN HOVER FLIGHT	57

TABLE OF CONTENTS - Continued

<u>Section</u>		<u>Page</u>
6.0	DEFINITION OF ACCEPTABLE AERODYNAMIC BOUNDARIES	61
6.1	Sensitivity Analysis of Stability Parameters and Related Stability Boundaries for Various Sling Loads	61
6.2	Stability Boundaries of Helicopter Sling Loads	63
6.3	Determination of Stable Flight Speeds for the Selected Helicopter Sling Loads	72
7.0	CURRENT TECHNOLOGY REVIEW	82
8.0	FORMULATION AND DEVELOPMENT OF CONCEPTUAL LOAD STABILIZATION SYSTEMS	84
8.1	Aerodynamic Load Stabilization With Rate Sensors and Vane Control Mounted on Beam	84
8.2	Sling-Load Stabilization Through Load Sensors and SAS Inputs	85
8.3	IR Sling-Load Display System	87
8.4	IR Sling-Load Monitor With Pitch and Roll Load Display and Pitch and Roll Rate Input to SAS	91
8.5	Gimbaled IR Active Load Monitor System	93
9.0	COST ESTIMATION OF PROPOSED LOAD STABILIZATION SYSTEM	95
9.1	Selected Sling-Load Stabilization System Concepts	103
9.2	System Trade-Off Analysis	110
10.0	METHODOLOGY FOR HELICOPTER SLING-LOAD STABILIZATION SYSTEM TRADE-OFF ANALYSIS	115
11.0	SIMULATOR DEMONSTRATIONS	118
11.1	Flight Simulator Equipment	118
11.2	Demonstration Objectives	121
11.3	Critical Dynamic Mode	123
11.4	Flight Demonstration Cases	123
11.5	Remarks	124
11.6	Typical Time Responses of Flight Simulations	125
11.7	Flight Simulator Validation	126
12.0	LOAD STABILIZATION SYSTEM PRELIMINARY DESIGN AND ANALYSIS	132
12.1	Design Analysis of Helicopter Sling-Load Stabilization System	132
12.2	Flight Simulation Demonstration on Large-Amplitude Flight Simulator	143
12.3	Flight Simulation Dynamic Time History	146
12.4	Description and Comments on the Flight Simulation Demonstration	147
13.0	CONCLUSIONS	149

TABLE OF CONTENTS - Concluded

<u>Section</u>		<u>Page</u>
LITERATURE CITED	• • • • •	152
APPENDIXES		
I. Nonlinear Body Aerodynamics	• • • • •	153
II. Coefficients and Derivatives for Analysis	• • • •	164
III. Helicopter Flight Simulation	• • • • •	196
DISTRIBUTION	• • • • •	216

LIST OF ILLUSTRATIONS

<u>Figure</u>		<u>Page</u>
1	Square Cylinder Data (Reference 2)	8
2	Square Cylinder Test Data (Reference 1)	11
3	Drag, Lift, and Pitching Moment vs Angle of Attack (Theory vs Tests, Reference 2)	12
4	Drag, Lift, and Pitching Moment vs Angle of Attack (8- by 8- by 20-Foot Container)	13
5	Drag, Lift, and Pitching Moment vs Angle of Attack (8- by 8- by 20-Foot Rounded End Container)	15
6	Geometry of Helicopter Sling-Load Pitch Plane	24
7	Externally Slung Helicopter Loads -- Axes System	26
8	Two-Degree-of-Freedom Load Model	28
9	Total System Block Diagram	33
10	Root Locus Plot for Case 5	37
11	Root Locus Plot for Case 6	38
12	Root Locus Plot for Case 17	39
13	Root Locus Plot for Case 29	40
14	Root Locus Plot for Case 41	41
15	Helicopter Flight Simulation -- Run 62	44
16	Flight Simulation of Helicopter/Sling-Load Dynamics -- Case 166(A)	45
17	Flight Simulation of Helicopter/Sling-Load Dynamics -- Case 166(B)	46
18	Flight Simulation of Helicopter/Sling-Load Dynamics -- Case 172(A)	47
19	Flight Simulation of Helicopter/Sling-Load Dynamics -- Case 172(B)	48
20	Flight Simulation of Helicopter/Sling-Load Dynamics -- Case 168(A)	49
21	Flight Simulation of Helicopter/Sling-Load Dynamics -- Case 168(B)	50
22	Flight Simulation of Helicopter/Sling-Load Dynamics -- Case 171(A)	51
23	Flight Simulation of Helicopter/Sling-Load Dynamics -- Case 171(B)	52
24	Flight Simulation of Helicopter/Sling-Load Dynamics -- Case 173(A)	53
25	Flight Simulation of Helicopter/Sling-Load Dynamics -- Case 173(B)	54
26	Flight Simulation of Helicopter/Sling-Load Dynamics -- Case 174(A)	55
27	Flight Simulation of Helicopter/Sling-Load Dynamics -- Case 174(B)	56
28	Axial Velocity vs Percent Rotor Radius	59
29	Sensitivity of Stable Maximum Flight Speed With Respect to Various Stability Parameters	62
30	Stability Boundaries of Helicopter Load -- Effect of Cable Lengths	65

LIST OF ILLUSTRATIONS - Continued

<u>Figure</u>	<u>Page</u>
31 Stability Boundaries of Helicopter Load -- Effect of $4 \times C_{n_8}$ Nominal (0.068) and Variable Cable Lengths	66
32 Stability Boundaries of Helicopter Load -- Effect of $0.5 \times C_{n_3}$ Nominal (0.068) and Variable Cable Lengths	67
33 Stability Boundaries of Helicopter Load -- Effect of $4 \times C_{y_8}$ Nominal (-0.205) and Variable Cable Lengths	68
34 Stability Boundaries of Helicopter Load -- Effect of $0.5 \times C_{y_8}$ Nominal (-0.205) and Variable Cable Lengths	69
35 Stability Boundaries of Helicopter Load -- Effect of C_{n_r} (Nominal = -0.00387)	70
36 Stability Derivative	81
37 Stability Boundaries of Helicopter Load -- Load Stabilization by Parachute	83
38 Rate Sensor Aerodynamic Load Stabilization	86
39 Load Stabilization With Rate Sensor and Accelerometer	88
40 IR Sling-Load Position Display	89
41 IR Active Load Stabilization	92
42 IR Gimbaled Load Monitor -- Active	94
43 Rate Sensor Aerodynamic Load Stabilization	98
44 Load Stabilization With Rate Sensor and Accelerometer	99
45 IR Sling-Load Position Display	100
46 IR Active Load Stabilization	101
47 IR Gimbaled Load Monitor -- Active	102
48 Loading Spreader Fixture Suspended by Four Load Cables	104
49 Adjustable Twist-Lock System	105
50 Retractable Flap System	106
51 Stabilizing Cable System With Cross-Stabilizing	107
52 Cable System With Longitudinal Stabilizing Cables	108
53 Auxiliary Cable System for Longitudinal and Lateral Stability, With Lateral Boom on Fuselage	109
54 Longitudinal Helicopter/Sling-Load Stabilization System Block Diagram	111
55 Lateral Helicopter/Sling-Load Stabilization System Block Diagram	112
56 Large-Amplitude Flight Simulator	119
57 Rotational Three-Axis Flight Simulator	122
58 Simulator Time Response -- Case 5(A)	128
59 Simulator Time Response -- Case 5(B)	129
60 Simulator Time Response -- Case 7(A)	130
61 Simulator Time Response -- Case 7(B)	131
62 Exact and Approximate Calculation of Mapping Circle Radius, r_c	159
63 Exact and Approximate Calculation of Mapping Coefficient, a_1	159
64 Exact and Approximate Calculation of Mapping Coefficient, a_0	160

LIST OF ILLUSTRATIONS - Continued

<u>Figure</u>		<u>Page</u>
65	Comparison of Coefficients Using Exact and Approximate Mapping Coefficients	161
66	Comparison of Test and Theoretical Coefficients for T-38 Fuselage	163
67	C_x , C_z , and C_m vs α	165
68	C_x , C_y , and C_n vs β	166
69	$C_{N\alpha}$ and C_m vs β	167
70	$C_{y\beta}$ and $C_{n\beta}$ vs α	168
71	C_{Nq} and $C_{m\beta}$ vs β	169
72	C_{y_r} and C_{n_r} vs β	170
73	Armored Reconnaissance/Airborne Assault Vehicle, M-551	171
74	C_x , C_z , and C_m vs α	172
75	C_x , C_y , and C_n vs β	173
76	$C_{N\alpha}$ and C_m vs β	174
77	$C_{y\beta}$ and $C_{n\beta}$ vs α	175
78	C_{Nq} and $C_{m\beta}$ vs α	176
79	C_{y_r} and C_{n_r} vs α	177
80	C_{Nq} and $C_{m\beta}$ vs β	178
81	C_{y_r} and C_{n_r} vs β	179
82	Truck, Cargo -- General Outline as Modified for Use in Computer Program	180
83	C_x , C_z , and C_m vs α	181
84	C_x , C_y , and C_n vs β	182
85	$C_{N\alpha}$ and C_m vs β	183
86	$C_{y\beta}$ and $C_{n\beta}$ vs α	184
87	C_{Nq} , C_{y_r} , $C_{m\beta}$, and C_{n_r} vs α	185
88	$C_{n\beta}$, C_{y_r} , $C_{m\beta}$, and C_{n_r} vs β	186
89	Command Post Carrier	187
90	C_x , C_z , and C_m vs α	188

LIST OF ILLUSTRATIONS - Concluded

LIST OF TABLES

<u>Table</u>	<u>Page</u>
I Typical Helicopter Sling Loads for Stabilization Study	4
II Sources of Aerodynamic Characteristics	18
III Maximum Acceptable Airspeed vs Load Configuration (Boeing/Vertol Flight Test Program)	21
IV Helicopter/Sling-Load Longitudinal Equations of Motion	25
V Helicopter/Sling-Load Lateral Equations of Motion	27
VI Summary of Pilot Model Variations	35
VII Summary of Dynamic Analysis Cases	36
VIII Load Evaluation	60
IX Effects of Various Stability Values and Cable Length on Airspeed	71
X Box (8- by 8- by 20-Foot)	76
XI Box (8- by 8- by 40-Foot)	77
XII Truck	78
XIII Tank	78
XIV Carrier	79
XV VH-34 Helicopter	79
XVI F-5 Aircraft	80
XVII OV-1 Aircraft	80
XVIII Rate Sensor/Aerodynamic Load Stabilization	95
XIX Rate Sensor and Accelerometer	96
XX IR Sling-Load Position Display	96
XXI IR Active Load Stabilization	97
XXII IR Gimbaled Load Monitor -- Active	97
XXIII Lifting Frequency of Sling-Load Category Lifted by CH-54 in Vietnam	110
XXIV Assigned Mission Frequency for Sling-Load Types Studied . .	114
XXV Stabilization System Trade-Off Approach	116
XXVI Cost Trade-Off Approach	117
XXVII Motion System Characteristics	118
XXVIII Projection System Characteristics	120
XXIX Stabilization System Gain Variation vs Speed, Load Stability Characteristics, and Cable Length	134
XXX Flight Simulator Cases Test Flown	145
XXXI Values per Line (Longitudinal Cases)	196
XXXII Values per Line (Lateral and Directional)	197

LIST OF SYMBOLS

A_x	Platform area of load
A_s	Frontal area of load
A_x/A_s	Fineness ratio of load
C_D	Drag coefficient
C_{D_C}	Viscous cross-flow drag coefficient
C_L	Lift coefficient
C_ℓ	Rolling moment coefficient
C_m	Pitching moment coefficient
C_{m_q}	Change in pitching moment coefficient with varying pitch rate
C_N	Body axis lift coefficient
C_n	Yawing moment coefficient
C_{n_q}	Change in yawing moment coefficient with varying pitch rate
C_{n_r}	Change in yawing moment coefficient with varying yaw rate
$C_{n_{\alpha_f}}$	Change in yawing moment coefficient with varying angle of attack as a function of fineness ratio
$C_{n_{\alpha_e}}$	Change in yawing moment coefficient with varying angle of attack for very large fineness ratio
$C_{n_{\beta}}$	Change in yawing moment coefficient with varying sideslip angle
C_{n_v}	Viscous contribution to viscous cross-flow drag coefficient
C_x, C_y, C_z	Force coefficients along X, Y and Z axes, respectively

LIST OF SYMBOLS - Continued

C_{y_r}	Change in side force coefficient with varying yaw rate
C_{y_β}	Change in side force coefficient with varying side-slip angle
c.m.	Center of mass
F_1	Front cable perturbed load
F_2	Rear cable perturbed load
f_k	Perturbation cable tensions, $k = 1, 2$
F_{k_0}	Reference steady motion cable tensions, $k = 1, 2$
F_x, F_z	Perturbation forces on helicopter due to load defined along X and Z axes, respectively
F_x', F_z'	Perturbation forces on helicopter due to load defined along X' and Z' axes, respectively
F_{x_L}, F_{z_L}	Perturbation forces defined along X_L and Z_L axes, respectively
g	Acceleration due to gravity
I_L, I_h	Pitch moment of inertia of load and of helicopter, respectively
K	Feedback gain
l	Distance between cable attachment points
l_1	Distance of forward cable's lower attachment point along X' axis
L, R	Cable length
M	Mass of helicopter plus load
m_h	Mass of helicopter

LIST OF SYMBOLS - Continued

M_i , x_k , z_i	Aerodynamic stability derivatives for helicopter, i = any input or perturbation
M_{i_L} , x_{i_L} , z_{i_L}	Aerodynamic stability derivatives for load; i = any input or perturbation
M_L	Mass of load
N	Feedback network
N_L	Distance of lower cable attachment points above X' axis
P	Roll rate
P_r	Routh's parameter
r	Yaw rate
s	Laplace transform operator
t	Time
U , \dot{U}	Helicopter velocity and acceleration, respectively, along X body axis
U_L , W_L	Perturbation velocities of X_L and Z_L axes
U_o , W_o	Reference steady motion velocities of X and Z axes
v , \dot{v}	Helicopter velocity and acceleration, respectively, along Y body axis
w , \dot{w}	Helicopter velocity and acceleration, respectively, along Z body axis
x , y , z	Helicopter body axes, origin at helicopter cm
x' , y' , z'	Helicopter body axes translated to load cm
x_L , y_L , z_L	Load body axes, origin at load cm
\bar{x}	Distance of forward upper cable attachment point from Z axis (defined positive along negative X axis)

LIST OF SYMBOLS - Continued

\bar{z}	Distance of upper cable attachment points below X axis
α	Angle of attack of helicopter
β	Sideslip angle of helicopter
β'	Reference steady motion distance of load cm from Z axis
Δ	Constant attitude angle from X' to X_L' axes (positive clockwise)
δ	Longitudinal stick deflection; input perturbation
δ_a	Lateral roll control
δ_e	Longitudinal pitch control
δ_p	Pilot control inputs
δ_r	Yaw control
δ_{LAT}	Lateral control deflection
δ_{RUD}	Rudder control deflection
η	Viscous cross-flow efficiency factor
η'	Reference steady motion distance of load cm from X axis
$\theta, \dot{\theta}, \ddot{\theta}$	Helicopter pitch angle, rate and acceleration, respectively
θ_o	Reference steady motion pitch attitude (from horizontal to X axis)
$\lambda, \dot{\lambda}$	Load pitch angle and rate, respectively
λ_o	Reference steady motion angle from Z axis to upper cable (positive clockwise)

LIST OF SYMBOLS - Continued

$\bar{\lambda}$

Total upper cable angle, $\bar{\lambda} = \lambda_0 + \lambda$

$\phi, \dot{\phi}, \ddot{\phi}$

Helicopter roll angle, rate and acceleration, respectively

$\phi_2, \dot{\phi}_2, \ddot{\phi}_2$

Angle, angular rate and angular acceleration, respectively, between helicopter Z-axis and the forward cable in the Y-Z plane

$\phi_3, \dot{\phi}_3, \ddot{\phi}_3$

Angle, angular rate and angular acceleration, respectively, between helicopter Z-axis and the aft cable in the Y-Z plane

$\phi_4, \dot{\phi}_4, \ddot{\phi}_4$

Angle, angular rate and angular acceleration, respectively, between the load Z_L -axis and the sling cable in the Y-Z plane

INTRODUCTION

Transportation of heavy loads slung externally from a helicopter has proved to be highly effective. Current techniques for suspending loads from helicopters in flight may result in the loads' assuming attitudes and exhibiting motions which can be attributed to the aerodynamic characteristics of the load. Typically, light loads with large surfaces exposed are most prone to experience disturbances which affect the stability of the transporting helicopter. Three types of undesirable motions are generally exhibited by the suspended load: pendular, yaw, and a combination of both. The pendular motion is most prevalent with relatively long cable lengths. Yaw motions can be encountered at virtually any cable length. The characteristics are currently accommodated by reducing the forward speed of the aircraft, which generally attenuates the aerodynamic forces on the suspended load until the motions are within tolerable levels. These factors preclude optimizing helicopter efficiency and productivity over a wide spectrum of loading conditions and may adversely affect stability and controllability of the aircraft.

With the advent of the next generation of transport helicopters, there exists a high probability of broader performance envelopes, relative to both speed and load-carrying capabilities. The work described by this report has been directed toward the analysis of those factors, both dynamic and aerodynamic, necessary to achieve acceptable behavior for a broad spectrum of loads when they are transported externally at forward speeds up to 150 knots equivalent airspeed (KEAS).

1.0 IDENTIFICATION AND CATEGORIZATION OF HELICOPTER SLING LOADS

1.1 INITIAL IDENTIFICATION

The initial task was an investigation to collect and specify basic external load data in terms of types of loads, sizes, weight, etc. To accomplish this, Northrop conducted data collection visits to the CDC Transportation Agency, Fort Eustis, Virginia; CDC Aviation Agency, Fort Rucker, Alabama; and Boeing/Vertol, Philadelphia, Pennsylvania. Based upon these visits, a Table of Organization and Equipment (TO&E) was developed to show all of the division level materiel which might be subjected to external transport by helicopter. In consideration of the largest quantity of items found in the TO&E (which would require helicopter lift for rapid and mobile deployment), as well as the weight, aerodynamic, and stability characteristics of the load, a candidate load list was developed.

Load Categorization

Aircraft, Helicopters and Airplanes

Data is available on the aerodynamics and geometry of the CH-34 and CH-47 helicopters. Pilot interviews have noted that the CH-34 is a stable load which may be carried up to at least 100 knots while the CH-47 is limited to a maximum speed of approximately 40 knots. As these represent well-known loads of great interest, they are particularly good cases to use in evaluating analyses, methods, and results.

Rectangular Box-Shaped Containers

Estimated data have been generated for a family of rectangular box-shaped containers which are representative of the cargo containers, vans, etc., which will constitute a large segment of the cargo to be carried in the future as external sling loads. The shapes involved have square cross-sections and varying fineness ratios.

Analyses involving these simple shapes aided in identifying the load characteristics which are conducive to the onset of load oscillations, as well as establishing the limiting speeds and stabilization required for successful carriage of the individual containers. Parametric studies have considered weight, cg, and inertia variations with each of the containers studied.

Trucks, Armored Personnel Carriers, etc.

Carrying characteristics of this type of load have been evaluated based upon estimated aerodynamic characteristics.

Netted Cargo

These loads are generally symmetrical and, when so rigged, can be carried at intermediate speeds. Analyses of these loads have considered differences in density as the major load variable, the load being considered aerodynamically as conical and with only secondary changes in shape.

Dense, High-Speed Loads; Howitzers, Tanks, etc.

These are the loads which present the least difficulty in carrying and which are least affected by aerodynamic forces.

Dense, Low-Speed Loads; Telephone Poles, Perforated Steel Plate

These loads, although they are very dense and heavy, are difficult to carry if held near the center of gravity. Analyses of these loads have added insight into the problem of carrying sling loads. Operationally, the difficulty in carrying these loads is generally overcome by supporting them near one end, rather than at the center of the load.

1.2 FINAL LOAD SELECTION

The typical helicopter sling loads studied in this program are shown in Table I. Due to the nonavailability of wind tunnel test and flight test data, the self-propelled tracked mortar, vehicle launched bridge, and howitzer load configurations were omitted. Flight test results indicate that the howitzer configuration does not create much problem in flight. Typical single-rotor helicopter (VH-34) and jet fighter aircraft (F-5) were studied as helicopter sling loads. Wind tunnel test data and flight data are available for these loads. These load configurations were considered aerodynamically and dynamically more meaningful for the studies. The basic load data of the helicopter sling loads studied in this program are summarized in Table I.

TABLE I. TYPICAL HELICOPTER SLING LOADS FOR STABILIZATION STUDY

Load Configuration	Model	Weight (pounds)	Dimensions (inches)			\bar{X}	\bar{Z}
			Length	Width	Height		
1. Container	Standard	5,000	240	96	96	120	48
2. Container	Standard	20,000	240	96	96	120	48
3. Cargo Truck	H-35	13,700	277	96	111	150	47
4. Sheridan Tank	XM-551	32,000	255	115	95	120	45
5. Command Post Carrier	H-113	19,300	192	106	98	94	45
6. Tandem-Rotor Helicopter	CH-47B	19,000	612	155	225	310	60
7. Single-Rotor Helicopter	VH-34	11,000	530	68	191	136	37
8. Jet Fighter Aircraft	F-5	10,000-15,000	563	330	165	300	15
9. Fixed-Wing Airplane	OV-1	10,500	525	504	155	165	41

\bar{X} , \bar{Z} (inches) Location of CG From Nose and Bottom of Load Configuration

2.0 LOAD ANALYSES

The loads selected for study were analyzed for force and moment measurements. Data for loads not deemed suitable for an analytical prediction of characteristics were obtained, where possible, from past experimental flight tests and wind tunnel programs.

2.1 CURRENTLY AVAILABLE BODY OF DATA

Literature searches and current investigations indicate that, in spite of the many and varied programs which have been and are dealing with this problem, there is no single source which summarizes the information that is known about the flight experiences where load oscillations have been encountered. Information available in military service operating manuals and contractor reports covers a limited number of loads and often lacks specifics concerning the quantitative data required for analyses.

Initial Northrop efforts on this program generated a summary of quantitative data relating to the definition of the critical loads and speeds sufficient for the analytical investigation to be accomplished. It would appear to be worthwhile to expand upon this and similar collections of information to provide a sound data base available to all investigators dealing with the external loads problem. It would be helpful if this collection of information would include means of access to any flight films showing load/helicopter oscillations.

2.2 DETERMINATION OF CRITICAL LOADS AND CARRYING SPEED LIMITATION

Analyses of the sling-load stability problem must begin with a quantitative definition of the problem. Information is required to establish the pertinent physical characteristics of critical loads, the nature of the load/helicopter oscillations involved, and the conditions under which the oscillations become sufficiently severe to impose a limitation on the carrying speed.

2.3 LOADS FOR INITIAL STUDIES

Initial studies used rectangular boxes of various lengths and with varying density, center of gravity, and moments of inertia for the externally slung loads. Use of this grouping of sling-load configurations permitted the generation of consistent aerodynamic data and aided in identifying the load characteristics and flight conditions which are conducive to the onset of load oscillations. Later studies analyzed other configurations.

2.4 SIMPLIFIED MATHEMATICAL MODELS FOR INITIAL STUDIES

Investigation involving simplified mathematical models of the helicopter/load configuration was used to gain insight into the basic nature of the instabilities involved. A two-degree-of-freedom model (pendulum plus yaw) was set up under the assumption of a carrying helicopter unaffected by load oscillations. Analyses of the roots of the resulting characteristic equation of the transient motion involved were conducted to aid in the understanding of the root causes of the load oscillations. Other simplified models were considered and were used during later stages of the program.

2.5 METHOD OF OBTAINING SLING-LOAD AERODYNAMICS

The aerodynamic analysis of the types of configurations which were considered for carriage by helicopter presents considerable difficulties, since these shapes are not streamlined for good aerodynamic performance. Aerodynamic methods basically designed to treat good aerodynamic shapes must be used to analyze bulky objects. The accuracy of the aerodynamic coefficients thus obtained becomes suspect, and an attempt must be made to determine the accuracy which is obtained.

The basic method which was used during the study contract to analyze the aerodynamic coefficients of slung helicopter loads was a computer program which was designed to analyze aircraft fuselages. This program analyzes the coefficients in two components. First a slender body calculation is made, using the basic methods outlined in Reference 1. A second component of the aerodynamic coefficients is obtained by using a viscous cross-flow theory. These two parts are added together, and this represents the complete aerodynamic coefficient.

The program computes five component force and moment coefficients-- C_N , C_m , C_y , C_n and C_ℓ --as functions of resultant angle of attack, roll angle, pitch rate and yaw rate. This permits the coefficients to be found for any body attitude. The method does not permit the calculation of the axial force coefficient, C_x .

This computer program is further described in Appendix I.

2.6 LIMITATIONS OF METHOD

The computer program was initially intended to treat slender bodies, and its use in analyzing slung helicopter loads such as cargo containers, trucks, etc., invalidates the slender body assumption and makes the results obtained of questionable accuracy. The program assumes that the frontal area of sections of the body change gradually in the axial direction. It was assumed that the initial cross-sectional area (at the nose) was zero and that a gradual buildup of area occurred. This means that, in analyzing

such shapes as the cargo container and the command post, a correction accounting for the instantaneous buildup of frontal area must be made to the machine calculations.

The program also does not contain any provision for computing the axial force coefficient, C_x , and thus supplemental methods must be used to estimate this coefficient.

In addition, the rolling moment coefficient predicted is based entirely on the slender body theory with no viscous cross-flow effect included. This makes this coefficient less likely to be accurate than the other coefficients.

2.7 ANALYSIS OF CARGO CONTAINERS

Lehmann² presents test data for square and circular cylinders at angles of attack between 0 and 90 degrees. Although the tests were performed with extremely small models, this was the only data available for box-like shapes of varying fineness ratios. It was decided to use the square cylinder data to check out and modify the prediction method, since the cargo container was of a similar shape.

Slender body theory and viscous cross-flow theory were used to obtain a comparison with this data. The theoretical value of C_{N_α} and a viscous cross-flow drag coefficient of 2 were used to obtain the correlation of Figure 1. This comparison shows that for the shorter cylinders the normal force was being overpredicted and, of course, no comparison was obtained for the axial force coefficient, C_x . The moment predicted was also in disagreement.

To improve and complete the comparison, modifications were made to the aerodynamics model. In predicting the normal force, it was determined that the potential or slender body contribution to the coefficient was of the form

$$C_{N_{pot}} = C_{N_\alpha} \sin \alpha \cos \alpha \quad (1)$$

where C_{N_α} is the theoretical slender body value obtained from Reference 1.

The viscous contribution was of the form

$$C_{N_{visc}} = C_{D_C} A_s / A_x \sin^2 \alpha \quad (2)$$

where C_{D_C} is the cross-flow drag coefficient.

● Test Data —— Slender Body - - - Viscous Cross-Flow —— Combined Theory

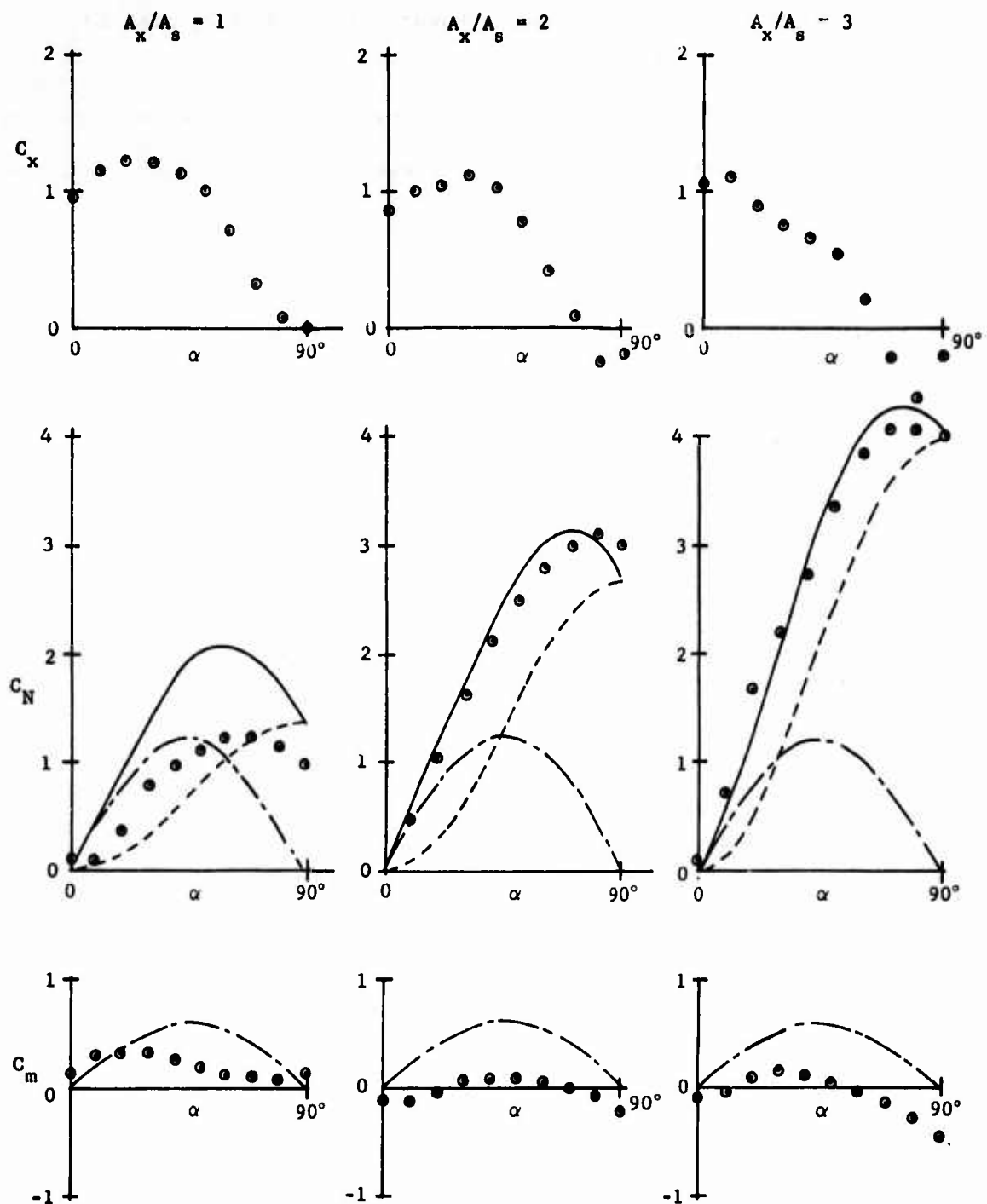
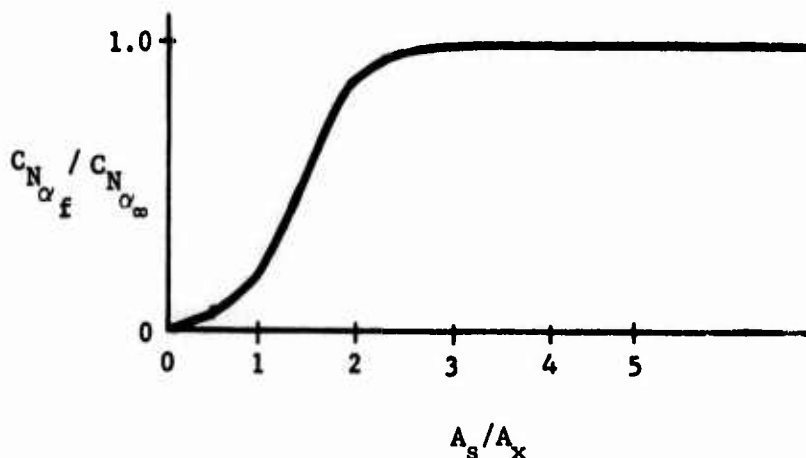


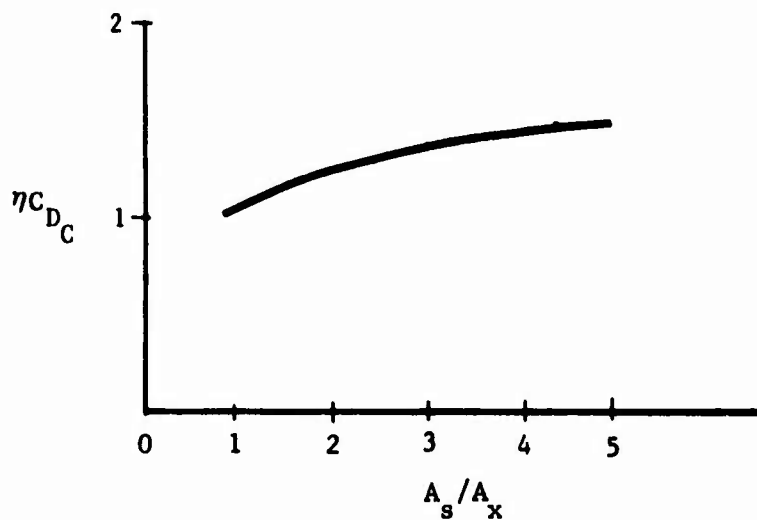
Figure 1. Square Cylinder Data (Reference 2).

To obtain better correlation, it was assumed that $C_{N_{\alpha_f}}$ and C_{D_C} would have to be functions of container fineness ratio. Therefore the test data was used to determine how these two parameters would vary. It was assumed that a parameter $C_{N_{\alpha_f}}$ should be used instead of $C_{N_{\alpha_{\infty}}}$ where $C_{N_{\alpha_f}}$ would be a function of fineness ratio. The curve below shows how this parameter was found to vary.



A similar variation was assumed to occur in the viscous cross-flow drag coefficient. In this case the value C_{D_C} was replaced by the parameters ηC_{D_C} where η was assumed to be a function of the fineness ratio.

Reference 3 indicates that, assuming a two-dimensional (i.e., a high fineness ratio) value of C_{D_C} , the value of ηC_{D_C} should vary as is shown in the curve below.



These values of C_N and $\frac{1}{2}C_D$ were then used to recompute the normal force coefficient for the three test cylinders.

To obtain the axial flow coefficient it was noted that for the cube the axial force and the normal force are identical, except that the normal force at 90-degree angle of attack is the axial force at 0-degree angle of attack and, similarly, the normal force at 0-degree angle of attack is the axial force at 90-degree angle of attack. It was postulated that the axial force would be independent of the body fineness ratio and this fact is substantiated to a reasonable degree by the test data. This permitted the axial force coefficient to be predicted by the equation for the normal force for the cube, with sine and cosine being reversed.

No method was found which would permit a valid expression to be determined for the pitching moment. In computing the pitching moment, however, it was assumed that the slender body component of the axial force acted at the body nose and that the viscous contribution was distributed evenly along the plane form. It is probable that these assumptions should be modified to obtain better moment agreement.

Figure 2 shows the correlation with Lehmann's test data which was obtained by making the above modifications. It appears that the axial and normal forces are predicted adequately but that the moment coefficient is not satisfactory. It should be noted, however, that the test moment coefficients are inconsistent in that they do not go to zero at 0-degree and 90-degree angle of attack. This may indicate that the test moment coefficients are not too reliable.

Figure 3 shows how the modified analytical method predicts the coefficients for an 8-by-8-by-20-foot container as compared to the two Lehmann models with fineness ratios spanning the containers.

After the above study was made, further data was obtained from an unpublished source. The theoretical comparisons with this data are shown in Figures 4 and 5. The container in Figure 4 shows a good correlation of D/q and L/q with a poor correlation of M/q . This seems to indicate that theoretical prediction of moments is unsatisfactory. The Figure 5 container had rounded ends and thus is not directly comparable to the theoretical results. The test values indicate lower values for D/q and higher values for L/q . For some reason the test moments are in better agreement with theory than the other comparisons show.

The modification parameters C_N and $\frac{1}{2}C_D$ as described above were then

used in the computer program to predict the rotary derivatives of the container. The matching of the static coefficients with test data should permit the calculation of more reliable rotary derivatives.

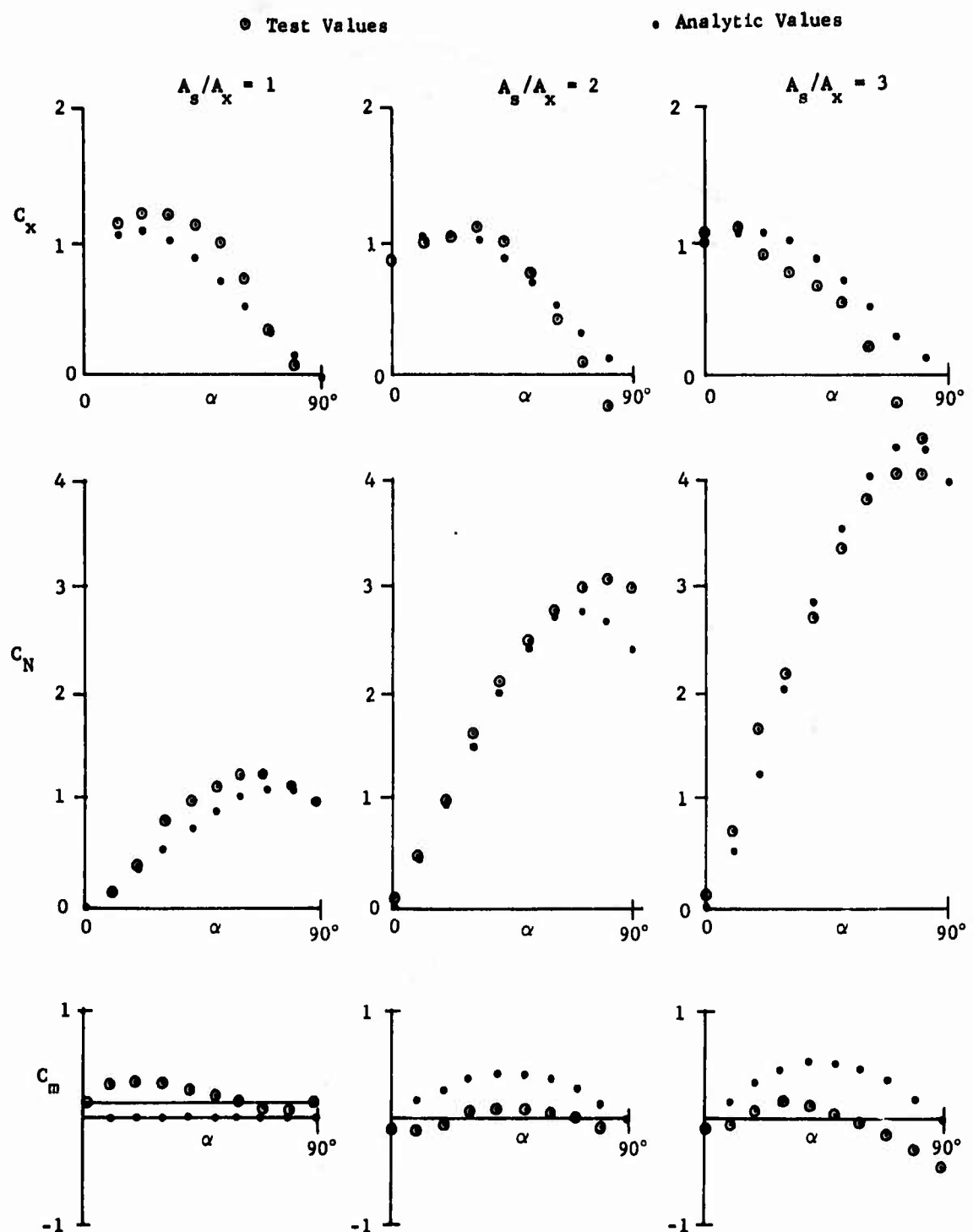


Figure 2. Square Cylinder Test Data (Reference 1).

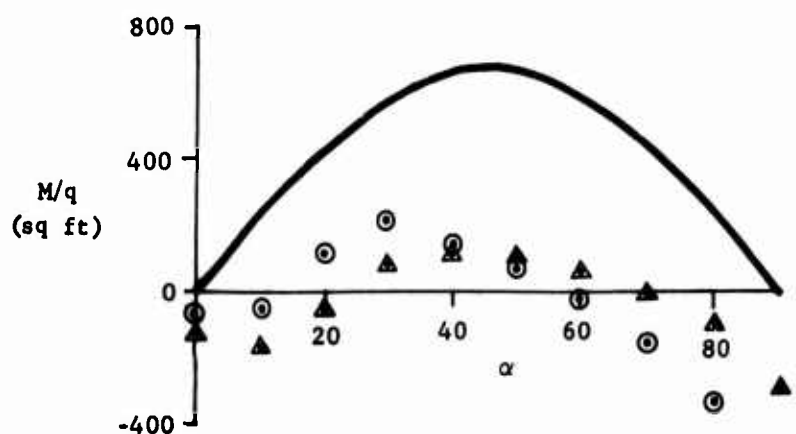
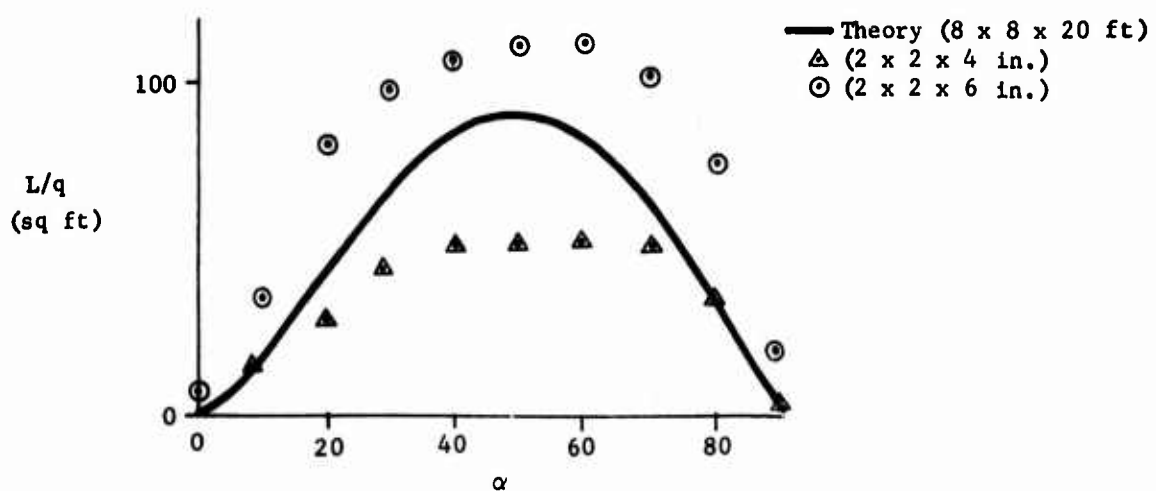
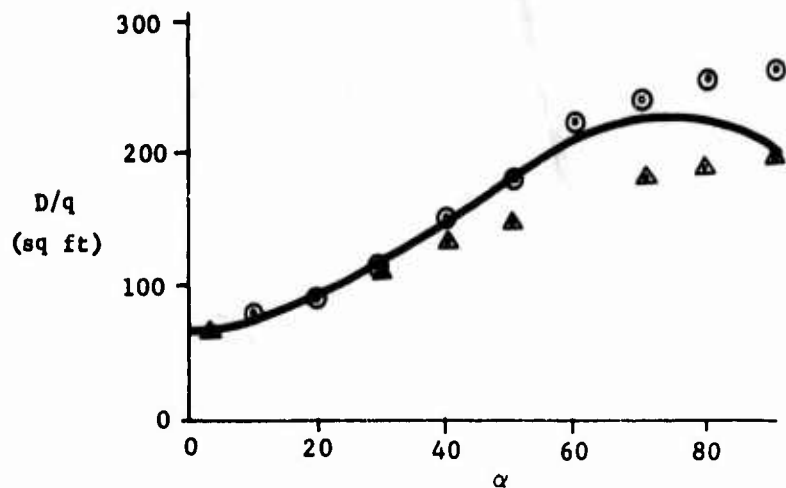


Figure 3. Drag, Lift, and Pitching Moment vs Angle of Attack (Theory vs Tests, Reference 2).

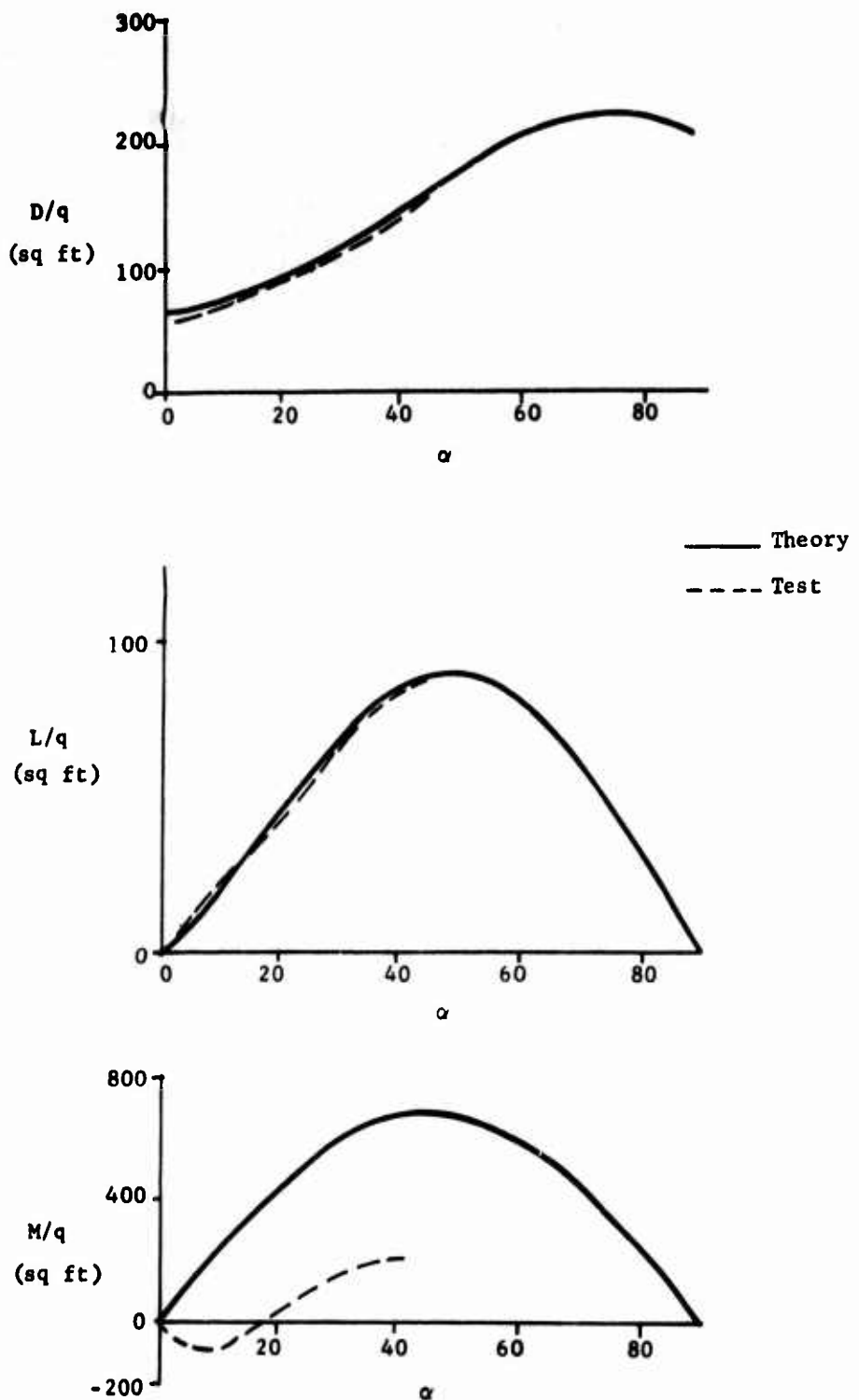


Figure 4. Drag, Lift, and Pitching Moment vs Angle of Attack (8- by 8- by 20-Foot Container).

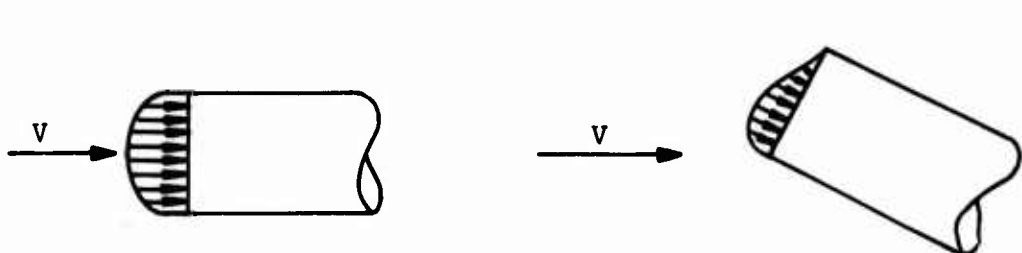
2.8 DISCUSSION OF ERRORS IN ANALYTICAL DATA

In order to determine the reliability of the theoretical predictions for the other configurations in this study, it is necessary to postulate the sources of error in the prediction of the pitching moment. The theoretical predictions are based on a combination of slender body theory and viscous cross-flow. The slender body theory relates the local normal force on a body to the rate of change of body cross-section. In the case of boxes such as those under consideration, the blunt face of the box represents an abrupt change of body cross-section and an impulsive lift force is predicted at the front of the box. This represents the total slender body contribution to the box's normal force and pitching moment.

The viscous cross-flow contribution accounts for separation on the upper surface by distributing a cross-flow drag along the body proportional to the local cross-sectional shape and to the cross-flow component of velocity. This results in a considerable component of lift or normal force but no contribution to the pitching moment (in the case of a container with moment center at the centroid of area).

In considering the actual flow about the box, one can postulate three possible areas of discrepancy to account for the disagreement between theory and test:

1. In applying the slender body theory, one applies an impulsive and highly localized force at the nose of the box. It seems that in actual fact this force would be distributed over a larger portion of the box and would result in less pitching moment than has been predicted. Test results (from an unpublished source) for a box with rounded corners are shown in Figure 5. Assuming that the rounding of the corners prevents separation on the lower surface, it would appear that these test results show a pitching moment more nearly representative of that to be expected due to a distribution of the slender body load on the box. From these tests it appears that perhaps the slender body load should be applied at somewhere near one-fourth of the body length.
2. The pressure distribution on the front face is such as to cause a restoring pitching moment as shown in the following sketch:



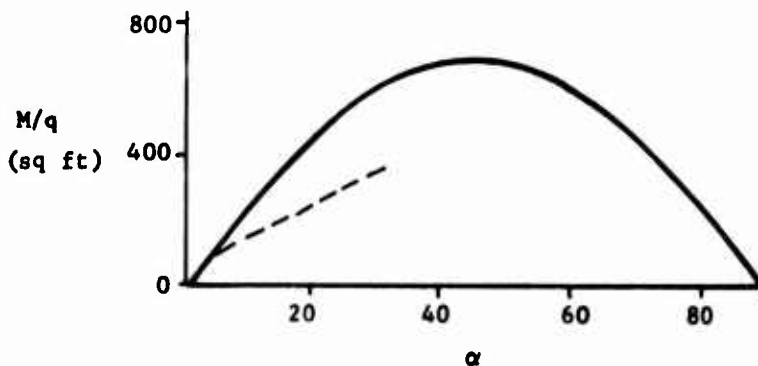
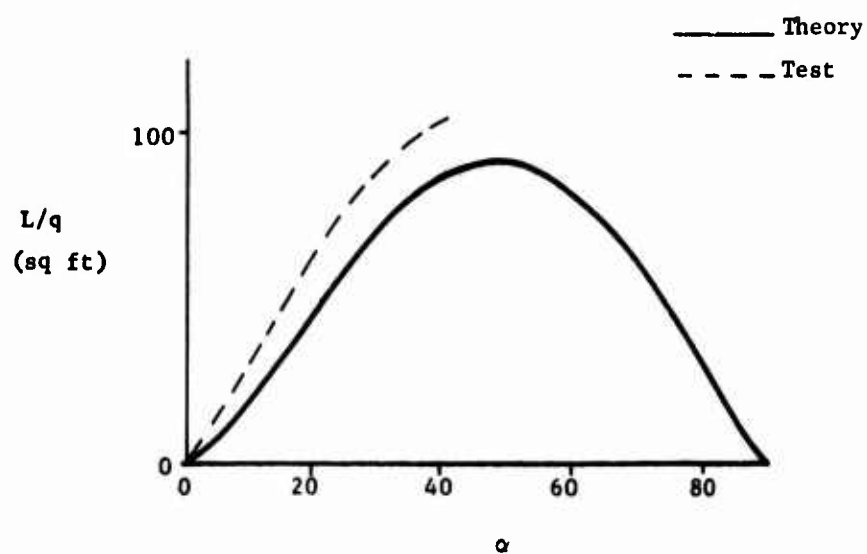
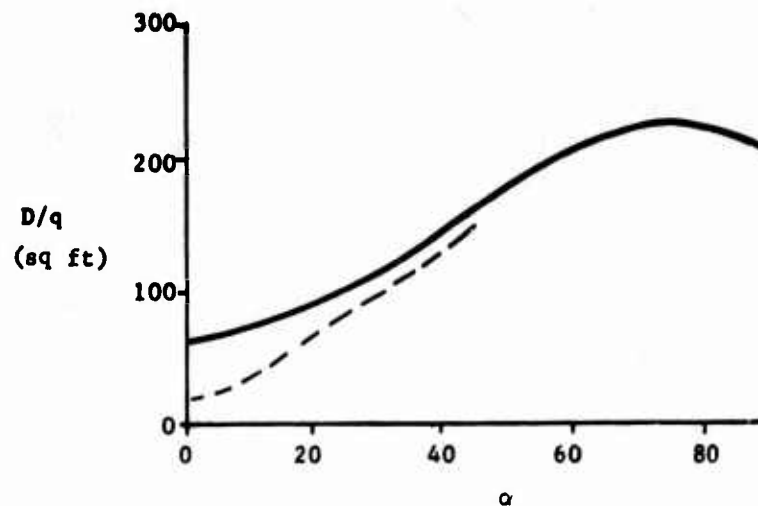
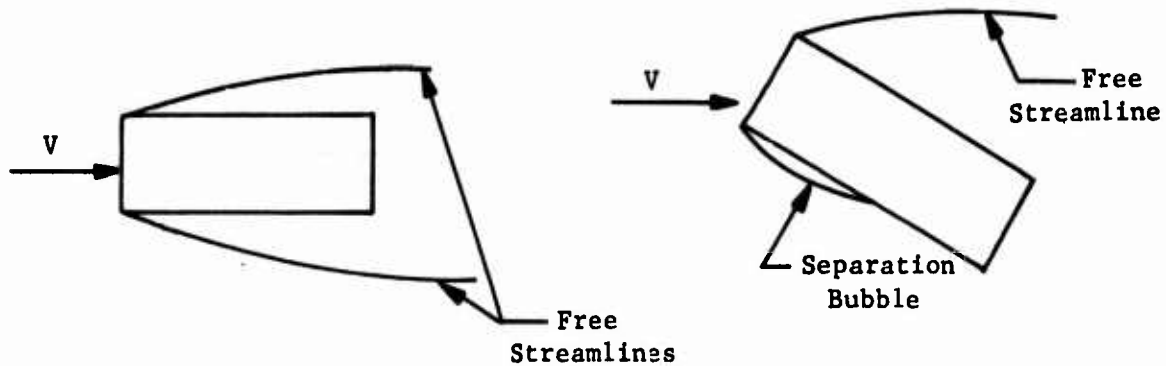


Figure 5. Drag, Lift, and Pitching Moment vs Angle of Attack (8- by 8- by 20-Foot Rounded End Container).

This shift in the pressure force on the front face cannot be accounted for theoretically but has been shown to exist in tests of flat plates.

3. The sharp corners of the front face cause the flow about the body to separate along the lower surface, causing a region of low pressure as shown in the following sketch:



The viscous cross-flow term in the theoretical calculations accounts for the separation effects on the upper surface but does not account for separation on the lower surface.

These three sources of error tend to cause a lower pitching moment than is predicted theoretically, especially at low angles of attack, and may account fully for the discrepancy noted.

On other configurations of this study (i.e., truck, tank, and command post carrier), items 2 and 3 above are less critical, since the front ends of these vehicles do not present blunt faces to the wind. In the case of the tank and the command post carrier, there is an impulsive force at the front of these vehicles in the slender body representation of the forces and moments.

It is not possible to include these effects in the theoretical calculations, except for the slender body effect, and the justification for modifying this may not be warranted.

2.9 ANALYSES OF OTHER SLING LOADS

Aerodynamic coefficients and derivations have also been computed for three other sling loads (a cargo truck, M-35A1; an armored reconnaissance/airborne assault vehicle, M-551; and a command post carrier, M-577A1), using the computer program. These results are presented in Appendix II.

This program required that the area, centroid of area, mapping circle radius, r_c , and one other coefficient of the mapping, a_1 , be estimated as continuous functions of distance along the axis, as is discussed in Appendix II. This required that an idealized description of the vehicles be used, since all of the protuberances and singularities cannot be treated analytically. The area variation and centroid of area were estimated from these outlines and the two mapping function coefficients, r_c and a_1 , were estimated by the following formulas:

$$r_c = \frac{b/2 + a/2}{2} \quad (3)$$

$$a_1 = \frac{b/2 - a/2}{2} \quad (4)$$

where a and b are the maximum horizontal and vertical dimensions.

A drag force at zero angle of attack was estimated from test data for similar shapes, using Reference 4. $\frac{TC}{DC}$ was estimated to be 1.13 in both the lateral and vertical directions.

2.10 SOURCES OF AERODYNAMIC CHARACTERISTICS USED IN THE DYNAMIC ANALYSIS OF VARIOUS SLING LOADS

Sources of aerodynamic characteristics used in the dynamic analysis of various proposed sling-load configurations studied in this program are summarized in Table II. These represent the best sources available for the various sling-load configurations.

TABLE II. SOURCES OF AERODYNAMIC CHARACTERISTICS

Load Configuration	Model	Weight (pounds)	Sources of Aerodynamic Characteristics
1. Container	Standard	5,000	University of Maryland Wind Tunnel
2. Container	Standard	20,000	University of Maryland Wind Tunnel
3. Cargo Truck	M-35	13,700	Northrop Analytical Data
4. Sheridan Tank	XM-551	32,000	Northrop Analytical Data
5. Command Post Carrier	M-113	19,300	Northrop Analytical Data
6. Tandem-Rotor Helicopter	CH-47B	19,000	Boeing/Vertol Wind Tunnel Data
7. Single-Rotor Helicopter	VH-34	11,000	Sikorsky Data
8. Jet Fighter Aircraft	F-5	10,000-15,000	Northrop Wind Tunnel Data
9. Fixed-Wing Airplane	OV-1	10,500	Grumman Wind Tunnel Data

3.0 PILOT INTERVIEWS

Interviews with pilots having flight experience with external loads were conducted to aid in listing critical loads and carrying speeds, and to ensure that analytical efforts focus on practical aspects of the carrying problem. Those interviewed include Northrop pilots with recent helicopter load-carrying experience and pilots from the 56th Marine Air Group stationed at El Toro Marine Air Station.

The following information has been categorized by type of load suspension rather than by the nature of the load, since the former represents a more clear-cut distinction.

3.1 SINGLE-POINT SUSPENSION

This is the most common type of load suspension. It is the standard CH-47 suspension technique and is used to transport 96 percent of the loads carried by the CH-54 in Vietnam.

Compact, heavy, dense loads are the easiest to transport. These are such things as armored vehicles, trucks and artillery pieces. A 2-1/2-ton truck, an A-1E aircraft and a D-5 bulldozer did not require retrim on air-speed once cruise speed had been established. The truck and bulldozer spun in a slow and apparently random manner (in the order of 30 seconds per revolution). The A-1E aircraft, with wings folded and props feathered, aligned quickly into the wind and exhibited small (2- to 3-degree) yaw oscillations.

The CH-46 helicopter is limited to a carrying speed of about 80 knots provided that it streamlines into the flow. It tends to hang in a broadside position at low speeds. The Marines use drag chutes to aid in establishing it in a streamlined position at low speed. Once the higher speed is attained, the CH-46 will generally stabilize without the chutes. This opinion does not agree with other known flight experience.

The CH-34 helicopter makes a stable load and may be carried to at least 100 knots.

A stripped CH-47 fuselage rotated about the hook in hover. In a climb at 40 knots the load exhibited a random ± 60 -degree yaw motion. In level flight the load assumed a stable position with a slight right yaw. Speed buildup was begun at 50 knots and the load remained stable in all maneuvers. The buildup was continued to a maximum speed of 70 knots, where the load remained stable. However, the trail angle reached a point where the aft end of the load was only 8 to 10 feet from the loading ramp (mother ship was also a CH-47). The helicopter was decelerated to 40-50 knots and a descent initiated. During this descent a very heavy pitching and yawing oscillation was excited in the load. The load turned broadside, imposing a very heavy deceleration, then yawed back to approximately zero yaw and pitched

down to an extremely nose-low altitude, which brought the aft end of the load very close to the ramp of the lifting helicopter. When forward speed was reduced to 30 knots, the oscillation damped. A maximum speed of 30 knots would then be imposed on this configuration. The normal retrieval configuration should, however, be somewhat more stable than this test configuration, which was stripped of most large removable items and so only weighed 3,700 pounds and had most window covers and doors removed.

Vans (approximately 8 by 8 by 20 feet with weights of about 10,000 pounds) tend to head into the wind but oscillate in yaw such that their carrying speed limit is about 40 knots. A UPS-1 Radar Van (approximately cube-shaped) has been carried at speeds up to 60 knots, experiencing oscillations only during deceleration.

Boeing/Vertol conducted tests with a shipping container(8 by 8 by 20 feet, 5,200 pounds). In hover, the container was stable to collective pitch excitations and exhibited a random slow rotation about the hook. The helicopter was accelerated to 50 knots and, during a climb, the container yawed from left to right ± 45 degrees, producing heavy accelerations in the helicopter. In level flight at 60 knots the container assumed a broad-side condition and occasionally made a complete rotation about the hook. This yaw motion, coupled with the resultant lateral and longitudinal swinging of the container, caused heavy, long-period accelerations and decelerations in the helicopter and required the pilot to make frequent control inputs to maintain the desired flight condition. The heavy load motions appeared likely to result in a collision between load and helicopter. A maximum speed of 40 knots was considered safe for normal maneuvering.

A 105 mm howitzer represented a high-density load which could be carried to power-limited speeds (greater than 130 knots in the case of the CH-47).

Long loads, such as telephone poles, perforated steel planking, etc., with load attachment at the center of gravity are generally very difficult to carry. They may be readily transported if held near one end.

Low-density loads, such as construction materials, lumber, C-rations and barbed wire, present the largest stability problem. In flight with these loads, it is frequently necessary to reduce airspeed and/or altitude to reduce the amplitude of sling-load oscillations. At a speed of 80 knots, a load consisting of a cargo net of C-ration cartons spun at about one revolution per 8 seconds. After a short while the load began a pendulum mode in roll. This oscillation imparted perceptible roll moments to the aircraft. Airspeed was reduced to 70 knots and then to 40 knots until the load became stable in both roll and spin. Airspeed was gradually increased to 70 knots and the load remained stable for the rest of the mission.

At least insofar as the single-point suspension load-carrying technique is concerned, sling-load operations are restricted to VFR conditions. Attempts to fly sling loads in IFR conditions have caused severe problems in load stability. The instrument and motion cues are too dissimilar to VFR or conventional IFR flight for the pilot to maintain effective control of the sling load.

3.2 TWO-POINT SUSPENSION

Boeing/Vertol has investigated two-point suspension systems with the points displaced both laterally and longitudinally. Wind tunnel tests showed that the laterally displaced system, as could be anticipated, was extremely prone to longitudinal swinging. The longitudinally displaced system exhibited good yaw restraint, control of load attitude, and minimum longitudinal swinging. It has been found that low density, aerodynamically unstable loads such as shipping containers were most stable when flown at slightly nose-down attitudes. Consequently, the ability to control load attitude is of extreme importance. As a result of the wind tunnel tests only the two-point longitudinally displaced system was carried over into the flight test program. The shipping container, stripped CH-47 fuselage, and 105-mm howitzer loads were flown with a 24-foot separation on 7.5- and 50-foot cables, with and without a spreader beam above the four nylon risers connected to the load. In addition, the shipping containers and the howitzer were flown on 100-foot cables. All three loads were also flown on a 7.5-foot cable length with a 12-foot separation. Results are summarized in Table III.

The two-point longitudinally displaced system resulted in greatly reduced load oscillations when compared with a conventional single-point system. Most striking was the fourfold improvement in maximum airspeed capability when carrying the CH-47 fuselage. Use of the spreader improved stability slightly but represented a weight penalty and increased load hookup time.

TABLE III. MAXIMUM ACCEPTABLE AIRSPEED VS LOAD CONFIGURATION
(BOEING/VERTOL FLIGHT TEST PROGRAM)

Configuration	Load		
	Shipping Container	CH-47	Howitzer
	Airspeed (knots)		
7.5-ft cable, 24-ft separation	120*	120*	135*
50-ft cable, 24-ft separation	65	50	---
100-ft cable, 24-ft separation	50	---	---
7.5-ft cable, 12-ft separation	115*	115*	135*

*Maximum airspeed of flight test

3.3 FOUR-POINT SUSPENSION

The Sikorsky CH-54 helicopter has provisions for the four-point suspension of loads which lend themselves to the use of this technique. The most representative loads are CONEX's, trucks and engineer equipment. Use of suitable rigging makes it possible to accommodate loads such as lumber, palletized equipment and house trailers.

Utilization of the four-point system in Vietnam has been limited to 4 percent of all CH-54 loads due to (1) the requirement for making center-of-gravity computations in order to maintain the in-flight stability of the CH-54, and (2) the time required to make a four-point hookup. Aside from these problems, it has been found that, in general, loads carried by four points are stable, permitting higher airspeeds than single-point suspension systems, and making possible prolonged instrument flight.

4.0 DERIVATION OF EQUATIONS OF MOTION FOR COMBINED HELICOPTER AND SLING LOAD WITH LOAD AERODYNAMICS

The equations derived by Abzug⁷ are for a load with no aerodynamics. These equations were extended to include the significant aerodynamic effects. The equations will accommodate single or double cable with attach points at any centerline point on the helicopter.

Figure 6 describes the geometry of the helicopter sling-load pitch plane. Table IV presents the basic helicopter and sling-load longitudinal equations. The lateral geometry and equations are presented in Figure 7 and Table V.

These equations were augmented with the appropriate stability augmentation system for analysis. Realistic simulation was achieved by computing euler angles instead of the integral of body rates.

4.1 FORMULATION OF SIMPLIFIED MATHEMATICAL MODELS FOR DYNAMIC ANALYSIS

The two-degree-of-freedom model shown in Figure 8 was set up assuming that the carrying helicopter is unaffected by the load or its oscillations. Also, for this simplified model, roll of the load with respect to the cable was assumed to be zero; i.e., the load plane of symmetry parallels the cable, which is assumed to lie on a straight line from the load center of gravity to the carrying helicopter support point.

With the above assumptions the equations of load motion may be set up as shown below:

ψ = Rotation of load about its z-axis, positive for nose right

β = Sideslip angle

ϕ = Rotation of load about its x-axis, positive counterclockwise roll

Side Force Equation

$$[mR\ddot{\phi} - C_{y\beta} \cdot q \cdot s \cdot \frac{R}{V} \dot{\phi} + W \sin \phi] + C_{y\beta} \cdot q \cdot s \cdot \psi = 0 \quad (5)$$

Yawing Moment Equation

$$[-C_{n\beta} \cdot q_{sb} \left(\frac{R}{V}\right) \dot{\phi}] + [I_z \ddot{\psi} - C_{n\beta} q_{sb} \dot{\phi} + C_{n\beta} q_{sb} \psi] = 0 \quad (6)$$

Combined Equations

The stability determinant can be set up from Equations (5) and (6) as follows:

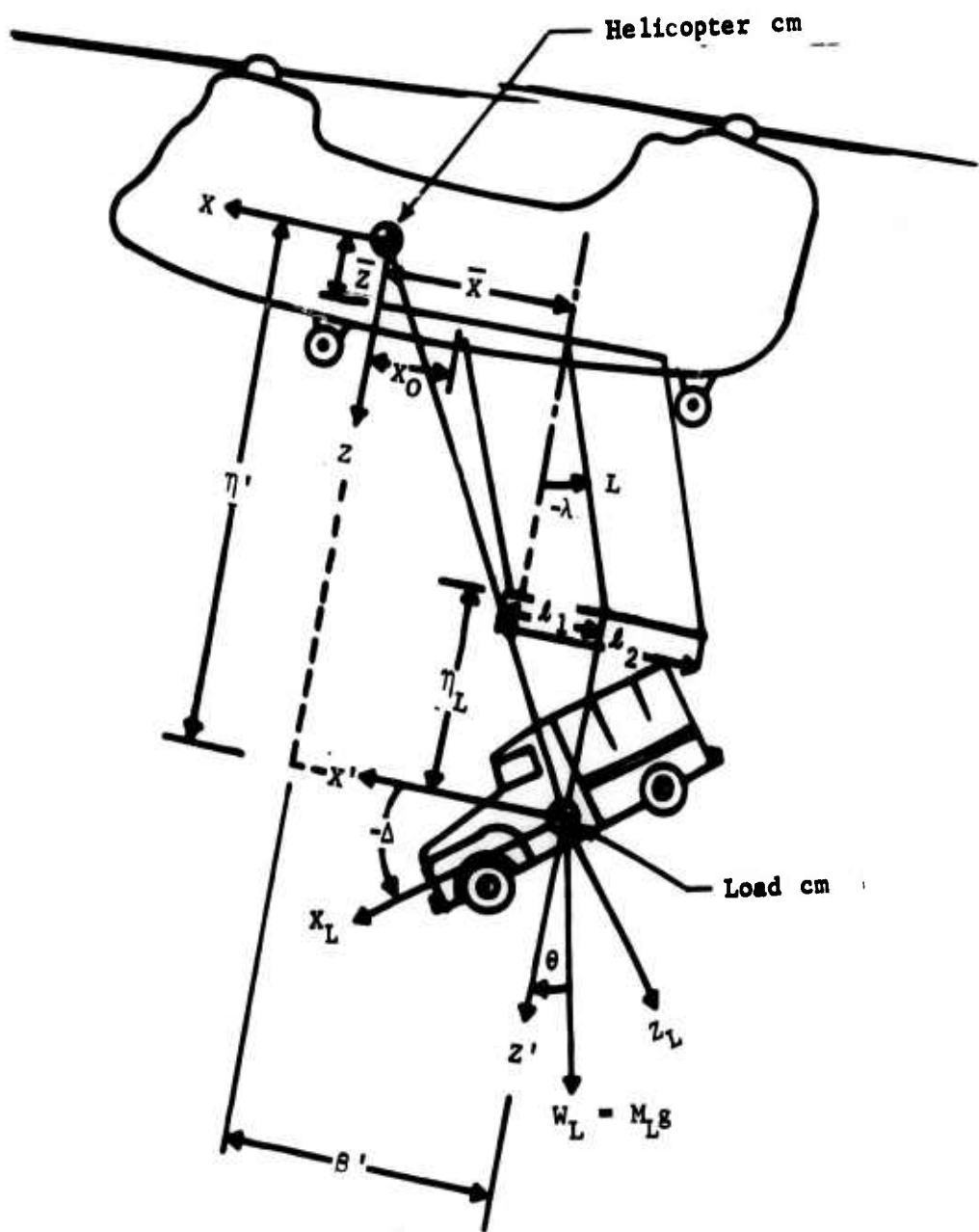


Figure 6. Geometry of Helicopter Sling-Load Pitch Plane.

TABLE IV. HELICOPTER/SLING-LOAD LONGITUDINAL EQUATIONS OF MOTION

$\frac{X_u}{H}$	$\frac{X_v}{H}$	$\frac{X_w}{H}$	$\frac{X_L}{H} \eta' s - \frac{Z_L}{H} s + s$	$\frac{X_L}{H} L (\cos \lambda_o) s^2$	0	0	0	$\frac{Z_L}{H}$
$-\frac{Z_u}{H}$	$s - \frac{Z_w}{H}$	$-\frac{X_L}{H} \theta' s^2$	$-\frac{X_L}{H} L (\sin \lambda_o) s^2$	$-\frac{L}{H} X_L s$				$\frac{Z_L}{H}$
		$-(U_o + \frac{Z_L}{H}) s$	$+\frac{L}{H} Z_L s$					
$X_L \eta' s$	$-X_L \theta' s$	$(L_{V_a} + M_{Lr}^2) s^2$	$M_L L (\eta' \cos \lambda_o$	0	0	0	M_6	
$-X_u$	$-X_u$	$+ [-U_o \theta' M_L - M_q] s$	$+ \theta' \sin \lambda_o) s^2$	$-L_{M_L} s$				
		$+ M_L s \eta'$	$+ \theta' \lambda$					
$(\cos \Delta) s$	$(\sin \Delta) s$	$\eta_L s^2 - \frac{Z_{D1}}{H} s$	$L \cos (\lambda_o - \Delta) s^2$	$\frac{\sin (\lambda_o - \Delta)}{H_L}$				
$-\frac{Z_{D1}}{H_L}$	$+\frac{X_{D1}}{H_L}$	$+ Z \cos \Delta$	$-L \frac{Z_{D1}}{H_L} s$	$-X_L$				
$(\sin \Delta) s$	$(\cos \Delta) s$	$-\theta_L s^2$	$-L \sin (\lambda_o - \Delta) s^2$	$\frac{\cos (\lambda_o - \Delta)}{H_L}$				
$-\frac{Z_{D2}}{H_L}$	$-\frac{X_{D2}}{H_L}$	$-(U_{L0} + \frac{Z_{D2}}{H_L}) s$	$-L \frac{Z_{D2}}{H_L} s$	$-X_2$				
$-X_{D2}$	$-X_{D2}$	$+ Z \sin \Delta$	$-L M_{D1} s$	$-\eta_L \sin \lambda_o$				
		$L_{V_L} s^2 - M_{D2} s$	$-P_{10} (\eta_1 \cos \lambda_o$	$-f_1 \cos \lambda_o$				
			$-P_{10} (\eta_1 \cos \lambda_o$	$-f_2 \sin \lambda_o$				
			$+ (f_2 - f_1)$	$\cos \lambda_o$				
			$\sin \lambda_o$					

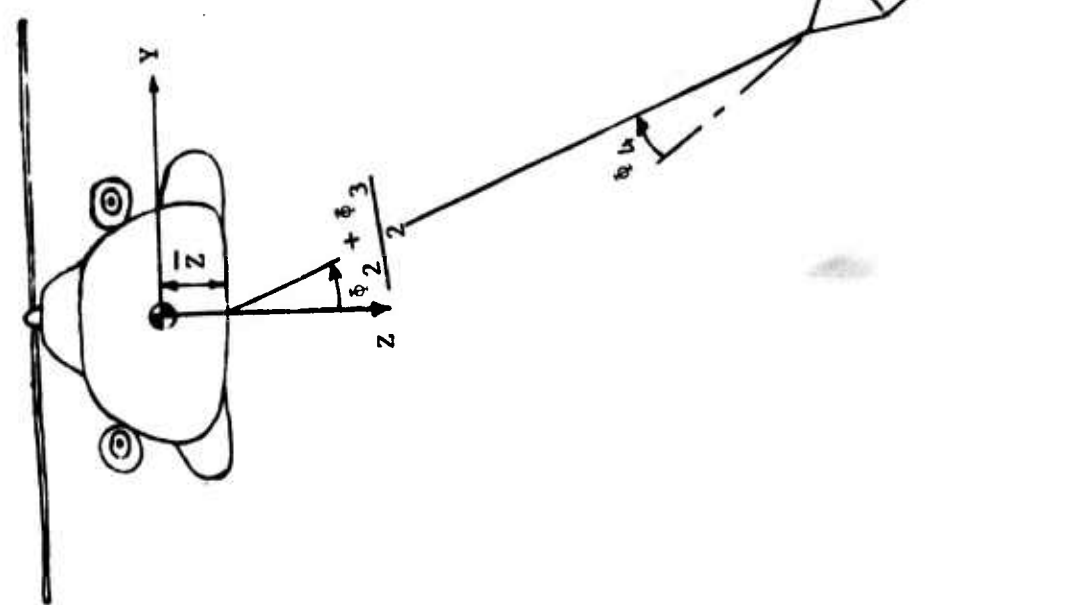
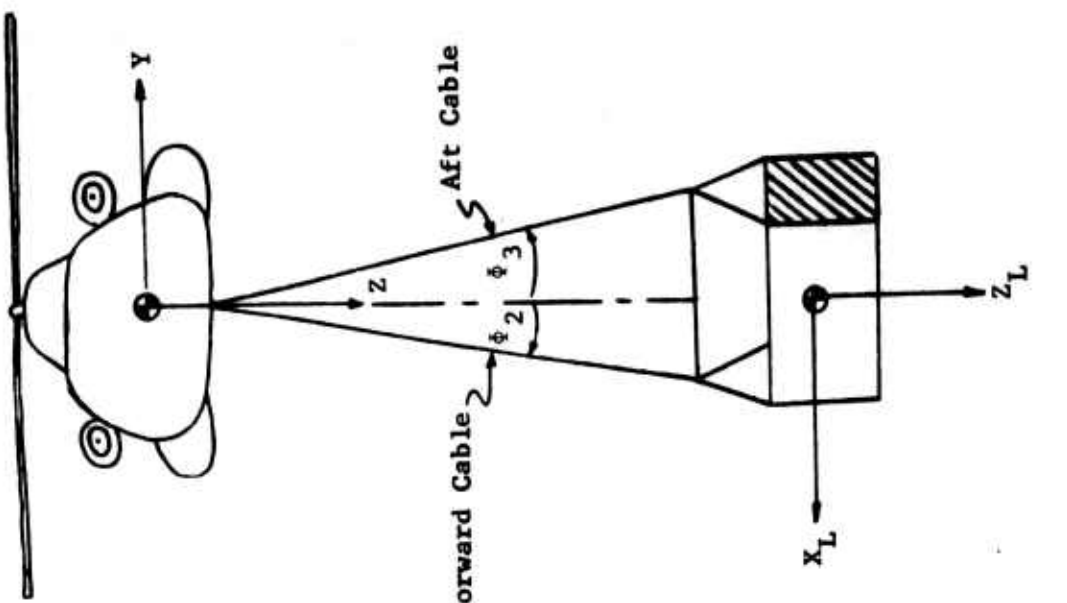


Figure 7. Externally Slung Helicopter Loads -- Axes System.

TABLE V. HELICOPTER/SLING-LOAD LATERAL EQUATIONS OF MOTION

$s - \frac{y_v}{N}$	$\frac{-N_L}{N} (L + \bar{Z}) S^2$ $-\frac{Y_P}{N} S - g$	$u_o S - \frac{Y_r}{N} S$	$\frac{-N_L}{N} \frac{L}{2} S^2$ $+C_1 \dot{\theta}_2 S + C_1 \dot{\theta}_3$	$\frac{-N_L}{N} \frac{L}{2} S^2$ $+C_1 \dot{\theta}_3 S + C_1 \dot{\theta}_4$	$c_{1\dot{\theta}_4} S$ $+C_1 \dot{\theta}_4$	v	$\frac{Y_r}{N} \dot{\theta}_{LAT}$	$\frac{Y_r}{N}$ $\dot{\theta}_{LAT}$
\dot{x}_v	$I_{x_h} S^2 - \mathcal{K}_p S$ $+N_L (L + \bar{Z})^2 S^2$	$-I_{x_h} S^2 - \mathcal{K}_r S$ $+N_L g (L + \bar{Z})$	$\frac{N_L}{2} (L + \bar{Z}) LS^2$ $+C_2 \dot{\theta}_2 S + C_2 \dot{\theta}_3$ $+N_L g L$	$\frac{N_L}{2} (L + \bar{Z}) LS^2$ $+C_2 \dot{\theta}_3 S + C_2 \dot{\theta}_4$ $+N_L g L$	$c_{2\dot{\theta}_4} S$ $+C_2 \dot{\theta}_4$	ϕ	$L_z \dot{\theta}_{LAT}$	L_z $\dot{\theta}_{LAT}$
$-N_v$	$-I_{x_h} S^2 - N_p S$	$I_{z_h} S^2 - N_r S$	$\frac{N_L}{4} g L_2$ $+C_3 \dot{\theta}_2 S + C_3 \dot{\theta}_3$	$\frac{N_L}{4} g L_2$ $+C_3 \dot{\theta}_3 S + C_3 \dot{\theta}_4$	0	ψ	$N_6 \dot{\theta}_{LAT}$	N_6 $\dot{\theta}_{LAT}$
$s - c_{4v}$	$-(L + \bar{Z}) S^2$ $-g + C_4 \dot{\theta}^2$	$u_o S + C_{4r} S$	$-\frac{L}{2} S^2 - \frac{g}{2}$ $+C_4 \dot{\theta}_2 S + C_4 \dot{\theta}_3$	$-\frac{L}{2} S^2 - \frac{g}{2}$ $+C_4 \dot{\theta}_3 S + C_4 \dot{\theta}_4$	0	ψ_2	$=$ $[c_{LAT}] +$ $[e_R]$	0
$-c_{5v}$	$I_{x_L} S^2 - C_5 \dot{\theta}^2$	$C_{5r} S$	$\frac{I_{x_L} S^2}{2} + C_5 \dot{\theta}_2$	$\frac{I_{x_L} S^2}{2} + C_5 \dot{\theta}_3$ $+C_5 \dot{\theta}_4$	$I_{x_L} S^2$ $+C_5 \dot{\theta}_4$	ϵ_3	0	ϵ_4

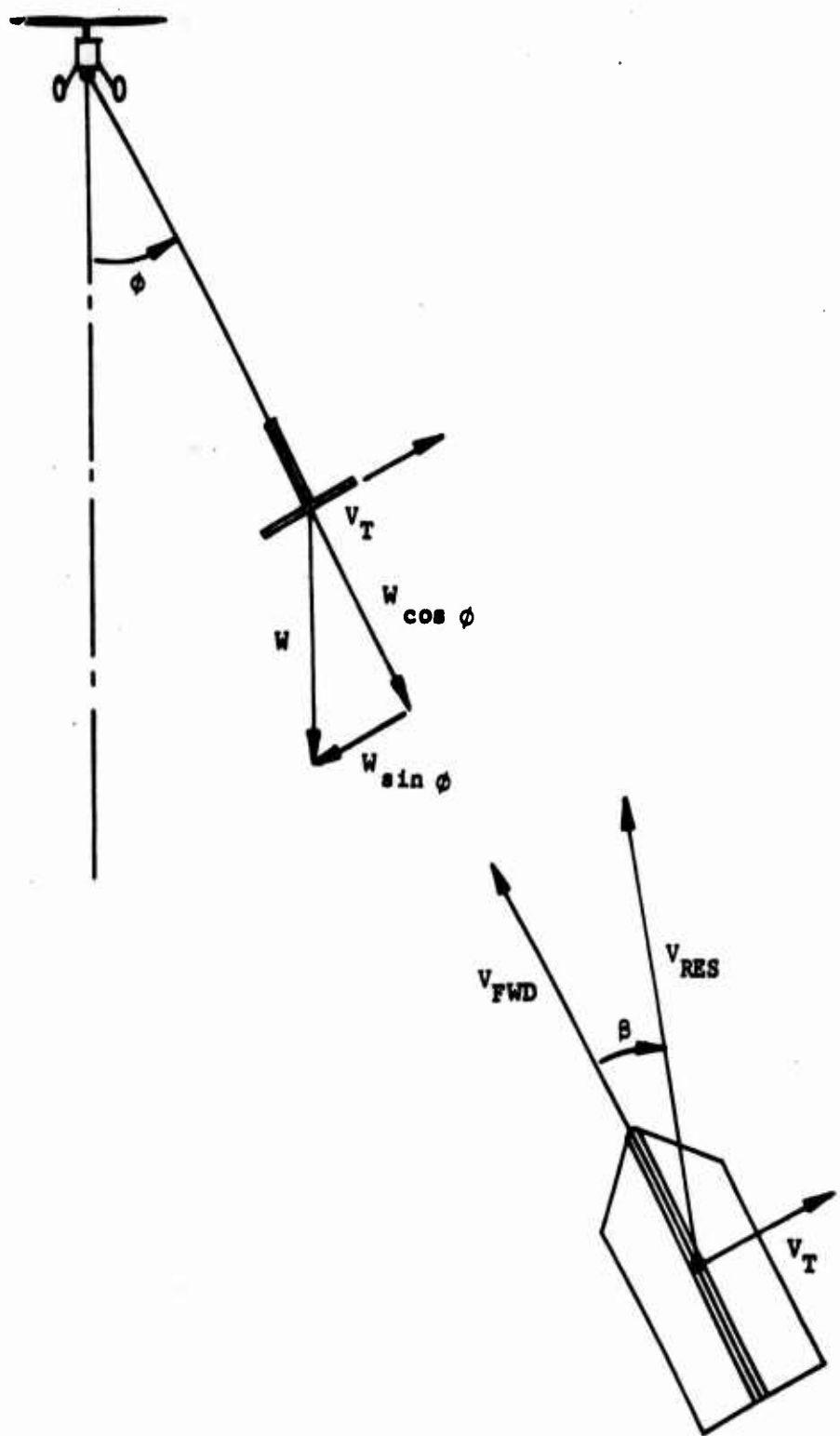


Figure 8. Two-Degree-of-Freedom Load Model.

$$\left[s^2 - \left(\frac{C_{y_B} q s R}{m R V} \right) s + \frac{W}{m R} \right] \phi + \left[\frac{C_{y_B} q s}{m R} \right] \dot{\psi} = 0 \quad (7)$$

$$\left[- \left(\frac{C_{n_V} q s b R}{I_z V} \right) s \right] \phi + \left[s^2 - \left(\frac{C_{n_V} q s b}{I_z} \right) s + \left(\frac{C_{n_B} q s b}{I_z} \right) \right] \dot{\psi} = 0 \quad (8)$$

$$\begin{aligned} |D_s| &= \text{Stability Determinant} \\ &= \begin{vmatrix} s^2 - \left(\frac{A}{V} \right) s + D & \frac{A}{R} \\ - \left(\frac{C R}{V} \right) s & s^2 - B s + C \end{vmatrix} \end{aligned} \quad (9)$$

where $A = \frac{C_{y_B} q s}{m}$,

$$B = \frac{C_{n_V} q s b}{I_z},$$

$$C = \frac{C_{n_B} q s b}{I_z},$$

and $D = \frac{W}{m R} = \frac{K}{R}$.

$$|D_s| = a s^4 + b s^3 + c s^2 + d s + e \quad (10)$$

where $a = 1$,

$$b = - \frac{q s}{m} \left[\frac{C_{n_V} b}{k_z^2} + \frac{C_{y_B}}{V} \right],$$

$$c = \frac{K}{R} + \frac{q s}{m} \left[\frac{C_{n_B} b}{k_z^2} + C_{y_B} \left(\frac{C_{n_V} q s b}{I_z V} \right) \right],$$

$$d = - \left(\frac{q q s b}{R I_z} \right) C_{n_V},$$

and $e = \left(\frac{q q s b}{R I_z} \right) C_{y_B}.$

For a stable system, the conditions on the coefficients of the stability determinant quartic are:

(a) a, b, d and $e > 0$

$$\text{i.e., } C_{n_y} < 0, C_{y_B} < 0, C_{n_B} > 0 \quad (11)$$

(b) $d(bc - ad) - b^2e > 0$

$$\left\{ - \left(\frac{C_{n_y} b}{k_z^2} + \frac{C_{y_B}}{V} \right) \left[\frac{g}{R} + \frac{q_s}{m k_z^2} \left(C_{n_B} b + \frac{C_{y_B} C_{n_y} q_s b}{m V} \right) \right] + \left(\frac{b g}{k_z^2 R} \right) C_{n_y} \right\} \\ + \frac{q_s}{m} \left(\frac{C_{n_y} b}{k_z^2} + \frac{C_{y_B}}{V} \right)^2 \frac{C_{n_B}}{C_{n_y}} > 0 \quad (12)$$

The results of this analysis are summarized in Section 6.

4.2 STABILITY ANALYSIS OF PENDULUM/YAW OSCILLATION MODE OF LOAD WITH DRAG CHUTE

4.2.1 Modification and Revision to Characteristic Equation

The pendulum/yaw oscillation mode model was analyzed further, and the effect of stabilizing drag chutes attached at the load centerline aft of the cg was included in the characteristic equation and in the stability parameter.

The following are the characteristic equation and stability parameters with the stabilizing drag chute effect included:

$$\lambda^4 + B \lambda^3 + C \lambda^2 + D \lambda + E = 0 \quad (13)$$

where $B = - \frac{1}{2 \mu} \left(C_{y_B} + \frac{1}{2} \cdot \frac{\ell^2}{k_z^2} \cdot C_{n_r} \right)$

$$C = \frac{g \ell^2}{4 R V^2} + \frac{1}{4 \mu} \cdot \frac{\ell^2}{k_z^2} \cdot \left(\frac{1}{2 \mu} C_{y_B} C_{n_r} + C_{n_B} - \frac{\ell_p}{\ell} C_{D_p} \right)$$

$$D = \frac{1}{8\mu} \cdot \frac{\ell^2}{k_z^2} \left[\frac{1}{\mu} \left(C_{n_p} C_{D_0} + \frac{\ell_p}{\ell} C_{y_p} C_{D_p} \right) - \frac{g\ell^2}{2RV^2} C_{n_r} \right]$$

$$E = \frac{g\ell^4}{16\mu R k_z^2 V^2} \cdot \left(C_{n_p} - \frac{\ell_p}{\ell} C_{D_p} \right)$$

$$\mu = \frac{2m}{\rho S \ell}$$

ℓ = reference dimension, ft

S_R = reference area, sq ft

R = cable length, ft

m = mass of load, slugs

$$C_{y_p} = \frac{\partial C}{\partial \beta} \text{ /rad}$$

$$C_{n_p} = \frac{\partial C}{\partial \theta} \text{ /rad}$$

$$C_{D_p} = \text{parachute drag coefficient} = \frac{D(\text{parachute})}{qS_R}$$

$$C_{n_r} = \frac{\partial C}{\partial \left(\frac{r\ell}{2V} \right)} \text{ /rad}$$

$$C_{D_0} = \text{load drag coefficient} = \frac{\text{Load Drag}}{qS_R}$$

V = flight speed, ft/sec

k_z = radius of gyration

ℓ_p = distance from chute attachment point to cg of load

g = gravity constant

4.2.2 Conditions for Stability

(a) $B, D, \text{ and } E > 0$

(14)

As the sign of C_{y_p} and C_{n_r} will almost certainly be negative for

configurations which would be considered, B should always be positive. Positive signs on D and E require that C_{n_p} be positive and that

$$\frac{1}{\mu} \left(C_{n_B} C_{D_o} + \frac{\ell_p}{\ell} C_{y_B} C_{D_p} \right) - \frac{g\ell^2}{2Rv^2} C_{n_r} > 0 \quad (15)$$

and

$$\left(C_{n_B} - \frac{\ell_p}{\ell} C_{D_p} \right) > 0 \quad (16)$$

$$(b) \text{ Routh's Parameter, } R = D(BC-AD)-B^2E > 0 \quad (17)$$

The modified and corrected Routh's stability parameter to include the effect of load drag and effect of stabilizing chute is presented in the following:

Let

$$B = b_1 \quad (18)$$

$$\text{where } b_1 = -\frac{1}{2\mu} \left(C_{y_B} + \frac{1}{2} \frac{\ell^2}{k_z} C_{n_r} \right)$$

$$C = \frac{C_1}{F^*} + C_2 \quad (19)$$

$$\text{where } C_1 = \frac{1}{4}$$

$$\text{and } C_2 = \frac{1}{8\mu^2} \frac{\ell^2}{k_z^2} C_{y_B} C_{n_r} + \frac{1}{4\mu} \frac{\ell^2}{k_z^2} \left(C_{n_B} - \frac{\ell_p}{\ell} C_{D_p} \right)$$

$$D = \frac{d_1}{F^*} + d_2 \quad (20)$$

$$\text{where } d_1 = -\frac{1}{16\mu} \frac{\ell^2}{k_z^2} C_{n_r}$$

$$\text{and } d_2 = +\frac{1}{8\mu^2} \frac{\ell^2}{k_z^2} \left(C_{D_o} C_{n_B} + \frac{\ell_p}{\ell} C_{y_B} C_{D_p} \right)$$

$$E = \frac{e_1}{F^*} \quad (21)$$

$$\text{where } e_1 = \frac{1}{16\mu} \frac{\ell^2}{k_z^2} \left(C_{n_B} - \frac{\ell_p}{\ell} C_{D_p} \right) \quad \text{and} \quad F^* = \frac{V^2 R}{\ell^2 g}$$

The results of this analysis are summarized in Section 6.

4.3 ANALYTICAL INVESTIGATION OF COUPLED HELICOPTER AND SLING-LOAD DYNAMICS

The dynamics of a large helicopter/VTOL vehicle carrying a sling load are very complex. The basic cargo-carrying vehicle may be unstable within the normal flight envelope and will therefore have associated stability augmentation systems. A pilot's ability to increase the stability of the system should be considered. Analysis should be done with various combinations of vehicles, loads, and control systems. Hence, an automated method of analyzing the total system stability was developed.

The digital computer program written to analyze the vehicle/load/pilot system was built up using a general-purpose subprogram designed to handle matrices and polynomials. In simplest terms, the computer program receives a matrix description of the total system, uses Cramer's rule to determine required transfer function, factors the transfer function to obtain poles and zeros of the system, and plots the resulting information to form a root locus. Since the differences in vehicle responses between the single- and tandem-rotor helicopter equipped with SAS are not significant for analyzing the sling-load dynamic problem, the tandem-rotor helicopter was used as the generalized helicopter model. The two-point suspension system was used, since some limited flight results were available, and the effect of a single-point suspension system could be estimated from the data presented in Section 6.3.

The method for generating the matrices which describe the system is most easily understood through an example. Consider the system diagrammed in Figure 9.

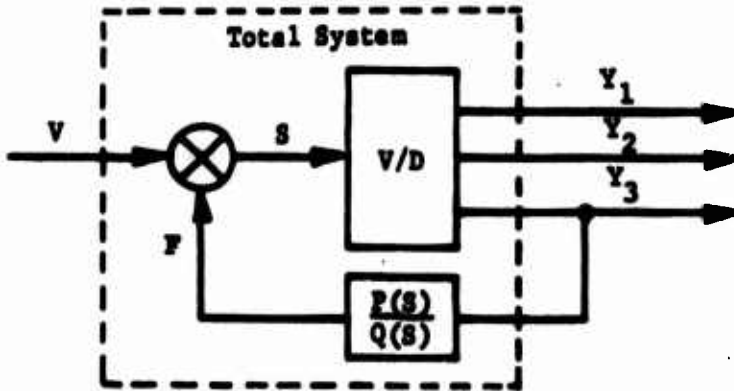


Figure 9. Total System Block Diagram.

The total system (indicated by the broken line) has the input V and the output Y_3 . The system consists of the vehicle dynamics with a feedback to an actuator. The standard matrix description of the vehicle dynamics is familiar.

$$\begin{bmatrix} V/D \end{bmatrix} \begin{bmatrix} Y_1 \\ Y_2 \\ Y_3 \end{bmatrix} = \begin{bmatrix} S \end{bmatrix} \quad (22)$$

Incorporating the feedback loop

$$F = \frac{P(S)}{Q(S)} \quad Y_3$$

into the matrix equation yields

$$\begin{bmatrix} A \end{bmatrix} \begin{bmatrix} Y_1 \\ Y_2 \\ Y_3 \end{bmatrix} = \begin{bmatrix} V \end{bmatrix} \quad (23)$$

The determinate of A is taken and factored to find the roots of the system. Cramer's rule is applied to the input and output to determine the zeros of the system.

Inertia characteristics of the 8- by 8- by 20-foot container were input in the program along with its inherent aerodynamic characteristics.

The equations of motion (Tables IV and V), representing the coupled helicopter/sling-load dynamics, and the helicopter SAS and modeled roll and yaw "pilot" controllers were used for the dynamic analyses.

The root locus analysis included (a) pilot model gain and lead stabilization, (b) helicopter SAS feedback, and (c) load feedback.

Table VI summarizes a set of pilot model variations. A roll pilot controller in the form of $-K_p (T_L S + 1) e^{-0.2S}$ was used, where K_p is the pilot gain and T_L is the pilot lead. For each case studied, K_p was varied in the steps 0.0, 0.05, 0.1, 0.2, and 0.4. The yaw pilot controller was fixed at $-0.1 (2.5S + 1) e^{-0.2S}$. There were eight vehicle-load configurations, with three pilot lead variations and five pilot gains for a total of 240 points. Of these, 39 were stable, although many of these were not necessarily flyable.

The 50-knot, 10-foot cable cases were quite stable at both $C_{n_p} = 0.5$ and $C_{n_p} = 2.5$. When the cable was increased to 100 feet, approximately half of

TABLE VI. SUMMARY OF PILOT MODEL VARIATIONS

No. of Stable Conditions	$C_{n_B} = 0.5$		$C_{n_B} = 2.5$			
	Velocity (knots)				C_L	T_L
	50	150	50	150		
5	5	Marginal to Unstable	5	Unstable	10	0
	4	3	3	Unstable	10	1.0
	4	3	3	Unstable	10	2.5
	3	Unstable	Unstable	Unstable	100	0
	2	Unstable	2	Unstable	100	1.0
	2	Unstable	Unstable	Unstable	100	2.5

the points were stable at a $C_{n_B} = 0.5$. At the high C_{n_B} all cases were unstable except two points at a pilot lead of $T_L = 0.2$. The 150-knot cases were all unstable except $C_{n_B} = 0.5$.

It should be noted that, while high speed and a long cable always decreased stability, pilot lead sometimes helped and sometimes hurt stability.

The high-speed, high C_{n_B} case was picked as a worst case for further investigation, with poor results. Both helicopter feedback and load parameter feedback were tried to stabilize this case. Differential cable angle and rate were fed back to the helicopter rudder, and total cable angle and rate were sent to the helicopter roll control. The pole-zero combination was so bad that the stabilization attempt usually led to an improvement in one set of poles at the expense of another.

It was concluded that, while further attempts would probably result in a theoretically stable helicopter, it would not be flyable.

The analysis was continued with the approach of Section 12.

Table VII summarizes the dynamic analysis cases. For cases 1 through 24, a $C_{n_B} = 0.5/\text{rad}$ was used; for cases 25 through 48, $C_{n_B} = 2.5/\text{rad}$. The even-numbered cases cover the area near the origin in expanded scale.

TABLE VII. SUMMARY OF DYNAMIC ANALYSIS CASES

Case No.	Velocity (knots)				C_L	T_L
	50	150	50	150		
1,2	13,14	25,26	37,38	10	0	
3,4	15,16	27,28	39,40	10	1.0	
5,6	17,18	29,30	41,42	10	2.5	
7,8	19,20	31,32	43,44	100	0	
9,10	21,22	33,34	45,46	100	1.0	
11,12	23,24	35,36	47,48	100	2.5	

Note that, in general, high roll controller gain around 0.4 or higher will lead to instability; 100-foot cable length cases are less stable than 10-foot cable length cases; the lower C_L cases are easier to stabilize than the cases with high C_L . Such results have been validated and substantiated by flight simulation.

Figures 10 through 14 are root locus plots for cases 5, 6, 17, 29, and 41.

4.4 OPTIMAL CONTROL ANALYSIS

The lateral equations of motion were converted to state variable form and checked to see that they gave the same solution as the derived equations. These equations were input to Northrop's FORTRAN Automatic Synthesis Program (FASP). The program is a FORTRAN version of the NASA Automatic Synthesis Program. The equations, control inputs, and performance index are input to the program which sets up the Riccati equation and solves for the optimal gains.

Many performance indexes were tried to reduce certain gains, and ratios of control power allocated to the rudder and aileron were used to minimize the total workload on the helicopter. The results are presented in Section 12.

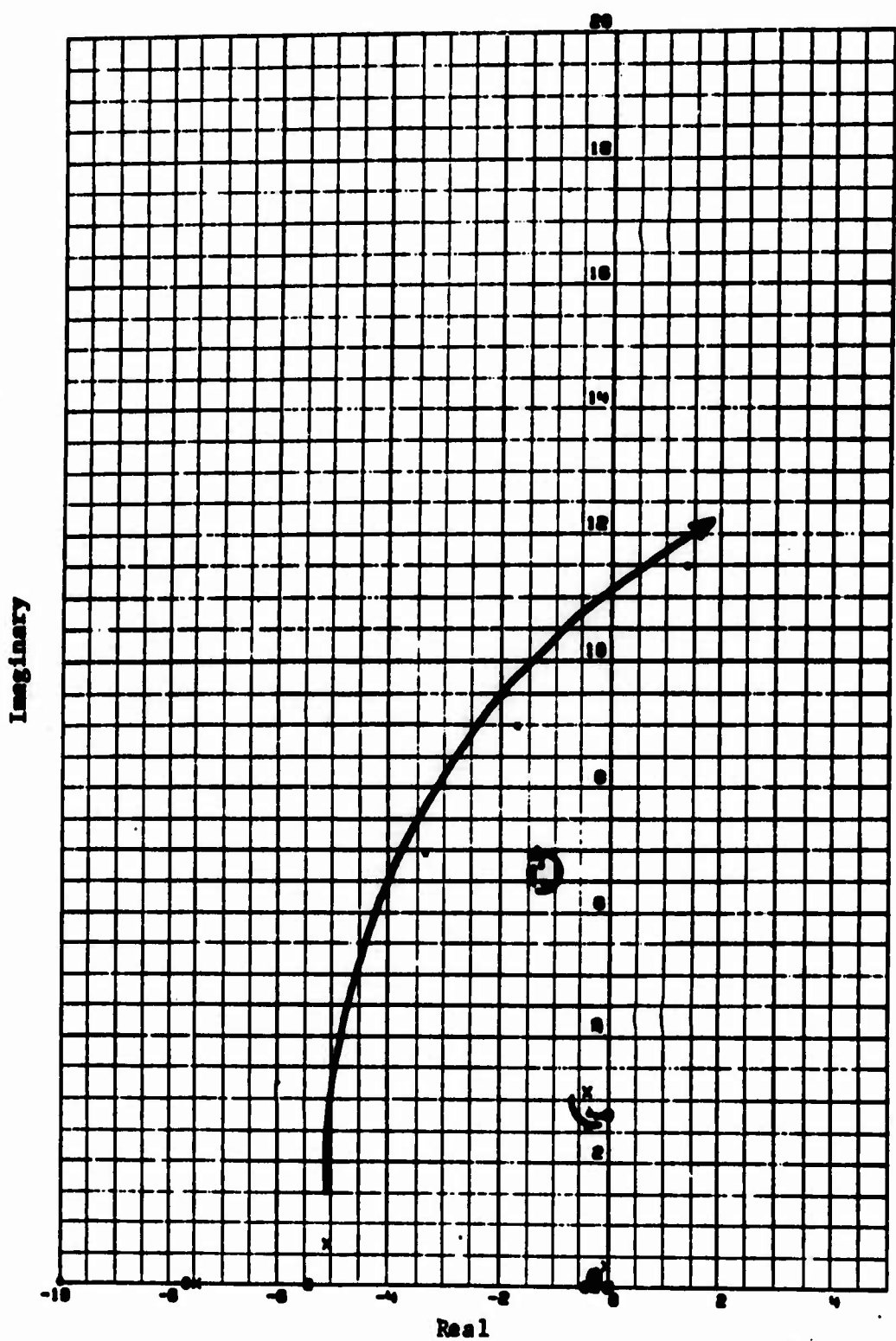


Figure 10. Root Locus Plot for Case 5.

Imaginary

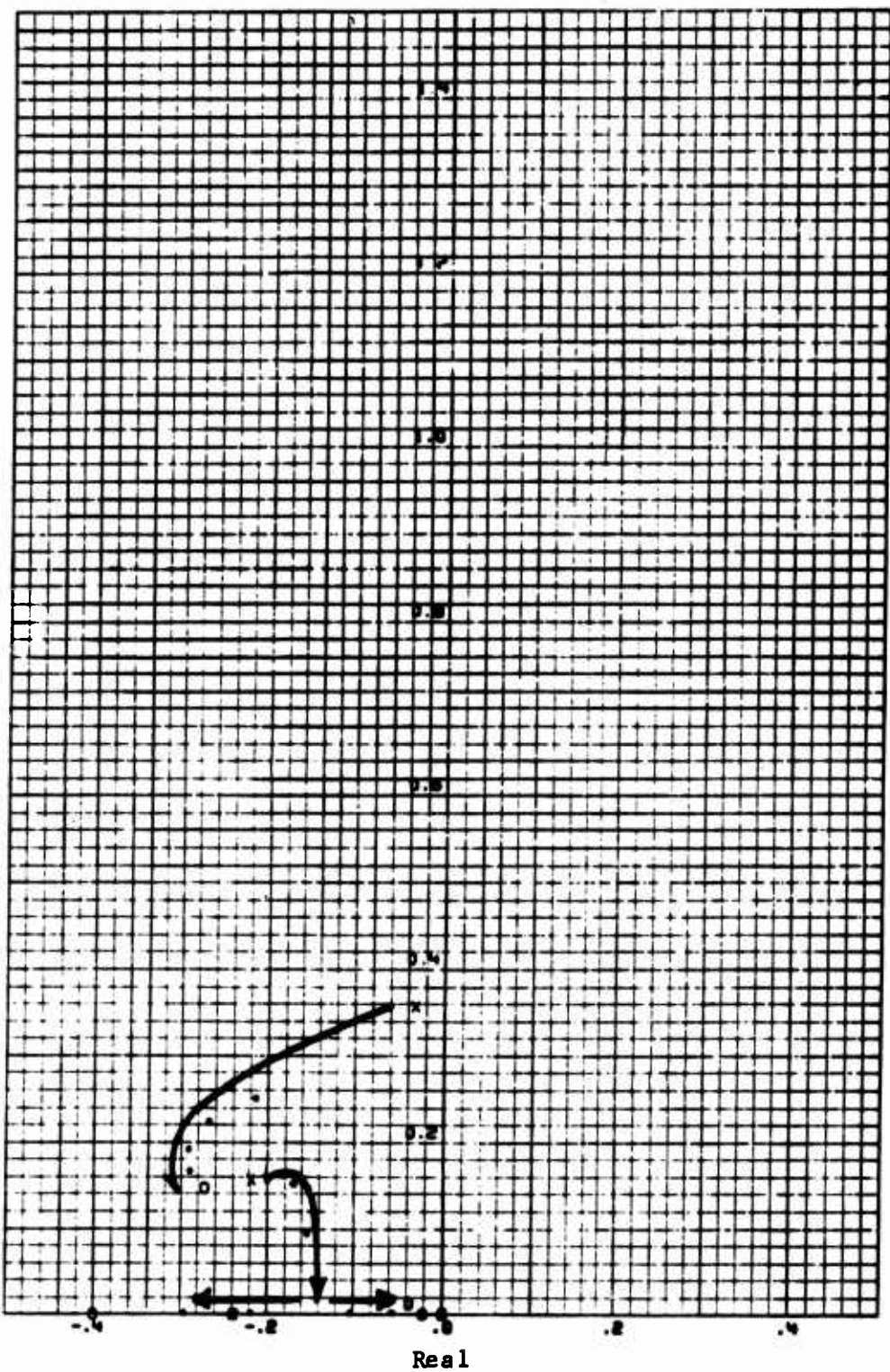


Figure 11. Root Locus Plot for Case 6.

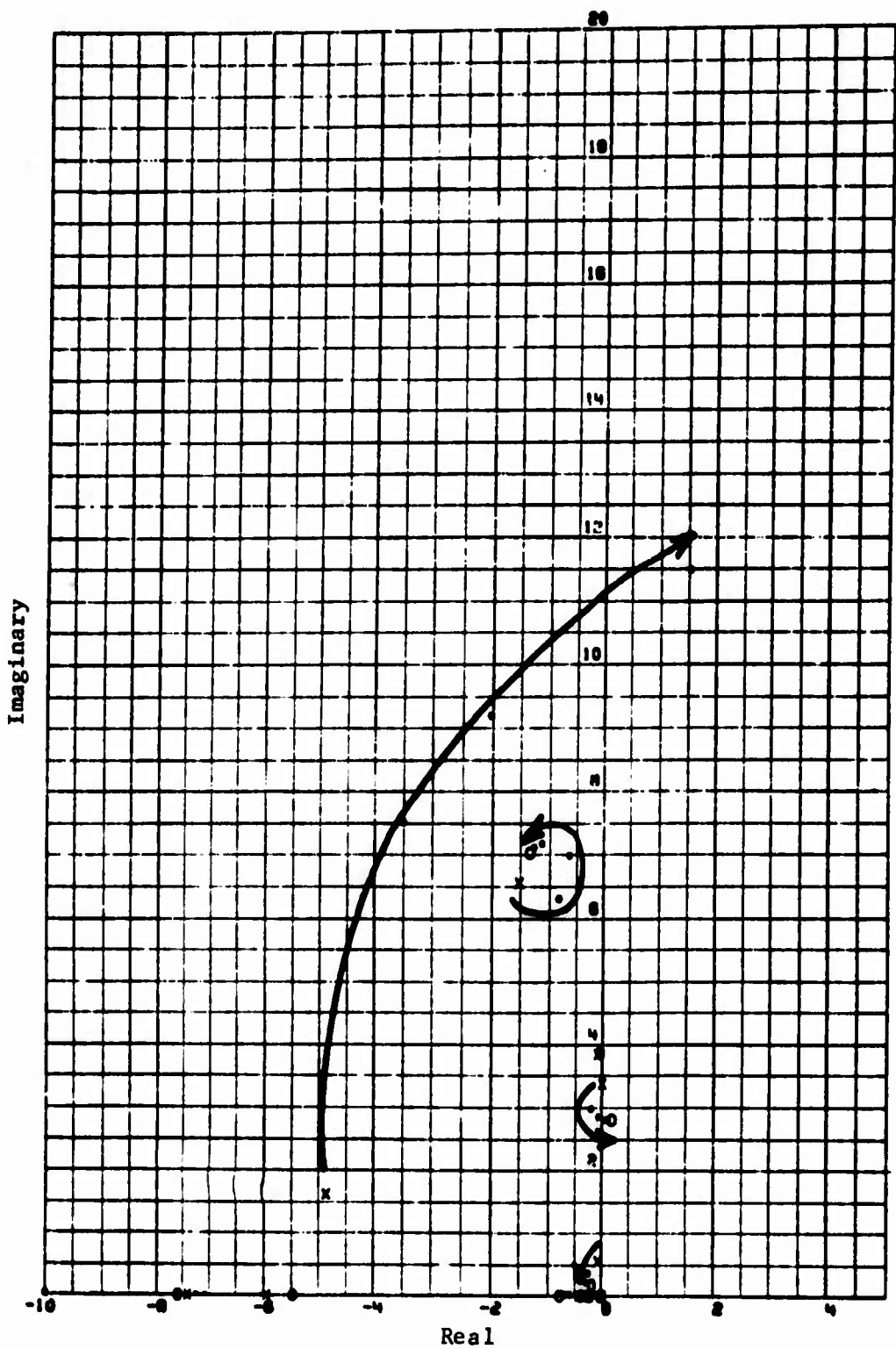


Figure 12. Root Locus Plot for Case 17.

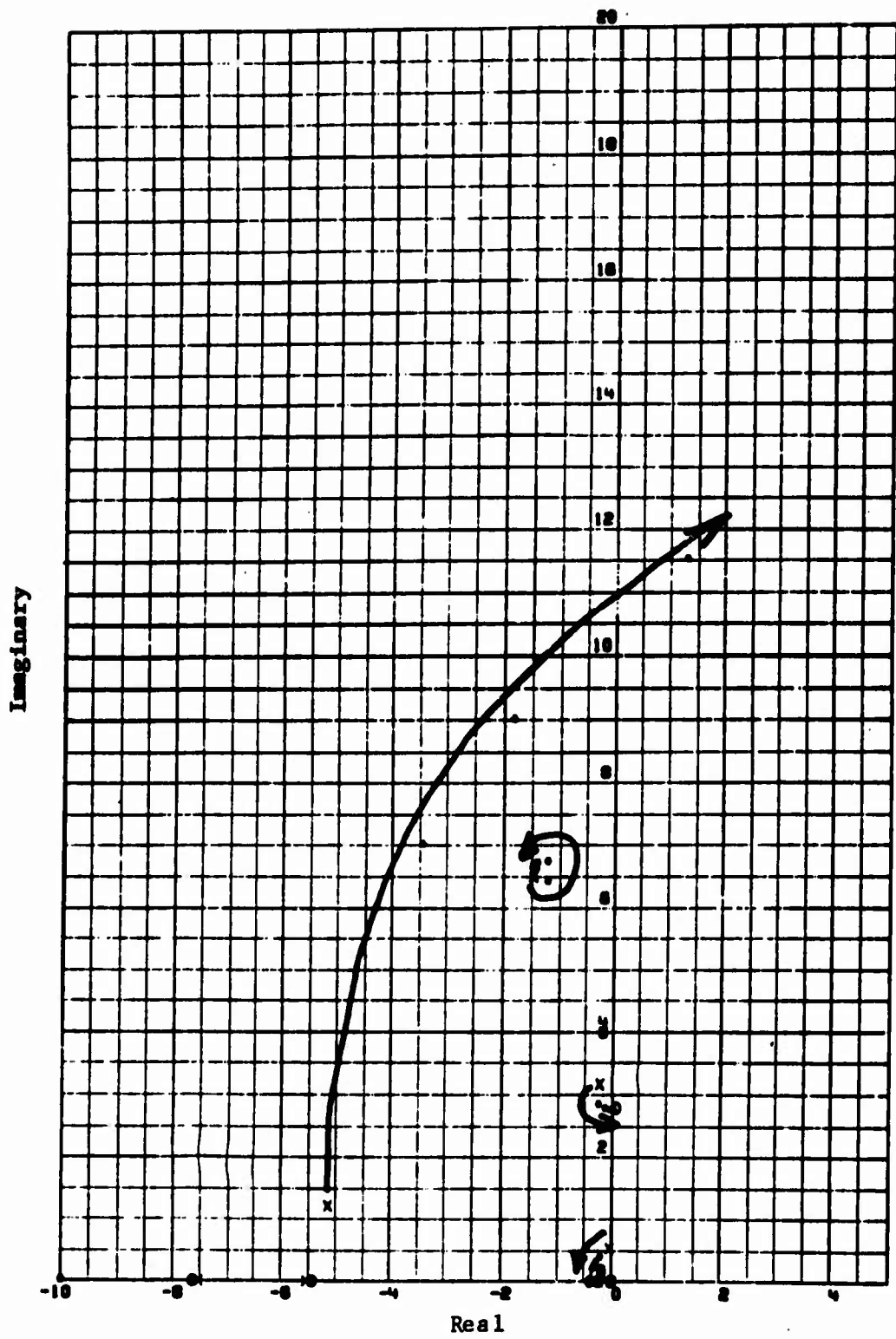


Figure 13. Root Locus Plot for Case 29.

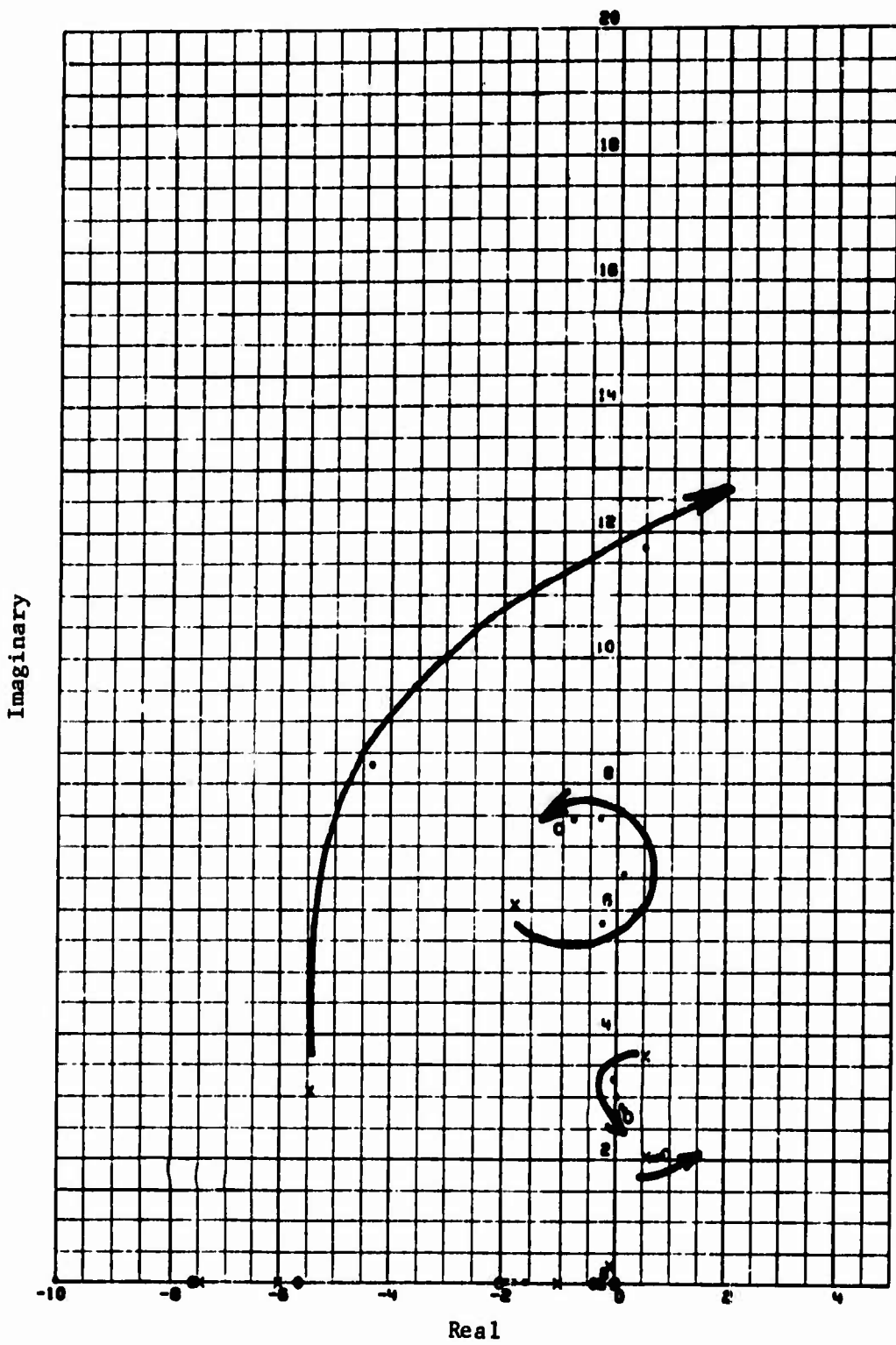


Figure 14. Root Locus Plot for Case 41.

4.5 HELICOPTER FLIGHT SIMULATION

A typical tandem helicopter was used as a model for checking out the program, using all the vehicle characteristics provided by Boeing/Vertol. Complete helicopter longitudinal, lateral, and directional stability augmentation systems were incorporated. Both step and pulse control inputs in longitudinal, lateral, and rudder control were applied to the tandem helicopter at flight speeds of 50, 100, and 150 knots. The output dynamic responses correlate closely with known results of the CH-47 helicopter. The coupled helicopter/sling-load dynamic equations of motion were also programmed and simulated.

Figure 15 is a strip chart recording of a typical flight simulation (Run No. 62, at 50 knots, with longitudinal control input of 1-inch pulse).

A complete set of simulation charts is presented in Appendix III.

4.6 FLIGHT SIMULATION OF HELICOPTER/SLING-LOAD DYNAMICS

Flight simulation of the helicopter/sling-load dynamics was conducted to validate and substantiate the analytical results. The simulation results (Figures 16 through 27) show good agreement, in that cases which were predicted to be stable showed heavily damped oscillations in the simulation, and cases that were predicted to be unstable showed divergent oscillations in the simulation. Cases 166 and 172 represent flight configurations with sling load but without aerodynamic forces and moments on the load for speeds of 50 and 150 knots. Cases 168, 171, 173, and 174 correspond to cases 5, 29, 17, and 41, respectively, of Section 4.3. The root locus shows a little damping for cases 5 and 29. Case 17 has almost no damping. Case 41 is unstable. The traces from the simulator have the same characteristics. The roll and yaw controllers are:

$$-0.05 (2.5 S+1)^{-0.2S} \quad \text{and}$$

$$-0.1 (2.5 S+1)^{-0.2S}$$

The scales for the analog tracings are as follows:

Per Line

δ_{LAT}	Lateral control deflection	0.1 in.
δ_{RUD}	Rudder control deflection	0.1 in.
$\dot{\phi}$	Helicopter roll acceleration	1 deg/sec ²
$\dot{\phi}$	Helicopter roll rate	0.5 deg/sec
ϕ	Helicopter roll angle	0.5 deg
$\ddot{\psi}$	Helicopter yaw acceleration	1 deg/sec ²

↓	Helicopter yaw rate	1 deg/sec
↓	Helicopter yaw angle	1 deg
$\ddot{\phi}_1$	Load front cable roll angular acceleration	5 deg/sec ²
$\dot{\phi}_2$	Load front cable roll angle	5 deg
$\ddot{\phi}_3$	Load rear cable roll angular acceleration	5 deg/sec ²
$\dot{\phi}_3$	Load rear cable roll angle	5 deg
$\ddot{\phi}_4$	Load roll acceleration	5 deg/sec ²
$\dot{\phi}_4$	Load roll angle	5 deg

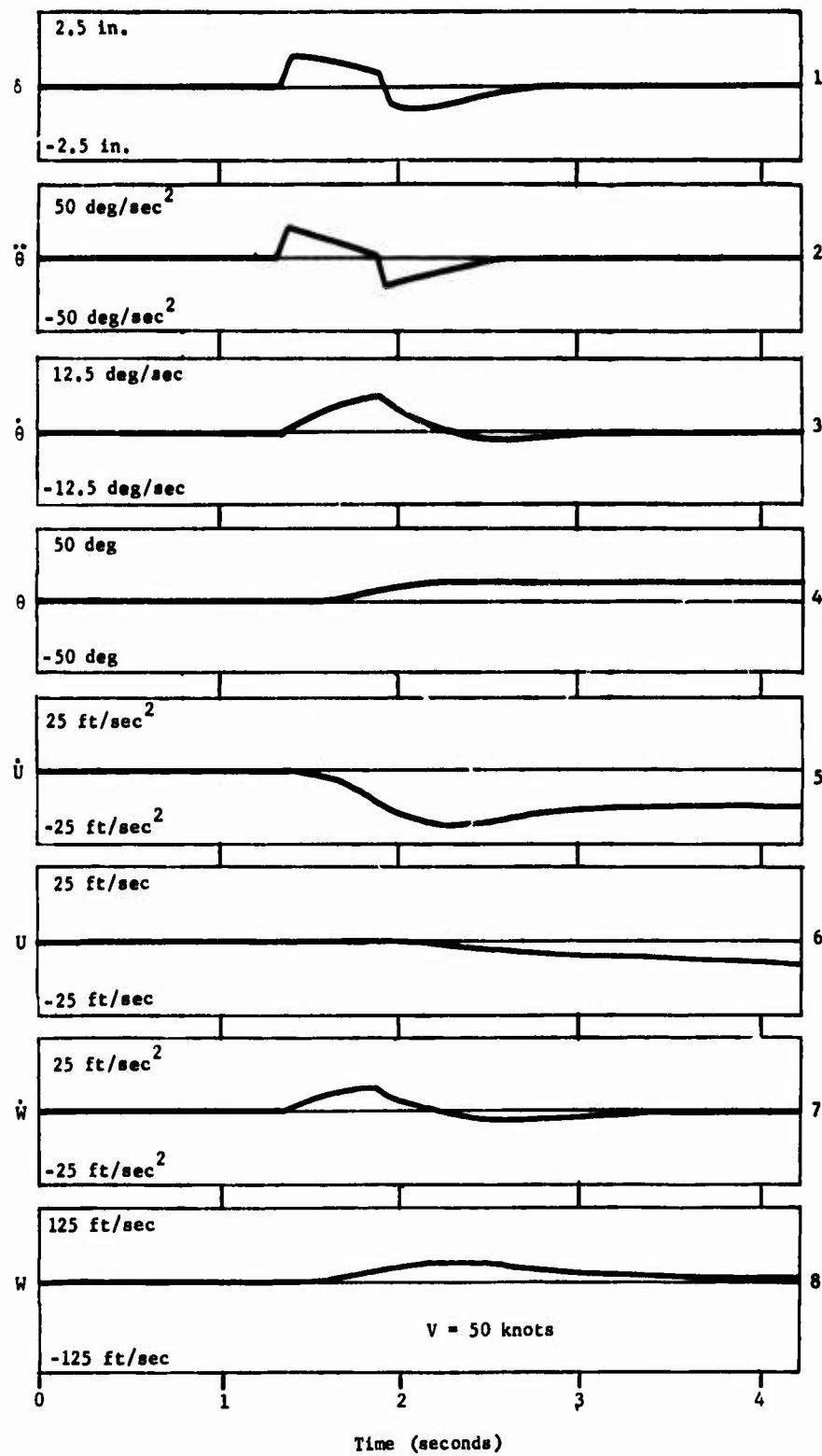


Figure 15. Helicopter Flight Simulation -- Run 62.

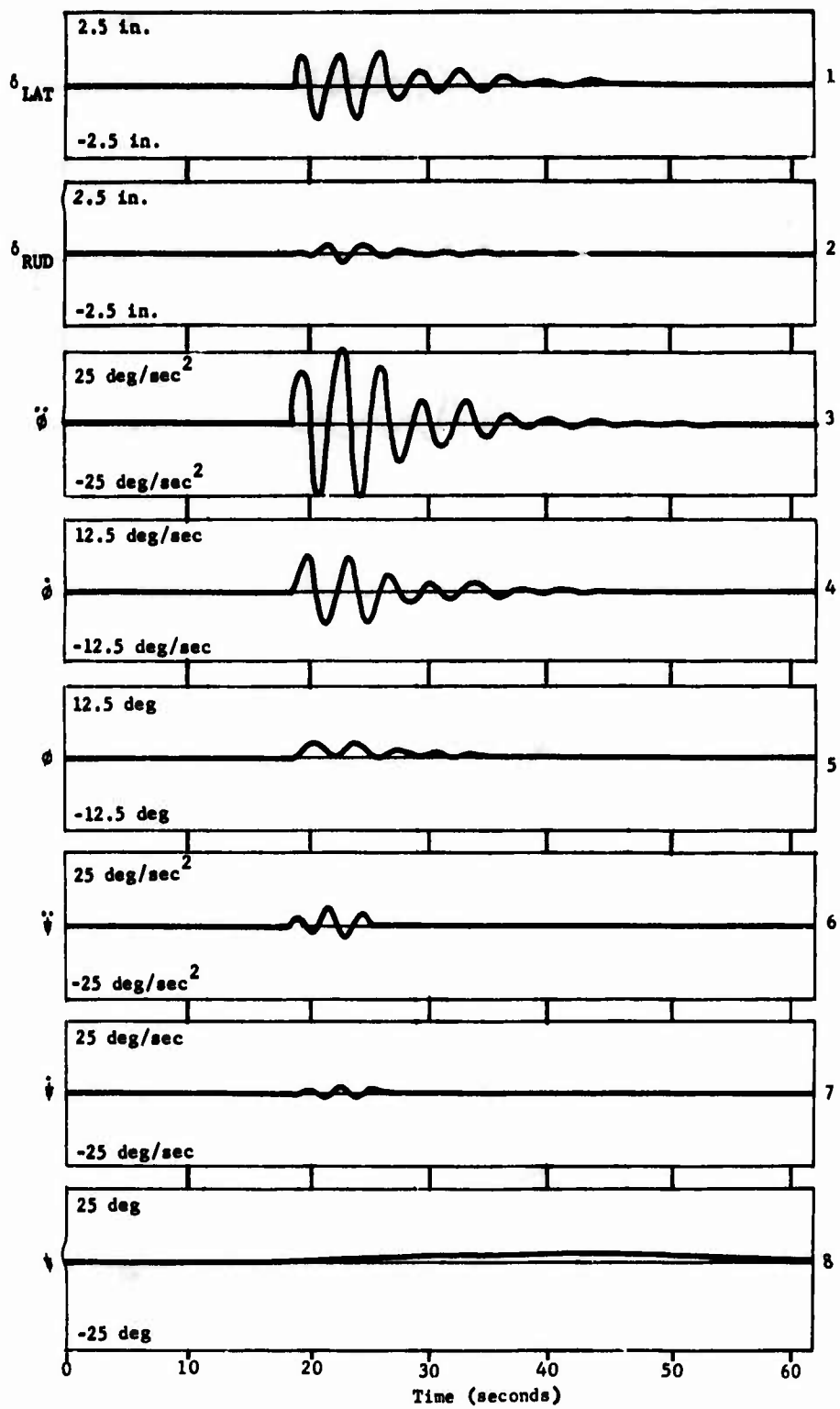


Figure 16. Flight Simulation of Helicopter/Sling-Load Dynamics -- Case 166 (A).

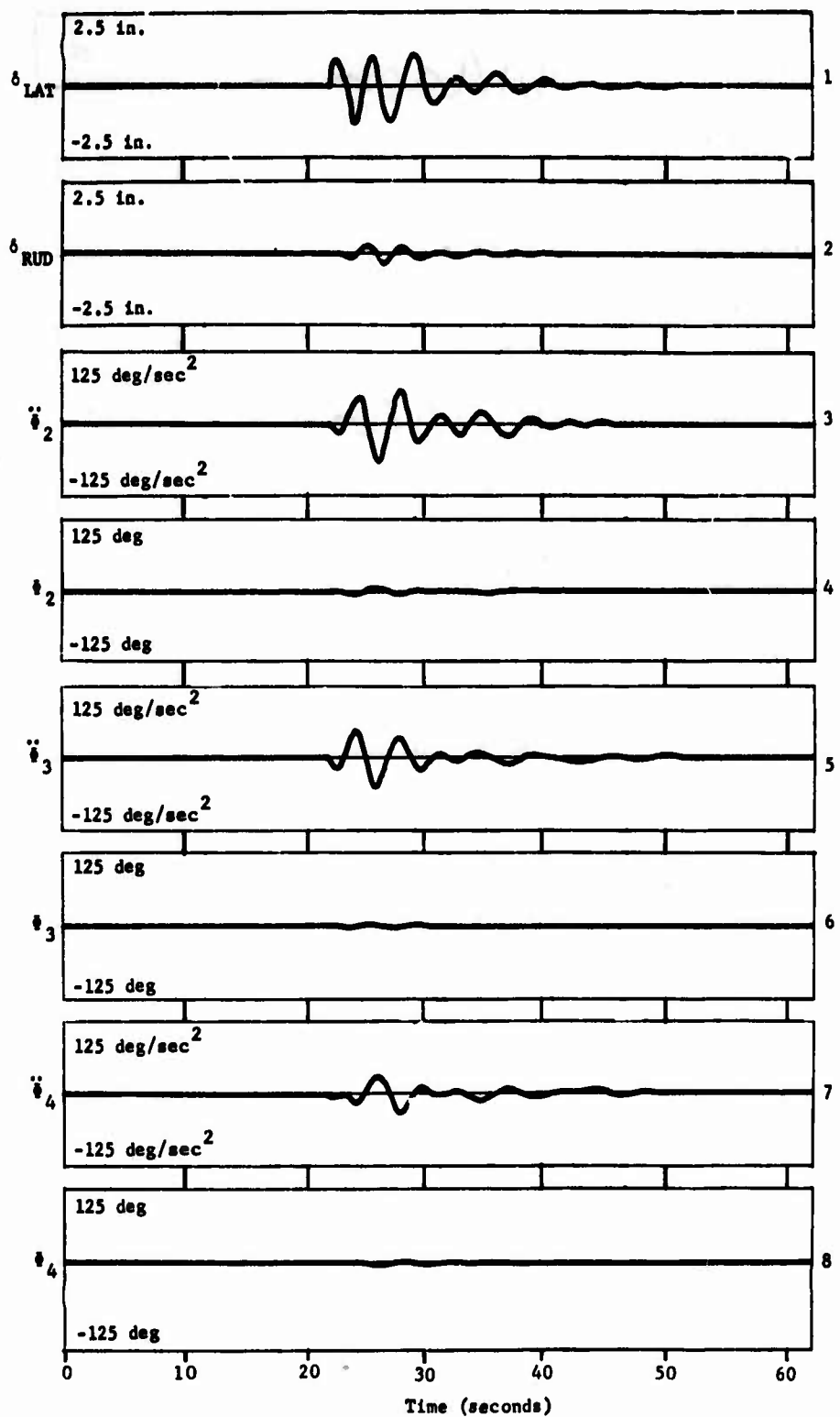


Figure 17. Flight Simulation of Helicopter/Sling-Load Dynamics -- Case 166 (B).

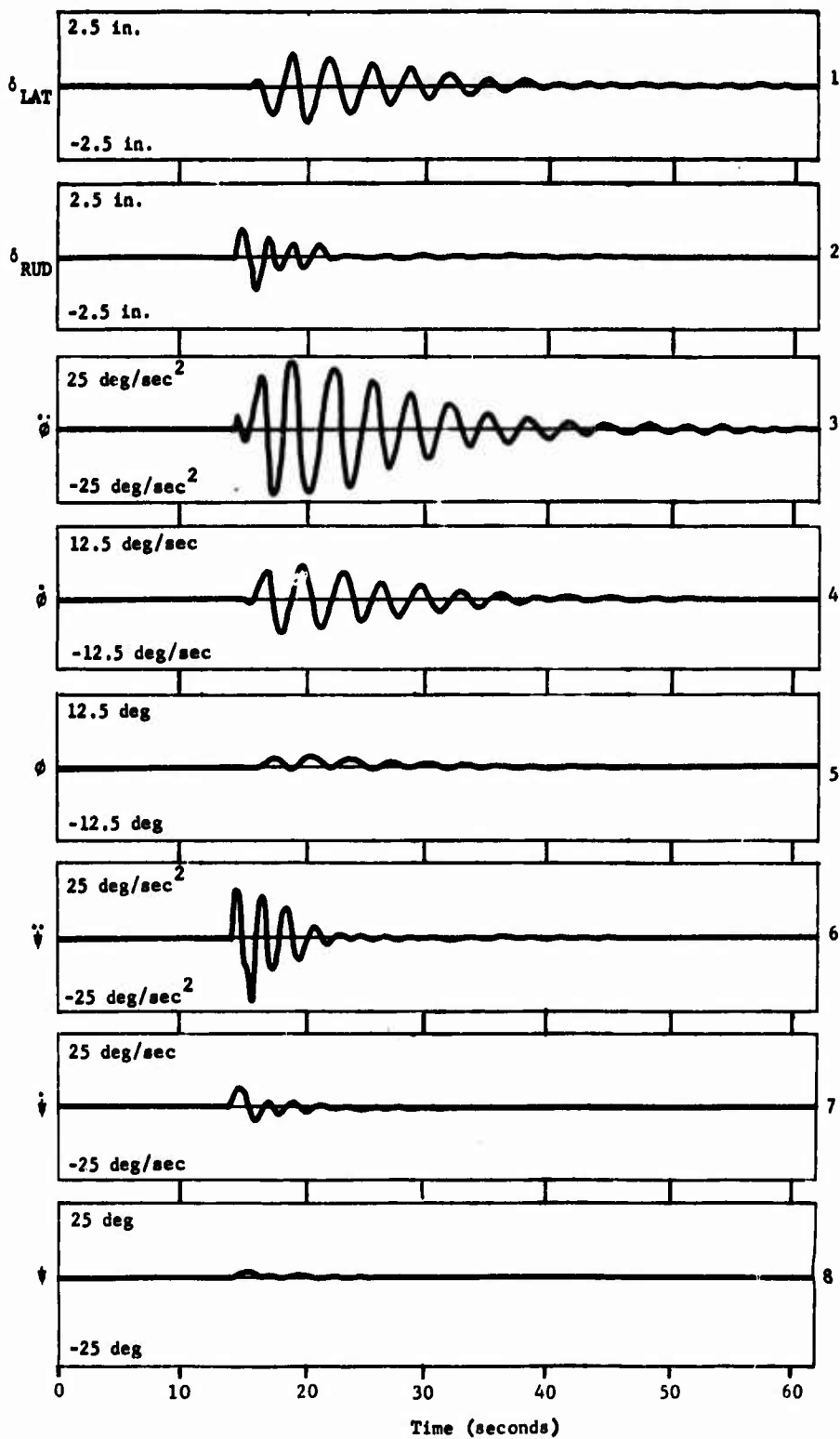


Figure 18. Flight Simulation of Helicopter/Sling-Load Dynamics -- Case 172 (A).

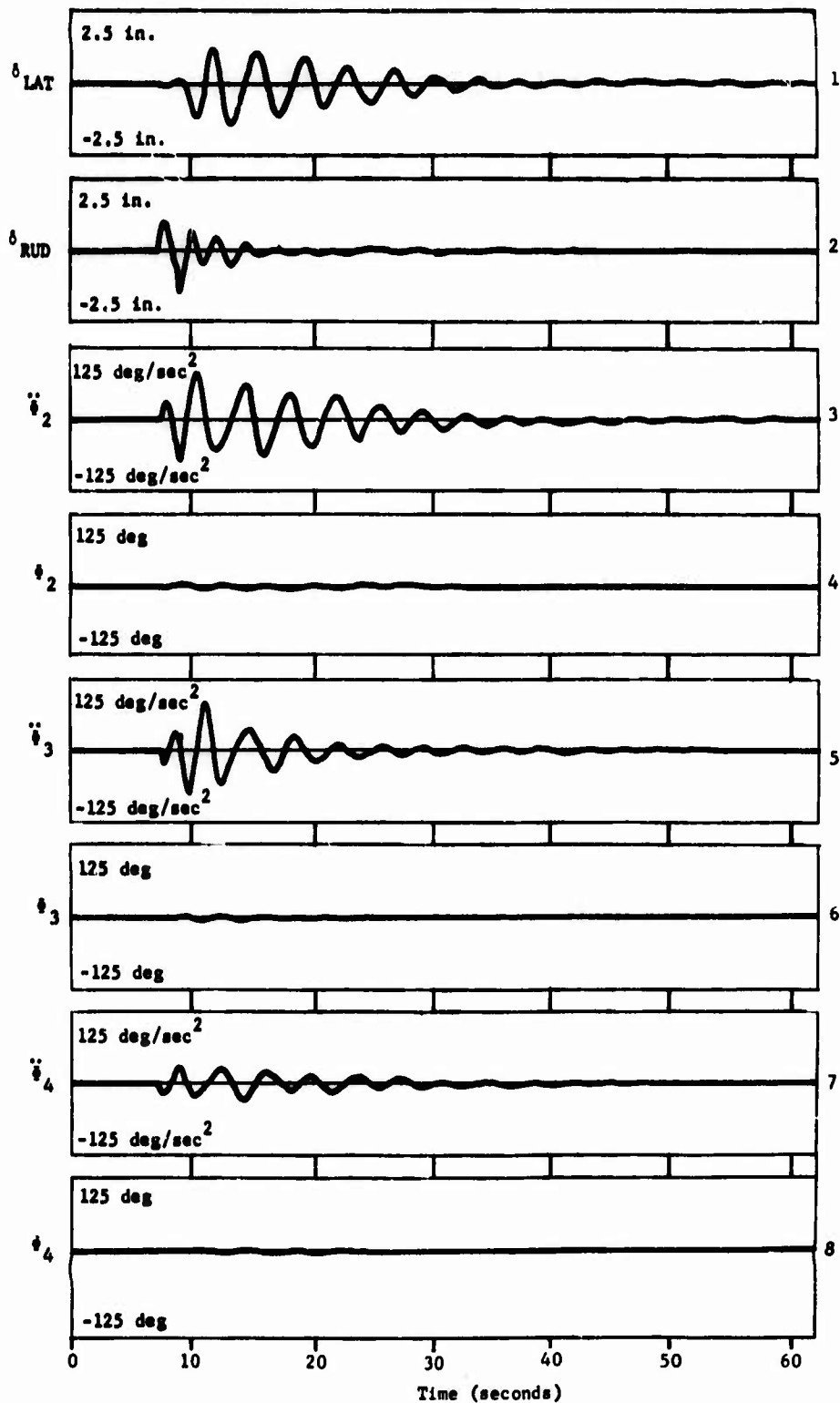


Figure 19. Flight Simulation of Helicopter/Sling-Load Dynamics -- Case 172 (B).

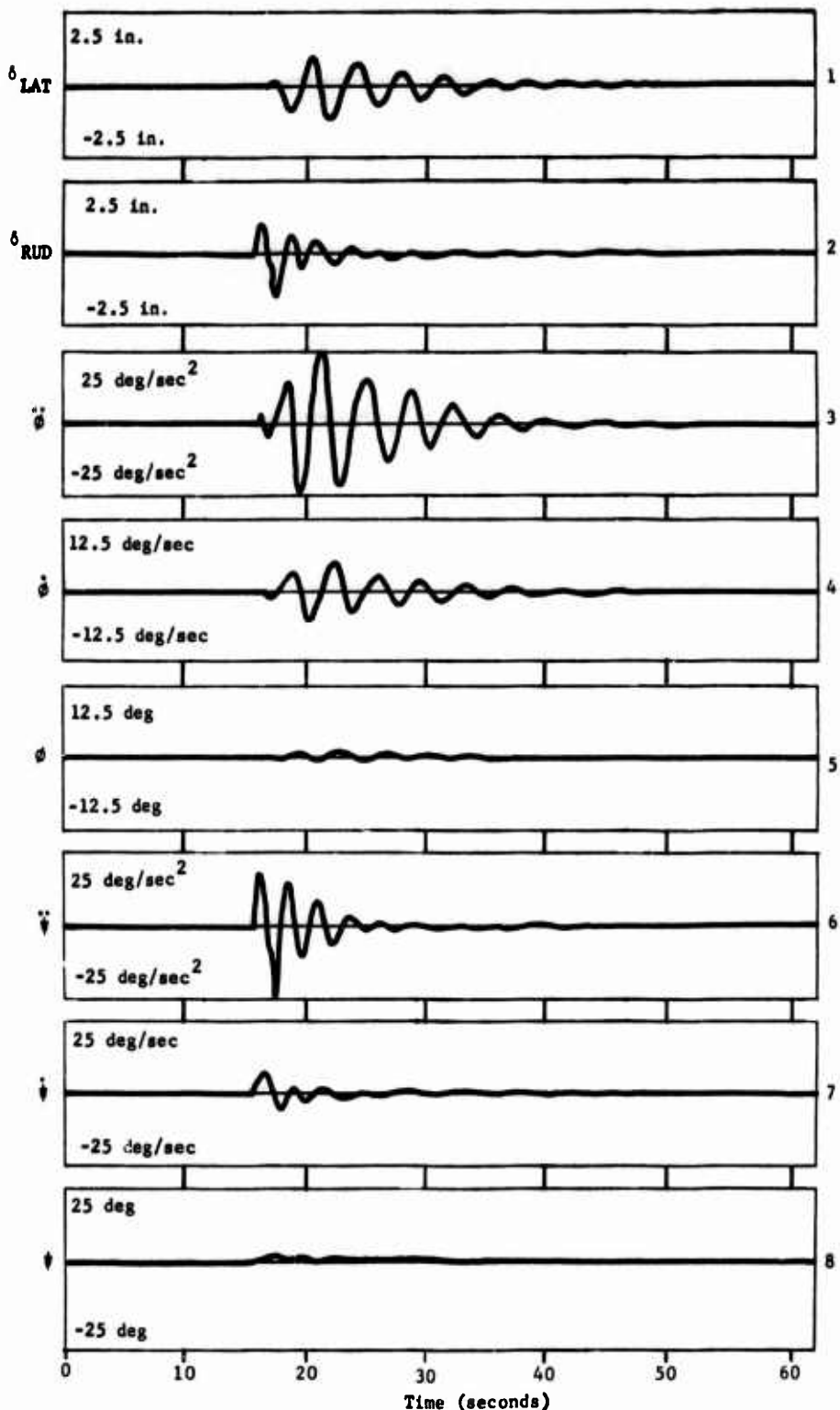


Figure 20. Flight Simulation of Helicopter/Sling-Load Dynamics -- Case 168 (A).

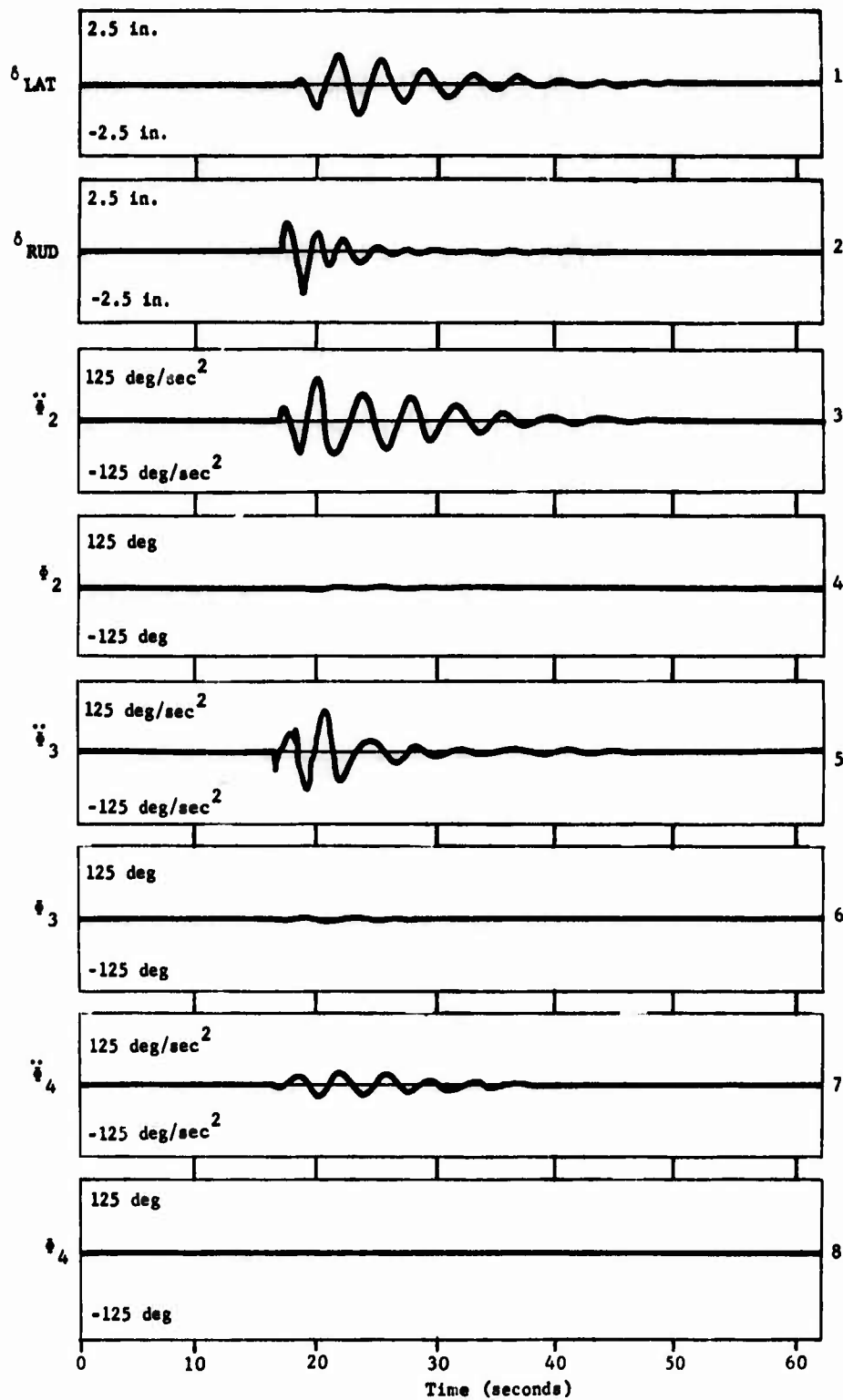


Figure 21. Flight Simulation of Helicopter/Sling-Load Dynamics -- Case 168 (B).

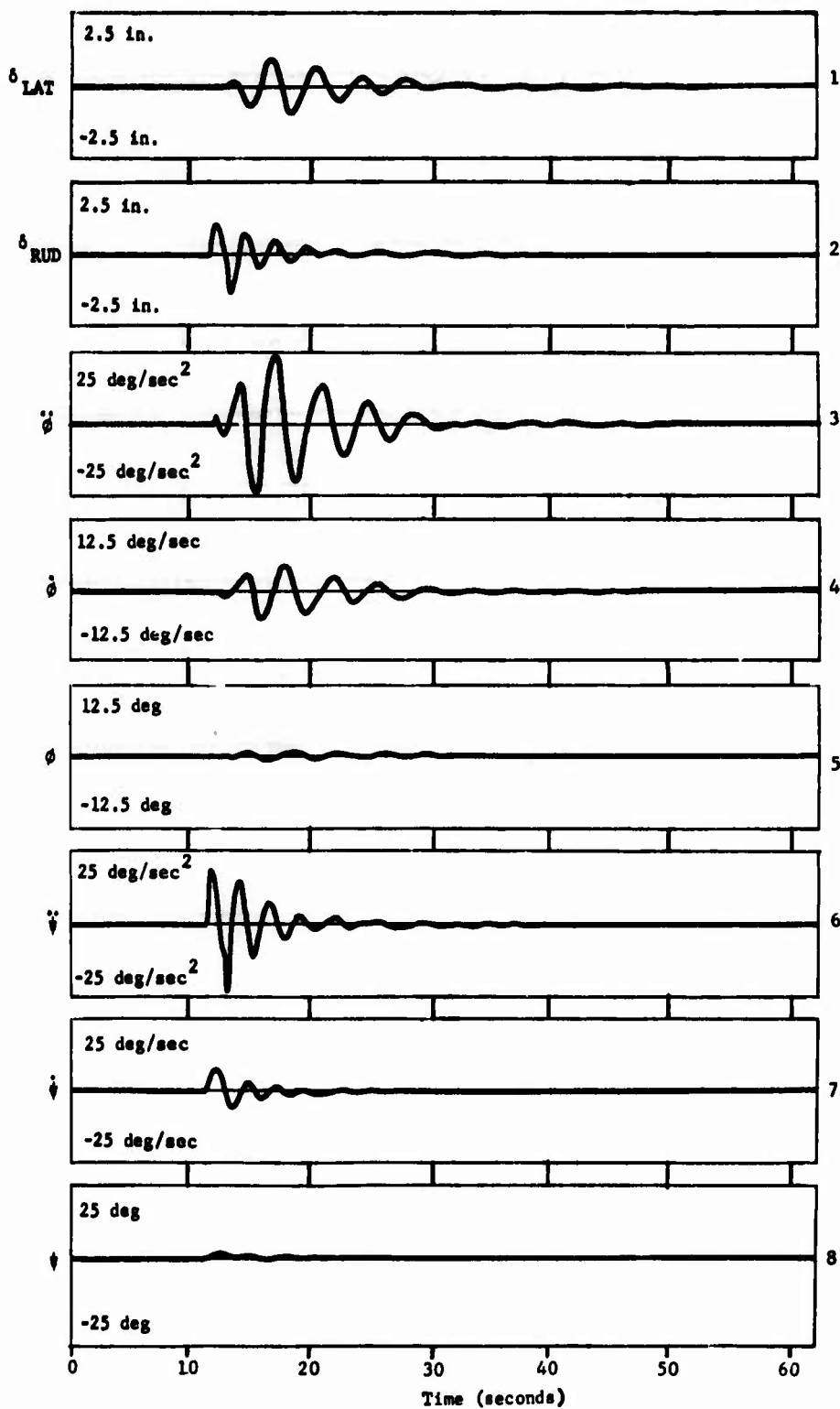


Figure 22. Flight Simulation of Helicopter/Sling-Load Dynamics -- Case 171 (A).

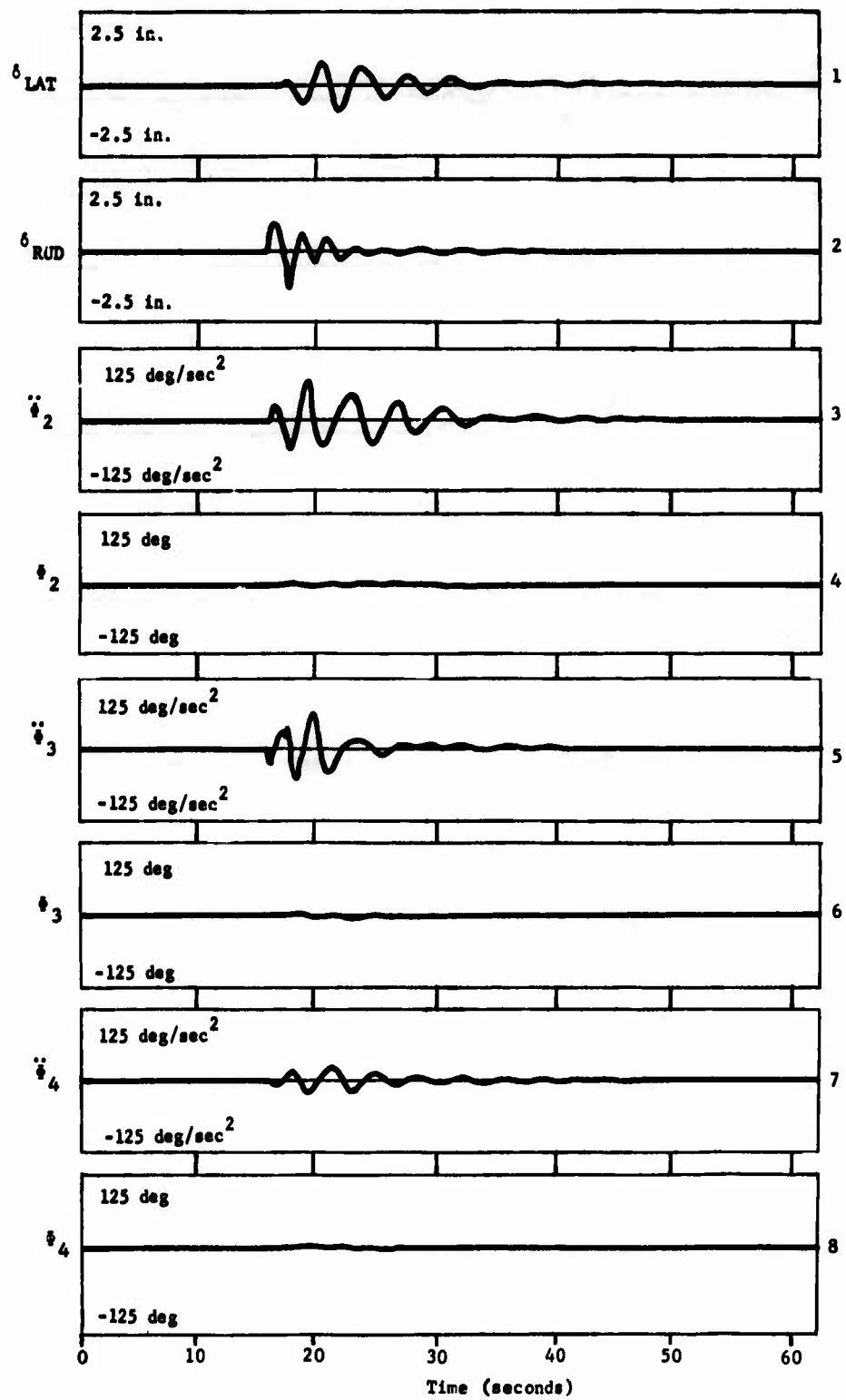


Figure 23. Flight Simulation of Helicopter/Sling-Load Dynamics -- Case 171 (B).

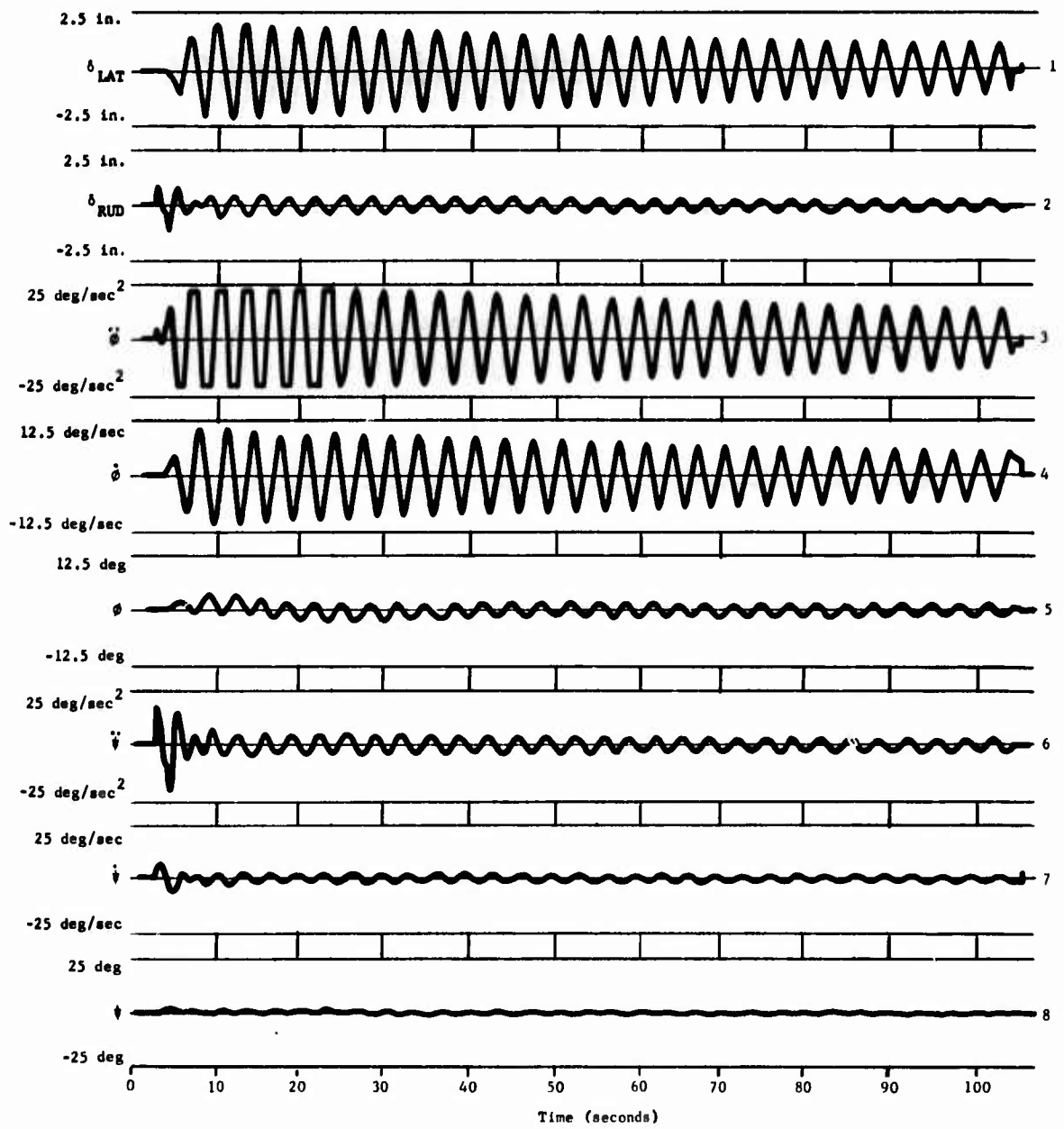


Figure 24. Flight Simulation of Helicopter/Sling-Load Dynamics -- Case 173 (A).

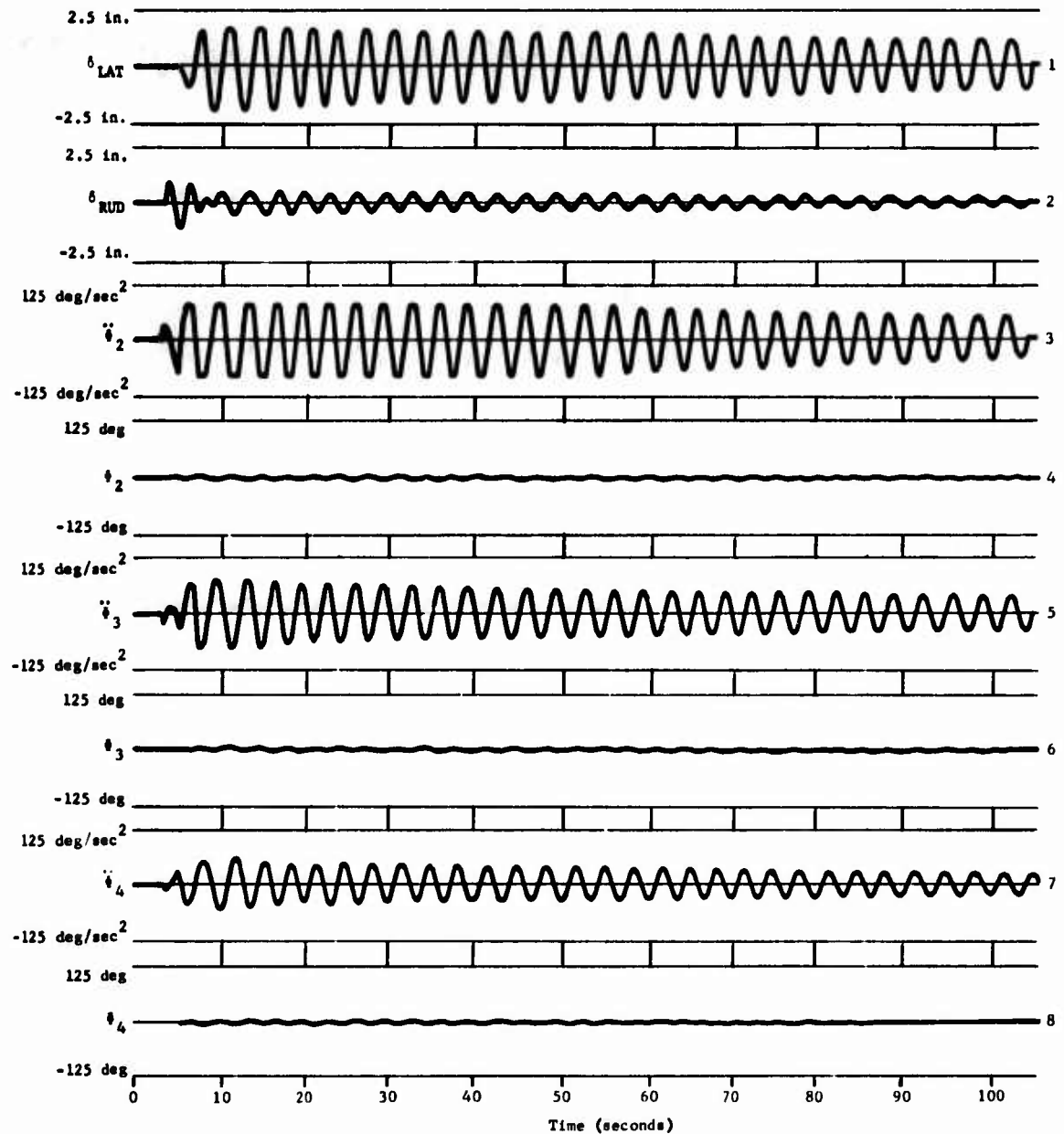


Figure 25. Flight Simulation of Helicopter/Sling-Load Dynamics -- Case 173 (B).

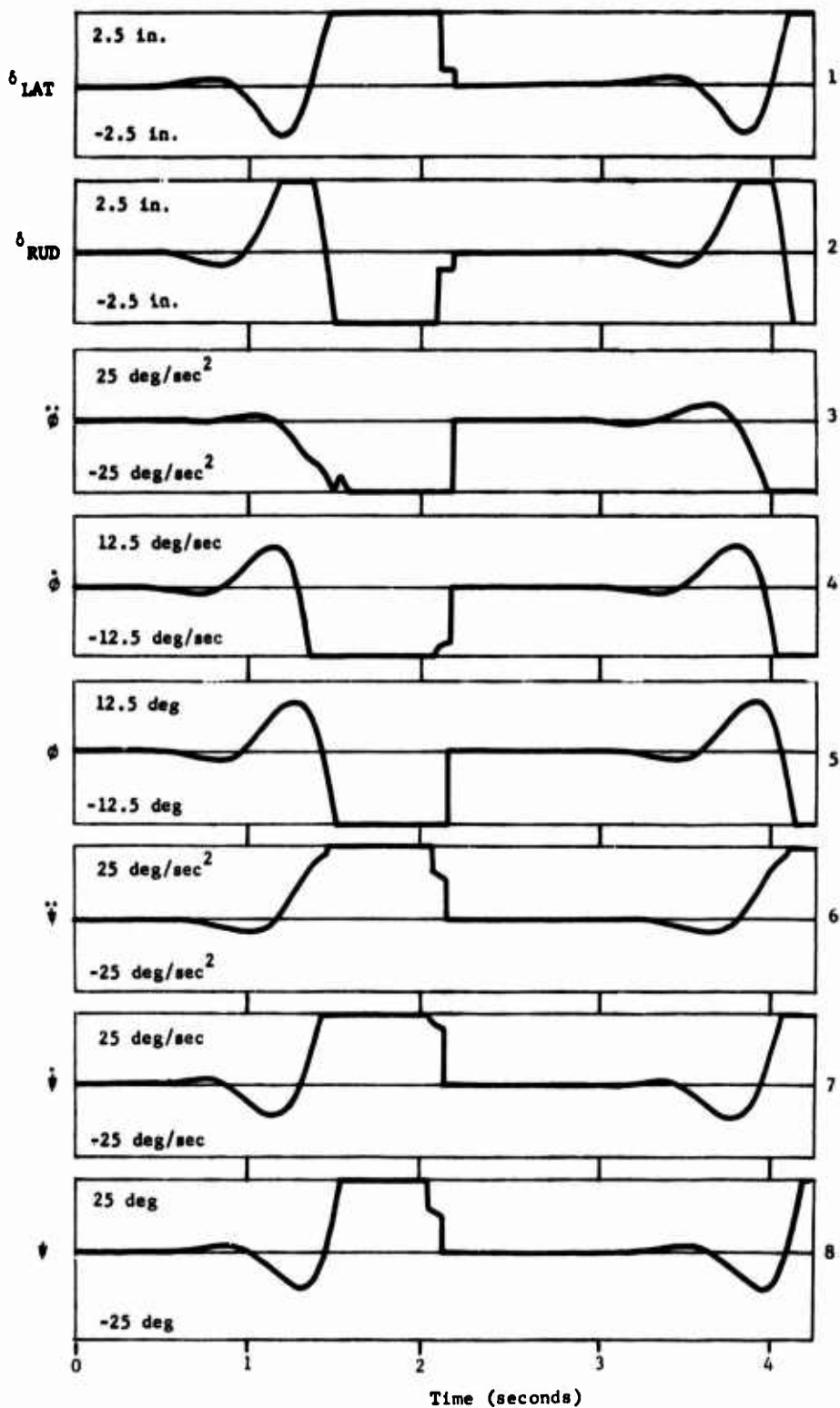


Figure 26. Flight Simulation of Helicopter/Sling-Load Dynamics -- Case 174 (A).

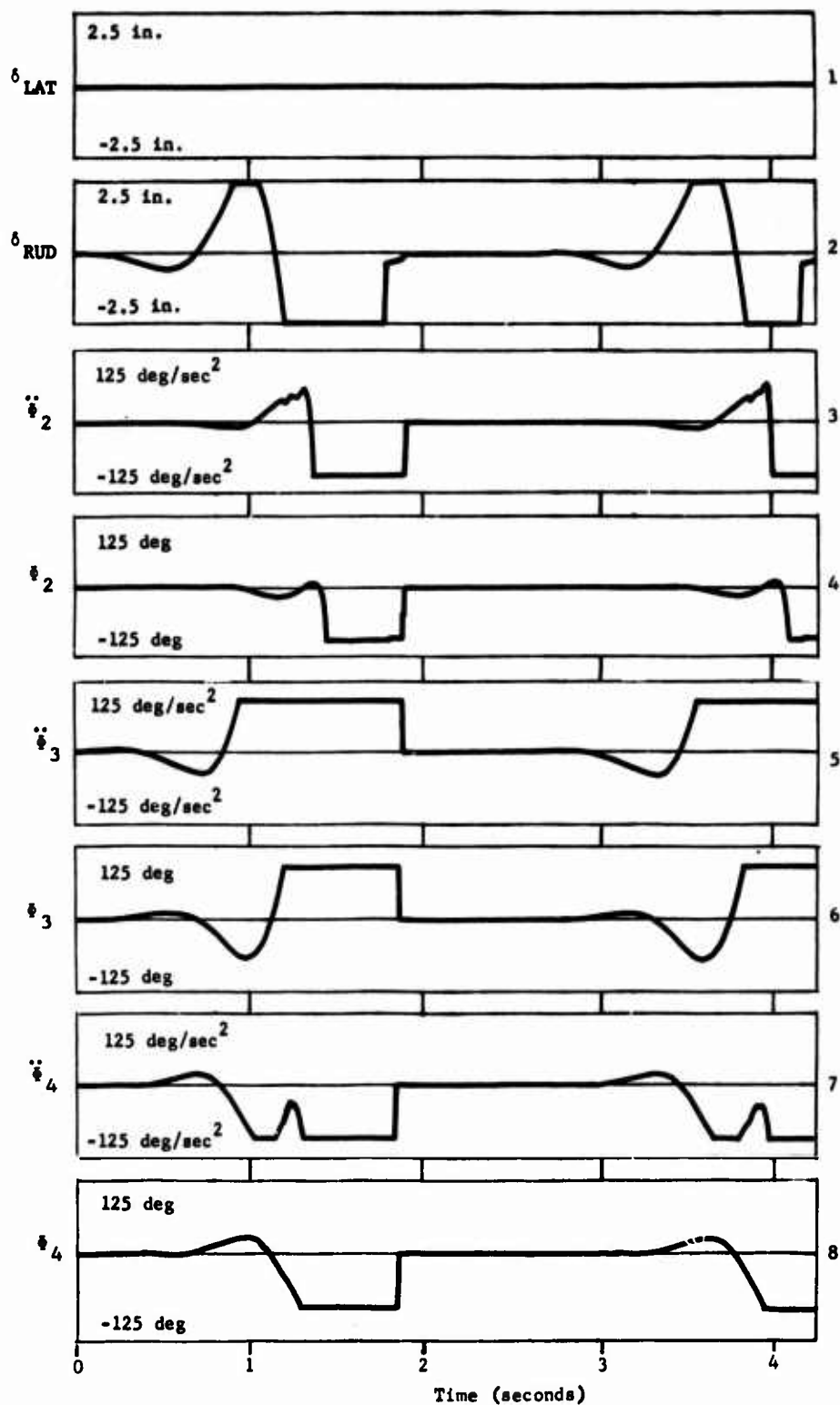


Figure 27. Flight Simulation of Helicopter/Sling-Load Dynamics -- Case 174 (B).

5.0 AERODYNAMIC EFFECTS OF FLOW FIELD ON THE SLING LOAD IN HOVER FLIGHT

This section examines the aerodynamic effects of the flow field on the sling load in hover flight.

The vertical velocity component of the hovering rotor flow field was obtained by idealizing the test data of Reference 8. This section presents the slipstream dynamic pressure as a function of radial location r/R and vertical location Z/R in the rotor field, and this data was reduced to the velocity distribution. The data was plotted and the somewhat idealized velocities of Figure 28 were obtained. The data indicated that at the rotor disc the velocity variations with r/R were approximately linear with a steady decay of the velocity near the tip with Z/R and an increase of velocity near the center of the rotor.

This data was for a rotor with a disc loading of 1.93. To obtain the vertical velocity field for a rotor of arbitrary disc loading, the data was generalized by replacing the velocity of the ordinate with the parameter $velocity/(disc\ loading)^{1/2}$. This permits the estimation of the hovering velocity field for a helicopter of any disc loading, assuming that a similar blade loading exists.

For the purposes of this study, estimates of the tangential velocity were made by assuming that at the rotor disc, both the normal and tangential components of velocity were linear functions of the radial location. By considering the flow of mass through the rotor blade and using the above assumptions, it is possible to express the thrust, T , and the torque, Q , in terms of the vertical and tangential velocities, U_T and V_T , respectively, as

$$T = \int_0^R 2\pi \frac{\rho r^3}{2} U_T^2 dr \quad (24)$$

and

$$Q = \int_0^R 2\pi \rho \frac{r^4}{R^2} U_T V_T dr \quad (25)$$

which can be integrated to give a relationship between U_T and V_T as

$$\frac{V_T}{U_T} = 5/4 C_Q/C_T \quad (26)$$

where C_T and C_Q are the thrust and torque coefficients, ρ the air density, and R the rotor radius.

This relationship, together with Figure 28, permits a rotor velocity field to be estimated for an arbitrary rotor if it is further assumed that the radial component of velocity is zero. In the absence of test data, it is not possible to estimate the accuracy of the tangential velocity component obtained.

From the above information, loads were worked out for three of the slung helicopter loads, the 8-by-8-by-20-foot container, the 8-by-8-by-40-foot container, and the command post carrier. The helicopter characteristics used were as follows:

Rotor diameter	92 feet
Thrust	76,000 pounds
Tipspeed	700 feet/second
Horsepower	13,000

The loads were located at a Z/R of 0.326 or approximately 15 feet below the rotor disc and were evaluated at three radial locations and at different yaw angles. The results obtained are shown in Table VIII.

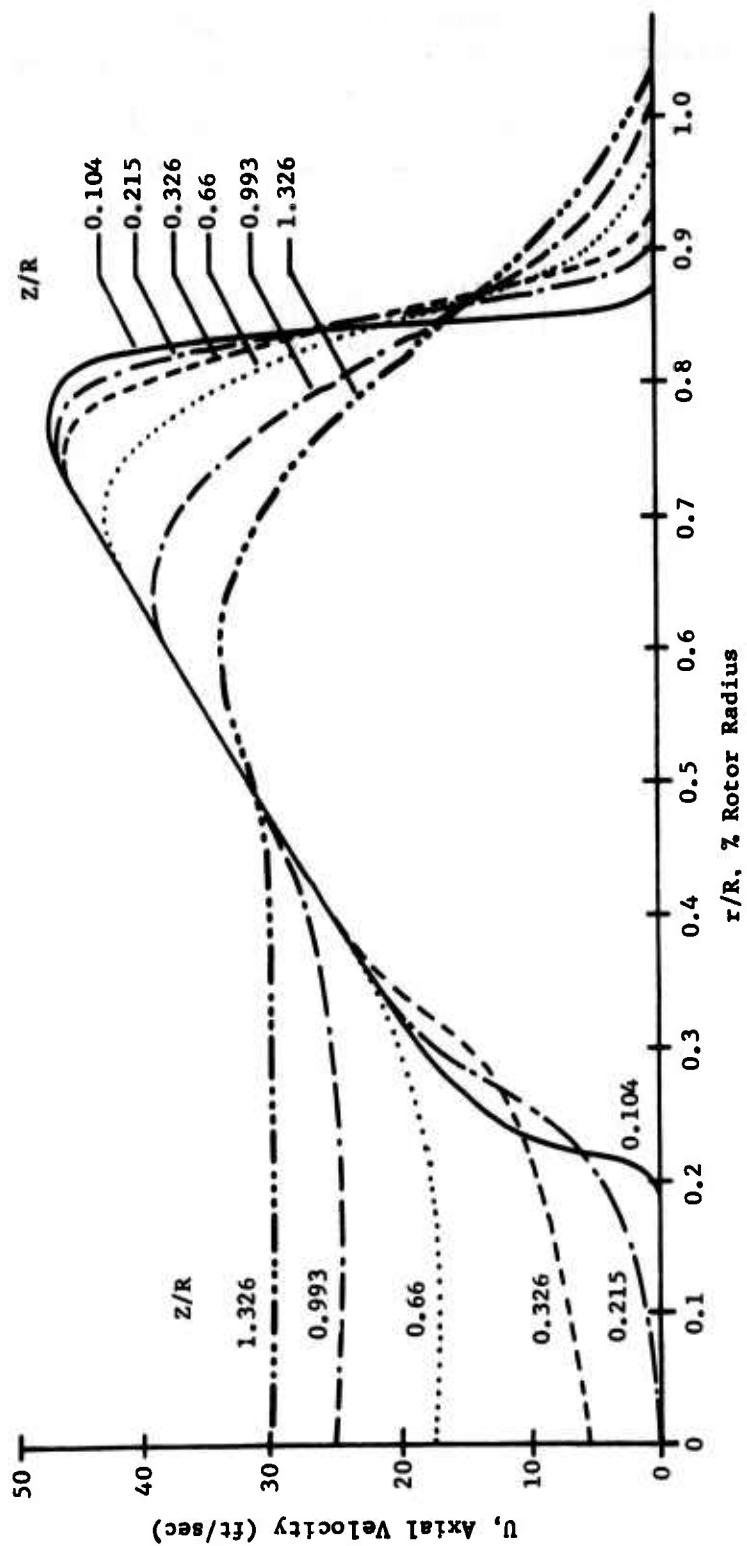


Figure 28. Axial Velocity vs Percent Rotor Radius.

TABLE VIII. LOAD EVALUATION

Configuration	Z/R	r/R	β (deg)	L (lb)	m (ft-lb)	y (lb)	n (ft-lb)
Container 8x8x20	0.326	0.0	0°	- 79.0	0.0	0.0	19.0
		0.375	0°	- 882.8	- 3626.1	26.2	91.4
		0.375	45°	- 871.7	- 2815.8	14.4	64.6
		0.375	90°	- 941.7	0.0	0.0	20.2
		0.75	0°	- 1178.3	4251.0	92.4	174.1
		0.75	45°	- 2130.9	4549.0	49.8	129.3
		0.75	90°	- 3171.7	0.0	0.0	19.9
Container 8x8x40	0.326	0.0	0°	- 707.2	0.0	0.0	346.9
		0.25	0°	- 1589.0	-18955.5	44.0	562.5
		0.25	45°	- 1462.5	-14861.1	29.6	457.8
		0.25	90°	- 1432.5	0.0	0.0	346.9
		0.5	0°	- 2664.0	-15014.7	114.2	1060.4
		0.5	45°	- 3500.8	-16733.5	68.5	752.9
		0.5	90°	- 4121.0	0.0	0.0	346.9
Command Post Carrier	0.326	0.0	0°	- 47.9	0.07	- 0.213	4.55
		0.375	0°	- 585.1	- 1669.3	13.2	17.0
		0.375	45°	- 585.9	- 1253.2	6.9	13.6
		0.375	90°	- 630.4	0.0	0.0	4.5
		0.75	0°	- 1406.8	2400.0	53.5	16.5
		0.75	45°	- 1656.1	2014.2	26.7	19.1
		0.75	90°	- 2225.1	0.0	0.0	4.5

6.0 DEFINITION OF ACCEPTABLE AERODYNAMIC BOUNDARIES

This section, using the data of preceding sections, establishes the boundaries of acceptable aerodynamic behavior for sling loads.

6.1 SENSITIVITY ANALYSIS OF STABILITY PARAMETERS AND RELATED STABILITY BOUNDARIES FOR VARIOUS SLING LOADS

The stability criteria were further developed. A typical CH-46 tandem helicopter was used as a model sling load. The maximum stable flight speed for such a sling load with single sling configuration was as previously established, about 20 knots. The basic major CH-46 stability parameters were then varied one at a time to analyze their sensitivity and influence on the overall load stability. The major stability parameters varied were the damping in yaw, drag, and side force with respect to sideslip angle, static yaw stability, and the sling-load weight. Other stability parameters, such as sling configurations, sling cable length, relative load vehicle mass, and inertial characteristics, were also investigated.

The sensitivity of the above-stated stability parameters, their effects on sling-load stability, and boundary for stable maximum flight speeds are summarized in Figure 29 for the typical CH-46 as a sling load, where

P/P_{base}	Stability parameter varied over basic stability parameter
C_{D_0}	Drag coefficient
C_{n_r}	Damping in yaw coefficient
Wt	Weight of sling load
C_{y_β}	Side force coefficient with respect to sideslip angle
C_{n_B}	Yaw moment coefficient with respect to sideslip angle

Note that varying damping in yaw has the same effect on load stability as varying weight of the sling load; this is also true for varying side force due to sideslip and static yaw stability characteristics.

Varying the basic drag coefficient does not influence sling-load stability significantly unless P/P_{base} exceeds 4.0 or higher. Increasing the damping

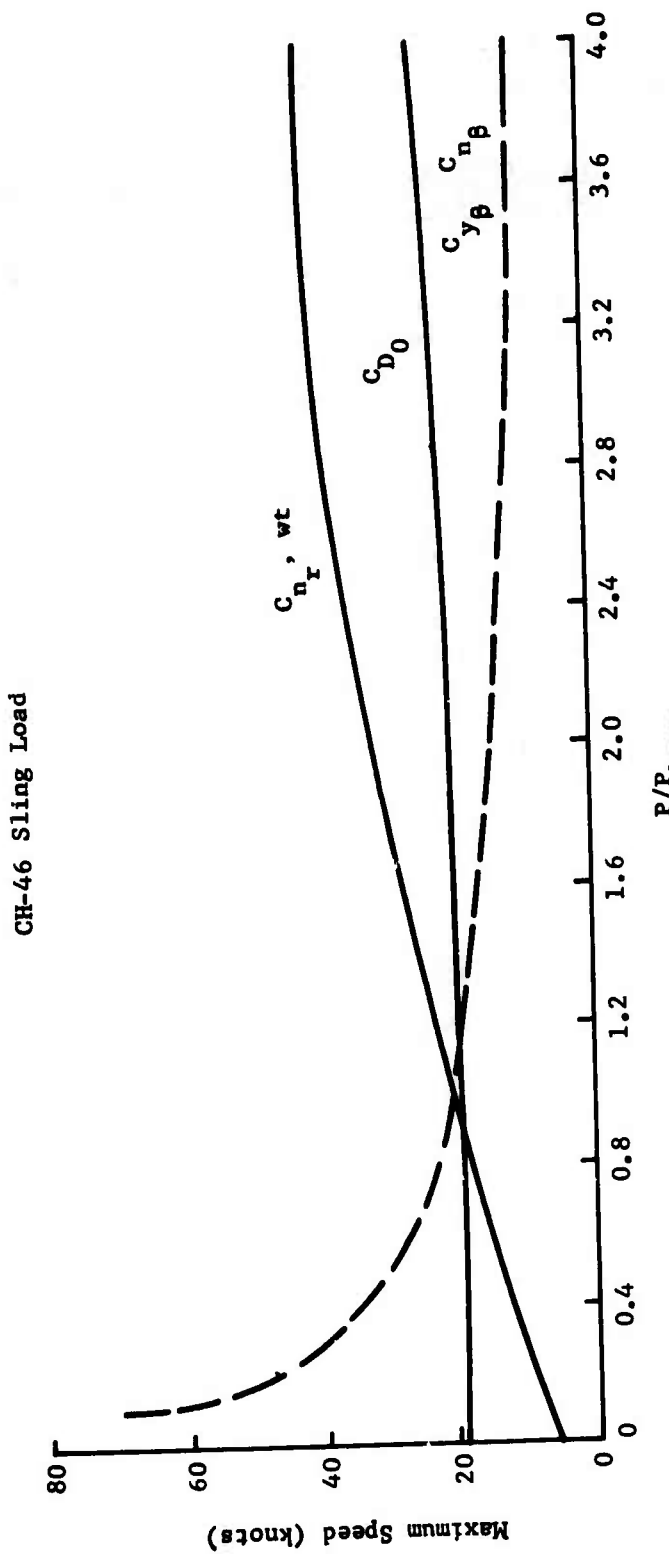


Figure 29. Sensitivity of Stable Maximum Flight Speed With Respect to Various Stability Parameters.

in yaw or the load weight by three times could improve the stable maximum flight speed to 40 knots, an increase by a factor of two. Load stability is shown to be very sensitive to side force due to sideslip angle and static yaw stability of the load. Decreasing to one-half of its original basic value could improve the maximum speed by 10 knots. Reducing the C_y and C_n

to one-tenth of its basic value could enable the CH-46 as a sling load to be carried at very high speed. The establishment of stability boundaries and sensitivity analysis for other sling-load configurations is shown in later sections.

6.2 STABILITY BOUNDARIES OF HELICOPTER SLING LOADS

Figures 30 through 35 show Routh's parameter for various airspeeds as a measure of the CH-46 load stability. These values of "R" are given for certain fixed values of the stability derivatives as a function of three different cable lengths in each plot.

The graphs clearly show that the longer the cable, the lower the airspeed at which system instability begins. In some cases the sign of Routh's parameter changes twice, indicating that there is a certain band of airspeeds in which the system is either stable or unstable. Also, the system is as sensitive when changing the cable length from 10 to 25 feet as it is when making the much larger change from 25 to 100 feet. This shows that small changes at the shorter cable lengths are the most critical.

Table IX shows the effects of various stability values and cable lengths on the airspeed at which instability first occurs. In the case where all three derivatives have their nominal value, and the cable length is 25 feet, this instability occurs at 19 knots. This means that this is the maximum airspeed at which the load can be carried.

Referring to Figures 32, 30 and 31, where $C_{n\beta}$ is 0.5, 1, and 4 times the nominal, it is seen that as $C_{n\beta}$ is reduced in value, the airspeed at which the load can be carried increases. Therefore it appears desirable that this derivative be reduced to a value as small as possible. Physically this might be accomplished by adding a dummy fin to the CH-46 load in such a way that the vertical stabilizing surfaces on the front and rear of the helicopter load are approximately equal. If this is done, then the values of the other two derivatives (C_{n_r} and $C_{y\beta}$) will increase. Table IX shows

these various "add fin" cases for different cable lengths and derivative values.

Comparing case 1 and case 6, for the same cable length of 25 feet, it is seen that this method increases the airspeed at which the load can be carried from 19 to 70 knots.

It was shown above that decreasing the cable length alone is stabilizing. Case 2 shows an "add fin" case in which reducing the cable length to 20 feet improves the maximum airspeed to 80 knots. Further decreasing the cable length to 10 feet (case 4) allows a further improvement to 125 knots. This method of decreasing $C_{n\beta}$ by some physical means appears very promising, and will be the subject of further research.

Referring to Figures 34, 30 and 33, where $C_{y\beta}$ is 0.5, 1, and 4 times the nominal, it is also seen that when this derivative is reduced in value the airspeed at which the load can be carried increases.

To decrease $C_{y\beta}$ physically, however, appears to be a much more difficult task than to make a comparable decrease in $C_{n\beta}$. Therefore the latter approach will be emphasized, and in view of the results obtained so far appears to be very promising.

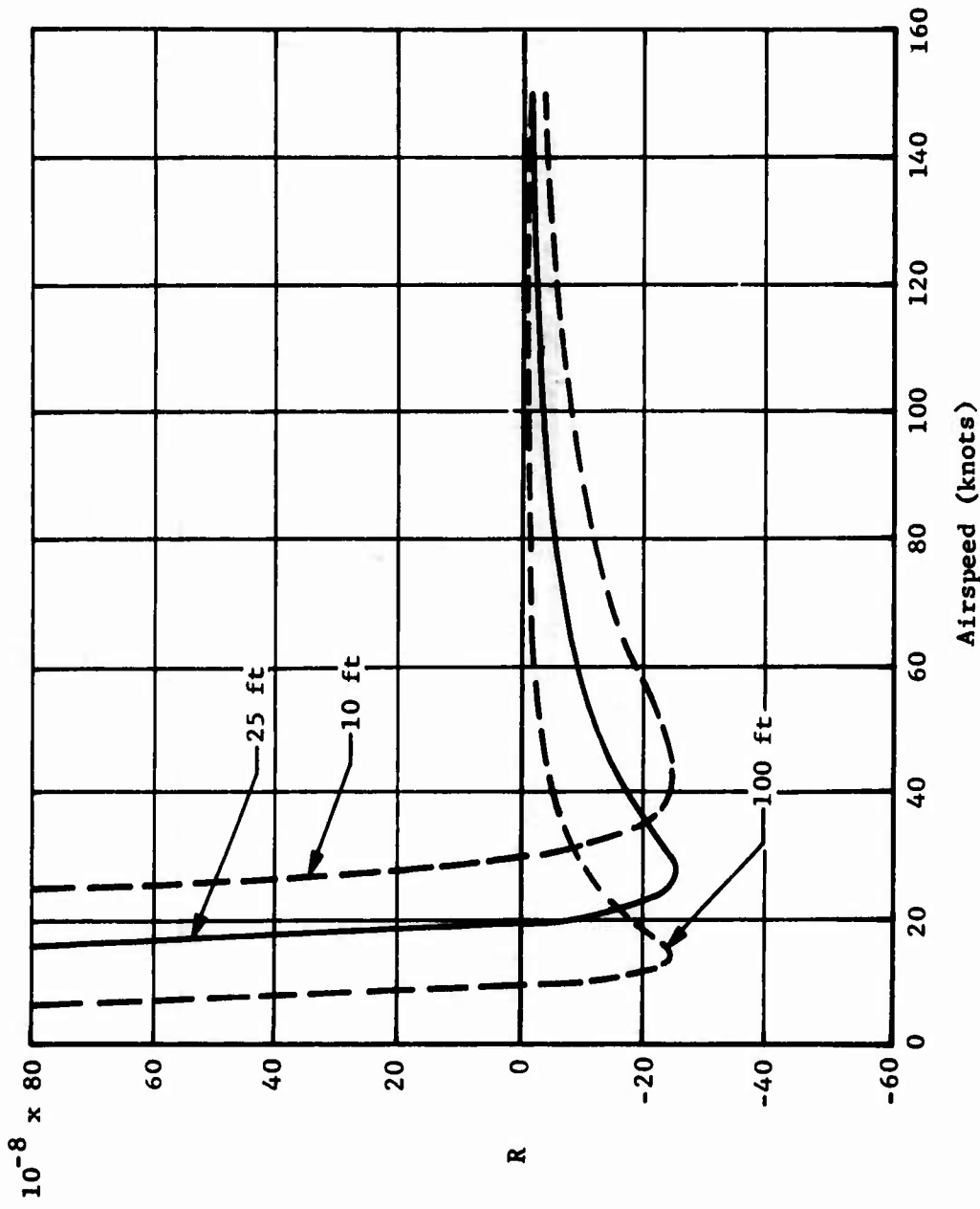


Figure 30. Stability Boundaries of Helicopter Load--Effect of Cable Lengths.

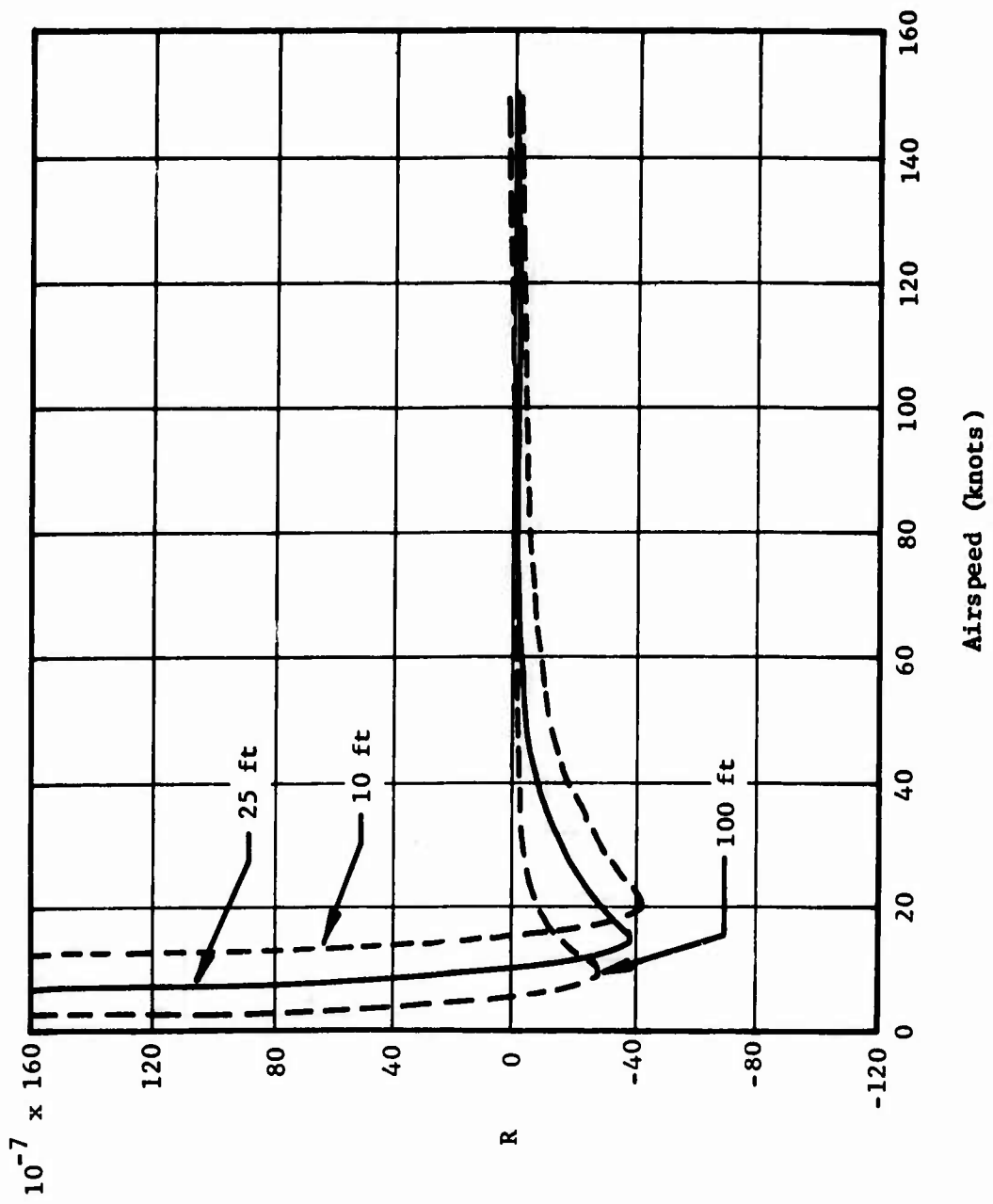


Figure 31. Stability Boundaries of Helicopter Load--Effect of $4 \times C_{n_\beta}$ Nominal (0.068) and Variable Cable Lengths.

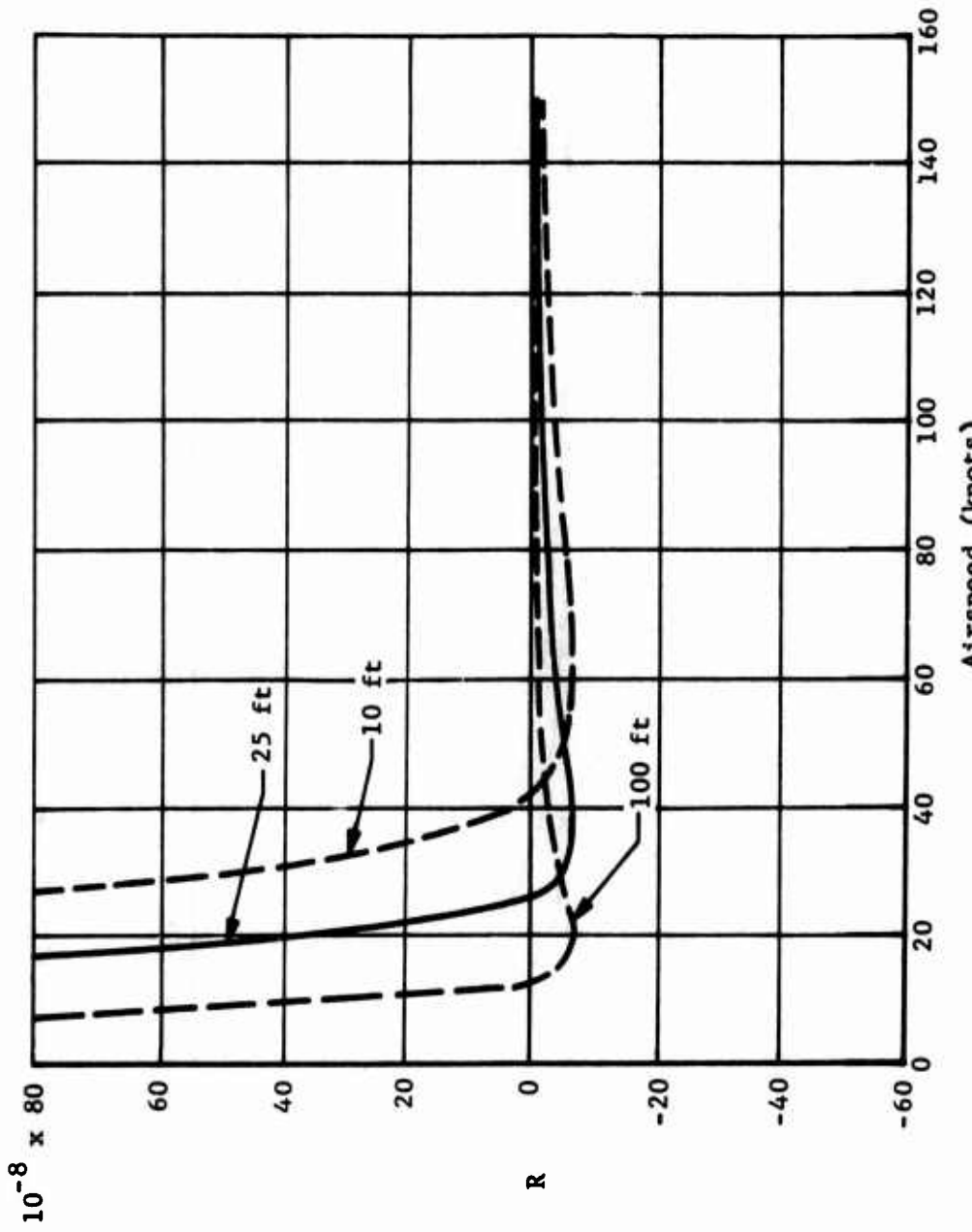


Figure 32. Stability Boundaries of Helicopter Load--Effect of $0.5 \times C_{n_B}$ Nominal (0.068) and Variable Cable Lengths.

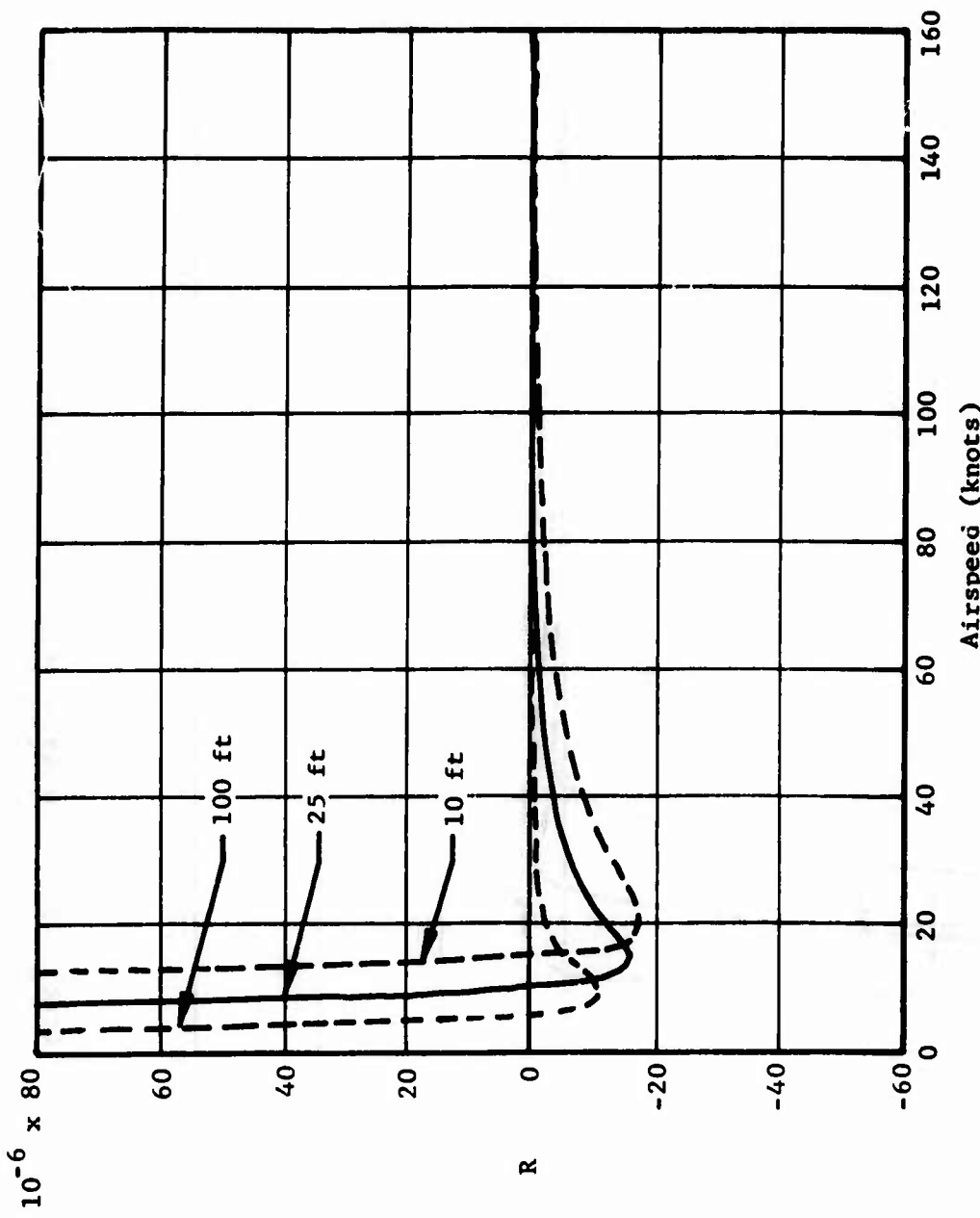


Figure 33. Stability Boundaries of Helicopter Load--Effect of $4 \times C_y$ Nominal (-0.205) and Variable Cable Lengths.

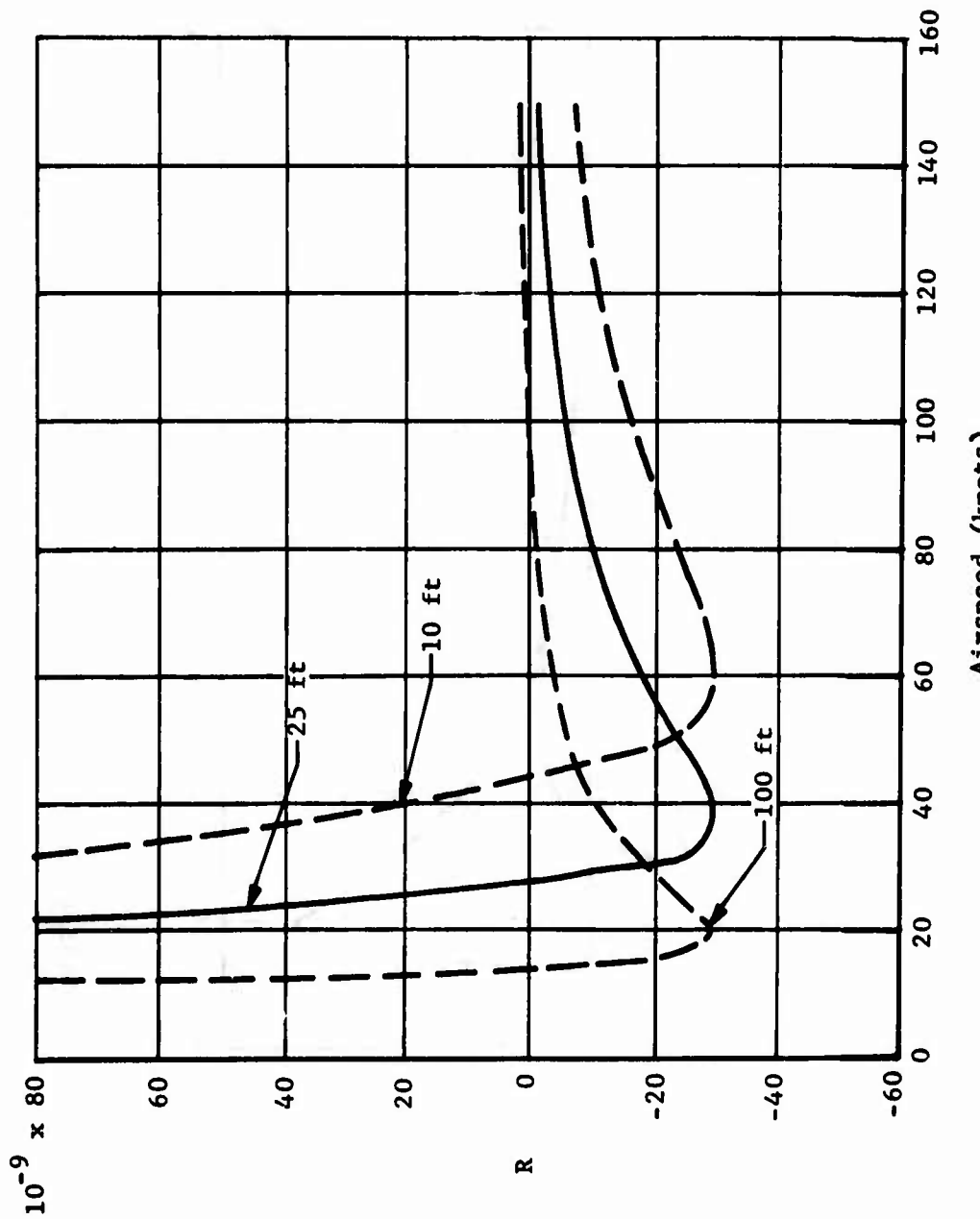


Figure 34. Stability Boundaries of Helicopter Load--Effect of $0.5 \times C_y \beta$ Nominal (-0.205) and Variable Cable Lengths.

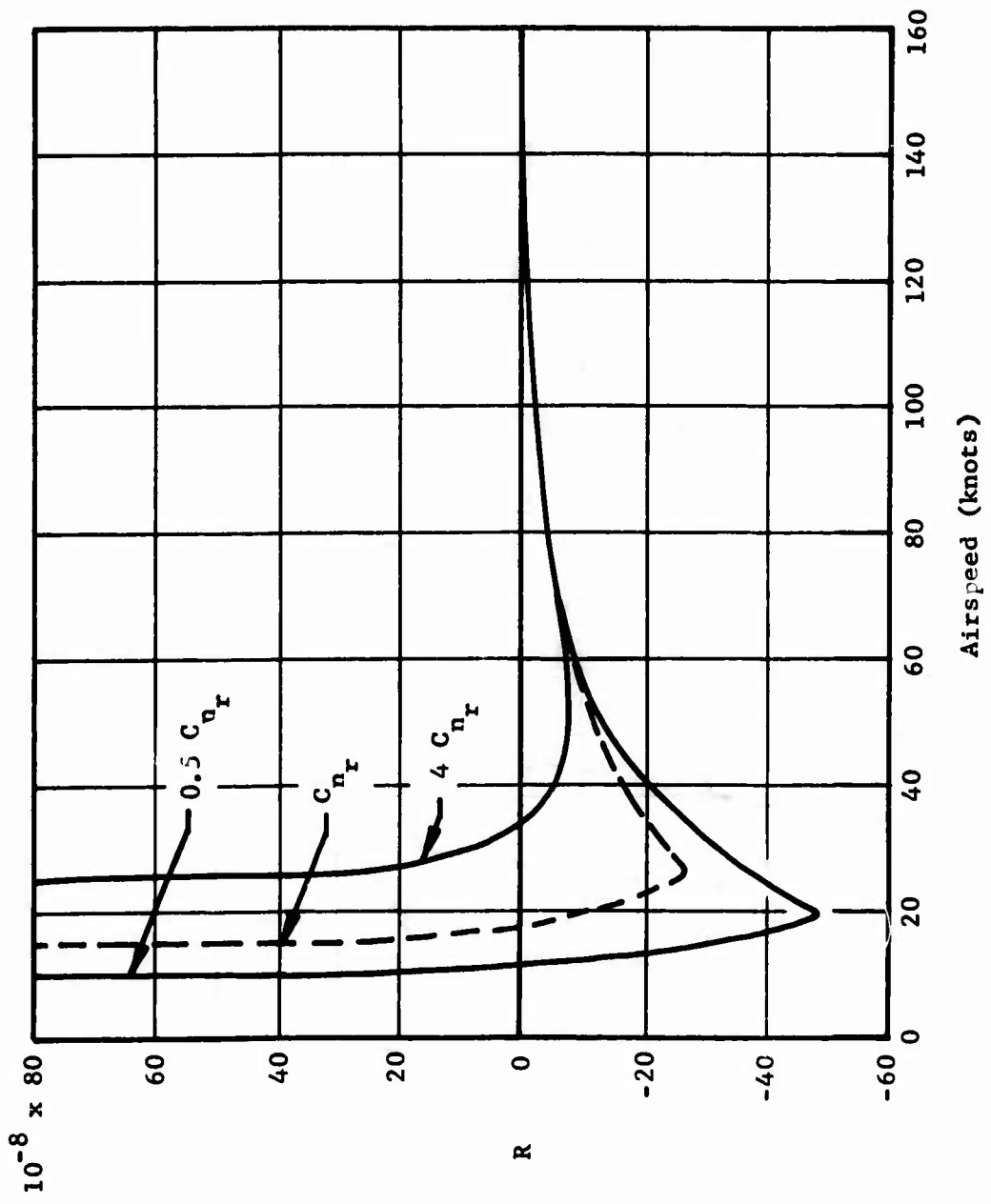


Figure 35. Stability Boundaries of Helicopter Load--Effect of C_{n_r} (Nominal = -0.00387).

TABLE IX. EFFECTS OF VARIOUS STABILITY VALUES AND CABLE LENGTHS ON AIRSPEED

Case No.	Configuration	C_{Y_B}	C_{n_B}	C_{n_r}	Cable Length (feet)	Maximum Stable Speed (knots)
1	Nominal	1.0	1.0	1.0	25	19
	Add Fin	1.5	0.1	2.0	20	
2	Add Fin	1.5	0.1	1.5	20	80
	Add Fin	1.5	0.1	2.0	10	
3	Add Fin	1.5	0.1	2.0	100	70
	Add Fin	1.5	0.1	2.0	25	
4	Add Fin	1.5	0.1	2.0	10	125
	Add Fin	1.5	0.1	2.0	100	
5	Add Fin	1.5	0.1	2.0	25	40
	Add Fin	1.5	0.1	2.0	70	
6	Add Fin	1.5	0.1	2.0	25	70
	Add Fin	1.5	0.1	2.0	70	

6.3 DETERMINATION OF STABLE FLIGHT SPEEDS FOR THE SELECTED HELICOPTER SLING LOADS

The following sling loads were investigated as part of the load stability analysis based on the methods developed earlier in the study.

8-by-8-by-20-foot Box (5,000 pounds)

8-by-8-by-20-foot Box (20,000 pounds)

8-by-8-by-40-foot Box (5,000 pounds)

8-by-8-by-40-foot Box (20,000 pounds)

Truck

Tank

Carrier

VH-34 Helicopter

F-5 Aircraft

OV-1 Aircraft

Three cable lengths were used: 10, 25, and 100 feet. Both one- and two-point suspensions were employed, as well as an optional 10-foot-diameter stabilizing parachute. Two different values of the $C_{n\beta}$ stability derivatives were used to determine the effects on the system.

Analysis

In general, it was found that the shorter the cable length, the more stable the system became. In the few cases where this was not so, the usual effects of the shorter cable were overpowered by other variables which were changed in the system.

The two-point load suspension, as would be expected, was considerably more stable than the single-point system. In many cases, merely going to the two-point arrangement was enough to greatly increase the stable airspeed of the system. This is one of the most significant improvements that can be made for all types of loads.

Various sizes of stabilizing parachutes were tried before it was finally decided that a 10-foot-diameter chute was the best compromise for all loads. Use of the parachute gave the most marked improvement in the single-point suspension case.

It was found during the investigation that stability increased when the value of $C_{n\beta}$ was made smaller. This, in general, held true for all loads

and all cable lengths. This effect alone was in most cases sufficient to give a marked improvement in system stability.

Each type of load is now considered individually, and the important factors which affect stability are pointed out. Tables X through XVII present the flight conditions and maximum stable airspeeds for each load.

Box (8-by-8-by-20-foot)

For the 5,000-pound case, the greatest stability is achieved with two-point suspension and a low value of $C_{n\beta}$.

For the 20,000-pound case, the largest improvement also results from two-point suspension and a low value of $C_{n\beta}$. With single-point suspen-

sion plus a chute, one case is found where the 100-foot cable shows more stability than the shorter lengths. Adding a chute in other cases shows narrow bands of instability with an improvement in the overall effect.

Box (8-by-8-by-40-foot)

For the 5,000-pound case, the best overall results are achieved with single-point suspension plus the parachute and low value of $C_{n\beta}$. A

speed of 150 knots is obtained with two-point suspension and a 10-foot cable.

For the 20,000-pound case, best results come from two-point suspension and a low value of $C_{n\beta}$. This combination appears to be the most effective one for most of the loads.

Truck

Best results for this type of load come from merely changing from one-to two-point suspension. This, by itself, will allow 150 knots stable airspeed for both cable lengths. This type of load, as with several of those to follow, is inherently unstable because of the minus sign of $C_{n\beta}$. For the single-point suspension without chute, changing from a minus to a plus value of $C_{n\beta}$ gives good results, with no other changes being necessary.

Tank

Best results for the tank also come from merely going to a two-point suspension system. For the single-point suspension without chute, using a plus value of the C_{n_B} derivative gives excellent results.

Carrier

This is similar to the two cases above, with a two-point suspension giving decided improvement. Again, the best arrangement for a single-point suspension comes from using a plus value of C_{n_B} .

VH-34 Helicopter

For single-point suspension, a stable airspeed of 150 knots can be obtained by either adding a 10-foot chute or reducing the C_{n_B} value to zero. For the two-point case, making C_{n_B} equal to zero gives very good results. The inherent C_{n_B} of this configuration for small sideslip angle is essentially zero. This explains why such a load could be carried at high speed, according to past flight experience.

F-5 Aircraft

Carrying the F-5 without the tail results in a very stable load for both one-and two-point suspension. When the tail is added, the best arrangement is single-point suspension with a 10-foot stabilizing parachute.

OV-1 Aircraft

Good results for this type of load are achieved by two-point suspension and a small value of C_{n_B} . For the single-point case, adding a para-chute will greatly improve the stability.

Conclusions

Several types of stability augmentation for helicopter sling loads have been discussed. Among these are two-point suspension, stabilizing parachutes, and changing the sign and value of the derivative C_{n_B} . By using these methods in the proper combination for each individual case, it is possible to greatly improve the stability of a given helicopter sling load.

Note: The physical meaning of the stability derivative C_{n_s} is as follows:

Mathematically, C_{n_s} is $\frac{\partial C_n}{\partial S}$; that is, the rate of change of yawing moment coefficient with respect to the sideslip angle. Axis system and nomenclature are shown in Figure 36. Aerodynamically, it is known to be the "weathercock stability." Aerodynamic configuration possesses weathercock stability if the yawing moment generated by the sideslip angle will reduce the sideslip angle.

Dynamically, positive weathercock stability means the configuration is statically stable. It is important to note that in such a complex multi-axis, multi-mass, helicopter/ting-load coupled dynamic system, static stability in one axis does not ensure stability of the overall system.

TABLE X. BOX (8-BY-8-BY-20-FOOT)

Weight (1b)	Susp (1 or 2)	Chute (10-ft)	Cable Length (ft)	Unstable Airspeed	$C_{n_B} = 2.5$	$C_{n_B} = 0.5$
5,000	1	0	10 25 100	40 20 10	X X X	
5,000	1	0	10 25 100	80 50 25		X X X
20,000	1	0	10 25 100	60 40 20	X X X	
20,000	1	0	10 25 100	150 100 50		X X X
20,000	1	1	10 25 100	150 40-50 20-30	X X X	
20,000	2	0	10 25 100	150 100 50	X X X	
20,000	2	0	10 25 100	150 150 125		X X X
5,000	2	0	10 25 100	80 50 25	X X X	
5,000	2	0	10 25 100	150 125 60		X X X

TABLE XI. BOX (8-BY-8-BY-40-FOOT)

Weight (lb)	Susp (1 or 2)	Chute (10-ft)	Cable Length (ft)	Unstable Airspeed	$C_n = 2.5$ β	$C_n = 0.5$ β
20,000	2	0	10	125	X	
			25	80	X	
			100	40	X	
20,000	2	0	10	150		X
			25	150		X
			100	100		X
20,000	1	0	10	80	X	
			25	60	X	
			100	30	X	
20,000	1	0	10	150		X
			25	125		X
			100	60		X
20,000	1	1	10	150	X	
			25	60-70	X	
			100	30-50	X	
5,000	1	0	10	50	X	
			25	30	X	
			100	15	X	
5,000	1	0	10	125		X
			25	70		X
			100	40		X
5,000	1	1	10	50-60	X	
			25	30-40	X	
			100	15-30	X	
5,000	2	0	10	70	X	
			25	40	X	
			100	20	X	
5,000	2	0	10	150		X
			25	100		X
			100	50		X

TABLE XII. TRUCK

Weight (1b)	Susp (1 or 2)	Chute (10-ft)	Cable Length (ft)	Unstable Airspeed	$C_n \beta = 2.5$	$C_n \beta = 0.5$
13,700	2	0	10	150	X	
			100	150	X	
13,700	2	0	10	150		X
			100	150		X
13,700	1	1	10	80	X	
			100	40	X	
13,700	1	0	10	150		X
			100	100		X

TABLE XIII. TANK

Weight (1b)	Susp (1 or 2)	Chute (10-ft)	Cable Length (ft)	Unstable Airspeed	$C_n \beta = 2.5$	$C_n \beta = 0.5$
32,000	1	1	10	80	X	
			100	40	X	
32,000	1	0	10	150		X
			100	150		X
32,000	2	0	10	150	X	
			100	150	X	
32,000	2	0	10	150		X
			100	150		X

TABLE XIV. CARRIER

Weight (1b)	Susp (1 or 2)	Chute (10-ft)	Cable Length (ft)	Unstable Airspeed	$C_n \beta = 2.5$	$C_n \beta = 0.5$
19,300	2	0	10	150	X	
			100	150	X	
19,300	2	0	10	150		X
			100	150		X
19,300	1	1	10	60	X	
			100	25	X	
19,300	1	0	10	150		X
			100	80		X

TABLE XV. VH-34 HELICOPTER

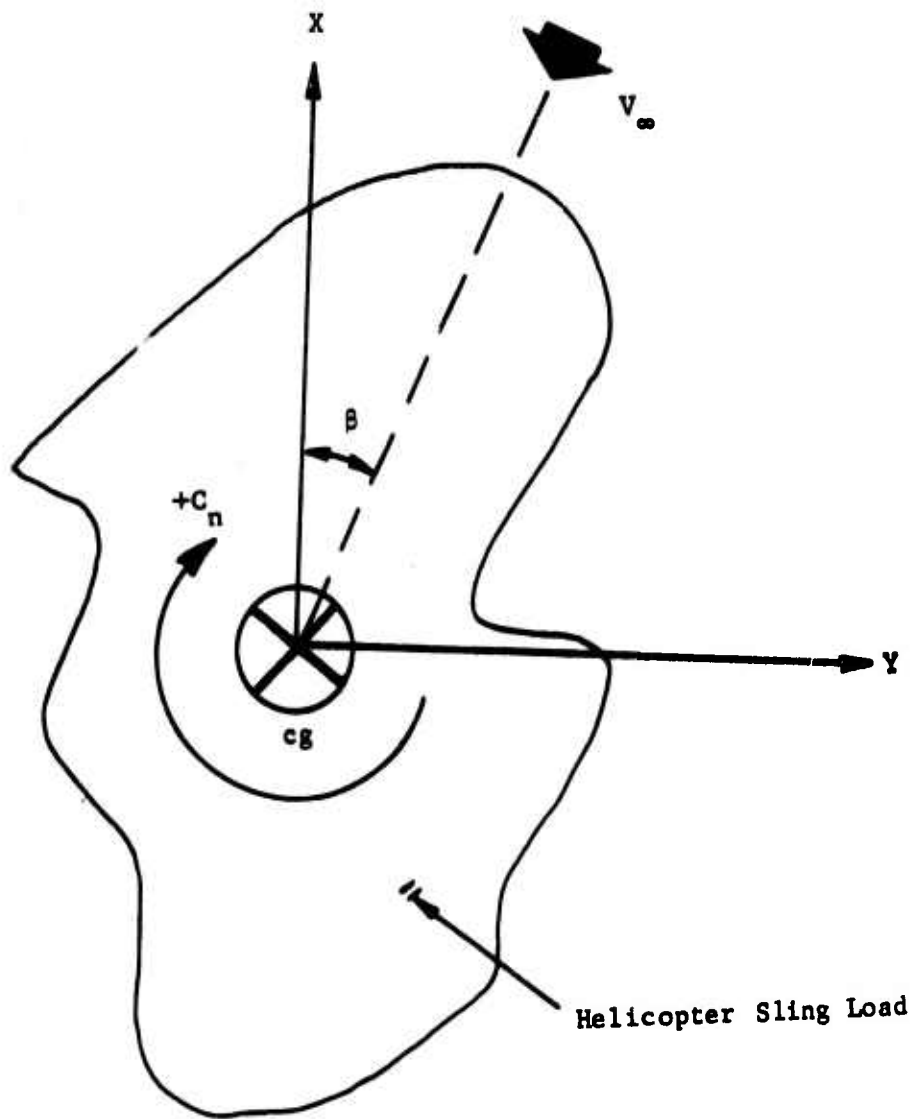
Weight (1b)	Susp (1 or 2)	Chute (10-ft)	Cable Length (ft)	Unstable Airspeed	$C_n \beta = 2.5$	$C_n \beta = 0.5$
11,000	1	0	10	80	X	
			100	25	X	
11,000	1	0	10	150		X
			100	150		X
11,000	2	0	10	150	X	
			100	50	X	
11,000	2	0	10	150		X
			100	150		X
11,000	1	1	10	150	X	
			100	150	X	

TABLE XVI. F-5 AIRCRAFT

Weight (1b)	Susp (1 or 2)	Chute (10-ft)	Cable Length (ft)	Unstable Airspeed	$C_{n\beta} = 2.5$	$C_{n\beta} = 0.5$
11,000	1	0	10	150	X	
			100	150	X	
11,000	1	0	10	100		X
			100	30		X
11,000	2	0	10	150	X	
			100	150	X	
11,000	2	0	10	150		X
			100	50		X
11,000	1	1	10	150		X
			100	125		X

TABLE XVII. OV-1 AIRCRAFT

Weight (1b)	Susp (1 or 2)	Chute (10-ft)	Cable Length (ft)	Unstable Airspeed	$C_{n\beta} = 2.5$	$C_{n\beta} = 0.5$
11,000	1	0	10	100	X	
			100	30	X	
11,000	1	0	10	150		X
			100	70		X
11,000	2	0	10	150	X	
			100	50	X	
11,000	2	0	10	150		X
			100	100		X
11,000	1	1	10	125	X	
			100	100	X	



X, Y Body Axes of Helicopter Sling Load

V_∞ Free Stream Velocity

β Sideslip Angle

C_n Yawing Moment Coefficient

$$= \frac{\text{Yawing Moment}}{(\text{Dynamic Pressure})(\text{Reference Area})(\text{Reference Length})}$$

Figure 36. Stability Derivative.

7.0 CURRENT TECHNOLOGY REVIEW

This section reviews the applicability or deficiencies of certain current load stabilization technology.

Figure 37, showing the effects of 25-foot stabilizing parachutes, indicates the increasing stability of the system with increased number of chutes for a CH-47 helicopter to be carried as a sling load. Going from one chute to two reduces the band of instability. When three chutes are used, the instability region is greatly narrowed.

There are, however, several disadvantages to using parachutes as a stabilizing device:

1. Figure 37 shows regions of instability for one to three parachute cases. Passing through these unstable airspeed regions may result in dangerous oscillations in the load. Even the three-chute configuration has a large unstable speed regime.
2. Considerable drag is added by the use of chutes, which means that additional power is required by the towing helicopter with a consequent decrease in performance.
3. Reports from pilots in Vietnam indicate that rigging drogue chutes to a load is difficult and time-consuming, and can be dangerous in a combat situation. Therefore, it would be highly desirable to stabilize the load by some means other than the use of drogue parachutes.

Spoilers and fins can be added to some loads to change certain aerodynamic derivatives. $C_{n\beta}$ can be changed by addition of fins or sometimes by a

change in the trim attitude of the load. Some aircraft are currently being carried with the tail removed to lower $C_{n\beta}$. When better criteria for

stability are developed, passive devices such as fixed fins and spoilers can contribute to carrying many loads.

Operational procedures are being developed to carry certain loads. A review of operational procedures has shown a wide variety of carry speeds for the same loads, reflecting limited experience and confidence in carrying sling loads.

Load sensors have not been developed much beyond the conceptual stage. Most aircraft sensors are not directly adaptable to load use because they give absolute measurements, rather than measurements relative to the helicopter. Rate sensors are generally usable; however, much development is needed in position and cable angle sensors.

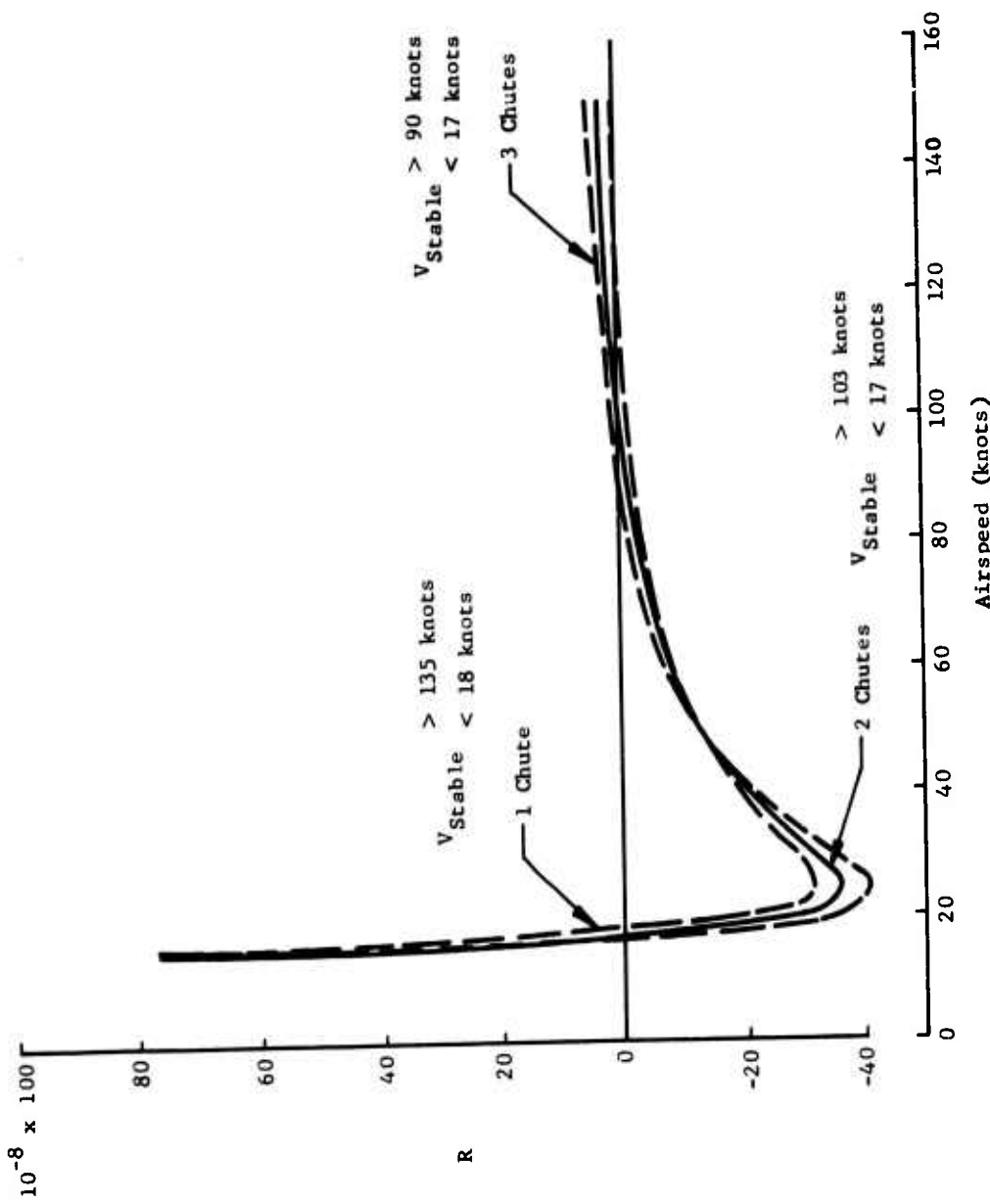


Figure 37. Stability Boundaries of Helicopter Load -- Load Stabilization by Parachute.

8.0 FORMULATION AND DEVELOPMENT OF CONCEPTUAL LOAD STABILIZATION SYSTEMS

Five conceptual load stabilization systems are described below. Each of the five approaches was selected because it supplies the basic information necessary to stabilize the load. Each should satisfy the load stabilization requirements. It is expected that they will differ significantly in performance and cost. Performance and cost were not studied beyond the depth reported herein. Comparative analyses and trade-offs were considered to be beyond the scope of this study.

Subsection 8.1 describes a concept that uses gyros mounted on a load beam and controls aerodynamic surfaces on that beam. Subsection 8.2 describes a similar concept in which the load rate information is fed to the helicopter SAS for control. Subsection 8.3 describes an infrared sensor display system that gives the pilot information on the load position. Subsection 8.4 describes an infrared sensor system that is connected to the helicopter SAS for control. Subsection 8.5 describes a system, similar to that in 8.4, that uses a gimbaled IR sensor.

8.1 AERODYNAMIC LOAD STABILIZATION WITH RATE SENSORS AND VANE CONTROL MOUNTED ON BEAM

The aerodynamic control technique consists of three axes of rate information coupled to three axes of moving surface stabilization, all fixed to a beam which is immediately above the load. The beam is required to move with the load and thus must provide for a three- or four-point attachment with minimum separation between the two.

One type of sensor package suitable for this application is two dual axis rate transducers (DART) mounted with their associated electronics and a rechargeable battery. The DART is a small, lightweight, rugged sensor capable of operation at wide temperature ranges (-65°F to +200°F) and high shock environments (100g continuous and 300g for 3 milliseconds). The DART has a rate threshold of 0.01 degree/second and a maximum rate output (selectable by resistor) of \pm 20 to \pm 300 degrees/second, with the full-scale output \pm 5 volts dc. The 3-ounce, 1-cubic-inch sensor requires only 4.3 watts power for the spin motors and internal electronics. Assuming an efficiency of 70 percent in the spin motor power supply and available battery power/weight ratio of 12 watt-hours/pound, the battery requirement would be less than 0.5 pound/hour of operation per sensor or 1.0 pound/hour for a three-axis package with redundant yaw outputs.

The unit, rigidly mounted to the beam, would contain batteries, two DARTS, a spin motor power supply, a battery status indicator and an on/off switch. Thirty seconds after turn-on the spin motors are up to speed and the unit is ready to provide signals to the beam control surface motor drivers.

The control system would consist of a fixed rear-mounted vertical stabilizer for directional load orientation with a control rudder and tab for

dynamic load damping about yaw. Near the vertical stabilizer would be a horizontal stabilizer with control elevators and tabs for dynamic pitch and roll load damping.

Fluidic control using ram air is also a possibility for study, since load stability at low speed is not as critical as at the higher speeds, where ram air pressure would become available to drive the tabs.

The yaw gyro output will be scaled and compensated, then coupled to the yaw tab. The gyro outputs will be scaled for a maximum value in the area of 30 degrees/second. The pitch and roll rate outputs will be scaled, compensated, and combined so that pitch rates drive the horizontal tabs in unison and roll rates drive the horizontal tabs differentially. An adjustment in the compensation circuit will provide for trimming out any long-term rate biases.

Although the DART sensor, with its piezoelectric pickoff and self-contained pickoff electronics, seems ideal for this application, the conventional single-axis rate gyro with spring restraint is also suitable. A typical gyro in this class is the Northrop GR-G7 with maximum output ranges of ± 10 degrees/second to ± 1000 degrees/second, depending upon the spring value at construction. These units are somewhat heavier, require more spin motor power, and also require an excitation signal for the pickoff and demodulation of the output.

Figure 38 is a schematic of this proposed configuration.

8.2 SLING LOAD STABILIZATION THROUGH LOAD SENSORS AND SAS INPUTS

This technique provides for sling-load stabilization with inputs to the craft SAS. A sensor unit would be mounted to an intermediate spreader beam or to the load directly. The two-axis rotational rate sensor and single-axis accelerometer would be powered by a cable from the craft. The cable would be suspended from a spring-loaded drum and provide craft-to-load distance (if not otherwise available) and carry the sensor outputs to the craft. One craft-mounted accelerometer with its input axis parallel to the roll axis is also required.

This system is suitable for a load supported with two cables, fore and aft, of equal separation on the craft and load. The load must also be suspended so that the motion about the roll axis is primarily pendulous from the craft, because the roll rate sensor will not be able to separate load-only roll and load-cable pendulous rates. The tandem support will result in equal load pitch rates and craft pitch rates; thus accelerometers are used to detect pitch pendulous motion. It is also assumed that the craft has a yaw rate output so that the craft-load differential rate can be generated.

The accuracy associated with low-cost rate sensors does not permit integration to obtain position for any long-term use; however, a representation of dynamic motion about a bias can be generated to about a 1- or 2-degree

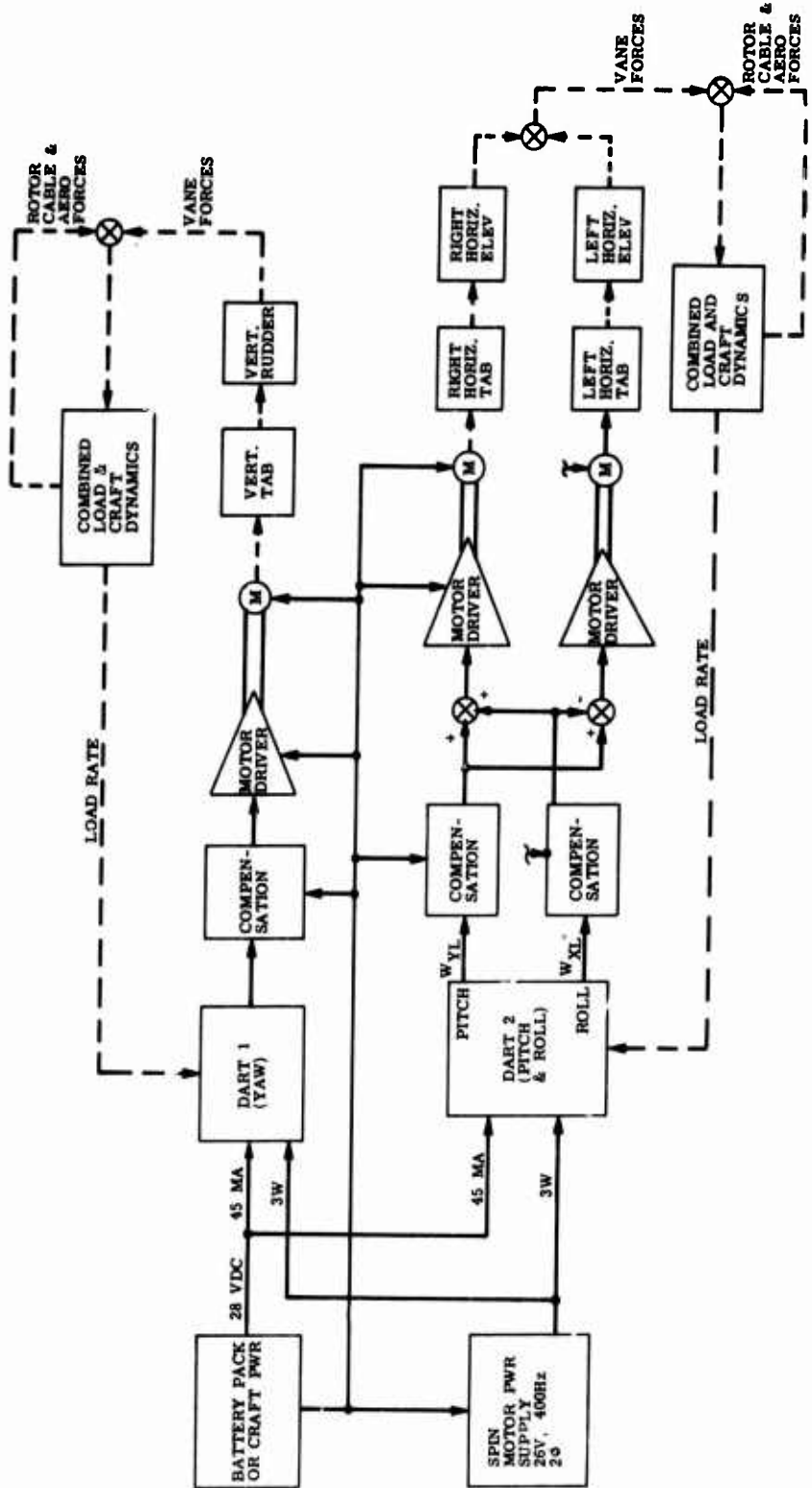


Figure 38. Rate Sensor Aerodynamic Load Stabilization.

accuracy for cockpit display. Thus, a periodic pitch motion of ± 10 degrees about a bias windage angle of 20 degrees would be displayed as ± 10 degrees about an unknown average.

The sensor package would contain a rate sensor for the yaw (Z) and roll (X) axis and an accelerometer with its input parallel to the X axis. The rate sensor envisioned is a dual axis rate transducer (DART) or two single-axis rate gyros of the type noted in the aerodynamic approach. The accelerometer in the load unit and in the craft would be of a class similar to the Systron Donner 431D. This sensor requires 28 volts dc (20 milliamperes), as does the DART, and both units have dc outputs, eliminating the need for signal generator excitation signals. The 4.5-ounce accelerometer has a nonlinearity of less than 0.05 percent of full range (available from 0.5g to 30g). The hermetically sealed unit with enclosed electronics will operate in temperatures from -40°F to $+200^{\circ}\text{F}$.

As shown in Figure 39, the compensated craft yaw (Z) rate is subtracted from the load yaw rate to generate a differential signal needed for SAS input. The compensation removes the bias output from the gyros and also will not pass very low rates, such as normal earth's rate input to the gyros. The differential yaw output is integrated for a cockpit display of position. The output is also differentiated for an angular acceleration input to SAS with an accuracy of about 0.03 degree/second².

The DART roll (X) axis output, assumed to be due to pendulous motion, is multiplied by cable length to generate a load velocity, relative to craft, along the Y axis. The relative Y velocity signal is fed to the SAS for load disturbance damping. The W_x output is integrated for display of roll pendulous angle, θ_x , and is differentiated for a Y acceleration output to SAS of about 0.08 foot/second² accuracy for a 150-foot cable.

The pitch (Y) pendulous acceleration used for SAS is determined by subtracting craft Y acceleration from the load X acceleration, both compensated so that biases are not passed. Thus, it is required that only the fore and aft cable lengths remain constant; any deviation from the load and craft not being parallel will not be reflected as signal, although this difference must be reasonably small in order to prevent Z acceleration from causing a significant differential output. The differential acceleration is integrated to generate the X velocity term for SAS input. The X velocity is divided by cable length for pendulous velocity and integrated for a display of θ_y .

8.3 IR SLING-LOAD DISPLAY SYSTEM

A passive IR system capable of displaying the sling-load position to the pilot consists of one shock-mounted receiver with a wide-angle 90-degree lens facing downward and four sources mounted on the load or on an intermediate beam just above the load. (See Figure 40.)

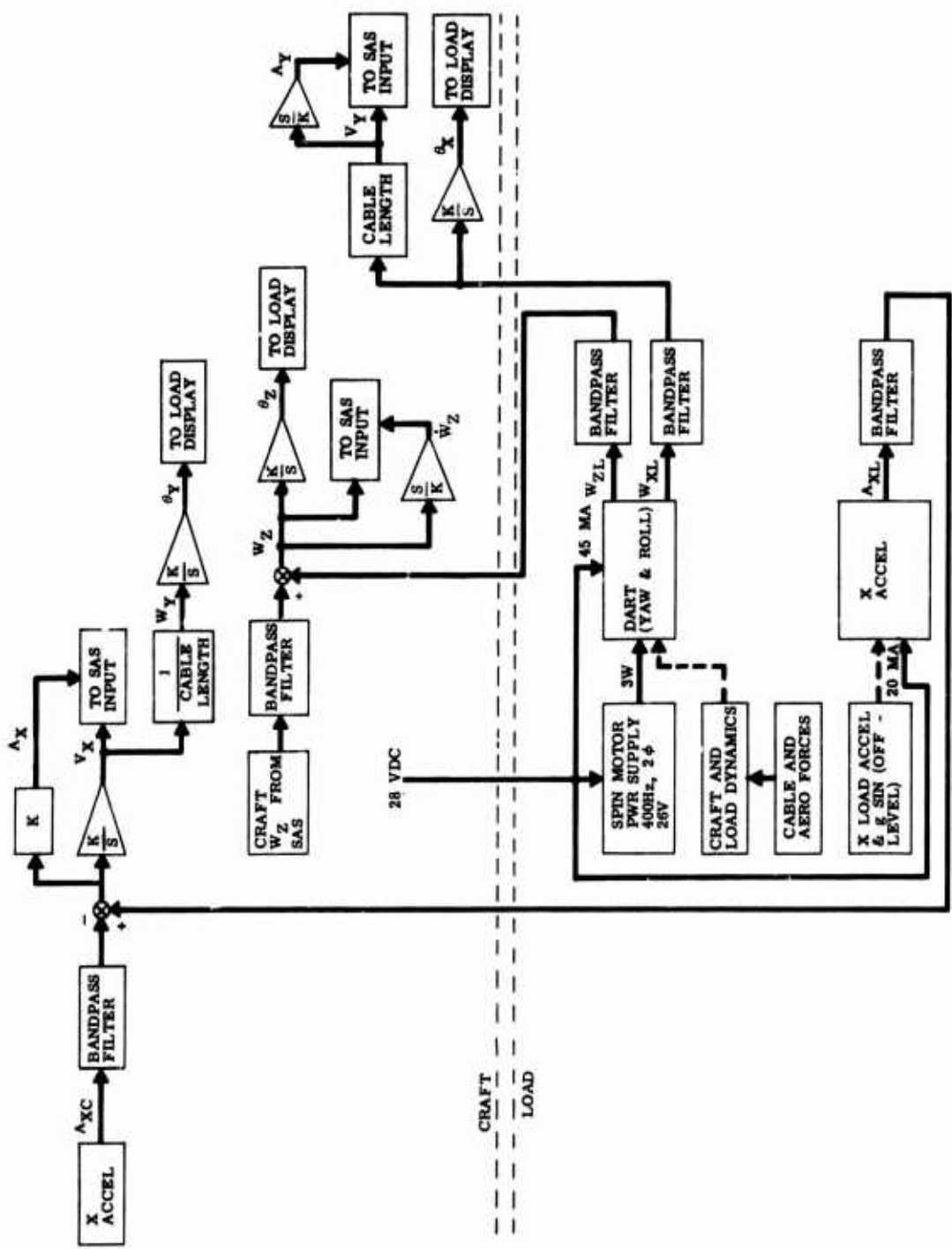


Figure 39. Load Stabilization With Rate Sensor and Accelerometer.

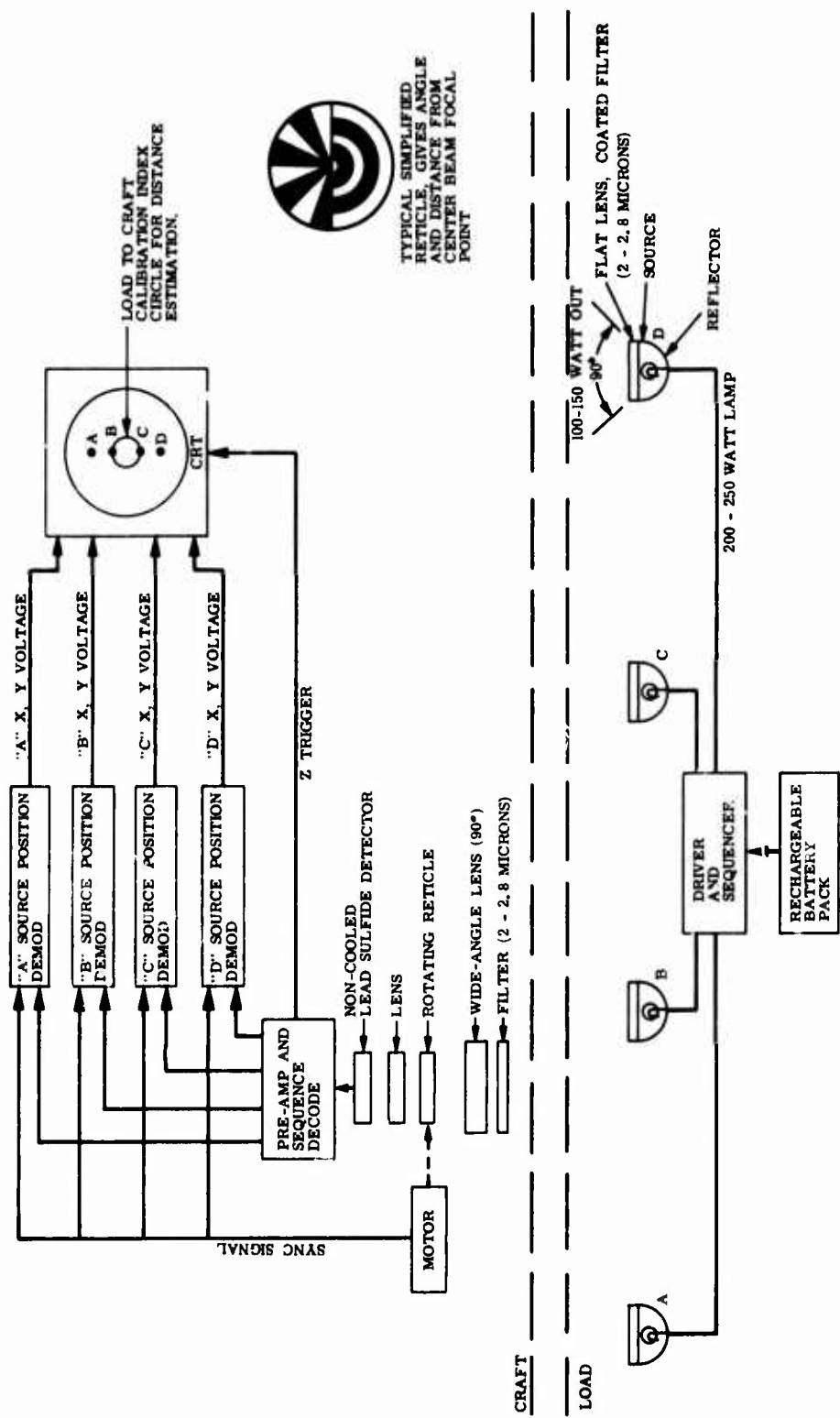


Figure 40. IR Sling-Load Position Display.

The sources envisioned are cesium iodide lamps mounted in a reflector cavity with about a 90-degree scatter. A flat lens over the cavity is coated with a 2- to 2.8-micron filter. The convection cooled sources are estimated to cost about \$100 each. Four sources may be required, due to the cable length range involved; i.e., well separated sources are required for good resolution at long distances but could be outside the field of view of the receiver at close range -- particularly with load sway. Some type of drive sequence will be required to define the given sources at the receiver -- perhaps a single pulse from "A" source, a double pulse from "B" source, etc., for "C" and "D". A rechargeable battery pack would provide for an electrically cableless system and have the added advantage of helping to guide the pilot over the load for sling attachment.

The estimated power input of 200 watts per source would require 12 pounds of battery per hour per source for a continuous source, but a more reasonable value for a pulsed system.

A source wavelength of 2 to 2.8 microns should provide an adequate signal through the expected adversities of rain, snow, fog, dust, smoke, etc.

The receiver envisioned is of the rotating reticle type with a wide-angle lens of about 90 degrees. This provides for about 1 degree of accuracy, is capable of observing multiple sources, and is less expensive than the gimbaled (which can only track one source) or mosaic receivers. A filter is required to reject background noise. The reticle, rotating at 300-900 rpm, is half composed of alternating radial segments of IR transparent and opaque material. The other half is composed of concentric alternating opaque on transparent segments, so that a beam focused in this area passes 50 percent of its energy to the cell behind it -- an effective calibration value. During the period the radial semicircular pattern passes across the beam, an ac signal is generated which has a peak-to-peak value proportional to the distance the beam is from the center. The start of the modulation relation to the reference index gives the azimuth of the beam; thus polar coordinates of the source are generated. A centered beam gives no modulation. Since a calibration voltage is generated during each revolution, and the modulated signal is demodulated relative to this value, no error is generated as a function of distance or other signal attenuation as long as a detectable signal is present.

Circuitry is required to decode the sequence and convert the chopper output to proper display drive signals, probably X and Y coordinate voltages if a cathode ray tube (CRT) is used for cockpit display.

A CRT display would show the four sources as dots on the screen, perhaps with the front dot of a higher brilliance to distinguish the yaw angle of the load with respect to the craft. Pitch and roll angles of the load up to ± 45 degrees could be displayed. A reference circle on the screen could be compared with dot separation in order to estimate load distance from the craft -- a particularly useful value during hover prior to hook-up.

8.4 IR SLING-LOAD MONITOR WITH PITCH AND ROLL LOAD DISPLAY AND PITCH AND ROLL RATE INPUT TO SAS

The IR active system envisioned consists of a single continuous source on the load with a single craft-mounted receiver for detecting the position of the load with respect to the craft. A review of state-of-the-art rotating reticle receivers indicates that with cable lengths beyond about 40 feet the yaw rate is no longer acceptable.

The yaw resolution problem was considered for a case where two sources are mounted at the extremes at a 24-foot beam; a 1-degree accuracy (3σ) detector, a 150-foot cable length and a 90-degree field-of-view lens are assumed. Under these conditions the yaw accuracy of a single reading degrades to 12.5 degrees. The pulse repetition rate with a state-of-the-art 900-rpm reticle does not permit averaging sufficient points with a tolerable delay to gain adequate accuracy. At short cable lengths, the yaw accuracy improves but the problem of the sources passing out of the field of view due to load motion then becomes significant. If additional sources with a smaller separation are also attached to the load or beam, then the data repetition rate decreases for each source, resulting in decreased accuracy.

If the case of the craft supporting a load with a single cable is considered, then yaw rate information to SAS is not relevant, since no craft yaw torque is capable of being transmitted to the load anyway. The system can now be optimized for providing the best possible pitch and roll information to SAS with the use of one continuous source. (See Figure 41.)

The source and detector units are the same as in the passive system, except that one continuous source is considered with a rechargeable battery pack to alleviate the power cable requirement and also provide information to the pilot prior to attachment. The receiver output data is averaged over a period and coupled to a display. The output is also differenced from the preceding average, divided by Δt and multiplied by cable length to generate the translational velocities required for SAS damping of pitch and roll disturbances.

The optimum data summation period for SAS rate input would be determined by a computer simulation. The error is assumed to be improved by $1/\sqrt{n}$ when n is the number of samples (uncorrelated data), but n must be sufficiently small so that the $n\Delta t$ delay in generating the rates is manageable. In the cases of sampling 15 points (1-second delay) the data is improved to an error probability of 1/4 degree, a rate error of 1/4 degree per second (3σ), and a translation rate error of about 0.6 foot per second (for 150-foot cable). The error rate may be acceptable, but the delay probably would not be. Conversely, a sample of one point gives a rate error probability of 39 feet per second (3σ) but a delay of only 67 milliseconds. Some compromise is obviously required for error and delay limits, based on the craft and load dynamics.

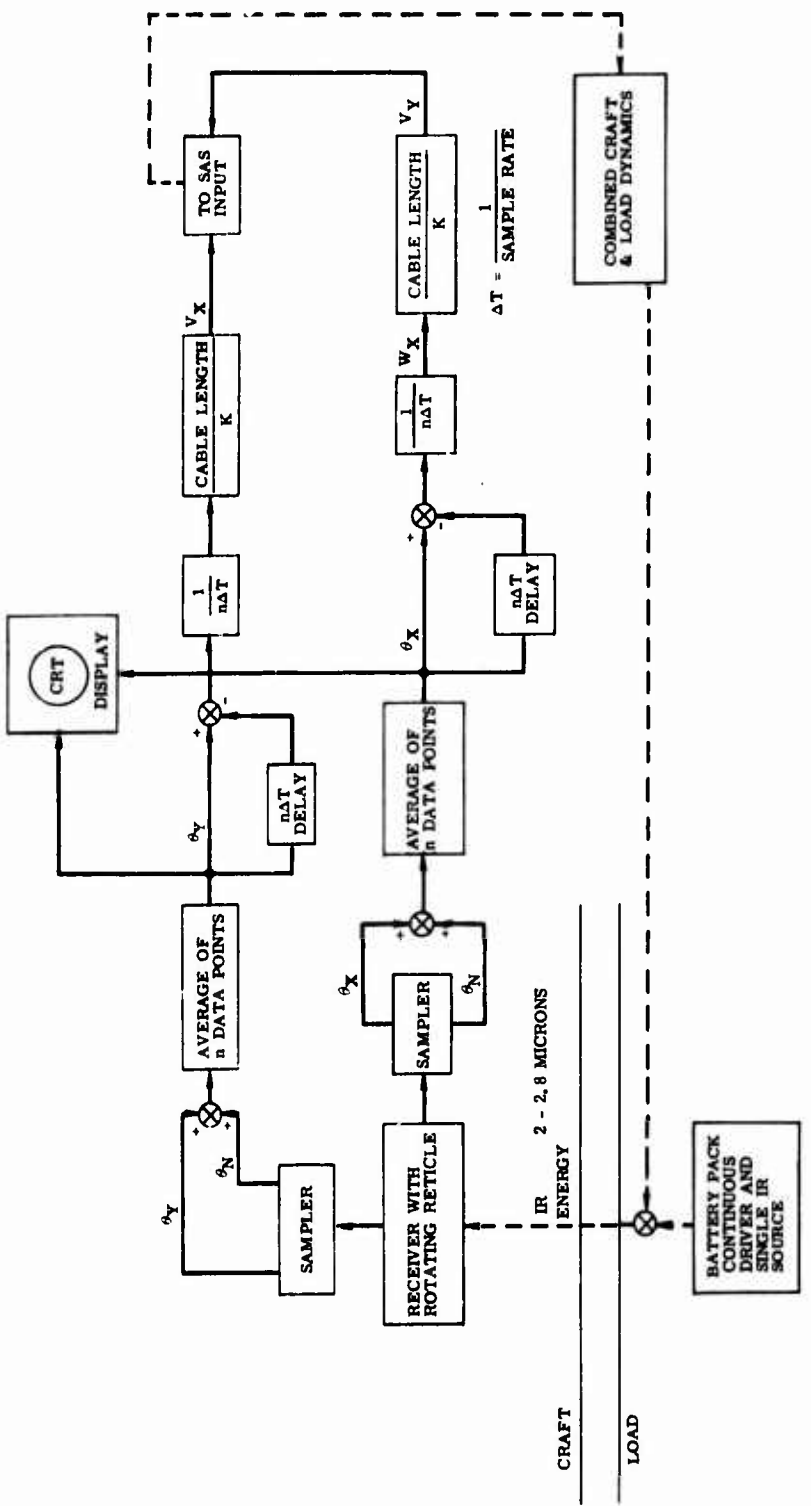


Figure 41. IR Active Load Stabilization.

8.5 GIMBALED IR ACTIVE LOAD MONITOR SYSTEM

The gimbaled IR sling-load monitor system consists of two coded sources mounted on the load and two gimbaled receivers mounted on the craft. Each gimbal set contains scan control capable of initiating a search pattern at turn-on. The source coding and receiver decoding provides for the acquisition of the proper signal. After the receivers have locked on, the sling-load motion data is derived from resolvers on each of the gimbals.

The near IR sources are envisioned as battery-powered cesium iodide lamps with a coded driver for each of the two and separated at about 24 feet on an intermediate beam directly above the load. The sources and receiver filters could be selected for a different wavelength as an alternate to the coding technique.

The sling-load rigging must be such that the beam moves with the load and also the load motion must be as near pendulous as possible, since the gimbal readout will not change with pitch or roll motion about the load axes.

The receivers are two-axis gimbal-mounted filter-lens-rotating reticle lead sulfide detector units. These units will require only about a 5-degree field-of-view lens, since they are null-seeking devices; thus the accuracy will be improved over the previously explained ungimbaled 90-degree field-of-view units. The gimbal readout angles should be accurate to at least $1/4$ degree (3σ). In addition, the data will be continuous and can be averaged over a period which should be adequate for the yaw rate generation required for craft SAS input to effect yaw load damping with the tandem cable configuration.

This configuration, as shown in Figure 42, is capable of providing three axes of position display. The pitch and roll position outputs are generated as the average of the two inner and outer gimbals, respectively. The yaw position output is the result of differencing the two roll gimbal outputs and compensating for cable length. The rates are the derivative of these signals, which should be relatively noise-free. X and Y velocities are generated as a function of cable lengths.

An added advantage of this system is that the pilot could use the receiver to help locate a landing area where a larger IR source is excited on the ground. The pilot could initiate a mode causing either receiver to scan areas around the craft for a brighter source and display the source on the CRT.

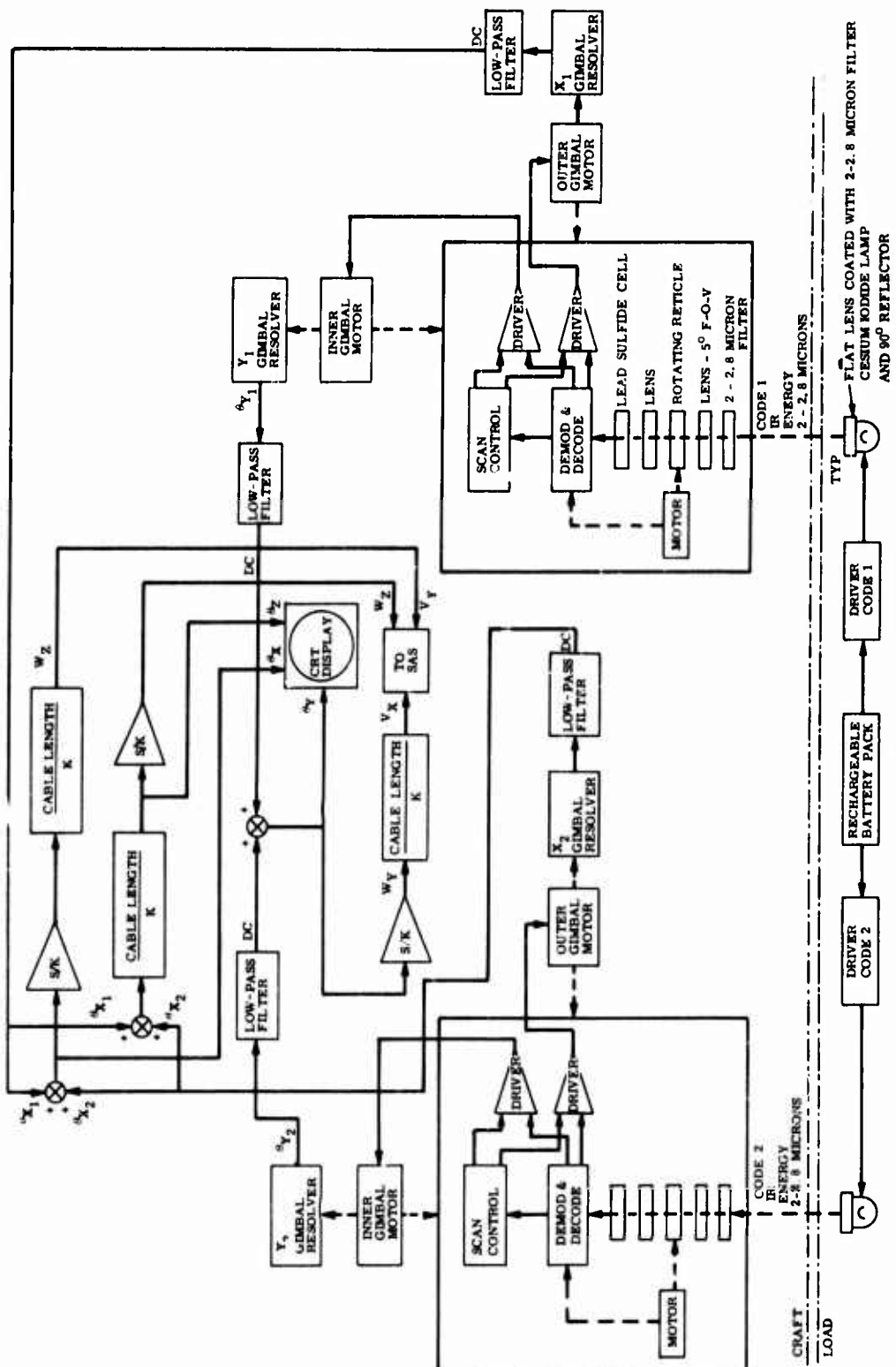


Figure 42. IR Gimbaled Load Monitor - Active

9.0 COST ESTIMATION OF PROPOSED LOAD STABILIZATION SYSTEM

Tables XVIII through XXII present cost estimates for the following:

<u>Table</u>		<u>Figure</u>
XVIII	Rate Sensor/Aerodynamic Load Stabilization	43
XIX	Rate Sensor and Accelerometer	44
XX	IR Sling-Load Position Display	45
XXI	IR Active Load Stabilization	46
XXII	IR Gimbaled Load Monitor -- Active	47

The function references in the tables correspond with the key letters appearing on the illustrations, which follow the tables.

TABLE XVIII. RATE SENSOR/AERODYNAMIC LOAD STABILIZATION

Function Reference (Figure 43)	1-5 Units	1000 Units
A	\$ 200	\$ 150
B	75	50
C	5,000	1,350
D	5,000	1,350
E	35	20
F	50	30
G	50	40
H	35	20
I	35	20
J	15	10
K	15	10
L	60	40
M	60	40
N	50	40
O	50	40
P	21,800	14,500
Q Packaging	1,000	600
R Cabling	200	150
Totals	\$33,730	\$18,460

TABLE XIX. RATE SENSOR AND ACCELEROMETER

Function Reference (Figure 44)	1-5 Units	1000 Units
A	\$ 500	\$ 400
B	500	400
C	25	15
D	25	15
E	25	15
F	25	15
G	25	15
H	20	10
I	20	10
J	20	10
K	20	10
L	20	10
M	20	10
N	20	10
O	20	10
P	20	10
Q	800	600
R	5,000	1,350
S	60	40
T Packaging	1,000	600
U Cabling	200	150
Totals	\$8,365	\$3,705

TABLE XX. IR SLING-LOAD POSITION DISPLAY

Function Reference (Figure 45)	1-5 Units	1000 Units
A	\$ 350	\$ 200
B	8,000	4,000
C	800	600
D	100	75
E	100	75
F	100	75
G	100	75
H	250	150
I	250	200
J Packaging	1,000	600
K Cabling	200	150
Totals	\$11,250	\$6,200

TABLE XXI. IR ACTIVE LOAD STABILIZATION

Function Reference (Figure 46)	1-5 Units	1000 Units
A	\$ 800	\$ 600
B	8,000	4,000
C	2,000	1,500
D	400	300
E Packaging	1,000	600
F Cabling	200	150
Totals	\$12,400	\$7,150

TABLE XXII. IR GIMBALED LOAD MONITOR -- ACTIVE

Function Reference (Figure 47)	1-5 Units	1000 Units
A	\$15,000	\$10,000
B	15,000	10,000
C	10	5
D	10	5
E	10	5
F	20	10
G	20	10
H	20	10
I	20	10
J	20	10
K	20	10
L	25	15
M	25	15
N	25	15
O	25	15
P	800	600
Q	100	75
R	100	75
S	50	30
T	50	30
U	250	200
V Packaging	1,000	600
W Cabling	200	150
Totals	\$32,800	\$21,895

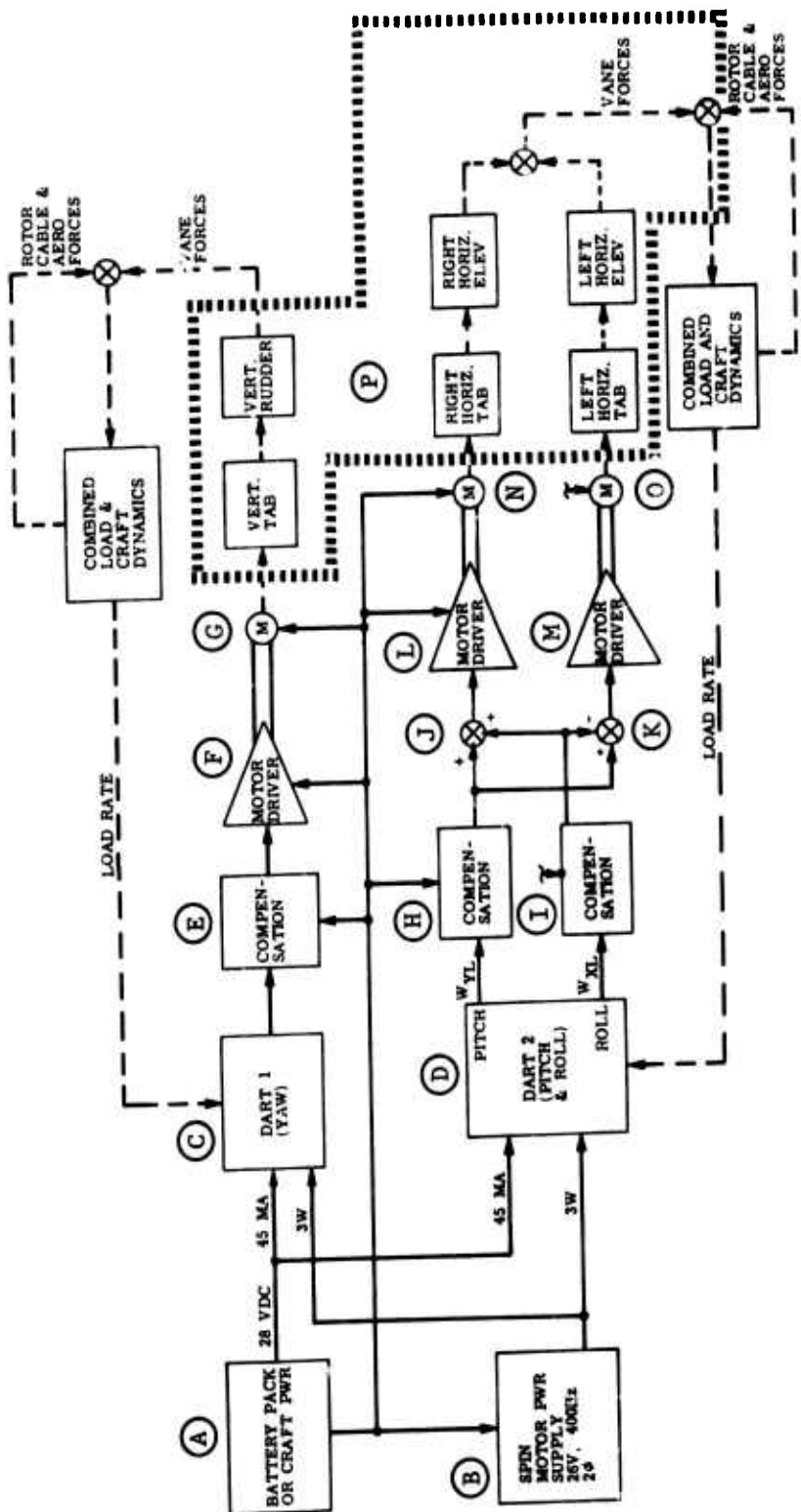


Figure 43. Rate Sensor Aerodynamic Load Stabilization.

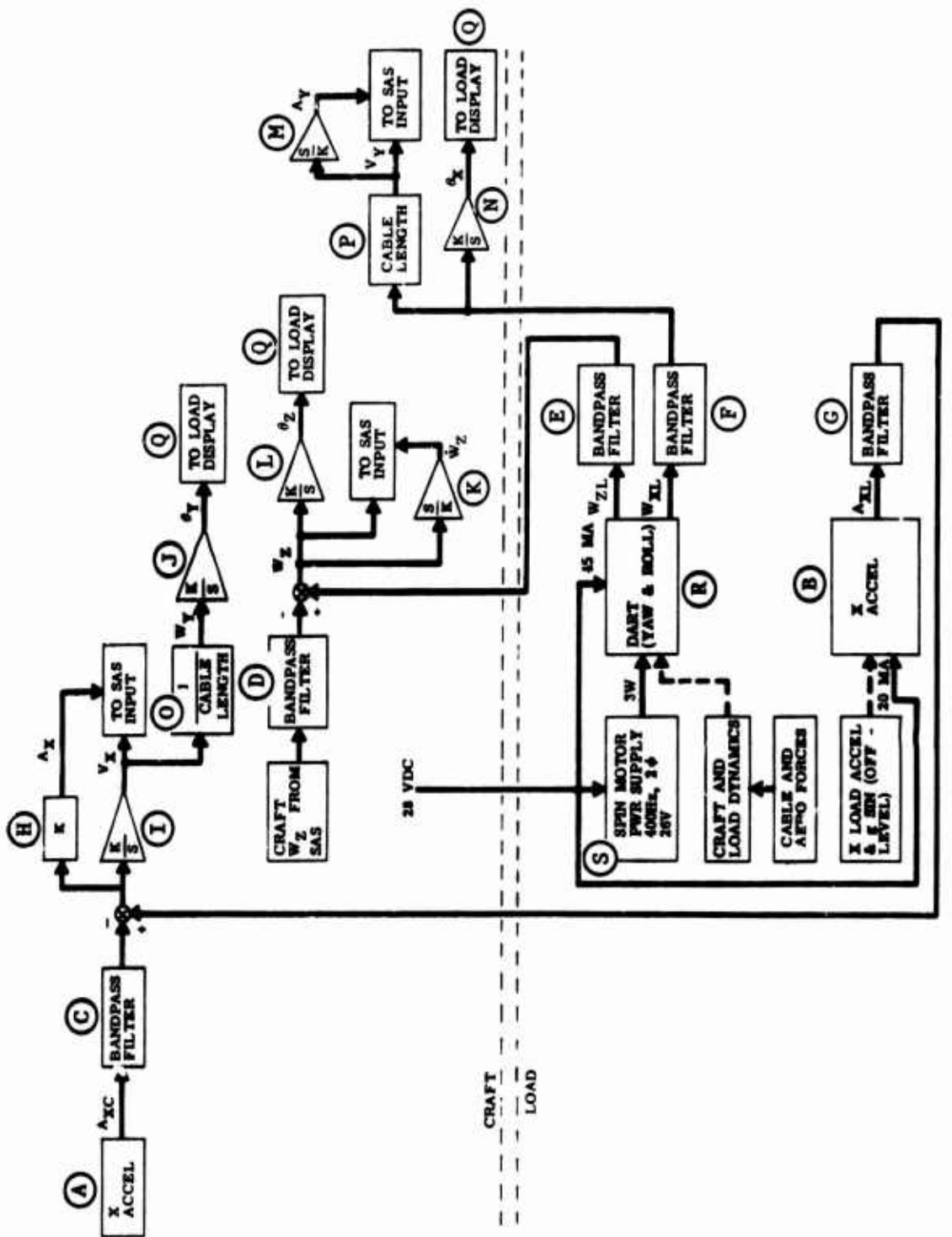


Figure 44. Load Stabilization With Rate Sensor and Accelerometer.

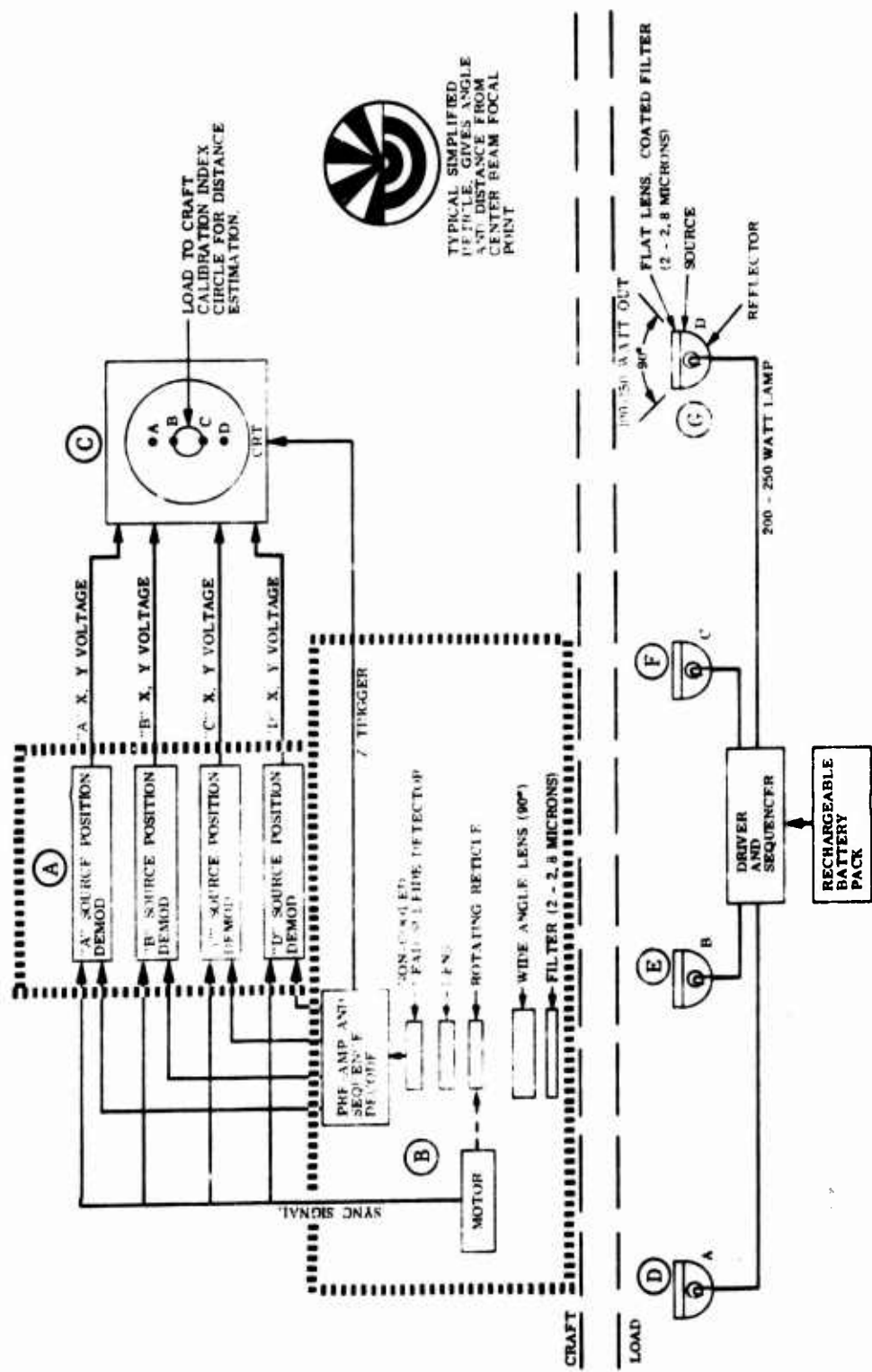


Figure 45. IR Sling-Load Position Display.

Reproduced from
best available copy.

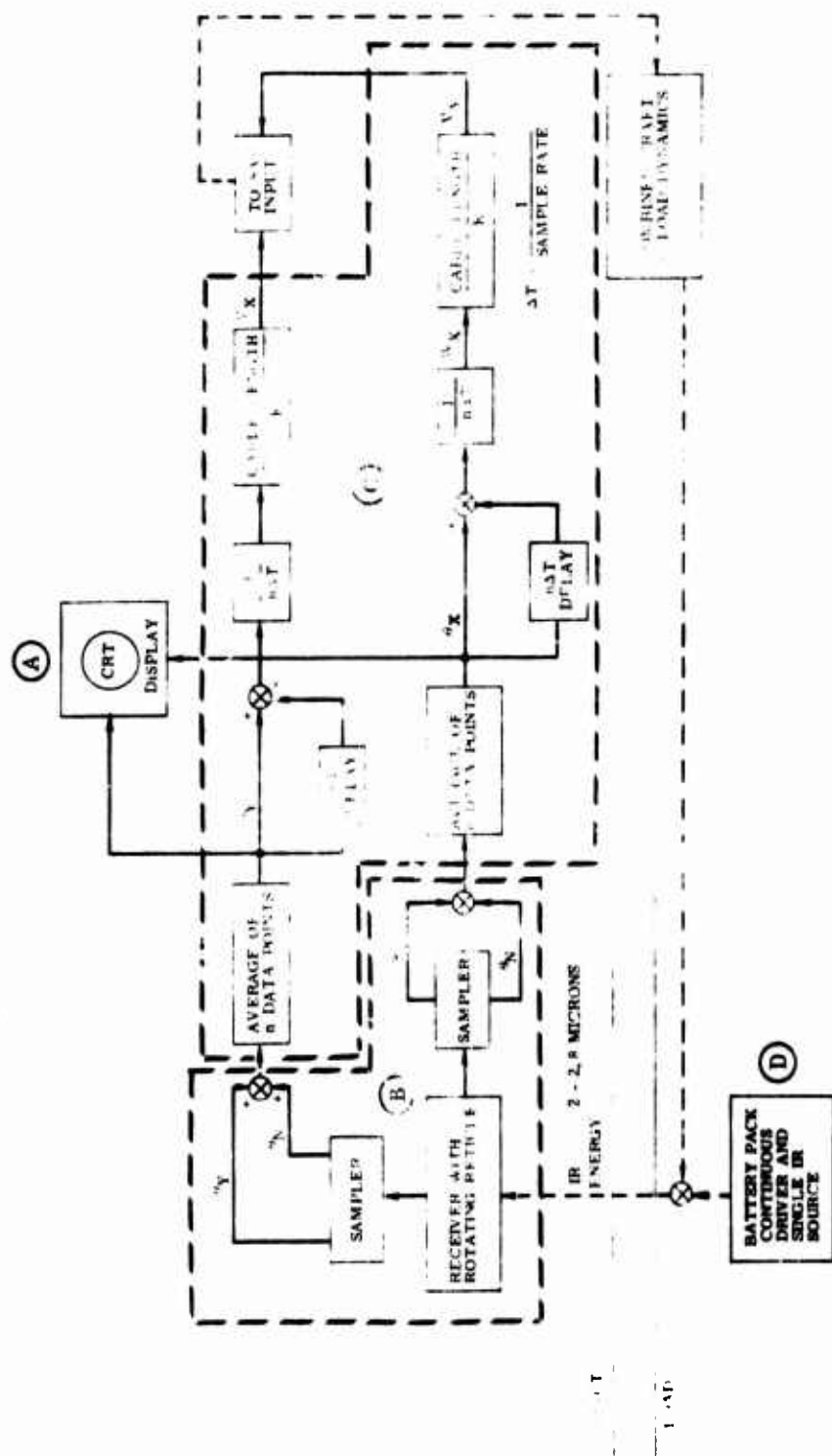


Figure 46. IR Active Load Stabilization.

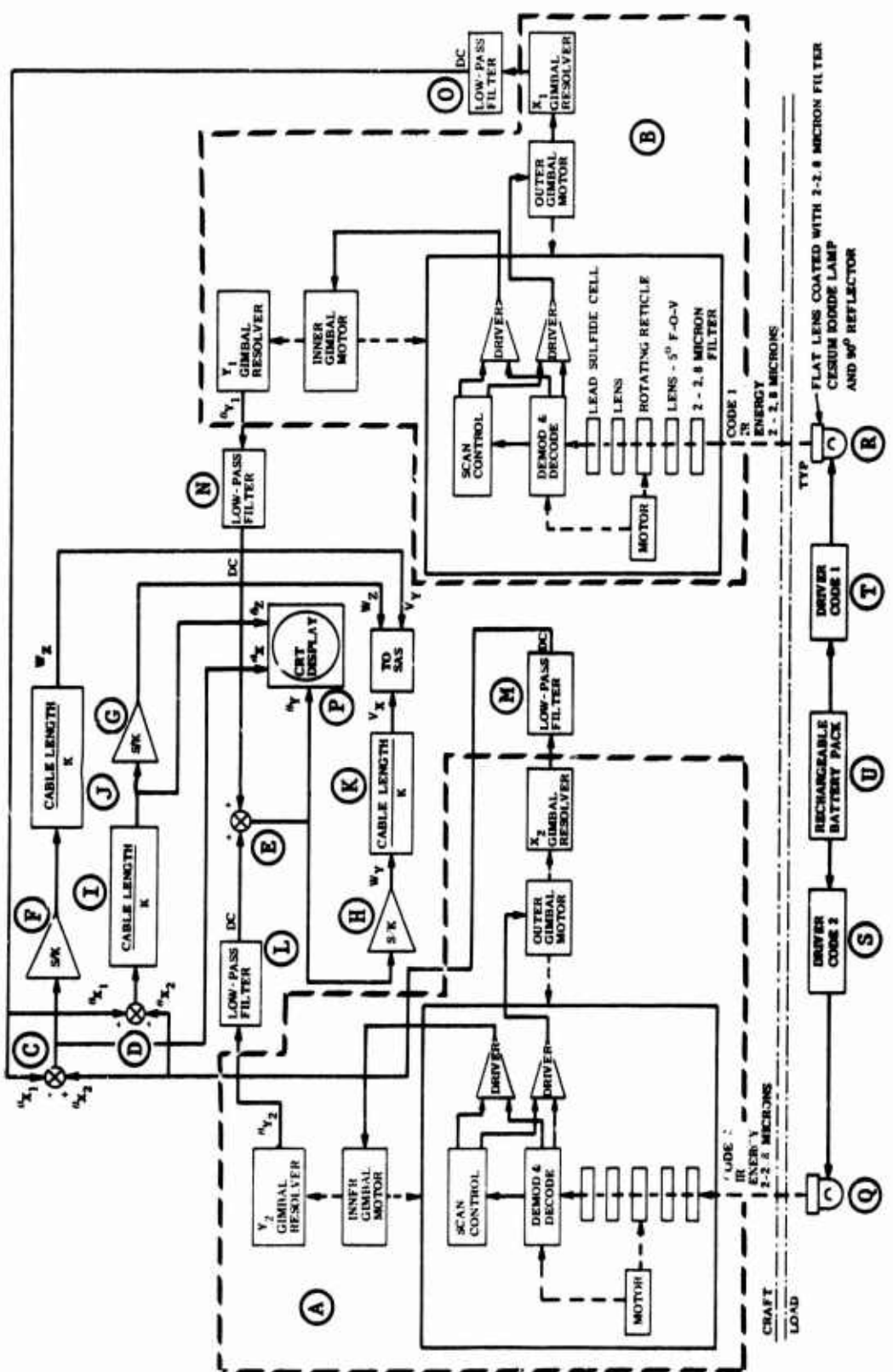


Figure 47. IR Gimbaled Load Monitor - Active

9.1 SELECTED SLING-LOAD STABILIZATION SYSTEM CONCEPTS

Various types of helicopter sling-load stabilization system approaches have been investigated: mechanical multi-cable system, mechanical load stabilizer, structural loading fixtures, passive and active aerodynamic systems, drogue stabilizer, and electronic stability augmentation system. Mechanical load stabilizer, passive aerodynamic load stabilization approach, and drogue stabilizer system all require further study to explore the applicability to various load configurations and to generate proper design mechanization.

Figure 48 presents a system concept optimized for carrying the container type of load. It consists of a loading spreader fixture suspended by four load cables. Lateral adjustment of the loading spreader could be made to carry loads with various widths, and side cables are used for carrying loads with various lengths by attaching the cable from the spreader arm to the bottom corner fitting of the container. The spreader fixture could be winched up and fitted into the bottom of the helicopter fuselage. Thus the top surface of the container is essentially flush with the bottom of the fuselage. The box structure of the spreader locking onto the fuselage could provide load stabilization in all axes. The load is snug fitted with the helicopter, thus enabling the helicopter to fly at maximum power limited speed.

Various locking mechanisms could be worked out such as shown in Figures 49 and 50. In Figure 49, an adjustable twist-lock type of locking system is used, while in Figure 50, no locking is engaged; a retractable flap serves to encase the load to prevent motion of load.

Figure 51 shows a load stabilization concept using a stabilizing cable system. As shown in the figure, the stabilizing cables form a box structure; thus load yaw, and longitudinal and lateral pendulum motion could be restrained. This concept could be applied to any load configuration with proper loading fixtures. It could be used for both winching or nonwinching load cable systems.

In Figure 52, the long cross-stabilizing cable system is eliminated, and a longitudinal stabilizing cable system is added. This system provides inherent stability for the load. The longitudinal stabilizing cable could also be used for active stabilization by a stabilizing winch/cable arrangement. A fore and aft cross-stabilizing cable system provides yaw stability. This approach could be applied to any load configuration.

Figure 53 illustrates a concept of load stabilization by an auxiliary cable system to provide longitudinal and lateral stability. A lateral boom on the fuselage provides added width for increasing stability. This concept could be applied to single, tandem, or any multiple suspension cable systems. Through these stabilizing cable systems, active load stabilization could be applied. Adding a small winch system to the stabilizing cable could provide active load damping. Safety release systems for all the stabilizing cables with high reliability could be mechanized without great difficulty. Since load stabilizing cables are not major load carrying cables, they should be considerably lighter.

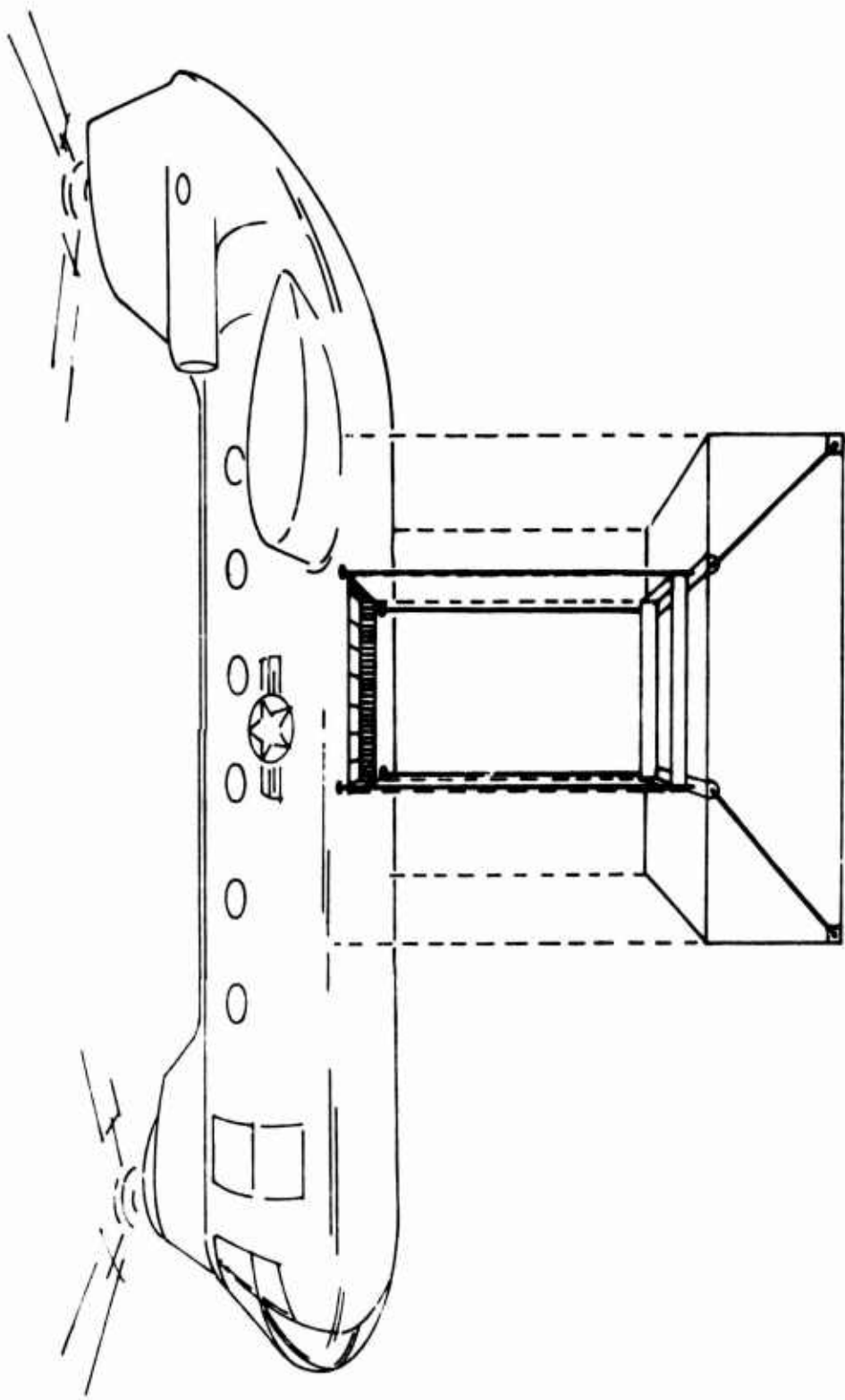


Figure 48. Loading Spreader Fixture Suspended by Four Load Cables.

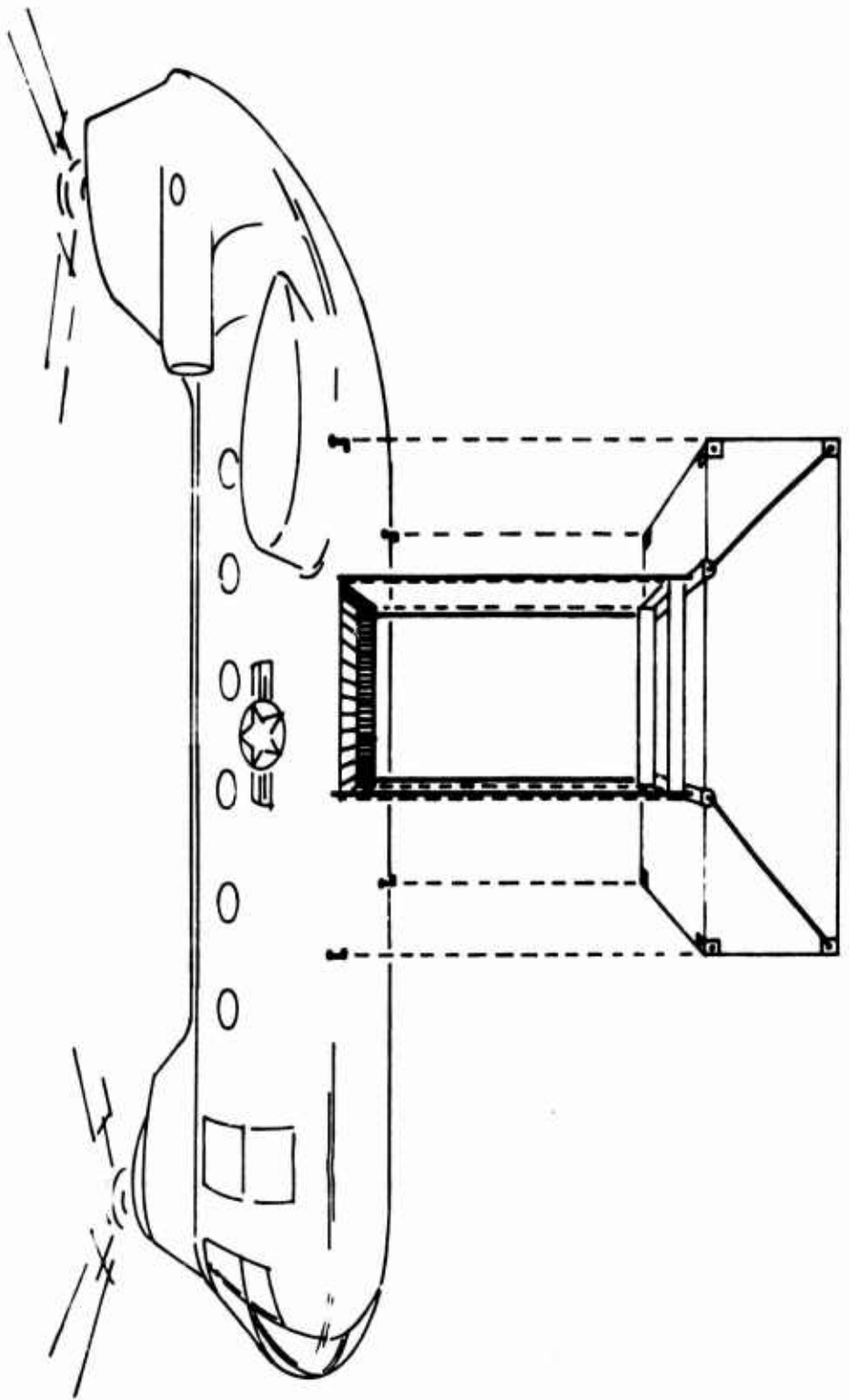


Figure 49. Adjustable Twist-Lock System.

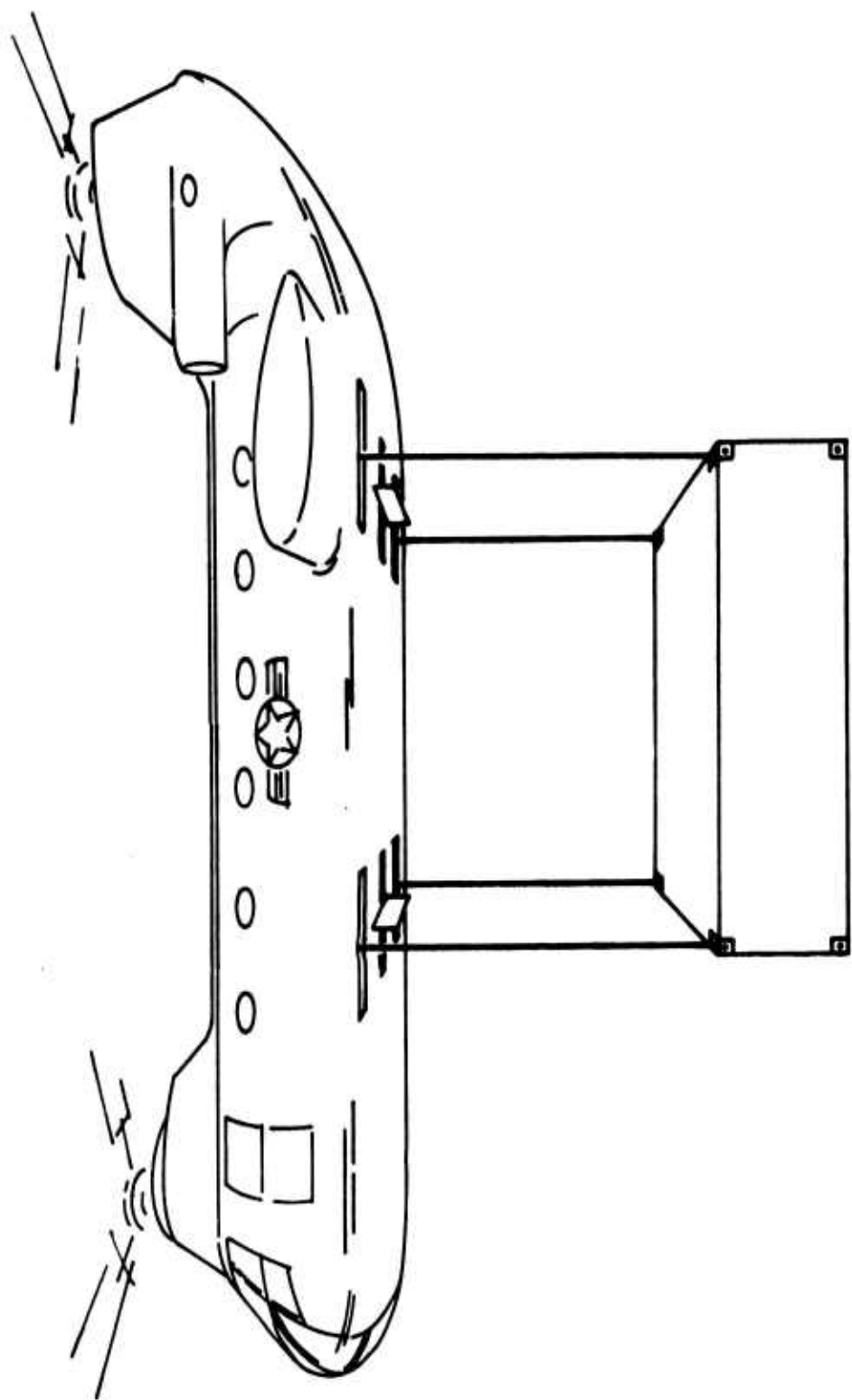


Figure 50. Retractable Flap System.

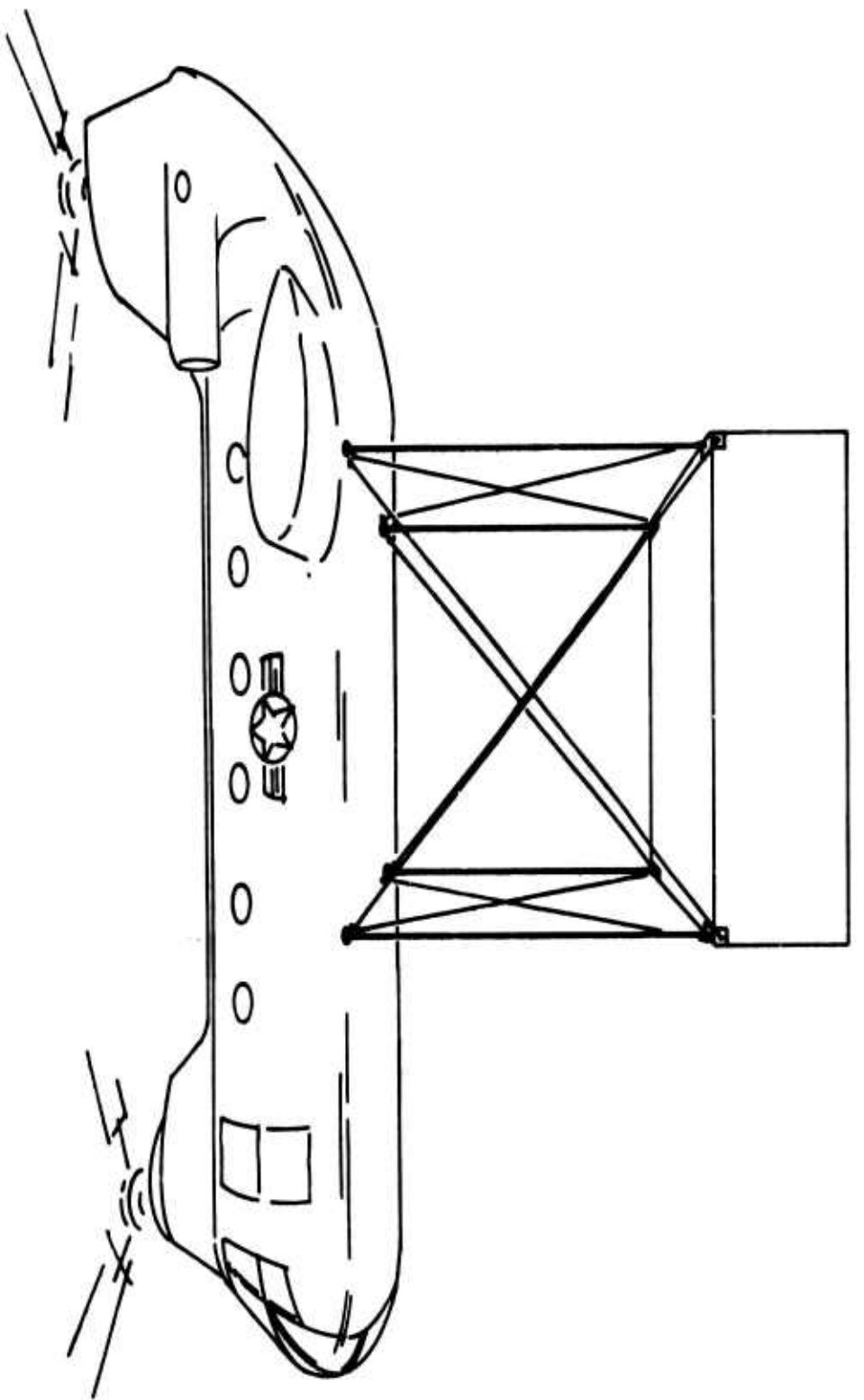


Figure 51. Stabilizing Cable System With Cross-Stabilizing.

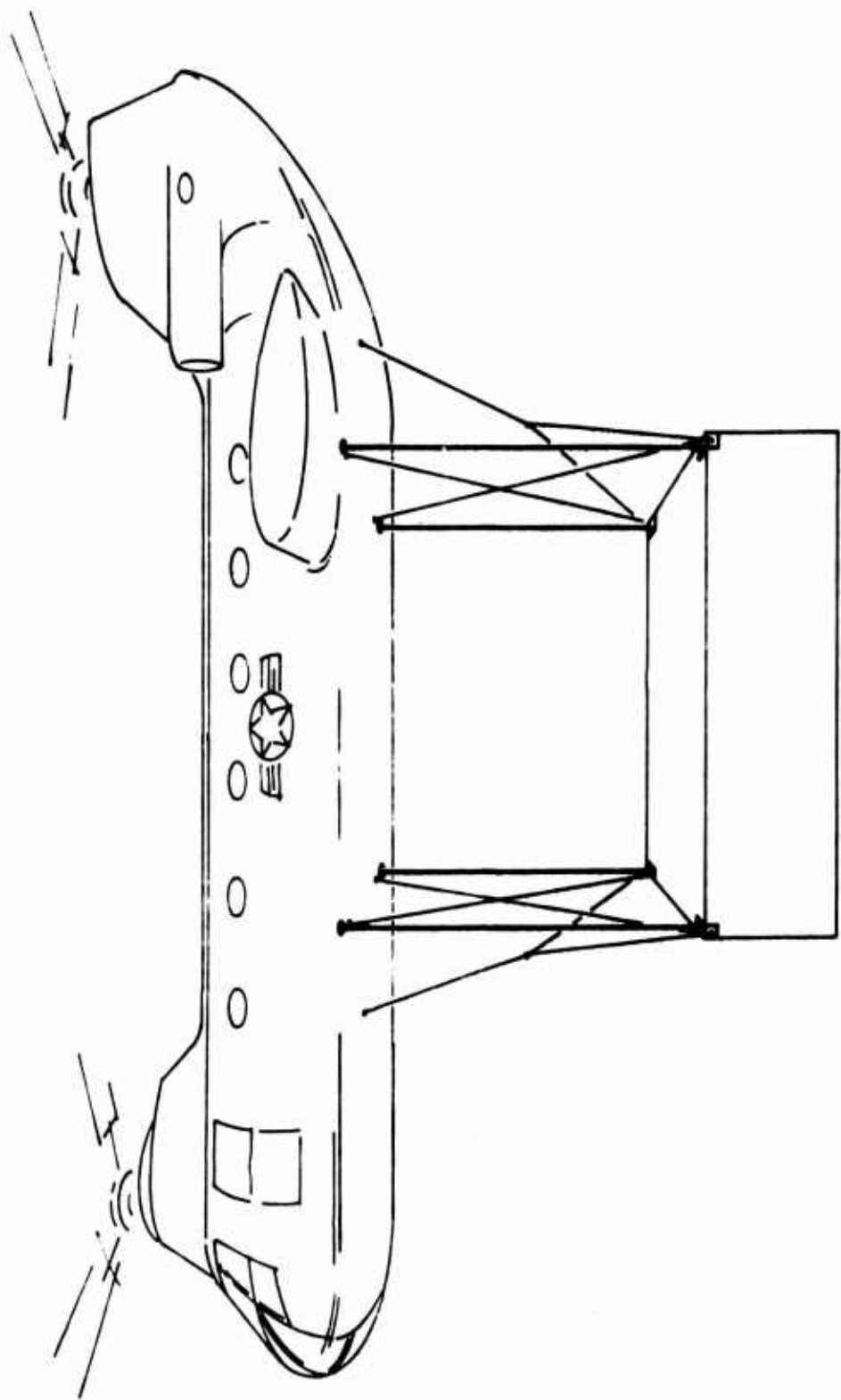


Figure 52. Cable System With Longitudinal Stabilizing Cables.

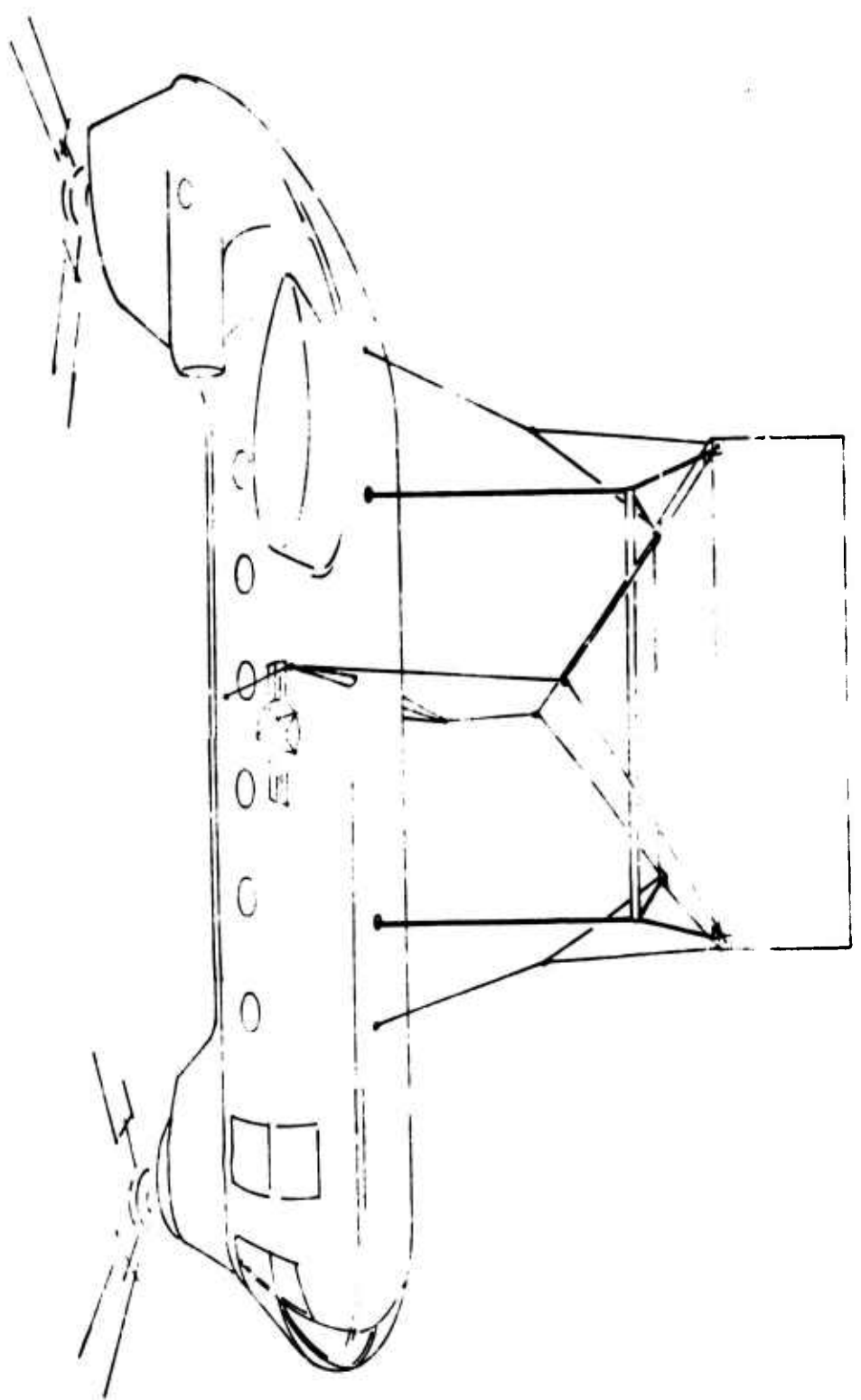


Figure 53. Auxiliary Cable System for Longitudinal and Lateral Stability, With Lateral Bow on Fuselage.

Block diagrams shown in Figures 54 and 55 represent the helicopter sling-load stabilization augmentation system concept in longitudinal and lateral sets. Preliminary investigation indicates that such a system approach is very promising. Further study is necessary to determine its effectiveness and practicality. The feedback system involves practically all the dynamic motion parameters of the helicopter and load. The complexity in implementing such a system approach needs to be carefully analyzed. The effectiveness of the presented conceptual systems has been substantiated by flight simulation.

9.2 SYSTEM TRADE-OFF ANALYSIS

Operational data concerning the frequency of lifting for various types of helicopter sling loads by the CH-54 helicopter in the Republic of Vietnam is presented in Table XXIII. This data obtained from the U.S.Army was used as a base for establishing the mission frequency of all the helicopter sling loads selected to be studied in this program. The given operational data does not include the mission frequency for lifting various types of helicopters and aircraft. The task of transporting helicopters and aircraft, damaged or undamaged, is frequently being carried out by various types of helicopters. The frequency of lifting the two types of rotary wing aircraft and two types of fixed-wing aircraft selected to be studied in this program is assumed to be 12 percent of the total operation. The frequency of lifting the command post carrier, also one of the sling-load configurations selected to be analyzed, is assumed to be 2 percent of the total operation. It is further assumed that the lifting frequency of 3 percent of the total operation is equal among the helicopters and aircraft (CH-47, VH-34, F-5 and OV-1) selected to be studied.

TABLE XXIII. LIFTING FREQUENCY OF SLING-LOAD
CATEGORY LIFTED BY CH-54 IN VIETNAM

Sling-Load Category	Lifting Frequency
Logistics (e.g., 8-by-8-by-20-foot container)	51.5%
Artillery (e.g., 155mm howitzer; Vulcan)	23.6%
Engineer (e.g., AVLB bridge; bulldozer)	18.6%
Transportation (e.g., trucks)	5.9%
Armor (e.g., M-551 Sheridan light tank)	0.4%
Infantry	0.0%

The mission frequencies established for all the selected sling-load configurations are summarized in Table XXIV.

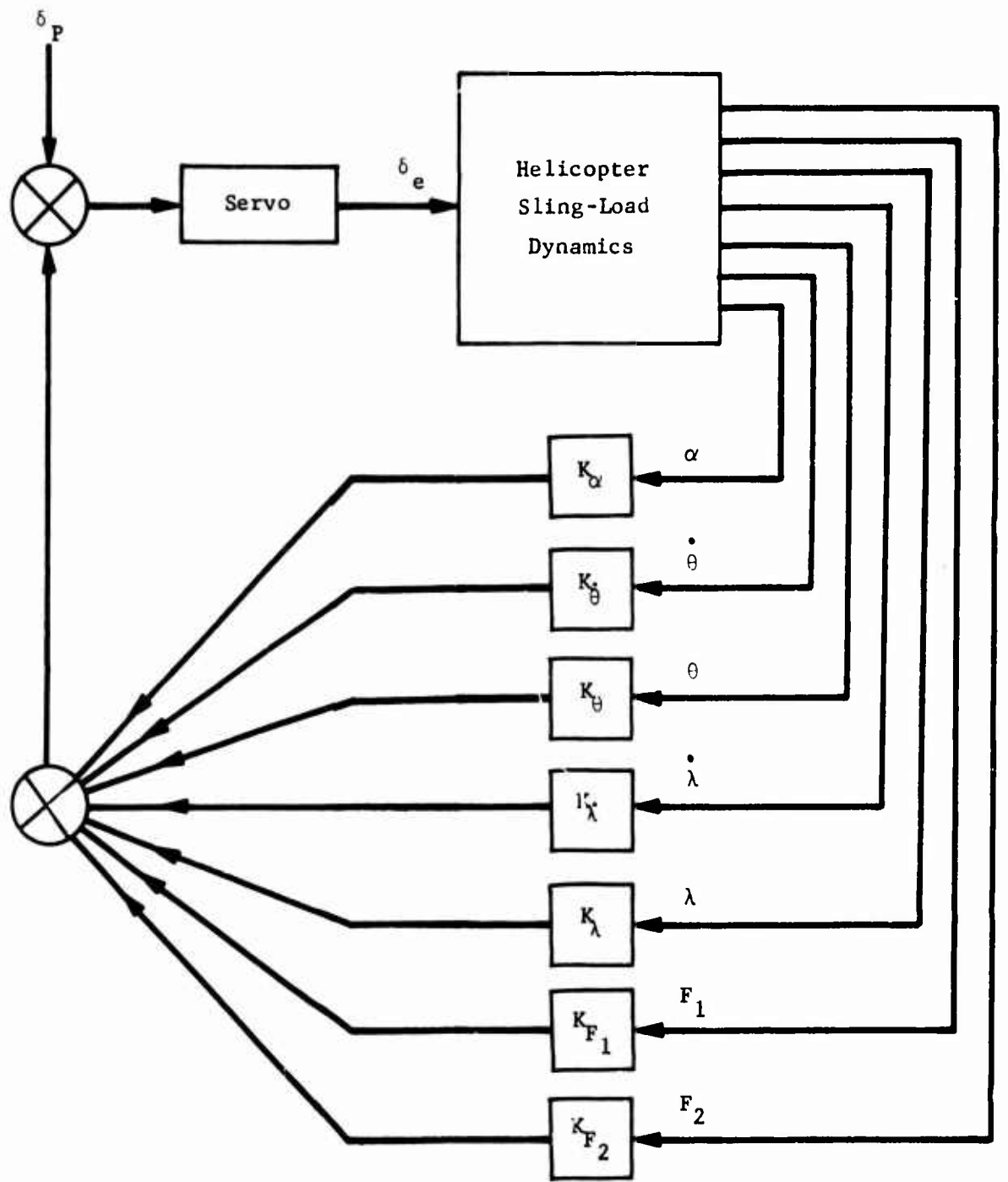


Figure 54. Longitudinal Helicopter/Sling-Load Stabilization System Block Diagram.

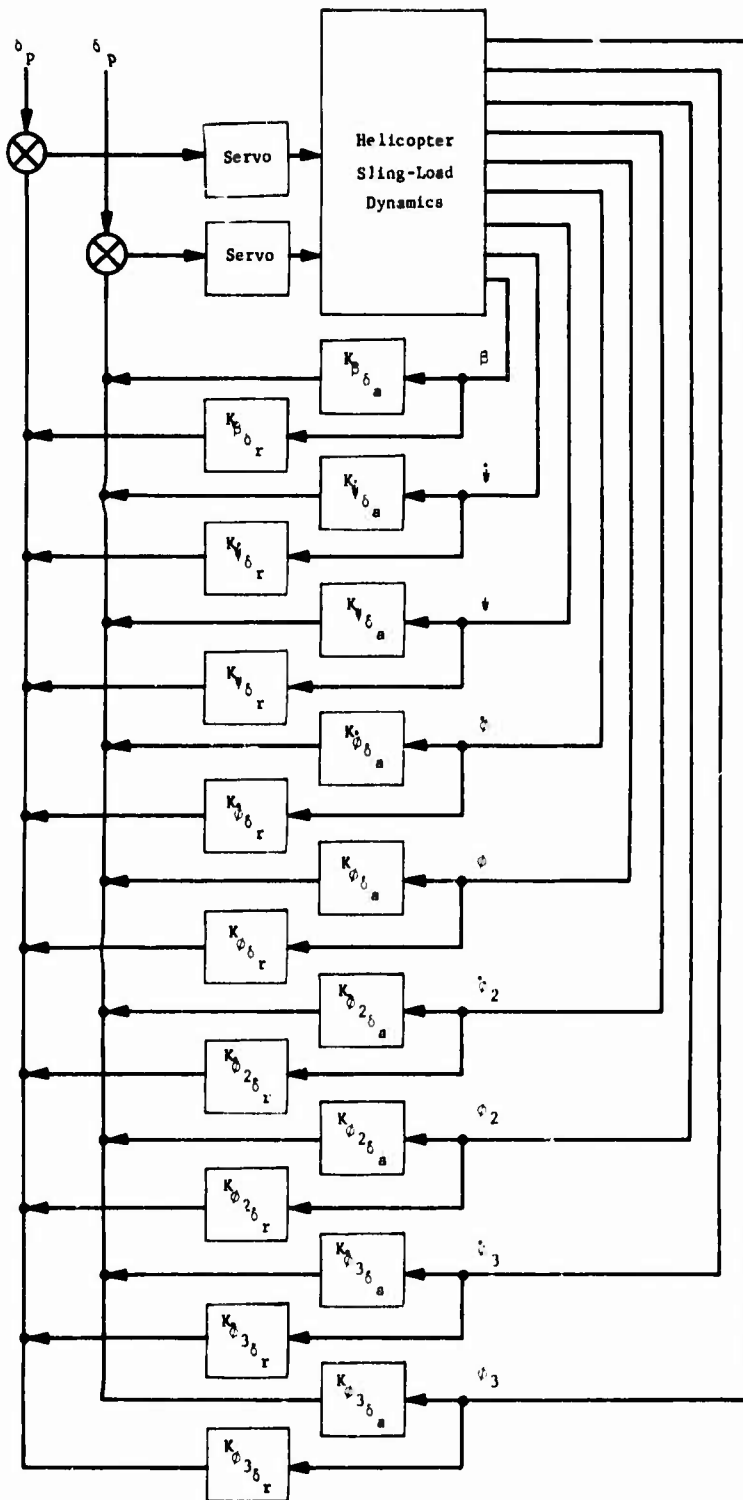


Figure 55. Lateral Helicopter/Sling-Load Stabilization System Block Diagram.

Nomenclature for Figure 55

α	Angle-of-attack of helicopter
$\dot{\theta}$	Helicopter pitch rate
θ	Helicopter pitch angle
$\dot{\lambda}$	Load pitch rate
λ	Load pitch angle
F_1	Front cable perturbed load
F_2	Rear cable perturbed load
β	Sideslip angle of helicopter
$\dot{\psi}$	Helicopter yaw rate
ψ	Helicopter yaw angle
$\dot{\phi}$	Helicopter roll rate
ϕ	Helicopter roll angle
$\dot{\phi}_2$	Front cable roll displacement angular rate
ϕ_2	Front cable roll displacement angle
$\dot{\phi}_3$	Rear cable roll displacement rate
ϕ_3	Rear cable roll displacement angle
K	Feedback gain
δ_p	Pilot control inputs
δ_a	Lateral roll control
δ_r	Yaw control

TABLE XXIV. ASSIGNED MISSION FREQUENCY FOR SLING-LOAD TYPES STUDIED

Sling-Load Types	Typical Model	Mission Frequency
Container	8 x 8 x 20	40%
Artillery	Howitzer	19%
Engineering	AVLB Bridge	17%
Cargo Truck	M-35	6%
Sheridan Tank	M-551	4%
Command Post Carrier	M-113	2%
Tandem-Rotor Helicopter	CH-47	3%
Single-Rotor Helicopter	VH-34	3%
Jet Fighter Aircraft	F-5	3%
Conventional Airplane	OV-1	3%

Referring to Section 8, the S_1 active aerodynamic load stabilization concept described first is chosen as a candidate system; the other system concepts described are combined to form S_3 , the so-called electronic load stabilization system, with block diagrams presented in Figures 54 and 55. The structural approaches with loading fixtures described in Subsection 9.1 are designated S_2 .

If the tandem cable system could not provide load stabilization at high speed for all types of container configurations, then the structural approach would no doubt prove cost-effective when compared with the other two selected approaches.

The disadvantages of the S_1 system are its uncertain applicability to large load configurations and its inflexibility.

Although the S_3 system may cost two to three times as much as the S_2 , its flexibility makes it the most promising type of load stabilization system.

10.0 METHODOLOGY FOR HELICOPTER SLING-LOAD STABILIZATION SYSTEM TRADE-OFF ANALYSIS

Several alternative design approaches for achieving in-flight load stabilization have been proposed. Methodology for conducting system trade-off studies was developed for evaluating the relative effectiveness of the proposed systems. Various methods for conducting trade-off studies and cost-effectiveness analyses were investigated. Due to the complexity of the total system and many unknown system parameters relating the load stabilization system to helicopter operation, the commonly applied methodology for conducting the trade-off analysis by parameter rating and scoring did not yield practical and meaningful indication of the real value of the proposed systems.

The methodology for conducting the trade-off studies between various design approaches for this study program is outlined in the following. Stabilization system effectiveness, operational effectiveness, and total system cost-effectiveness were taken into consideration.

Total system stability for flight speeds up to 150 knots is the single most important measure of system effectiveness in performance. Maximum stable flight speeds were determined for each system design approach in carrying various types of loads. Table XXV illustrates the approach.

A1, A2, A3, B1, and B2 are various helicopter sling loads that differ in mass, inertia, aerodynamic or dynamic characteristics in Type A or B load category. Maximum stable flight speeds, V^{\max} , were determined for Systems I through V in carrying various loads. Mission frequency in numbers of missions per year, for example, and average range per mission were established. From the maximum stable flight speed chart, mission data and helicopter operational data, the cost data in Table XXVI was obtained.

The cost of each stabilization system design approach was also established. Complexity and maintainability are reflected in the total system costs. The gain in investment (the cost savings for a total mission derived from the increase in mission speeds through the use of a load stabilization system) was then determined. The real value of various proposed stabilization systems thus could be assessed in conjunction with the cost-effectiveness of the total system.

TABLE XXV. STABILIZATION SYSTEM TRADE-OFF APPROACH

Sling Load	System					Mission Frequency	Mission Range
	I	II	III	IV	V		
	Maximum Stable Speed						
A							
A1	V_{IA1}	V_{IIA1}	V_{IIIA1}	V_{IVA2}	V_{VA1}	M_{A1}	R_{A1}
A2	V_{IA2}	V_{IIA2}	V_{IIIA2}	V_{IVA2}	V_{VA2}	M_{A2}	R_{A2}
A3	V_{IA3}	V_{IIA3}	V_{IIIA3}	V_{IVA3}	V_{VA3}	M_{A3}	R_{A3}
A4	V_{IA4}	V_{IIA4}	V_{IIIA4}	V_{IVA4}	V_{VA4}	M_{A4}	R_{A4}
B							
B1	V_{IB1}	V_{IIB1}	etc.	etc.	etc.	M_{B1}	R_{B1}
B2	V_{IB2}	etc.	etc.	etc.	etc.	etc.	etc.
C							
C1							
C2							
D							
D1							
D2							
E							
F							
G							

TABLE XXVI. COST TRADE-OFF APPROACH

Sling Load	System Mission Cost				
	System I	II	III	IV	V
A					
A1	\$ _{IA1}	\$ _{IIA1}	\$ _{IIIA1}	\$ _{IVA1}	\$ _{VA1}
A2	\$ _{IA2}	\$ _{IIA2}	\$ _{IIIA2}	\$ _{IVA2}	\$ _{VA2}
A3	\$ _{IA3}	\$ _{IIA3}	\$ _{IIIA3}	\$ _{IVA3}	\$ _{VA3}
A4	\$ _{IA4}	\$ _{IIA4}	\$ _{IIIA4}	\$ _{IVA4}	\$ _{VA4}
B					
B1	\$ _{IB1}	etc.	etc.	etc.	etc.
B2	etc.	etc.	etc.	etc.	etc.
C					
C1					
C2					
D					
E					
F					
G					
	\$ _{Sys I}	\$ _{Sys II}	\$ _{Sys III}	\$ _{Sys IV}	\$ _{Sys V}

11.0 SIMULATOR DEMONSTRATIONS

This section describes the simulators used to validate the significant analytical studies performed, and summarizes the objectives and results of the demonstrations.

11.1 FLIGHT SIMULATION EQUIPMENT

The simulators used in the demonstrations are located in the Northrop Aerosciences Laboratory in Hawthorne, California. Equipment includes the large-amplitude flight simulator, the rotational three-axis flight simulator, associated computing facilities, and data acquisition and processing systems.

11.1.1 Large-Amplitude Flight Simulator

The cockpit, spherical screen, and projection systems are carried as a unit on the end of a 30-foot moving beam as shown in Figure 56. The beam is attached to a single two-axis base gimbal which is supported by a fixed pedestal. Two electrohydraulic servos control the vertical and lateral translation of the beam-mounted unit containing the cockpit, screen, and projector. The cockpit is gimbaled to provide pitch, roll, and yaw rotations which are controlled by electrohydraulic servos. Hydraulic power is provided by a central source, 3000 psi hydraulic supply, and distribution system.

Table XXVII summarizes the motion system displacement, velocity, and acceleration performance characteristics.

The motion system produces cockpit motions in precise phase and amplitude corresponding to the electrical motion system signals provided by the computer. The purpose is to provide the pilot with highly realistic perceptual cues related to actual motions of the simulated aircraft.

TABLE XXVII. MOTION SYSTEM CHARACTERISTICS

Motion	Displacement	Peak No-Load Velocity	Stall Acceleration
Vertical	± 10 ft*	± 11.9 ft/sec	± 2.5g
Lateral	± 10 ft*	± 9.0 ft/sec	± 1.7g
Pitch	± 25°	± 1.0 rad/sec	± 2.1 rad/sec ²
Yaw	± 20°	± 1.3 rad/sec	± 8.4 rad/sec ²
Roll	± 20°	± 1.0 rad/sec	± 6.5 rad/sec ²

*Measured at the pilot's eye

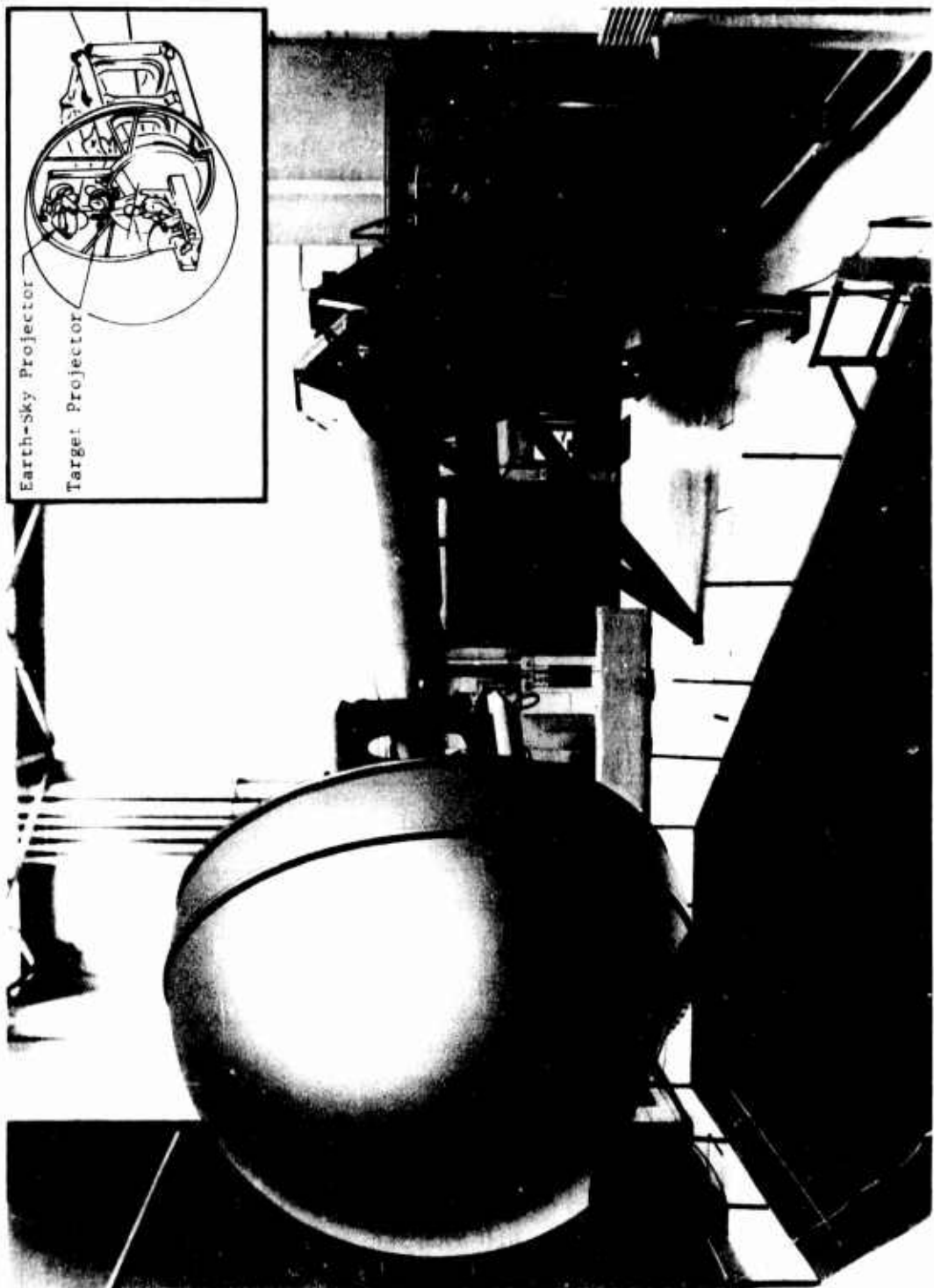


Figure 56. Large-Amplitude Flight Simulator.

An onboard visual display projection system utilizes a wide-angle, 8-foot-radius spherical projection screen. The major components of the projection system are the earth-sky projector and the target projector.

The earth-sky projector provides the pilot with a realistic visual representation of his outside environment, including a brown earth and a featureless blue sky. The earth-sky projector is mounted in a single multiple-axis gimbal system that allows the visual scene to be rotated by servo drives controlled by computer signals, thus duplicating the motion produced by the vehicle being simulated. The earth-sky projector is shown in Figure 56.

Target information, either air-to-air, or air-to-ground, is displayed on a CRT located above the pilot's head. This information is projected on the spherical projection screen and positioned in elevation and azimuth by two front surfaced mirrors which are rotated relative to each other and to the optical axis of the incoming light beam. The elevation and azimuth pointing mirrors control the position of a 15-degree field-of-view projection cone. Although the primary purpose of the projector is for air-to-air simulation, it has many air-to-ground applications. The target projector is also shown in Figure 56.

Table XXVIII summarizes the visual display projection system displacement, velocity, and acceleration characteristics.

TABLE XXVIII. PROJECTION SYSTEM CHARACTERISTICS

Earth-Sky Projector			
Motion	Displacement	Peak No-Load	Stall
		Velocity	Acceleration
Roll	Continuous	9.7 rad/sec	36.0 rad/sec ²
Pitch	Continuous	2.1 rad/sec	23.0 rad/sec ²
Yaw	Continuous	10.0 rad/sec	50.0 rad/sec ²
Target Projector			
F.O.V. 15 x 15 degrees		AR = As Required	
Motion	Displacement	Peak No-Load	Stall
		Velocity	Acceleration
Elevation	Continuous	6.0 rad/sec	38.8 rad/sec ²
Azimuth	Continuous	6.6 rad/sec	20.9 rad/sec ²
Focus	AR	AR	AR

11.1.2 Rotational Three-Axis Flight Simulator

This device was developed to simulate flight tasks requiring strong visual cues of real work information for the pilot -- such as V/STOL takeoff and landing, air-to-ground weapons delivery, and general low-altitude operations. The external world display is adapted from the proven de Florez point light source technique (separate display from the one described for the large simulator). This simulator also provides a complementary capability to the large-amplitude flight simulator.

The simulator hardware consists of a cockpit, with rotational motion (± 15 -degree pitch, ± 15 -degree yaw, ± 15 -degree roll) and heave (± 9 inches), which is located within a 12-foot-radius hemispherical screen as shown in Figure 57. The screen is fabricated in rigid fiberglass segments; the segments are assembled for precise curvature and the joints are sealed. A high quality, undistorted image presentation is the result. A point light source projection system produces a continuous-moving, 6-degree-of-freedom, wide-angle visual display to the pilot. The display is presented with appropriate perspective, size, and position relative to the observer, thus simulating the visual world as viewed from any desired position in space. The wide coverage of the visual display, both laterally and vertically, presents a continuous world to either side as well as above and below the pilot. Angular visual displacements are ± 20 degrees in pitch and roll and continuous in yaw; translations depend upon transparency scale. Visual and motion servo performance is designed to meet the flight envelope of all V/STOL and conventional aircraft.

The point source projection system uses a very small, intense light source to project a display object (such as a transparency terrain feature) onto a screen. The image is projected in color with terrain texture and three-dimensional objects shown. Alternate rigid transparencies may be used for scale and display variation. Flexible roll transparencies provide extended flight path capabilities. Appropriate supporting structure drives and control are used to move the light source and display-object relative to one another. The supporting structure and the drives and controls present general engineering problems and are not unique to the point source system.

11.2 DEMONSTRATION OBJECTIVES

The objectives of the flight simulator demonstration were:

1. To simulate the helicopter/sling-load flight dynamics with a man in the loop.
2. To demonstrate the physics of helicopter/sling-load flight dynamic problems.
3. To validate the results of the analytical studies.

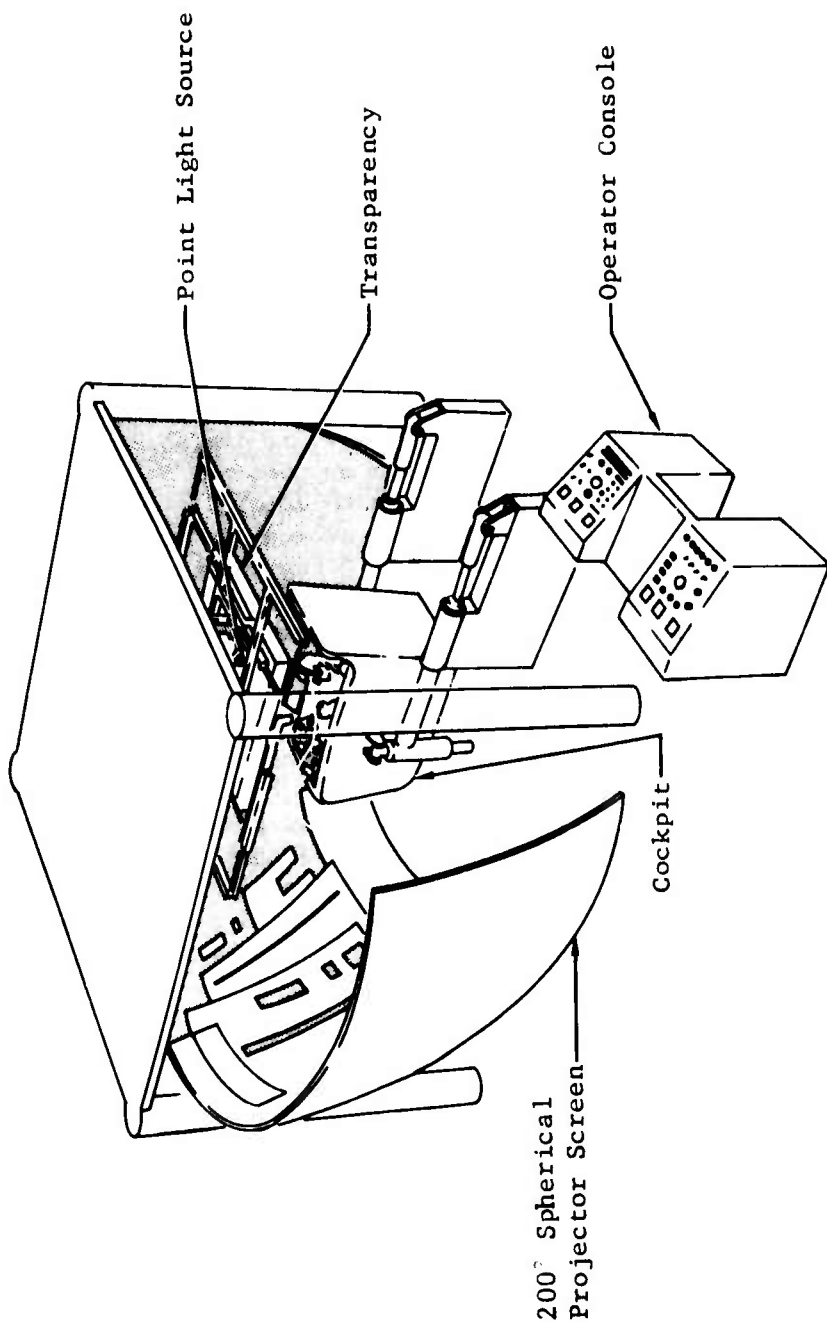


Figure 57. Rotational Three-Axis Flight Simulator.

The demonstration made use of a generalized helicopter model based on CH-47B flight characteristics, with typical SAS.

The sling-load model was a typical 8-by-8-by-20-foot container -- tandem cable configuration.

11.3 CRITICAL DYNAMIC MODE

The lateral-directional modes were chosen for flight simulator demonstration due to the following considerations:

1. The longitudinal modes were decoupled for ease of flight handling on the simulator. This made it possible to demonstrate and prove the critical dynamics problem. Non-helicopter pilot or non-flyer would have difficulty flying the simulator with all the modes and load dynamics coupled.
2. Lateral-directional modes are the most critical flight dynamic modes, especially for high-speed flight.
3. Such simulation could directly validate the analytical results obtained from dynamic modeling of the critical lateral-directional modes.

11.4 FLIGHT DEMONSTRATION CASES

The following cases were simulated:

1. Basic helicopter with SAS, no sling load; $V = 50$ knots.
2. Basic helicopter with SAS, no sling load; $V = 150$ knots.
3. Basic helicopter with SAS, sling load attached, without load aerodynamics; $V = 150$ knots.
4. Basic helicopter with SAS, typical sling load with all the aerodynamic characteristics included and $C_n^{\beta} = 0.5/\text{radian}$; $V = 50$ knots.
5. Basic helicopter with SAS, typical sling load with all the aerodynamic characteristics included and $C_n^{\beta} = 0.5$ radian; $V = 150$ knots.
6. Basic helicopter with SAS, typical sling load with all the aerodynamics included and $C_n^{\beta} = 2.5/\text{radian}$; $V = 50$ knots. (NOTE: This is not the inherent C_n^{β} of the load; it is used here to study and demonstrate its effect.)

7. Basic helicopter with SAS, typical sling load with all the aerodynamics included and $C_n = 2.5/\text{radian}$; $V = 150$ knots.
 θ

11.5 REMARKS

1. Cases 1 and 2:
 - a. No indications of any problem.
 - b. Very smooth in flying.
 - c. Disturbances could be easily controlled.
 - d. All participants could handle the flight with ease.
2. Case 3:
 - a. Analytical results show there should be no problem.
 - b. It was demonstrated that this is so.
 - c. Some of the "pilots" could fly for short duration.
 - d. With some practice, it could definitely be handled.
3. Case 4:
 - a. Same as 2.a.
 - b. Same as 2.b.
 - c. Duration of stable flight shortened compared to 2.c.
 - d. Disturbance or "pilot" error could cause difficulty in control.
 - e. This is all due to lack of experience.
4. Case 5:
 - a. Analytical results show that the system is stable but the stability is somewhat marginal.
 - b. One "pilot" could fly for a short duration but there is no room for error.
 - c. Some "pilots" who did relatively well in previous easier cases could not handle this case.

5. Case 6:

- a. Same as 4.a.
- b. One "pilot" had to struggle hard to stabilize the helicopter.
- c. Difficulty in controlling is due to marginal stability and lack of piloting experience.

6. Case 7:

- a. Analytical results show that the system is unstable.
- b. Simulator's results substantiated this.

The flight simulations conducted in the Northrop flight simulator have demonstrated the physics of the problem.

11.6 TYPICAL TIME RESPONSES OF FLIGHT SIMULATIONS

Typical time responses obtained from the large-scale simulator are shown in Figures 58 through 61. These correspond to Cases 5 and 7 as described in the preceding text. There are two sets of tracings on each set, with the recording of eight variables for each set. The recordings are described as follows:

Set A

<u>Channel</u>	<u>Variable</u>	<u>Scale (per line)</u>
1	δ_{LAT} , lateral control deflection	0.1 in.
2	δ_{RUD} , rudder control deflection	0.1 in.
3	$\ddot{\phi}$, helicopter roll acceleration	1 deg/sec ²
4	$\dot{\phi}$, helicopter roll rate	0.5 deg/sec
5	ϕ , helicopter roll angle	0.5 deg
6	$\ddot{\psi}$, helicopter yaw acceleration	1 deg/sec ²
7	$\dot{\psi}$, helicopter yaw rate	1 deg/sec
8	ψ , helicopter yaw angle	1 deg

Set B

<u>Channel</u>	<u>Variable</u>	<u>Scale (per line)</u>
1	δ_{LAT} , lateral control deflection	0.1 in.
2	δ_{RUD} , rudder control deflection	0.1 in.
3	$\ddot{\phi}_2$, load front cable roll acceleration	5 deg/sec ²
4	$\dot{\phi}_2$, load front cable roll angle	5 deg
5	$\ddot{\phi}_3$, load rear cable roll acceleration	5 deg/sec ²
6	$\dot{\phi}_3$, load rear cable roll angle	5 deg
7	$\ddot{\phi}_4$, load roll acceleration	5 deg/sec ²
8	$\dot{\phi}_4$, load roll angle	5 deg

Case 5 (Figures 58 and 59) is marginally stable, as predicted analytically. Oscillations exist which the pilot cannot remove. However, he can prevent their building up beyond acceptable limits. It can be expected that, with greater experience, good pilots would eventually succeed in stabilizing (damping) the oscillations for Case 5.

Case 7 (Figures 60 and 61) is definitely unstable, as predicted analytically. Here the oscillations build up and the pilot is unable to stop their growth. Eventually the oscillations reach unacceptable limits. It is doubtful that the pilot could gain enough experience ever to stabilize under these conditions, short of reducing airspeed.

11.7 FLIGHT SIMULATOR VALIDATION

Programming for the flight simulation was further refined. On July 13th and 14th, 1971, the chief project test pilot on the Boeing/Vertol HLH program test flew the Northrop rotational flight simulator, simulating a typical tandem-rotor helicopter with sling load. His major comments are summarized as follows:

1. Pitch, roll, and yaw flight dynamics of the flight simulator are representative of those of the CH-47B at both 50 knots and 150 knots flight speeds.
2. Some pitch oscillations occurred following input pulses apparently caused by load at 50 knots flight speed with a 10-foot sling. The longitudinal pendulum frequency is about right and the pitch attitude oscillation is fairly representative.

3. At 150 knots flight speed, the pilot tends to come into phase with the pitch attitude oscillation, just as he would to the longitudinal linear acceleration.
4. One condition with very stable weathercock stability of the load at 150 knots flight speed resulted in immediate instability.
5. Lag in pitch response to longitudinal control results in a long period of divergent longitudinal control oscillation. This situation was corrected on the July 14 flight simulator testing.
6. It is recommended that the longitudinal motion be incorporated in the flight simulation.
7. It is desirable to incorporate the airspeed sweep capability to evaluate the effect of increasing airspeed on the load behavior.

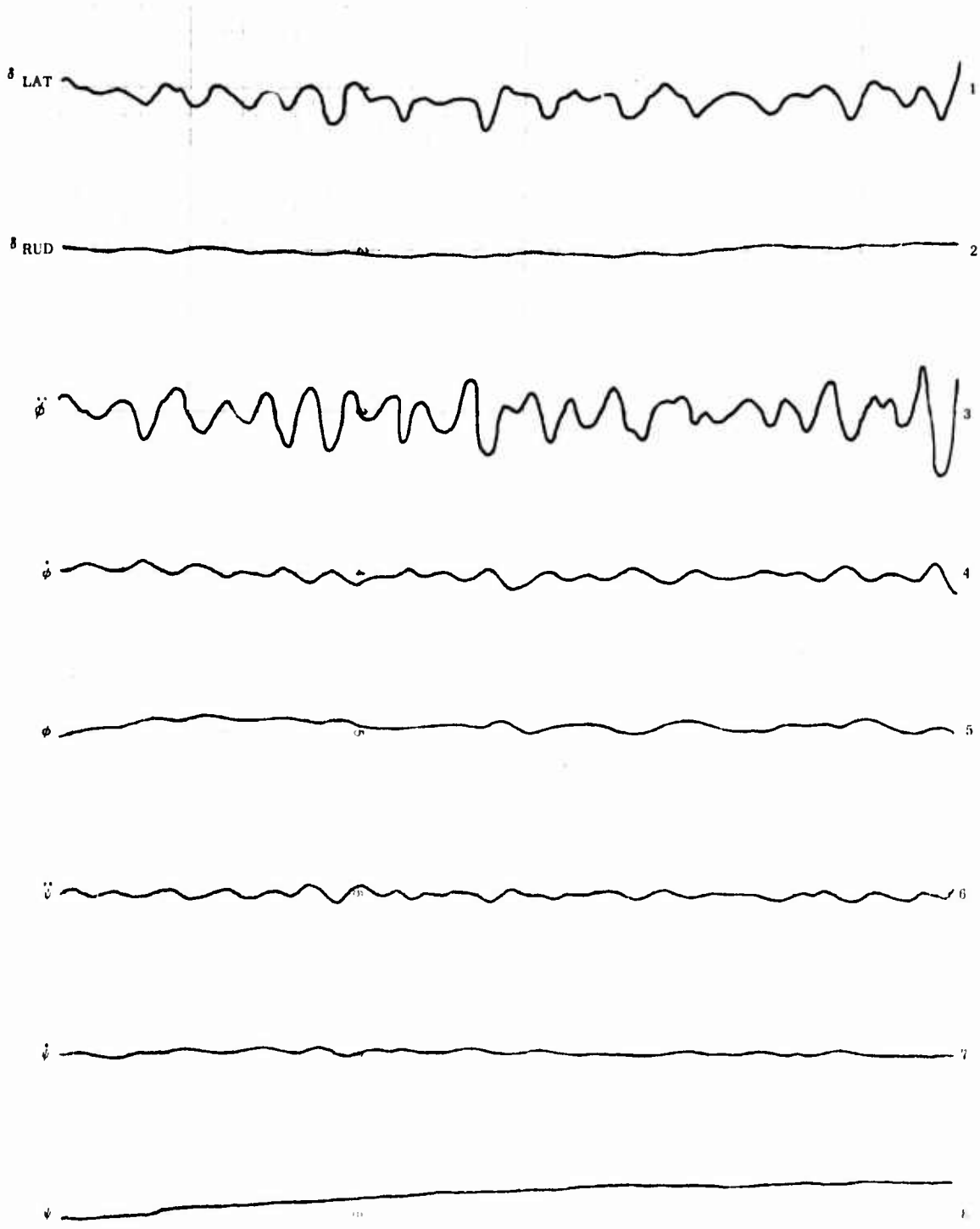


Figure 58. Simulator Time Response -- Case 5(A).

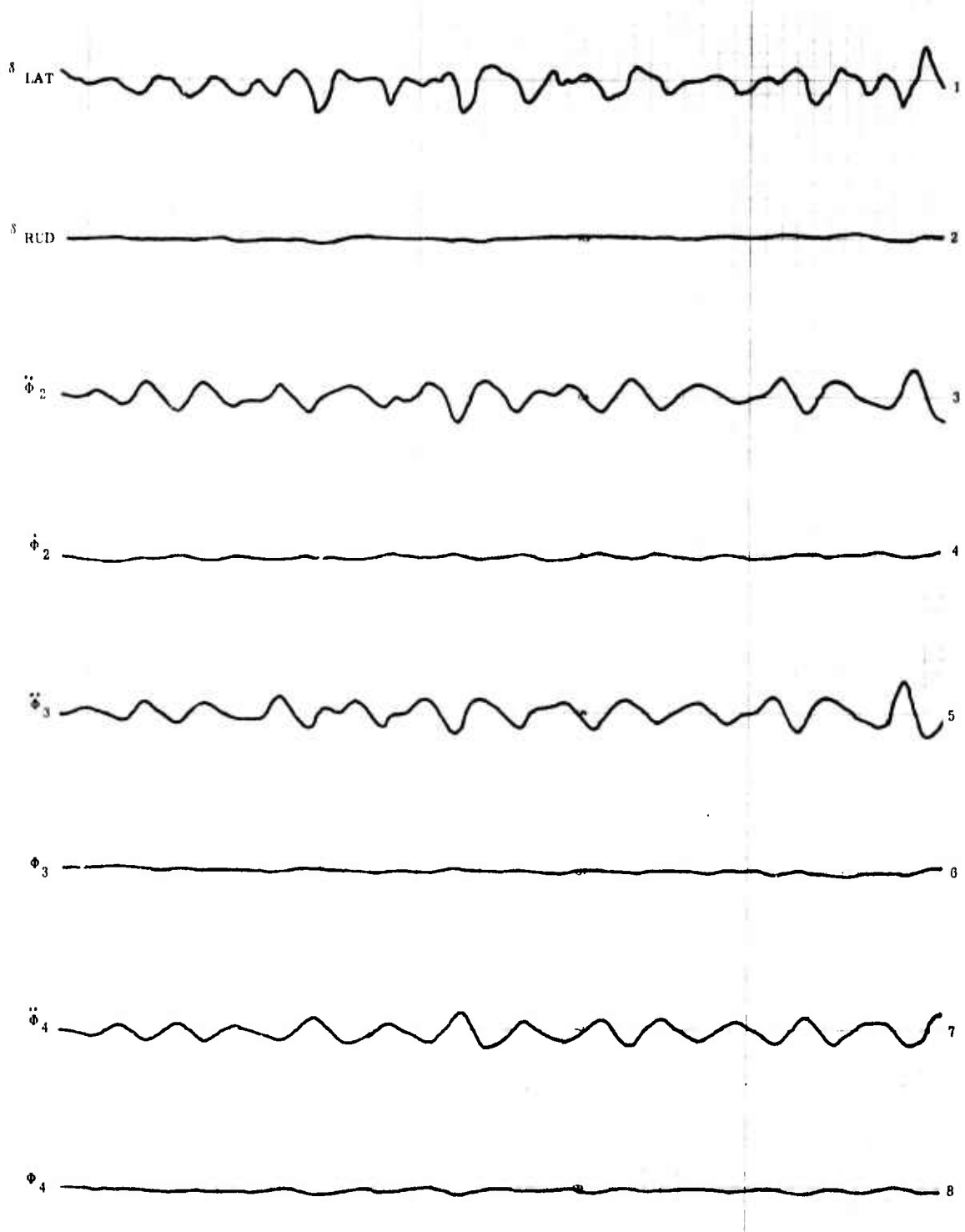


Figure 59. Simulator Time Response -- Case 5(B).

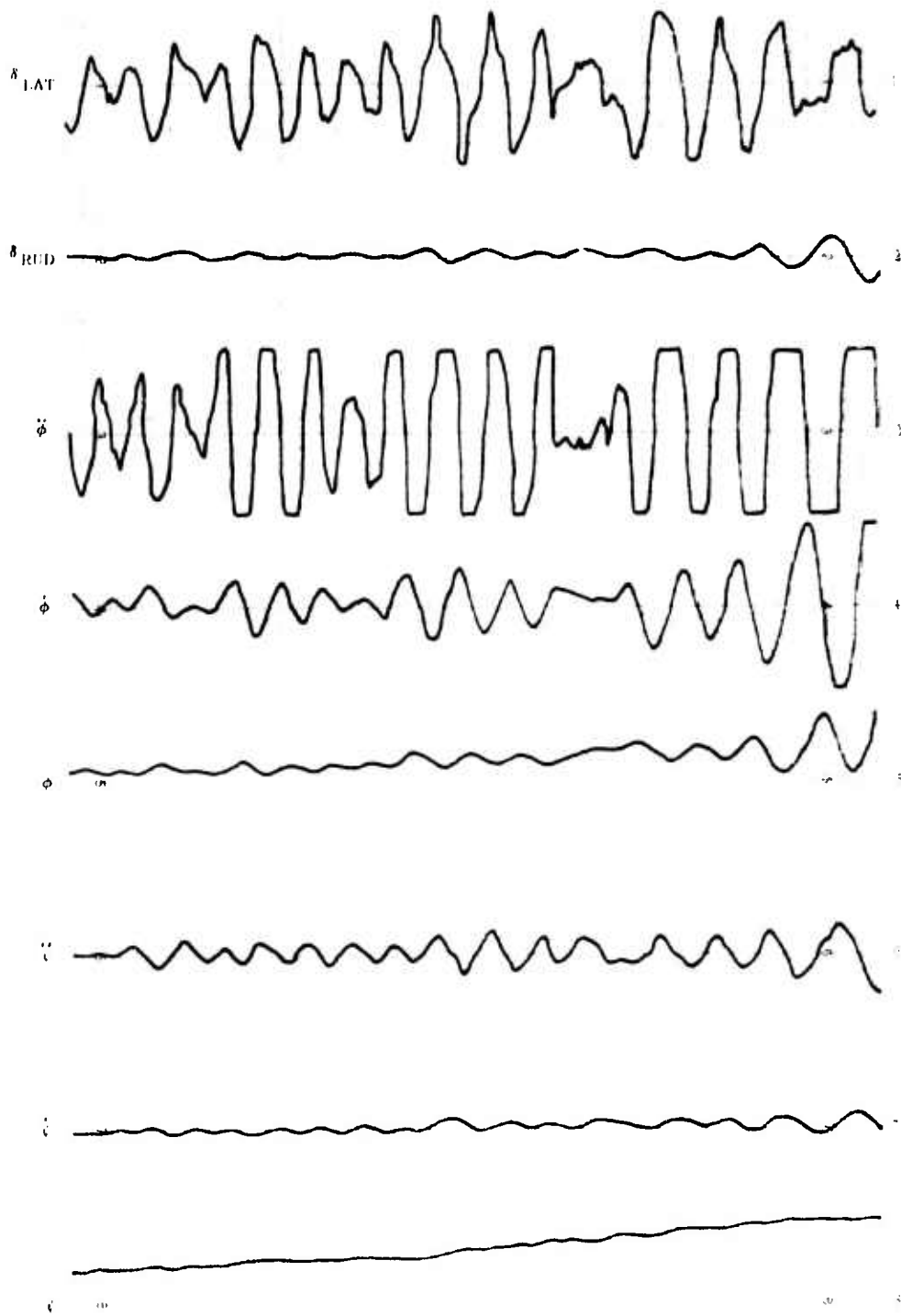


Figure 60. Simulator Time Response -- Case 7(A).

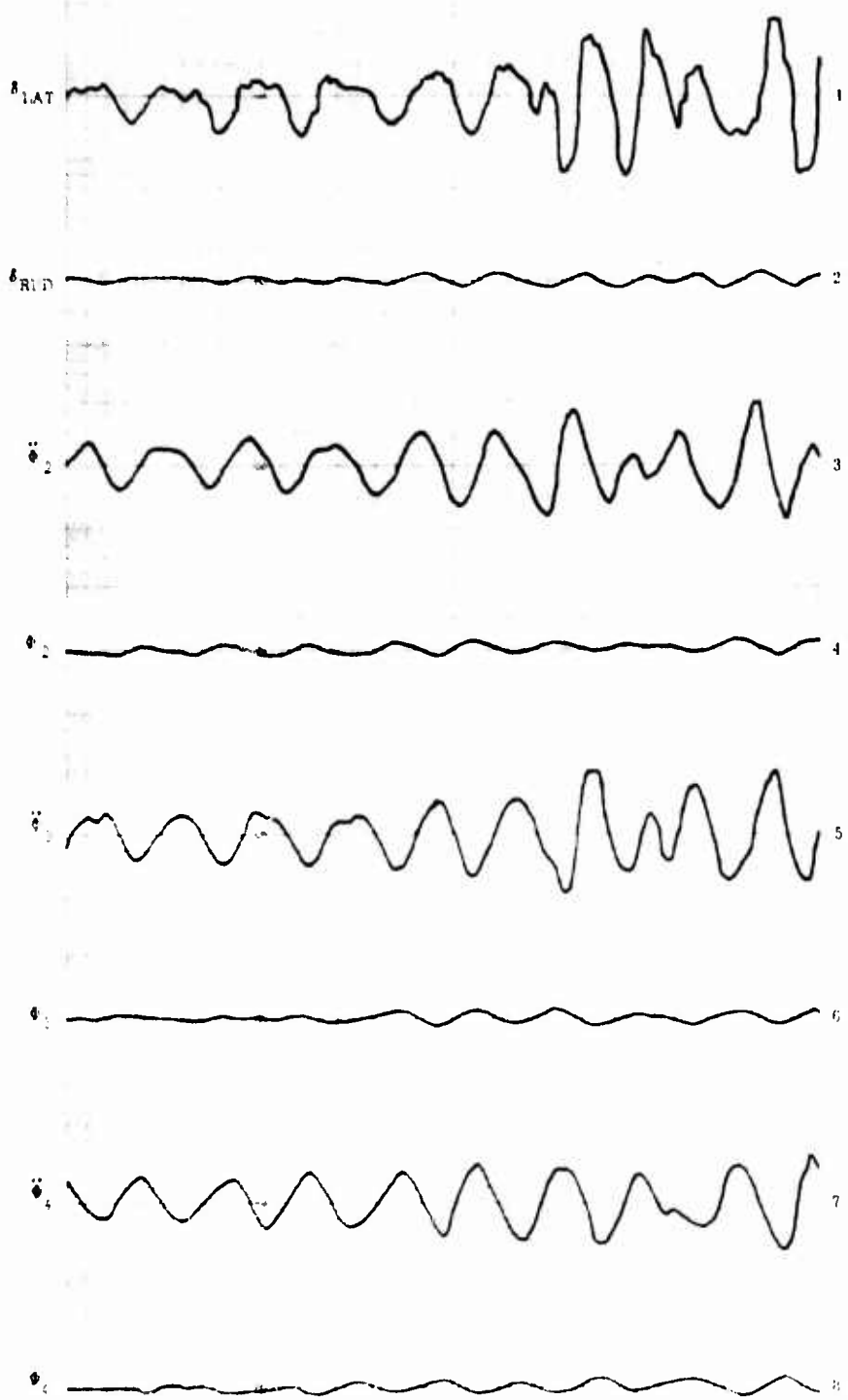


Figure 61. Simulator Time Response -- Case 7(B).

12.0 LOAD STABILIZATION SYSTEM PRELIMINARY DESIGN AND ANALYSIS

This section discusses the verification of the preliminary design of the candidate stabilization system through the use of the moving-base simulator.

12.1 DESIGN ANALYSIS OF HELICOPTER SLING-LOAD STABILIZATION SYSTEM

The conceptual black box stabilization system presented in Subsection 9.1 has been synthesized by utilizing a version of the FORTRAN Automatic Synthesis Optimal Control Program (Reference 9). The equations were transformed into state variable equations so that they could be used in the optimization program. All the stabilization system gains are determined and optimized for flight conditions at speeds of 50, 100, and 150 knots (84, 168, and 253 feet/second). Due to the extensive amount of work required to synthesize and optimize the system, it is not practical to analyze and design the load stabilization system to cover all the selected load configurations. Reasonable bounds of weathercock stability characteristics of the load are chosen to study the variations of the stabilization system gains. Three cable lengths, 10 feet, 30 feet, and 50 feet, are considered in the analysis of the system gains.

As shown in Table XXIX, the stabilization system gains for the proposed load stabilization system vary significantly with speed, weathercock stability characteristics of the load configuration, and sling cable length. As an aid in interpreting the computer printout comprising Table XXIX, the mnemonics used are described below.

<u>Mnemonic</u>	<u>Description</u>
VDA	Gain from side velocity to lateral roll control
PHIDA	Gain from helicopter roll angle to lateral roll control
PHIDDA	Gain from helicopter roll rate to lateral roll control
PSIDA	Gain from helicopter yaw angle to lateral roll control
PSIDDA	Gain from helicopter yaw rate to lateral roll control
P2DA	Gain from front cable roll displacement angle to lateral roll control
P2DDA	Gain from front cable roll angular rate to lateral roll control
P3DA	Gain from rear cable roll displacement angle to lateral roll control
P3DDA	Gain from rear cable roll angular rate to lateral roll control

<u>Mnemonic</u>	<u>Description</u>
VDR	Gain from side velocity to yaw control
PHIDR	Gain from helicopter roll angle to yaw control
PHIDDR	Gain from helicopter roll rate to yaw control
PSIDR	Gain from helicopter yaw angle to yaw control
PSIDDR	Gain from helicopter yaw angle rate to yaw control
P2DR	Gain from front cable roll displacement angle to yaw control
P2DDR	Gain from front cable roll angular rate to yaw control
P3DR	Gain from rear cable roll displacement angle to yaw control
P3DDR	Gain from rear cable roll angular rate to yaw control
NBETA LOAD	Factor times "Normal" N_B load
CABLE LEN	Cable length
V	Velocity in feet/second
Q	Q in the performance index

It is not implied that this is the only set of gains that will stabilize the load or that the one set of gains will stabilize only the indicated flight condition. This set of 36 combinations of loads and speeds was computed using the same performance index. Another set of optional gains was computed using a different performance index with very little change in the gains.

TABLE XXIX. STABILIZATION SYSTEM GAIN VARIATION VS SPEED,
LOAD STABILITY CHARACTERISTICS, AND CABLE LENGTH

VDA	V= 84	Q=	0.1000		
NPETA LOAD =		5	1	-1	-5
CABLE LEN = 10		-0.0049	-0.0066	-0.0065	-0.0050
CABLE LEN = 30		0.0005	-0.0065	-0.0080	-0.0088
CABLE LEN = 50		0.0063	-0.0062	-0.0094	-0.0130
VDA	V= 168	Q=	0.1000		
NBETA LOAD =		5	1	-1	-5
CABLE LEN = 10		0.0374	-0.0022	-0.0071	-0.0022
CABLE LEN = 30		0.0023	-0.0044	-0.0147	-0.0133
CABLE LEN = 50		-0.0062	-0.0137	-0.0227	-0.0291
VDA	V= 253	Q=	0.1000		
NBETA LOAD =		5	1	-1	-5
CABLE LEN = 10		-0.0046	-0.0080	-0.0151	0.0004
CABLE LEN = 30		-0.0206	-0.0212	-0.0301	-0.0052
CABLE LEN = 50		-0.0288	-0.0307	-0.0407	-0.0162
PHIDA	V= 84	Q=	0.1000		
NRETA LOAD =		5	1	-1	-5
CABLE LEN = 10		0.3723	0.3631	0.3904	0.4909
CABLE LEN = 30		0.4317	0.3627	0.3832	0.4663
CABLE LEN = 50		0.5712	0.3844	0.3799	0.4377
PHIDA	V= 168	Q=	0.1000		
NRETA LOAD =		5	1	-1	-5
CABLE LEN = 10		0.8730	0.2250	0.2016	0.4338
CABLE LEN = 30		0.5345	0.4941	0.1738	0.3622
CABLE LEN = 50		0.4439	0.3687	0.1620	0.2746
PHIDA	V= 253	Q=	0.1000		
NRETA LOAD =		5	1	-1	-5
CABLE LEN = 10		0.2862	0.4956	0.0803	0.3762
CABLE LEN = 30		0.2134	0.1726	-0.0134	0.4958
CABLE LEN = 50		0.1629	0.0947	-0.0457	0.5899

TABLE XXIX - Continued

PHIDDA	V= 84	Q=	0.1000		
NBETA LOAD =		5	1	-1	-5
CABLE LFN = 10		0.5812	0.6105	0.6498	0.7560
CABLE LEN = 30		0.5033	0.6538	0.7397	0.9039
CABLE LEN = 50		0.4492	0.6257	0.7299	0.9360
PHIDDA	V= 168	Q=	0.1000		
NBETA LOAD =		5	1	-1	-5
CABLE LFN = 10		0.5065	0.2436	0.4285	0.7483
CABLE LEN = 30		0.5771	0.3425	0.4713	0.9381
CABLE LEN = 50		0.6186	0.4794	0.5530	1.0940
PHIDDA	V= 253	Q=	0.1000		
NBETA LOAD =		5	1	-1	-5
CABLE LFN = 10		0.5790	0.2438	0.5223	0.9254
CABLE LEN = 30		0.5619	0.4169	0.5756	1.4580
CABLE LEN = 50		0.6431	0.5344	0.6548	2.0480
PSIDA	V= 84	Q=	0.1000		
NBETA LOAD =		5	1	-1	-5
CABLE LFN = 10		0.2107	0.1747	0.1643	0.1604
CABLE LEN = 30		0.1702	0.1562	0.1547	0.1571
CABLE LEN = 50		0.1634	0.1471	0.1458	0.1505
PSIDA	V= 168	Q=	0.1000		
NBETA LOAD =		5	1	-1	-5
CABLE LFN = 10		0.2920	0.1529	0.1422	0.2032
CABLE LEN = 30		0.2391	0.1780	0.1393	0.1821
CABLE LEN = 50		0.2116	0.1780	0.1489	0.1787
PSIDA	V= 253	Q=	0.1000		
NBETA LOAD =		5	1	-1	-5
CABLE LFN = 10		0.2973	0.2054	0.1533	0.2421
CABLE LEN = 30		0.2368	0.2022	0.1468	0.2564
CABLE LEN = 50		0.2187	0.1939	0.1505	0.2800

TABLE XXIX - Continued

PSIDDA	V= 84	Q=	0.1000		
NBETA LOAD =		5	1	-1	-5
CABLE LEN = 10		0.2912	0.0574	-0.0829	-0.3516
CABLE LEN = 30		-0.1415	-0.0183	-0.0625	-0.2219
CABLE LEN = 50		-0.5741	-0.1294	-0.0955	-0.1588
PSIDDA	V= 168	Q=	0.1000		
NBETA LOAD =		5	1	-1	-5
CABLE LEN = 10		-2.4430	-0.2198	0.0087	-0.4014
CABLE LEN = 30		-1.0380	-1.5370	0.0750	-0.0867
CABLE LEN = 50		-0.7595	-0.7533	0.1996	0.3885
PSIDDA	V= 253	Q=	0.1000		
NBETA LOAD =		5	1	-1	-5
CABLE LEN = 10		0.1946	-2.5810	1.0310	0.1291
CABLE LEN = 30		0.2729	0.1519	1.5130	0.0421
CABLE LEN = 50		0.5987	0.8092	1.7680	0.2376
P2DA	V= 84	Q=	0.1000		
NBETA LOAD =		5	1	-1	-5
CABLE LEN = 10		-0.2431	-0.2785	-0.3015	-0.3486
CABLE LEN = 30		1.5880	0.8858	0.7316	0.5450
CABLE LEN = 50		4.1480	2.7120	2.2310	1.7900
P2DA	V= 168	Q=	0.1000		
NBETA LOAD =		5	1	-1	-5
CABLE LEN = 10		2.0070	0.3877	0.1638	-0.1814
CABLE LEN = 30		1.6810	4.2180	2.8930	1.4190
CABLE LEN = 50		2.0360	3.9810	4.5350	3.0950
P2DA	V= 253	Q=	0.1000		
NBETA LOAD =		5	1	-1	-5
CABLE LEN = 10		0.9142	1.1540	1.1030	0.0254
CABLE LEN = 30		2.7040	3.3570	4.5450	1.8150
CABLE LEN = 50		4.1850	4.6440	6.2180	3.6800

TABLE XXIX - Continued

P2DDA	V= 84	Q= 0.1000			
NBETA LOAD =		5	1	-1	-5
CABLE LEN = 10		-0.2538	-0.2502	-0.2440	-0.2285
CABLE LEN = 30		0.3705	0.1827	0.1457	0.1371
CABLE LEN = 50		0.0138	-0.1062	-0.1790	-0.1657
P2DDA	V= 168	Q= 0.1000			
NBETA LOAD =		5	1	-1	-5
CABLE LEN = 10		-0.1686	0.0102	-0.0742	-0.0870
CABLE LEN = 30		-0.2061	1.4660	0.6735	0.5244
CABLE LEN = 50		-0.2953	0.6998	0.4076	0.4361
P2DDA	V= 253	Q= 0.1000			
NBETA LOAD =		5	1	-1	-5
CABLE LEN = 10		-0.1035	0.8538	0.1774	0.0782
CABLE LEN = 30		0.3250	0.6721	0.7172	1.0620
CABLE LEN = 50		0.5534	0.6864	0.5404	1.9890
P3DA	V= 84	Q= 0.1000			
NBETA LOAD =		5	1	-1	-5
CABLE LEN = 10		-0.6237	-0.5596	-0.5348	-0.4983
CABLE LEN = 30		-2.4820	-1.5240	-1.3090	-1.0560
CABLE LEN = 50		-5.0400	-3.3520	-2.7960	-2.2700
P3DA	V= 168	Q= 0.1000			
NBETA LOAD =		5	1	-1	-5
CABLE LEN = 10		-2.9110	-1.3410	-0.9099	-0.4932
CABLE LEN = 30		-1.9560	-4.8250	-3.3780	-1.6580
CABLE LEN = 50		-2.2360	-4.1890	-4.8250	-3.1890
P3DA	V= 253	Q= 0.1000			
NBETA LOAD =		5	1	-1	-5
CABLE LEN = 10		-0.8833	-1.5360	-1.5490	-0.3529
CABLE LEN = 30		-2.5010	-3.0810	-4.6710	-1.7280
CABLE LEN = 50		-3.9480	-4.3900	-6.1830	-3.3710

TABLE XXIX - Continued

P3DDA	V= 84	Q=	0.1000		
NBETA LOAD =		5	1	-1	-5
CABLE LEN = 10		-0.4626	-0.4474	-0.4418	-0.4309
CABLE LEN = 30		-1.1840	-0.6985	-0.5697	-0.4319
CABLE LEN = 50		-0.9678	-0.4660	-0.2536	-0.0661
P3DDA	V= 168	Q=	0.1000		
NBETA LOAD =		5	1	-1	-5
CABLE LEN = 10		-0.5962	-1.0470	-0.7581	-0.5940
CABLE LEN = 30		-0.1982	-2.4860	-1.3380	-0.7350
CABLE LEN = 50		-0.0098	-1.2350	-0.8861	-0.3745
P3DDA	V= 253	Q=	0.1000		
NBETA LOAD =		5	1	-1	-5
CABLE LEN = 10		-0.2251	-2.0010	-0.8612	-0.6013
CABLE LEN = 30		-0.5722	-1.0930	-1.1440	-0.9128
CABLE LEN = 50		-0.7231	-0.9660	-0.7846	-1.2290
VDR	V= 84	Q=	0.1000		
NBETA LOAD =		5	1	-1	-5
CABLE LEN = 10		-0.0059	-0.0149	-0.0210	-0.0360
CABLE LEN = 30		-0.0136	-0.0228	-0.0295	-0.0447
CABLE LEN = 50		-0.0323	-0.0319	-0.0381	-0.0542
VDR	V= 168	Q=	0.1000		
NBETA LOAD =		5	1	-1	-5
CABLE LEN = 10		-0.2084	-0.0096	-0.0357	-0.1141
CABLE LEN = 30		-0.1705	-0.0606	-0.0543	-0.1307
CABLE LEN = 50		-0.1539	-0.0896	-0.0827	-0.1657
VDR	V= 253	Q=	0.1000		
NBETA LOAD =		5	1	-1	-5
CABLE LEN = 10		-0.4162	-0.746	-0.0686	-0.2334
CABLE LEN = 30		-0.2560	-0.1181	-0.0987	-0.2683
CABLE LEN = 50		-0.2170	-0.1350	-0.1374	-0.3306

TABLE XXIX - Continued

PHIDR	V= 84	Q=	0.1000		
NBETA LOAD =		5	1	-1	-5
CABLE LEN = 10		-0.3130	-0.7043	-0.9173	-1.3440
CABLE LEN = 30		-0.3400	-0.8247	-1.0500	-1.4520
CABLE LEN = 50		-0.4381	-0.8686	-1.1170	-1.5460
PHIDR	V= 168	Q=	0.1000		
NBETA LOAD =		5	1	-1	-5
CABLE LEN = 10		-1.3070	-0.1793	-0.9636	-2.0520
CABLE LEN = 30		-1.5920	-0.5496	-1.1130	-2.1330
CABLE LEN = 50		-1.6440	-1.0540	-1.3990	-2.4090
PHIDR	V= 253	Q=	0.1000		
NBETA LOAD =		5	1	-1	-5
CABLE LEN = 10		-2.0720	-0.0336	-1.2250	-2.5620
CABLE LEN = 30		-1.8600	-0.9265	-1.4180	-2.7920
CABLE LEN = 50		-1.8120	-1.2760	-1.6820	-3.2430
PHIDR	V= 84	Q=	0.1000		
NBETA LOAD =		5	1	-1	-5
CABLE LEN = 10		0.1210	-0.1034	-0.2220	-0.4254
CABLE LEN = 30		0.3958	0.3010	0.2410	0.1259
CABLE LEN = 50		0.5036	0.4887	0.4961	0.4827
PHIDR	V= 168	Q=	0.1000		
NBETA LOAD =		5	1	-1	-5
CABLE LEN = 10		0.5028	0.1067	-0.1478	-0.4277
CABLE LEN = 30		0.5002	0.0667	0.1355	0.1249
CABLE LEN = 50		0.4913	0.1764	0.2155	0.4459
PHIDR	V= 253	Q=	0.1000		
NBETA LOAD =		5	1	-1	-5
CABLE LEN = 10		0.3665	0.0798	0.1034	-0.2596
CABLE LEN = 30		0.2706	0.1831	0.3982	-0.0100
CABLE LEN = 50		0.3169	0.2667	0.5430	-0.1246

TABLE XXIX - Continued

PSIDR	V= 84	Q=	0.1000		
NBETA LOAD =		5	1	-1	-5
CABLE LEN = 10		0.2357	0.2635	0.2702	0.2725
CABLE LEN = 30		0.2665	0.2749	0.2758	0.2744
CABLE LEN = 50		0.2707	0.2799	0.2805	0.2781
PSIDR	V= 168	Q=	0.1000		
NBETA LOAD =		5	1	-1	-5
CABLE LEN = 10		0.1212	0.2768	0.2824	0.2423
CABLE LEN = 30		0.2068	0.2613	0.2838	0.2584
CABLE LEN = 50		0.2349	0.2613	0.2789	0.2607
PSIDR	V= 253	Q=	0.1000		
NBETA LOAD =		5	1	-1	-5
CABLE LEN = 10		0.1077	0.2410	0.2767	0.2034
CABLE LEN = 30		0.2095	0.2431	0.2803	0.1849
CABLE LEN = 50		0.2283	0.2497	0.2782	0.1468
PSIDDR	V= 84	Q=	0.1000		
NBETA LOAD =		5	1	-1	-5
CABLE LEN = 10		2.1200	3.1960	3.7370	4.7910
CABLE LEN = 30		2.4050	3.6810	4.2580	5.2720
CABLE LEN = 50		2.7180	3.8760	4.5340	5.6510
PSIDDR	V= 168	Q=	0.1000		
NBETA LOAD =		5	1	-1	-5
CABLE LEN = 10		8.9020	2.6350	6.5400	11.8600
CABLE LEN = 30		10.7000	4.9370	7.5420	12.7100
CABLE LEN = 50		10.9300	7.6540	9.1140	14.3400
PSIDDR	V= 253	Q=	0.1000		
NBETA LOAD =		5	1	-1	-5
CABLE LEN = 10		19.4700	3.0220	10.6300	20.0200
CABLE LEN = 30		17.2700	10.1300	12.4200	21.6600
CABLE LEN = 50		15.5000	12.4200	14.6200	24.3900

TABLE XXIX - Continued

P2DR	V= 84	Q= 0.1000			
NBETA LOAD =		5	1	-1	-5
CABLE LEN = 10		0.1384	0.2613	0.3190	0.4247
CABLE LEN = 30		-0.1614	0.3089	0.4099	0.5187
CABLE LEN = 50		-1.7900	0.5240	0.9802	1.3720
P2DR	V= 168	Q= 0.1000			
NBETA LOAD =		5	1	-1	-5
CABLE LEN = 10		-6.5350	0.3844	1.2500	1.9340
CABLE LEN = 30		-2.1560	-3.5610	3.1910	4.0790
CABLE LEN = 50		1.9840	-0.6183	6.2130	8.3210
P2DR	V= 253	Q= 0.1000			
NBETA LOAD =		5	1	-1	-5
CABLE LEN = 10		7.0910	-4.3880	3.3250	3.9750
CABLE LEN = 30		11.6800	0.3789	9.5880	8.3330
CABLE LEN = 50		16.6200	9.0880	15.8900	14.7200
P2DDR	V= 84	Q= 0.1000			
NBETA LOAD =		5	1	-1	-5
CABLE LEN = 10		0.4122	0.3484	0.3199	0.2762
CABLE LEN = 30		0.7208	0.6288	0.5617	0.4449
CABLE LEN = 50		2.2490	1.8680	1.6100	1.2550
P2DDR	V= 168	Q= 0.1000			
NBETA LOAD =		5	1	-1	-5
CABLE LEN = 10		1.0140	1.0190	0.7193	0.4894
CABLE LEN = 30		4.2890	3.1180	2.1580	0.8781
CABLE LEN = 50		6.4670	5.9610	4.2310	1.5700
P2DDR	V= 253	Q= 0.1000			
NBETA LOAD =		5	1	-1	-5
CABLE LEN = 10		4.4740	1.9560	1.0230	0.5648
CABLE LEN = 30		6.7350	5.6210	2.7650	0.3163
CABLE LEN = 50		8.5350	8.0630	4.3300	-0.6680

TABLE XXIX - Concluded

P3DR	V= 84	Q=	0.1000		
NBETA LOAD =		5	1	-1	-5
CABLE LEN = 10		-0.2394	-0.2637	-0.2678	-0.2655
CABLE LEN = 30		0.5721	-0.1392	-0.2439	-0.3033
CABLE LEN = 50		3.5370	0.6016	0.0574	-0.3410
P3DR	V= 168	Q=	0.1000		
NBETA LOAD =		5	1	-1	-5
CABLE LEN = 10		11.9400	0.0648	-0.9756	-1.4040
CABLE LEN = 30		6.8020	7.0980	-1.7510	-3.0160
CABLE LEN = 50		2.5880	4.6950	-3.3480	-6.1160
P3DR	V= 253	Q=	0.1000		
NBETA LOAD =		5	1	-1	-5
CABLE LEN = 10		-1.3150	9.0400	-3.4290	-3.8130
CABLE LEN = 30		-6.2200	4.0610	-7.9820	-7.3010
CABLE LEN = 50		-11.5100	-4.7850	-13.0800	-12.8400
P3DDR	V= 84	Q=	0.1000		
NBETA LOAD =		5	1	-1	-5
CABLE LEN = 10		-0.1995	-0.1521	-0.1312	-0.0887
CABLE LEN = 30		-0.2397	-0.1066	-0.0140	0.1470
CABLE LEN = 50		-1.1460	-0.9048	-0.6033	-0.1807
P3DDR	V= 168	Q=	0.1000		
NBETA LOAD =		5	1	-1	-5
CABLE LEN = 10		0.7085	-0.9796	-0.6535	-0.2509
CABLE LEN = 30		-2.6150	-2.5390	-1.8800	-0.3153
CABLE LEN = 50		-4.8490	-4.9870	-3.6300	-0.8206
P3DDR	V= 253	Q=	0.1000		
NBETA LOAD =		5	1	-1	-5
CABLE LEN = 10		-3.2530	-1.7850	-1.1680	-0.1945
CABLE LEN = 30		-5.7080	-4.9850	-2.6660	0.2649
CABLE LEN = 50		-7.6320	-7.4670	-3.9700	0.9773

12.2 FLIGHT SIMULATION DEMONSTRATION ON LARGE-AMPLITUDE FLIGHT SIMULATOR

On January 19 and 20, 1972, final flight simulation demonstrations were conducted on the Northrop new large-amplitude flight simulator. Personnel of the U. S. Army Air Mobility Research and Development Laboratory participated in the flight testing of the new flight simulator. The case configurations are listed below. Pilot participation is indicated in Table XXX.

Case Configuration:

1.0 Basic helicopter with basic SAS, no sling load:

Typical CH-47B

1.1 $V = 50$ knots

1.2 $V = 100$ knots

1.3 $V = 150$ knots.

2.0 Basic helicopter with basic SAS, with sling load, without sling load aerodynamics:

$V = 150$ knots, $L = 10$ feet.

3.0 Helicopter with sling load, basic SAS, typical 8- by 8- by 20-foot container, 20,000 pounds, nominal load aerodynamics:

3.1 $V = 50$ knots

3.2 $V = 100$ knots

3.3 $V = 125$ knots

3.4 $V = 150$ knots.

4.0 Effect of sling-load cable length:

4.1 $V = 50$ knots, $L = 10$ feet

4.2 $V = 50$ knots, $L = 100$ feet.

(Helicopter and sling-load characteristics same as case 3.0).

5.0 Effect of sling-load weathercock stability characteristics:

5.1 $V = 125$ knots, $L = 10$ feet, nominal weathercock stability, similar to case 3.0

5.2 $V = 125$ knots, $L = 10$ feet, 5x nominal weathercock

5.3 $V = 125$ knots, $L = 10$ feet, unstable weathercock.

6.0 Procedural stabilization approach:

6.1 $V = 125$ knots, $L = 10$ feet, regular SAS, unstable weathercock

6.2 $V = 125$ knots, $L = 10$ feet, regular SAS, nominal weathercock.

7.0 Active aerodynamic stabilization system:

$V = 150$ knots, $L = 10$ feet, 5x nominal weathercock, 20,000-pound load.

8.0 Passive aerodynamic stabilization inherent characteristics modification:

8.1 $V = 125$ knots, $L = 10$ feet, 5x nominal weathercock, same as 5.2

8.2 $V = 125$ knots, $L = 10$ feet, neutral weathercock.

9.0 Black box load stabilization system (LSS) load stabilization augmentation system:

9.1 $V = 150$ knots, $L = 10$ feet, basic SAS, 5x nominal weathercock

9.2 Same as 9.1, except with best optimized LSS.

TABLE XXX. FLIGHT SIMULATOR CASES TEST FLOWN

Cases	R. Lane	D. Simon	E. Forehand	J. Savage
1.1	X	X	X	
1.2				
1.3	X	X		
2.0	X	X	X	
3.1	X			
3.2		X		
3.3	X	X	X	X
3.4	X	X		
4.1	X	X		
4.2				
5.1 = 3.3	X	X		
5.2	X	X		
5.3	X	X		
6.1 = 5.3		X		
6.2 = 3.3	X			
7.0	X	X		
8.1 = 5.2	X	X		
8.2	X	X		
9.1	X	X	X	X
9.2	X	X	X	X

12.3 FLIGHT SIMULATION DYNAMIC TIME HISTORY

A time history of the 32 parameters listed below was recorded. Strip chart recordings are available on request.

δ_{LAT} Lateral control deflection
 δ_{RUD} Rudder control deflection
 $\ddot{\phi}$ Helicopter roll acceleration
 $\dot{\phi}$ Helicopter roll rate
 ϕ Helicopter roll angle
 $\ddot{\psi}$ Helicopter yaw acceleration
 $\dot{\psi}$ Helicopter yaw rate
 ψ Helicopter yaw angle

$\dot{\phi}_2 - \dot{\phi}_3$ Load yaw angle
 $\dot{\phi}_2 + \dot{\phi}_3$ Load roll angle
 $\ddot{\phi}_2$ Load front cable roll angular acceleration
 $\dot{\phi}_2$ Load front cable roll angle
 $\ddot{\phi}_3$ Load rear cable roll angular acceleration
 $\dot{\phi}_3$ Load rear cable roll angle
 $\ddot{\phi}_4$ Load roll acceleration
 $\dot{\phi}_4$ Load roll angle

δ_{LONG} Longitudinal control deflection
 $\ddot{\theta}$ Helicopter pitch acceleration
 $\dot{\theta}$ Helicopter pitch rate
 θ Helicopter pitch angle
 \ddot{U} Helicopter longitudinal acceleration
 \dot{U} Helicopter longitudinal velocity
 \ddot{W} Helicopter vertical acceleration
 \dot{W} Helicopter vertical velocity

"	Helicopter pitch acceleration
θ	Helicopter pitch rate
θ	Helicopter pitch angle
"	Sling cable pitch acceleration
λ	Sling cable pitch rate
λ	Sling cable pitch angle
F ₁	Front cable tension
F ₂	Rearward cable tension

12.4 DESCRIPTION AND COMMENTS ON THE FLIGHT SIMULATION DEMONSTRATION

The following description and comments were provided by Mr. D. Simon.

"The subject simulator/simulation was evaluated for a period of approximately 2 hours and 45 minutes on 20 January 1972. The simulator provided 5 degrees of cockpit motion (± 25 degrees pitch, roll, and yaw; ± 14 feet of near vertical and lateral translation), and a visual real-world type projection on a hemispheric screen which was rigidly attached to and moved with the cockpit. Cockpit instrumentation consisted of several basic flight instruments for IFR and four tape gages representing external load motion. The load stabilization system (LSS) was an ideal mechanization of numerous sensors (load mounted accelerometers, cable angle, cable angle rate, gyros, etc.) which were massaged, as required, in a computer and introduced into the ship's system SAS. The external load simulation was that of an 8 by 8 by 20-foot container weighing 20,000 pounds and suspended via two cables of equal length, 10 and 100 feet below the aircraft (distances were measured from the belly-mounted hooks to the center of gravity of the box).

"The scope of the test conditions was limited to four airspeeds, two cable lengths, and one load configuration due to the programming of non-variable stability derivatives. Thus, when the simulation was engaged the pilot found himself trimmed at a given airspeed (50, 100, 125 or 150 knots) and altitude (1000 feet). Power (collective pitch) was fixed at a pre-determined setting and cyclic inputs had no significant effect on airspeed or altitude. The test agenda was with and without cockpit motion, external load, and load stabilization.

"In comparing this simulation with those with which the undersigned has "flown" previously, an overall rating of good is assigned to the 100, 125, and 150-knot conditions. The 50-knot conditions with the external load were considered unsatisfactory. This rating takes into account the strong points, in terms of realism and qualitatively assessed validity, as well as the deficiencies and limited flight envelope. The most interesting characteristic which enhanced my opinion of the simulation was the vividly

demonstrated effect of dynamic pressure (airspeed) and the load's inherent static directional stability on load and load/aircraft behavior. In general, the lateral-directional characteristics were excellent while the longitudinal characteristics were fair to poor, due in part to less effort on the part of the contractor to optimize this mode. Additionally, it appeared that the lack of fore and aft cockpit motion was a significant factor; in fact, the load-induced low-frequency longitudinal accelerations which the pilot interprets as pitch attitude changes under IFR conditions could not be reproduced in this simulation. It is felt that this is an important aspect of the load stabilization problem in cruising flight which cannot be ignored.

"The point-light-source projections of the real world which Northrop has been using for their fighter simulation work was utilized in this program. It was acknowledged that the statement of work did not define effort to properly adapt the projection system to the helicopter environment. Such effort should be included in any future use of the simulator for helicopter work.

"As a concluding observation, it should be noted that the load stabilization system employed in this instance was, in fact, a clinically ideal arrangement containing all the sensors theoretically necessary to work the problem. This load stabilization system (LSS) solved the problem within the scope of this test and established some sort of academic baseline. The real worth of the program would appear to lie with the demonstrated use of the Northrop 'beam' simulator as a tool to study helicopter stability and control problems, particularly with the pilot in the loop."

13.0 CONCLUSIONS

A broad spectrum of sling loads has been subjected to load stability analysis. Cable length, type of suspension (single or two point), the optional use of a stabilizing parachute, and different values of $C_n \beta$, the weather-

cock stability factor, were taken as variables. The following conclusions were reached for the defined loads:

Box (8-by-8-by-20 feet) - For both 5,000- and 20,000-pound loads, the greatest stability is achieved with two-point suspension, short cables and a low value of weathercock stability. In one case, the 20,000-pound load, using single-point suspension plus a drag chute, stability was greater with a 100-foot cable than with shorter lengths.

Box (8-by-8-by-40 feet) - For a 5,000-pound load, the best overall results were obtained with single-point suspension, a drag chute and a low value of weathercock stability. Stability at a speed of 150 knots was obtained with two-point suspension and a 10-foot cable. For a 20,000-pound load, best results were obtained with two-point suspension and a low value of weathercock stability.

Truck - Best results for this type of load came about merely by changing from single- to two-point suspension. This permits 150 knots stable airspeed for cable lengths up to 100 feet. For the single-point suspension without chute, changing the weathercock stability factor from negative, which is inherent in this type of load, to positive, gives good results.

Tank - As in the case of the truck load, best results for the tank come from going to a two-point suspension system. For the single-point suspension without chute, using a positive value of the weathercock stability factor gives excellent results.

Carrier - Results were similar to those for the truck and tank.

VH-34 Helicopter - For single-point suspension, a stable airspeed of 150 knots can be obtained either by adding a 10-foot drag chute or by reducing the weathercock stability value to zero. The same applies for the two-point suspension case. The inherent weathercock stability of this configuration for small sideslip angles is essentially zero. This explains why past experience shows that such a load could be carried at high airspeeds.

F-5 Aircraft - Carrying the F-5 without the tail results in a very stable load for both single- and two-point suspensions. With tail added, the best arrangement is single-point suspension with a 10-foot drag chute.

OV-1 Aircraft - Good results for this type of load are achieved by two-point suspension and a small value of weathercock stability. For the single-point case, adding a parachute will greatly improve stability.

Considerable drag is added by the use of chutes for stabilization, which means that additional power is required by the towing helicopter, with a consequent decrease in performance. Furthermore, reports from pilots in Vietnam indicate that rigging chutes to a load is difficult and time-consuming, and can be dangerous in a combat situation. Therefore, it would be highly desirable to stabilize the load by some means other than by the use of drag chutes.

Reduction in weathercock stability in order to increase the airspeed at which a CH-46 load might be carried could be physically accomplished by adding a dummy fin to the CH-46 in such a way that the vertical stabilizing surfaces on the front and rear of the helicopter load were approximately equal.

In addition to simple single- and two-point suspension systems, with and without drag chutes for increased stabilization, several more sophisticated systems were conceived and their effectiveness substantiated by flight simulation. These included a variety of mechanical load stabilizers, aerodynamic load stabilization with rate sensors and a beam with control surfaces secured to the load, display systems for monitoring sling-load position, and systems which would provide rate and acceleration inputs to the helicopter's stability augmentation system. Cost estimates have been made for these concepts. Their effectiveness has been verified by flight simulation. Further study would be required to determine practicality.

The final flight simulation effort, conducted on the new Northrop large-amplitude flight simulator, has provided further validation of the analytical findings of this study program and has substantiated the effectiveness of the selected helicopter sling-load stabilization augmentation system concept.

In general, the overall helicopter/sling-load stability degrades with increasing speed for a constant weathercock load stability characteristic. At high flight speeds, strong weathercock load stability or unstable weathercock load stability characteristics lead to overall helicopter/sling-load dynamic instability.

The selected load stabilization system (electronic) is complex in implementation but very versatile. Overall system stability is very sensitive to varying flight configurations and conditions. For each specific flight configuration and condition, the optimized load stabilization system is extremely effective. Practical implementation of the proposed concept and a complete evaluation with respect to the promising mechanical stabilization approaches require further study.

In the course of this program, efforts were made to locate aerodynamic data on various load configurations to be studied. Due to the nonavailability of accurate wind tunnel or flight test data on the aero characteristics of most of the load configurations, analytical techniques were used to predict those aero characteristics. Wind tunnel aerodynamic data and flight test

data are needed to develop a good model of the loads. It is known that nonlinear effects of the containers cause them to be difficult to carry. The incorporation of more realistic experimental data from large-scale wind tunnel tests in the design analysis and system analysis of all the promising load stabilization systems would uncover the real effectiveness or deficiencies of the various stabilization approaches in a realistic environment. System mechanization and design could then be optimized, based on realistic load characteristics and system dynamics. System trade-off methodology would be improved to deal more meaningfully with cost effectiveness comparisons.

LITERATURE CITED

1. Sacks, A. H., AERODYNAMIC FORCES, MOMENTS, AND STABILITY DERIVATIVES FOR SLENDER BODIES OF GENERAL CROSS SECTION, NACA Technical Note 3283, November 1954.
2. Lehmann, Maurice J. W., THE AERODYNAMIC CHARACTERISTICS OF NON-AERODYNAMIC SHAPES, GAM/AE/68-6, June 1968, AD 838-823.
3. Hayes, William C. Jr., and Henderson, William P., SOME EFFECTS OF NOSE BLUNTNESs AND FINENESS RATIO ON THE STATIC LONGITUDINAL AERODYNAMIC CHARACTERISTICS OF BODIES OF REVOLUTION AT SUBSONIC SPEEDS, NACA Technical Note D-650, February 1961.
4. Gowen, F. E., and Perkins, E. W., DRAG OF CIRCULAR CYLINDERS FOR A WIDE RANGE OF REYNOLDS NUMBERS AND MACH NUMBERS, NACA Technical Note 3960, June 1953.
5. Hoerner, S. F., FLUID DYNAMIC DRAG, published in 1958 by the author, 148 Buseed Drive, Midland Park, N.J.
6. AUTOMATIC CONTROL CONSIDERATIONS FOR HELICOPTERS AND VTOL AIRCRAFT WITH SLING LOADS, STI Technical Report No. 138-1, November 1965.
7. Abzug, M. J., DYNAMICS AND CONTROL OF HELICOPTERS WITH TWO-CABLE SLING LOADS, TRW Systems, AIAA Paper No. 70-929.
8. McKee, J. W., and Naeseth, R. L., EXPERIMENTAL INVESTIGATION OF THE DRAG OF FLAT PLATES AND CYLINDERS IN THE SLIPSTREAM OF A HOVERING ROTOR, NACA Technical Note 4239, April 1958.
9. Kesler, D. F., FORTRAN AUTOMATIC SYNTHESIS OF OPTICAL CONTROL PROGRAM, Northrop Corporation, Aircraft Division, Report No. NOR 69-22, June 1970.

APPENDIX I

NONLINEAR BODY AERODYNAMICS

To evaluate the body contribution to the aerodynamic derivatives of aircraft, it is necessary to include the range of flight conditions which is likely to be encountered in operation. This requires the aircraft to operate at extensive angles of attack and sideslip, since the flight attitude near hovering flight is not determined by aerodynamic forces but rather from the application of power. There is, however, an area of flight where the aerodynamic and power effects will tend to be of the same order of magnitude and where neither component can be safely neglected.

Nonlinear aerodynamics is important in treating the aircraft behavior in the region where both aerodynamic forces and power are important in supporting the aircraft weight.

To obtain the total aerodynamics of bodies at large angles of attack and sideslip, it is necessary to treat both the potential flow contribution and the viscous effects. This study utilized slender body theory for the potential contributions, while two methods of treating the viscous effects were examined. The first method, using vortex tracking, was found to be unreliable within the present state of the art and is not discussed here. The second method, using the viscous crossflow concept, is described in this appendix.

1. SLENDER BODY THEORY

To completely represent the aerodynamic forces and moments on a body, it is necessary to combine both the potential and the viscous contributions. The potential contribution is determined by the use of slender body theory. The development of the equations representing the slender body solutions is an adaptation of the methods of Sacks.¹ The basic equations were modified to account for large angles of attack and sideslip. The ability to handle arbitrary body shapes was attained by introducing a method of obtaining a mapping function for an arbitrary body shape.

A computer program was written which computes five component force and moment coefficients as functions of resultant angle of attack, roll angle, yaw velocity, and pitching velocity. From these coefficients the aerodynamic derivatives can be easily obtained.

The equation for the forces and moments given by Reference 1 when modified to eliminate the rolling velocity, the effect of which can be considered negligible for a body, and the time derivatives, can be written in complex form:

$$Y - iL = 2\pi\rho U_o \bar{A}_1 \Big|_{x=\ell} + \rho U_o \left[S\bar{R} + U_o \frac{d}{dx} (S\bar{Z}_c) \right]_{x=\ell} \quad (27)$$

$$N - iM = -2\pi\rho U_o \int_0^\ell (x - x_{cg}) \frac{\partial \bar{A}_1}{\partial x} dx - \rho U_o \int_0^\ell (x - x_{cg}) \frac{\partial}{\partial x} \left[S\bar{R} + U_o \frac{d}{dx} (S\bar{Z}_c) \right] dx \quad (28)$$

$$L' = 1/2 \rho U_o \bar{R} \oint_{x=\ell} Fd(z\bar{z}) - 2\pi\rho$$

$$I \int_0^\ell \bar{R} A_1 dx - \rho U_o \int_0^\ell \bar{R} \frac{d}{dx} (S\bar{Z}_c) dx \quad (29)$$

The evaluation of these equations requires that the complex potential

$$F = B(x) \ln z + \sum_{n=1}^{\infty} A_n(x) / z^n + D(x) \quad (30)$$

be known. When the residue of the potential $A_1(x)$ is known, the only difficulty in evaluating the total forces and moments arises in evaluating the first term of the moment equation above:

$$\bar{R} \oint Fd(z\bar{z})$$

The rest of the terms are readily evaluated.

Sacks has shown that

$$B(x) = \frac{U}{2\pi} \int_{-\infty}^{\infty} \frac{dS}{dx} \quad (31)$$

It remains to evaluate the coefficients $A_n(x)$, since the coefficient $D(x)$ is not required.

The coefficients $A_{in}(x)$ can be evaluated by re-expressing Equation (30) in terms of the mapping circle plane coordinate, ζ ; i.e.,

$$F = B(x) \ln \zeta + \sum_{n=1}^{\infty} A_{in}(x) / \zeta^n \quad (32)$$

Sacks shows that this expression can be evaluated from the coefficients of the mapping from the circle plane:

$$Z = \zeta + a_0 + \sum_{n=1}^{\infty} a_n / \zeta^n \quad (33)$$

and is expressible as

$$F = \bar{R} \sum_{n=1}^{\infty} a_n / \zeta^n - R r_c^2 / \zeta + T_N(\zeta) \quad (34)$$

where $\zeta = r e^{i\theta}$ and $T_N(\zeta)$ is the portion of the potential required to satisfy the boundary conditions of the body and is equivalent to the following expression:

$$\begin{aligned} T_N(\zeta) = r_c^2 U_0 \left\{ - \sum_{n=0}^N \left(a'_n - 2n \frac{r'}{r_c} a_n \right) \frac{\zeta^{-(n+1)}}{n+1} \right. \\ \left. + \sum_{m=0}^N \sum_{n=0}^N \left[m \left(\frac{nr'}{r_c} a_m \bar{a}_n - a_m \bar{a}'_n \right) \right. \right. \\ \left. \left. + n \left(\frac{mr'}{r_c} \bar{a}_n a_m - \bar{a}_n a'_m \right) \right] \frac{\zeta^{(n-m)}}{(n-m) r_c^{2(n+1)}} \right\} + H \ln \zeta \quad (35) \end{aligned}$$

The coefficient H , by comparison with the coefficient $B(x)$, can be shown to be

$$H = \frac{U_0}{2\pi} \frac{ds}{dx} \quad (36)$$

A comparison of the two expressions for F gives the expression

$$A_1(x) = \bar{R}a_1 - Rr_c^2 U_o \left\{ a'_o + \sum \left[m \left(\frac{(m-1) r'_c}{r_c} a_m \bar{a}_{m-1} - a_m \bar{a}'_{m-1} \right) / r_c^{2m} \right. \right. \\ \left. \left. + (m-1) \left(\frac{mr'_c}{r_c} \bar{a}_{m-1} a_m - \bar{a}_{m-1} a'_m \right) / r_c^{2m} \right] \right\} - \frac{a'_o U_o}{2\pi} \frac{dS}{dx} \quad (37)$$

$$U_o = U_\infty \cos \alpha \quad (38)$$

with this expression and the definition of R (again with $\rho = \frac{d}{dt} = 0$)

$$R = - \left[r \cos \phi + q \sin \phi \right] (x - x_{cg}) \\ - i \left[U_\infty \sin \alpha + (q \cos \phi - r \sin \phi)(x - x_{cg}) \right] \quad (39)$$

This expression for R has been modified from the definition of Reference 1 to utilize the resultant angle of attack and roll angle instead of angle of attack and sideslip.

All of the necessary information is now available to solve Equations (27) and (28) if it is assumed that the coefficients of the mapping function, Equation (33), are known. The expression

$$R \oint_{x=\ell} F d(z\bar{z})$$

can be evaluated by integration by parts to be

$$R \oint F d(z\bar{z}) = R \left[F z\bar{z} \left| \begin{array}{l} |z_o| e^{i(2\pi + \omega_o)} \\ |z_o| e^{i\omega_o} \end{array} \right. - \oint z\bar{z} dF \right]_{x=\ell} \\ = - R \left[\oint_{x=\ell} z\bar{z} dF \right] \\ = - R \left[\oint_{x=\ell} z(\zeta) \bar{z}(\zeta) \frac{dF}{d\zeta} d\zeta \right] \quad (40)$$

since the first term of the integration by parts is imaginary. On the surface of the body, Z can be represented by the expression

$$\bar{Z}_B = \bar{\zeta}_c + \bar{a}_o + \sum_{n=1}^N \frac{\bar{a}_n}{\bar{\zeta}_c^n} = \frac{r_c^2}{\bar{\zeta}_c} + \bar{a}_o + \sum_{n=0}^N \bar{a}_n \frac{\bar{\zeta}_c^n}{r_c^{2n}} \quad (41)$$

and the expression for F can be differentiated with respect to ζ and the residue of the integral can be obtained.

Thus, assuming that a mapping function is available, it is possible to solve Equations (27), (28) and (29) for Y , L , N , M and L' as functions of α , ϕ , q , and r . Also, by direct differentiation or by perturbing either α , ϕ , q , or r , it is possible to obtain the derivatives of the coefficients as well. The above analysis can also be readily extended to include either the rolling velocity or the time-dependent behavior of the coefficients, should these be desired. In the treatment of these equations it has been assumed that the forward velocity can be resolved into an axial and a crossflow component which permits the equations to be solved at angles of attack up to 90 degrees.

2. SIMPLIFIED METHOD OF OBTAINING MAJOR MAPPING COEFFICIENTS

To obtain a handbook method of using slender body theory, it is necessary to find an approximate method for estimating the most important coefficients of the mapping function in a simplified fashion. An examination of Equations (27) and (28) shows that, except for the term A_1 , all the variables are independent of the mapping; i.e., they can be obtained directly from the body geometry and flight attitude. In addition, it can generally be assumed that the rolling moment of the body can be considered negligible. It can also be shown that the derivatives of Y , L , N , and M with respect to q and r are dependent only on the radius of the mapping circle and the coefficient a_1 . The other coefficients enter into the derivatives with respect to angle of attack and sideslip (or resultant angle of attack) through the $\cos \alpha$ terms appearing in Equation (37). It appears from this expression that coefficients other than r_c , a_o , and a_1 may be neglected in treating the body. This would imply the simplification of Equation (37) to the form

$$A_1(x) \approx \bar{R}a_1 - Rr_c^2 - r_c^2 U_o a_o' - \frac{a_o U_o}{2\pi} \frac{dS}{dx} \quad (42)$$

This approximation and a suitable method of estimating r_c , a_o , and a_1 would permit a relatively simple procedure to be outlined for treating the potential contribution to the body aerodynamics. The most suitable method

of approximating these three coefficients is to treat a_0 as if it were equivalent to the centroid of the cross section, and to estimate r_c and a_1 from the maximum vertical and lateral dimensions of the body. If $2a$ is the maximum lateral dimension and $2b$ is the maximum vertical dimension, then by letting

$$r_c = \frac{a+b}{2} \quad (43)$$

$$a_1 = \frac{b-a}{2} \quad (44)$$

one obtains a relatively good approximation for these coefficients. These approximations have been made for the T-38 body and their values are compared with those obtained from an analog mapping method and shown in Figures 62 through 64. Considering the complexity of the chosen body, it is considered that the agreement obtained is quite good. The effects on the coefficients of using these approximate values and neglecting all other coefficients are shown in Figure 65.

It is felt that this is an adequate demonstration of the capabilities of predicting this portion of the body aerodynamics.

3. VISCOUS CROSSFLOW

The viscous crossflow concept assumes that the effects of an angle of attack or sideslip can be estimated by treating only the component of dynamic pressure in the crossflow plane, and that the forces exerted at each segment of the body are independent of those sections forward or aft of this segment. This treats the body by what is essentially a strip theory based on local two-dimensional values of the body drag.

Using this concept, one can write the incremental force on any segment in the form

$$\frac{d}{dx} (Y - iL)_{visc} = \frac{\rho}{2} \left[C_{D_y} c_y v_o |v_o| - i C_{D_z} c_z w_o |w_o| \right] \quad (45)$$

where $(C_{D_y} c_y)$ and $(C_{D_z} c_z)$ are local values of the crossflow drag areas per unit length in the yaw and pitch directions, respectively.

To include the effects of pitching and yawing velocity, it is necessary to define the crossflow velocity components v_o and w_o as

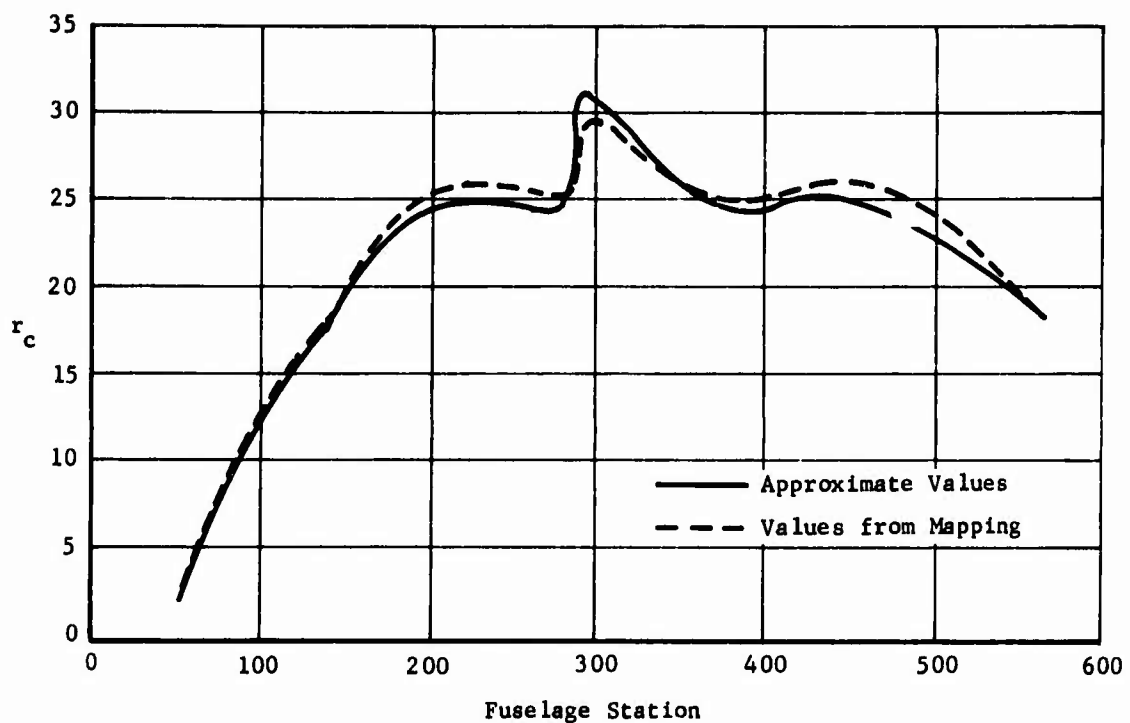


Figure 62. Exact and Approximate Calculation of Mapping Circle Radius, r_c .

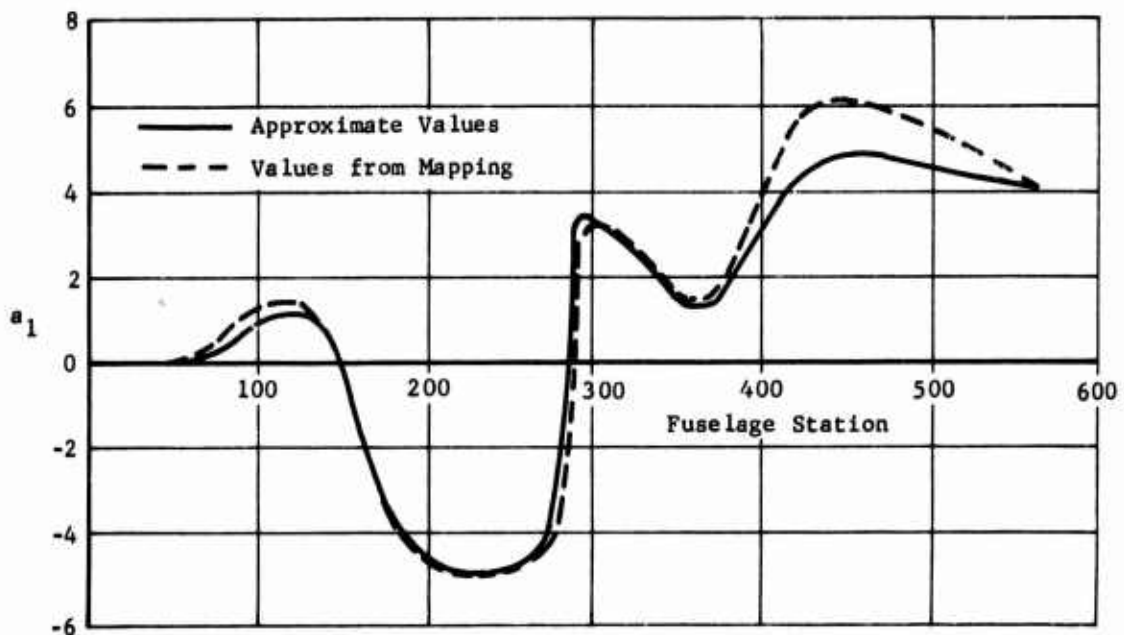


Figure 63. Exact and Approximate Calculation of Mapping Coefficient, a_1 .

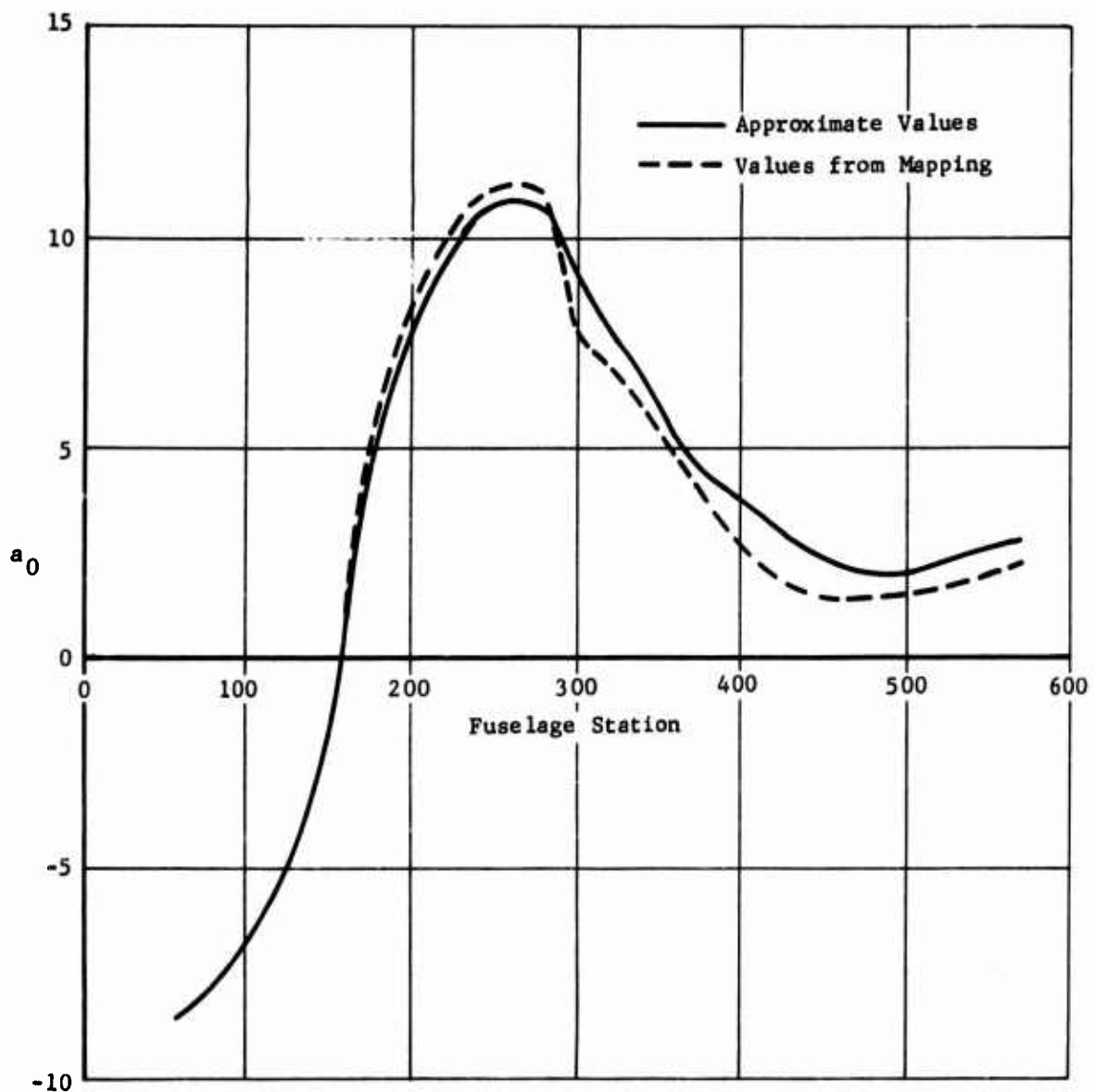


Figure 64. Exact and Approximate Calculation of Mapping Coefficient, a_0 .

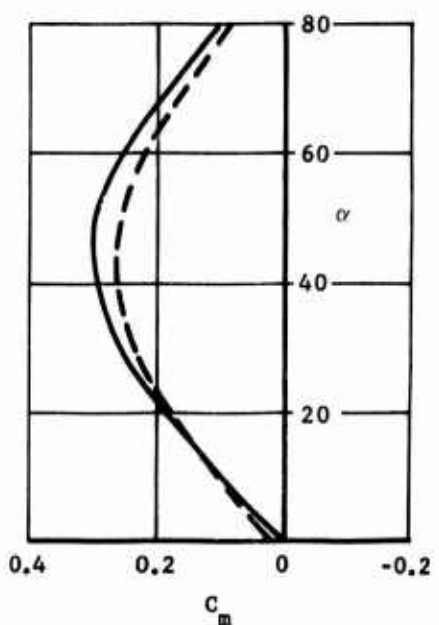
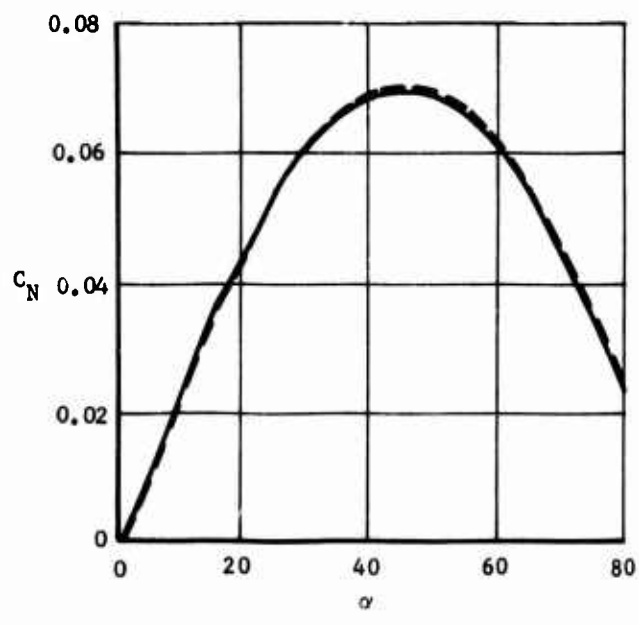
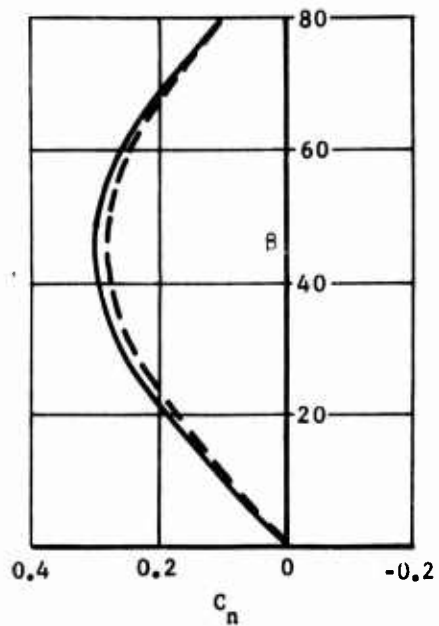
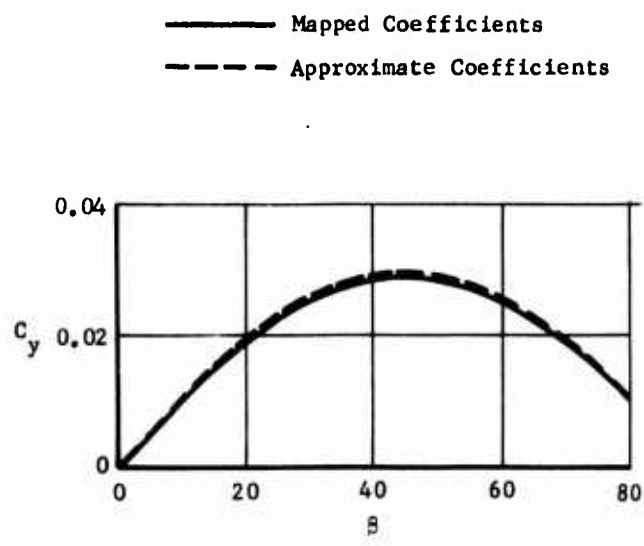


Figure 65. Comparison of Coefficients Using Exact and Approximate Mapping Coefficients.

$$V_o = U \sin \alpha \sin \phi - r(x - x_{cg}) \quad (46)$$

$$W_o = -U \sin \alpha \sin \phi - q(x - x_{cg}) \quad (47)$$

With these definitions and Equation (45), one can write the viscous contributions to the forces and moments as

$$[Y - iL]_{visc} = \frac{\rho}{2} \int_0^L \left[C_{D_y} C_y V_o |V_o| - i C_{D_z} C_z W_o |W_o| \right] dx \quad (48)$$

$$[N - iM]_{visc} = -\frac{\rho}{2} \int_0^L (x - x_{cg}) \left[C_{D_y} C_y V_o |V_o| - i C_{D_z} C_z W_o |W_o| \right] dx \quad (49)$$

The above formulations permit the viscous contributions to Y, L, N, and M to be computed as functions of α , ϕ , q , and r . No attempt has been made to include a viscous contribution to rolling moment, since it does not seem to be a significant contribution to the overall aircraft aerodynamics. Nor is it possible to formulate a model which would include acceleration effects of the body. It is believed that the above formulations give the most significant effects due to viscosity.

The values for the crossflow drag coefficients can be obtained by considering two-dimensional section data for the shape under consideration or a similar shape. Calculations made thus far have shown that treating the body as an equivalent ellipse will give reasonable values for the viscous forces and moments.

Calculations were made for the T-38 body, using the following equation for the crossflow drag coefficient:

$$C_{D_o} = 2C_f \left(1 + \frac{a_e}{b_e} \right) + 1.1 \left(\frac{b_e}{a_e} \right) \quad (50)$$

with $C_f = 0.0075$.

It was assumed that a_e and b_e , which in Equation (50) are the ellipse semi-axes parallel and perpendicular to the crossflow, respectively, were the maximum dimensions of the local T-38 cross section.

The results obtained with this equation, together with the slender body values, are compared with test data in Figure 66.

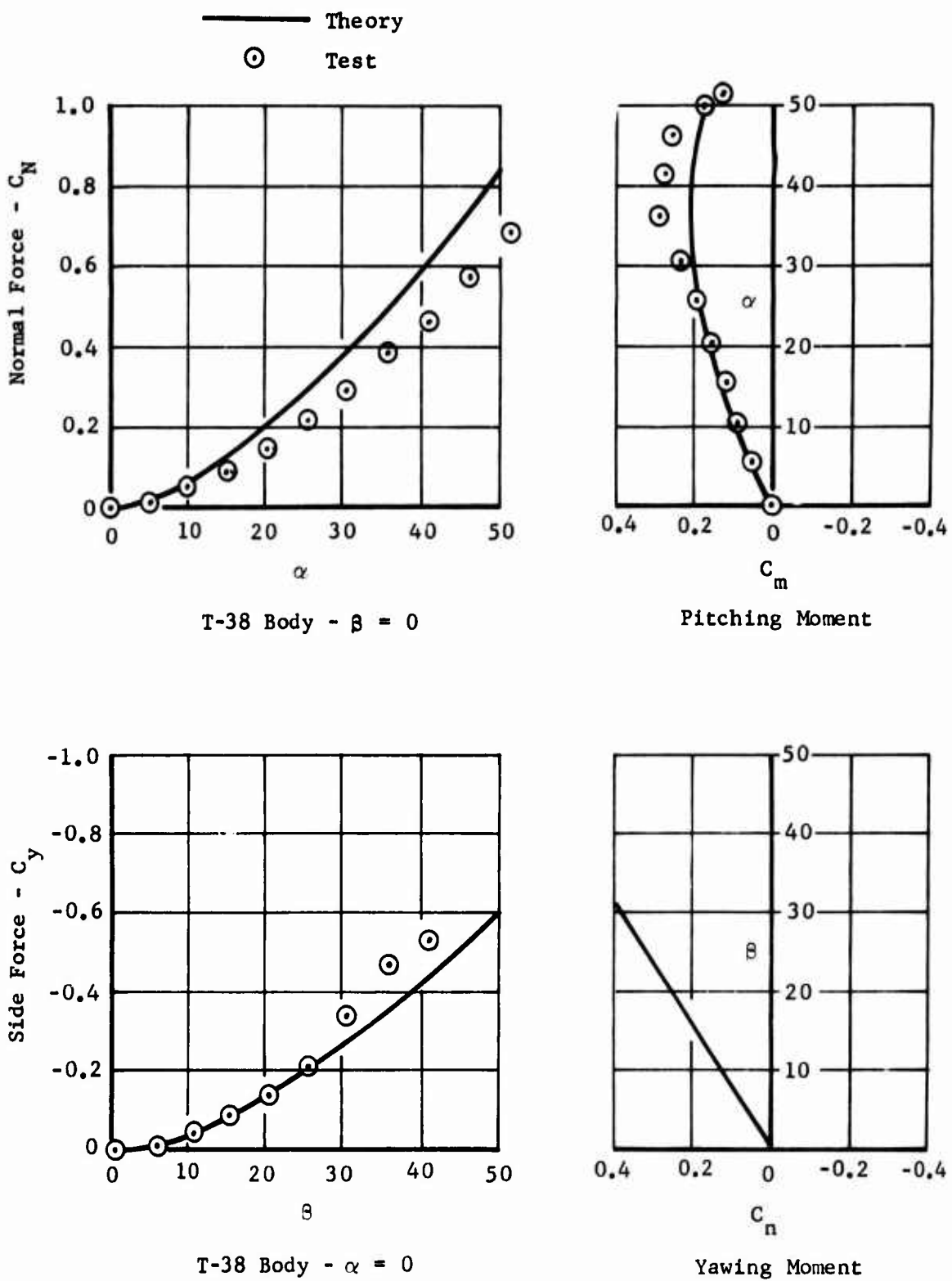


Figure 66. Comparison of Test and Theoretical Coefficients for T-38 Fuselage.

APPENDIX II

COEFFICIENTS AND DERIVATIVES FOR ANALYSIS

For the purpose of study on this contract, cargo containers with three different fineness ratios were analyzed. These containers had a square front face and fineness ratios of $A_x/A_s = 1, 2.5$, and 5.0 . Also analyzed were three other configurations: a cargo truck, M-35A1; an armored reconnaissance/airborne assault vehicle, M-551; and a command post carrier, M-577A1.

Figures 67 through 72 show the coefficients and derivatives for the cargo containers. In all cases the reference area was the frontal area, the reference length was the container length normal to the front face, and the moment center was at the centroid.

Figure 73 shows the armored reconnaissance/airborne assault vehicle, M-551 (tank), as used in the study. The outline of the vehicle was smoothed out to input to the computer program as shown on the figure. Figures 74 through 81 show the coefficients and derivatives obtained for this vehicle. The reference area was the maximum frontal area, the reference length was the vehicle length, and the center of moment was $0.5 l_{ref}$ behind the nose and $0.185 l_{ref}$ above the lower track.

Figure 82 shows the truck which was analyzed and the modifications to the outline used in the analysis. Figures 83 through 88 show the coefficients and derivatives obtained. The reference area was the maximum frontal area, the reference length was the vehicle length, and the center of moments was $0.49 l_{ref}$ behind the nose and $0.14 l_{ref}$ above the lower outline as modified.

Figure 89 shows the command post carrier which was analyzed. Figures 90 through 97 show the derivatives obtained for this configuration. The reference area was the maximum frontal area, the reference length was the vehicle length, and the moment center was $0.5 l_{ref}$ aft of the nose and $0.216 l_{ref}$ above the lower track.

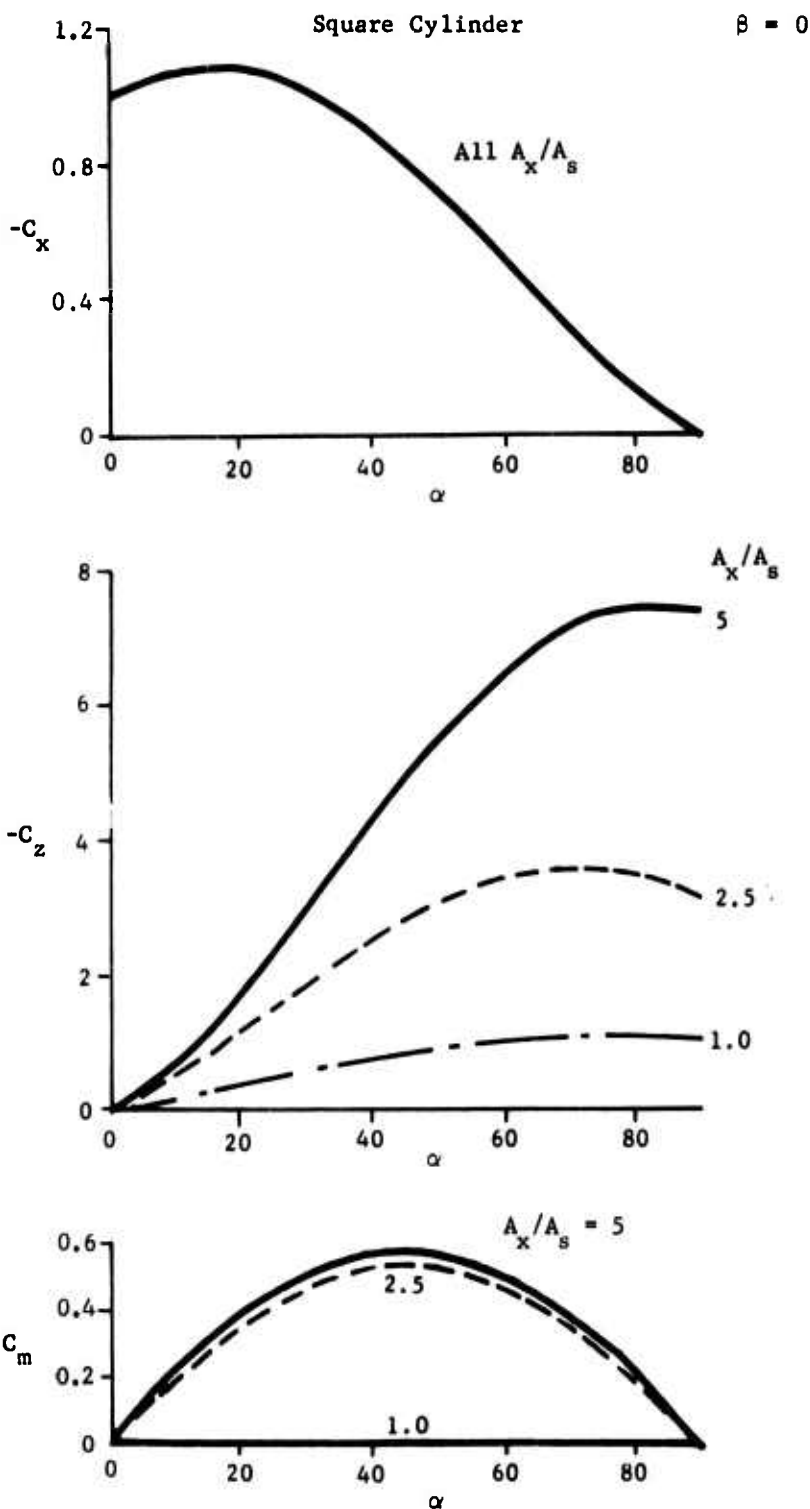


Figure 67. C_x , C_z , and C_m vs α .

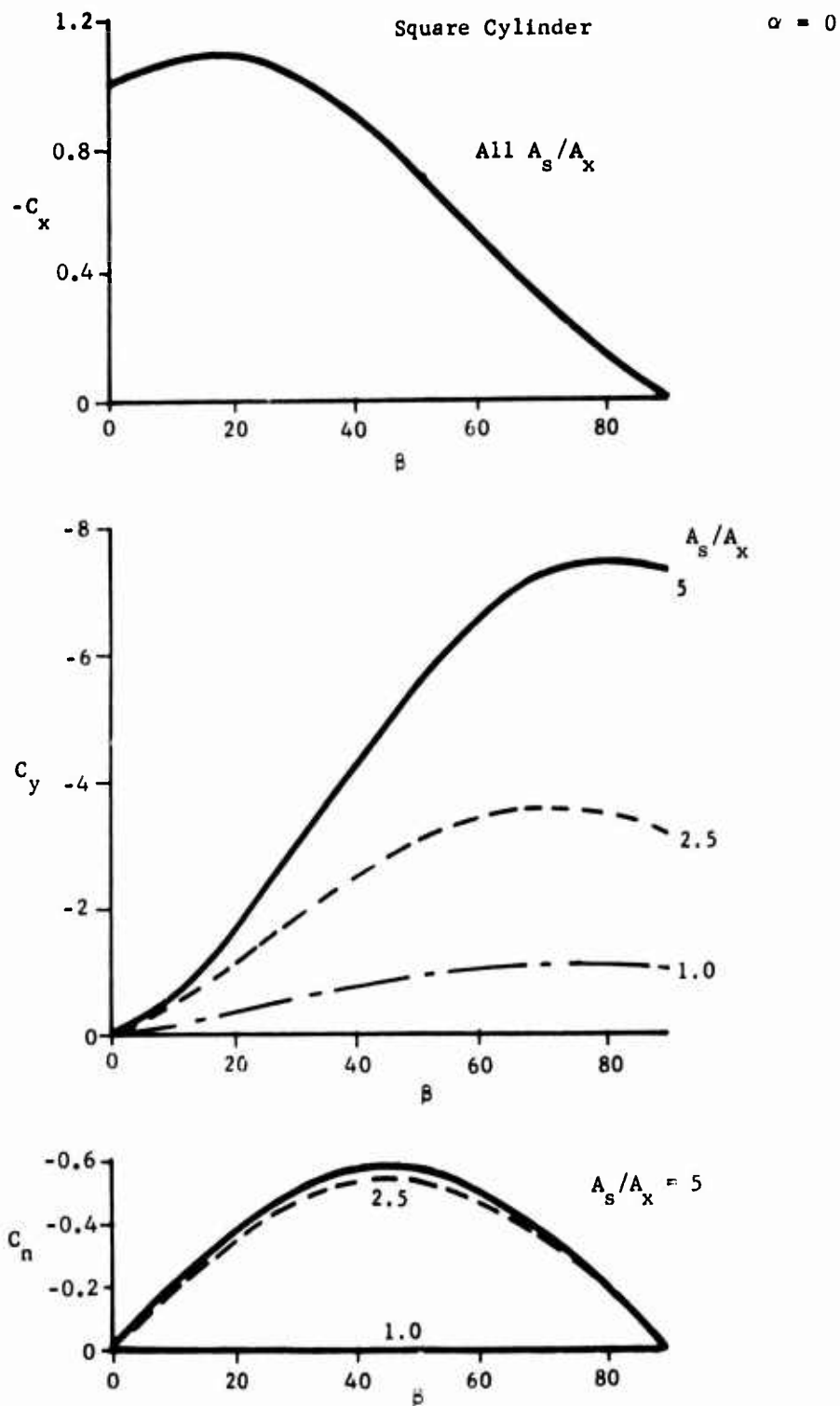


Figure 68. C_x , C_y , and C_n vs β .

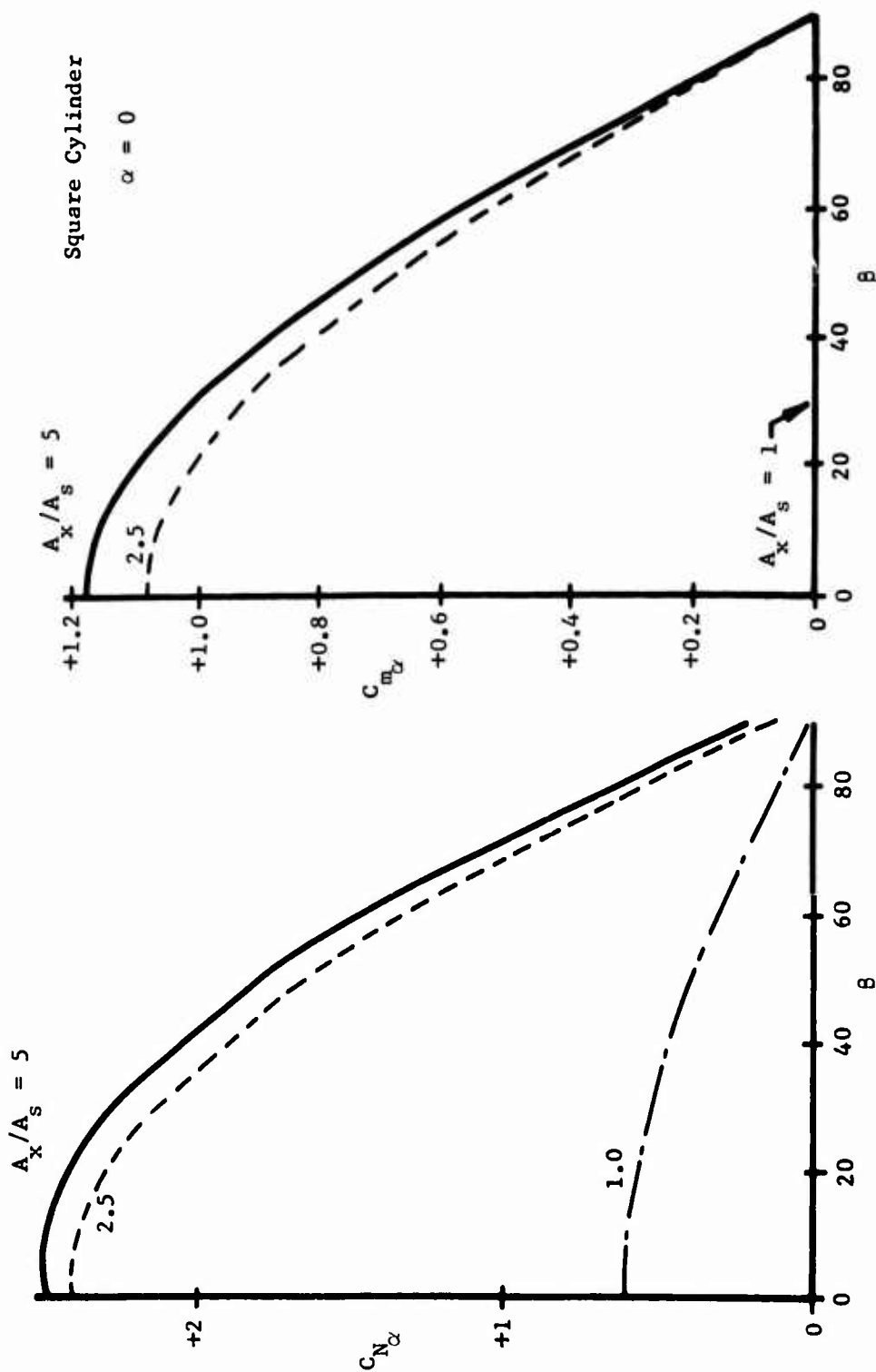


Figure 69. C_{N_α} and C_{m_α} vs β .

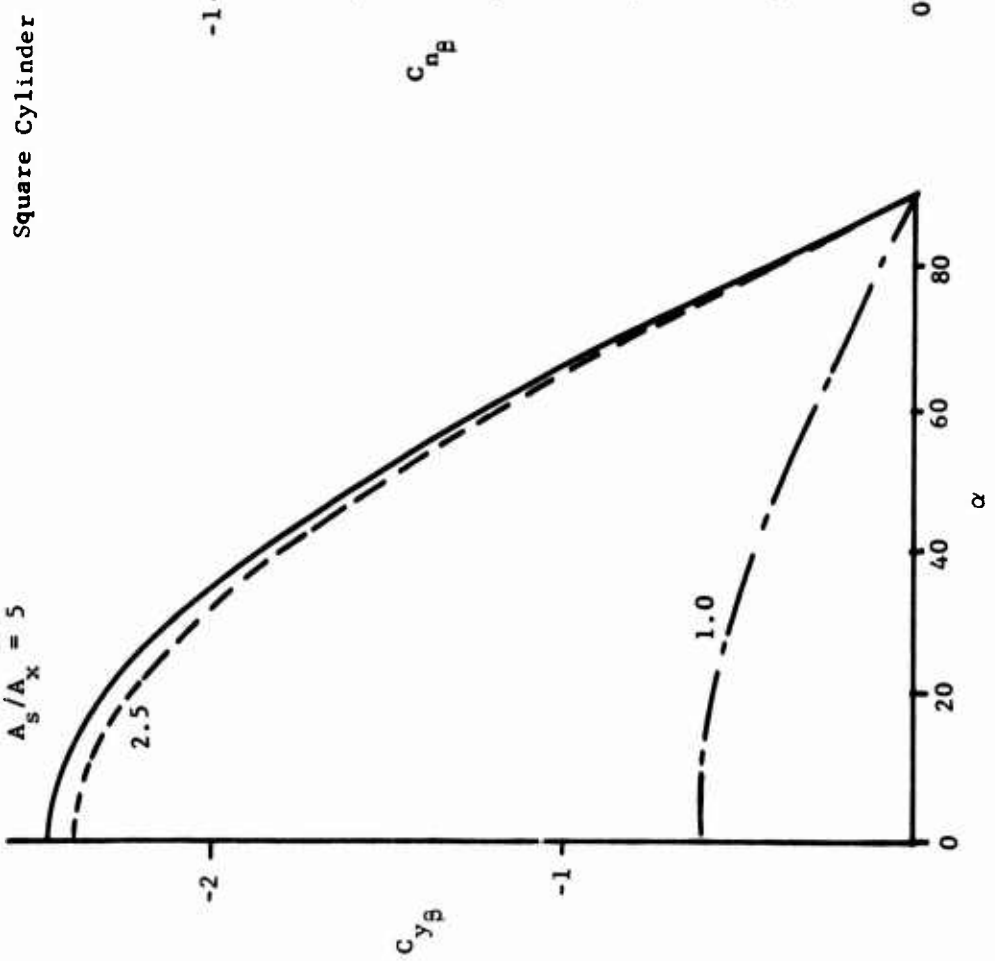
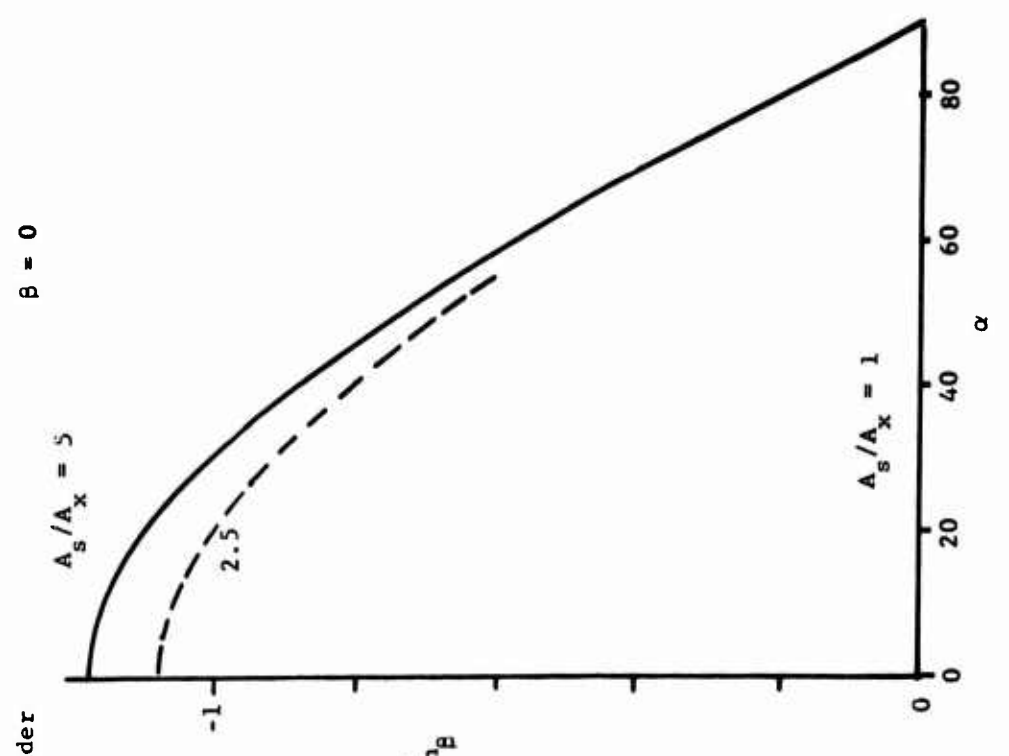


Figure 70. $C_{y\beta}$ and $C_{n\beta}$ vs α .

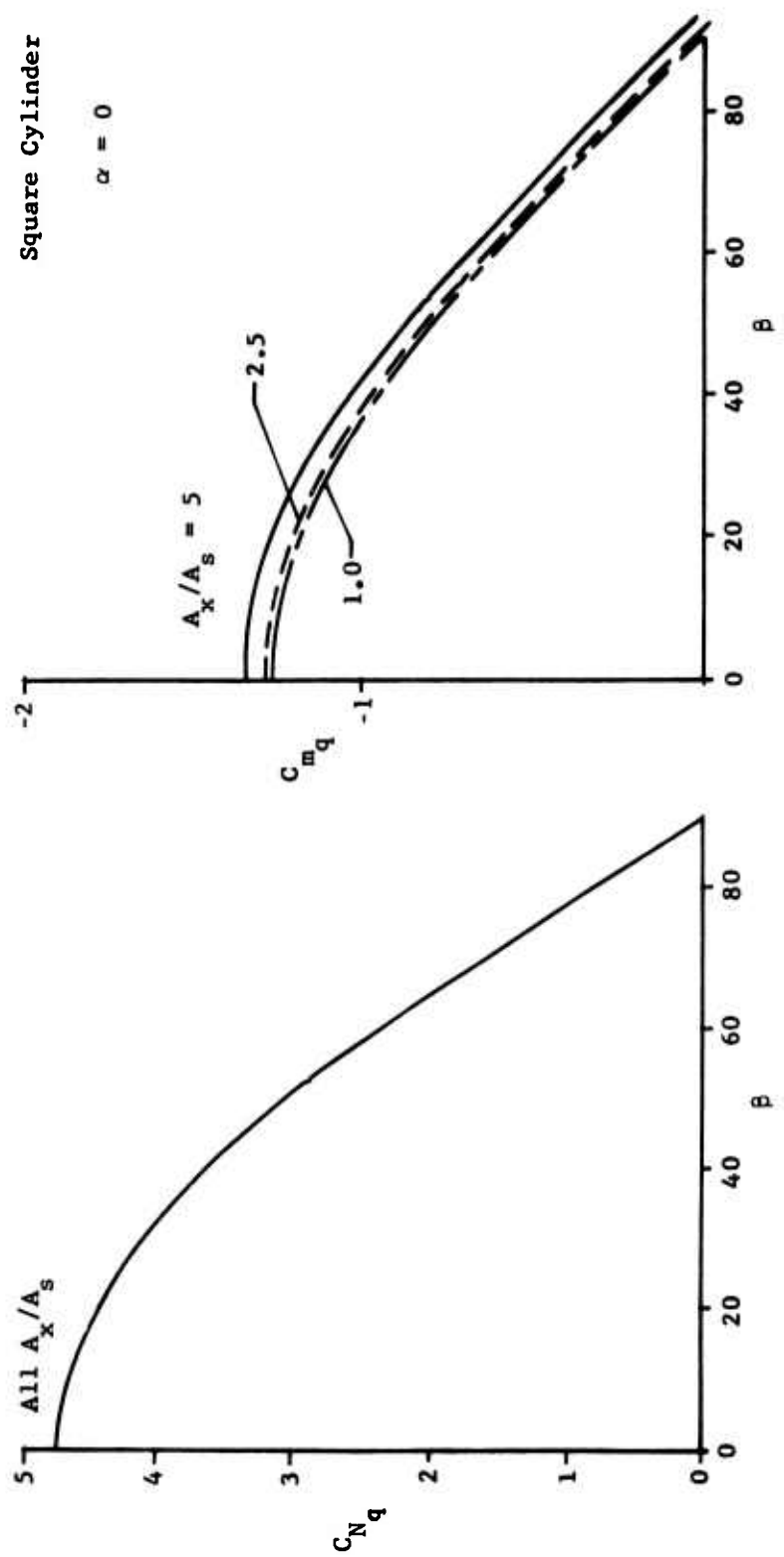


Figure 71. C_{N_q} and C_{m_q} vs β .

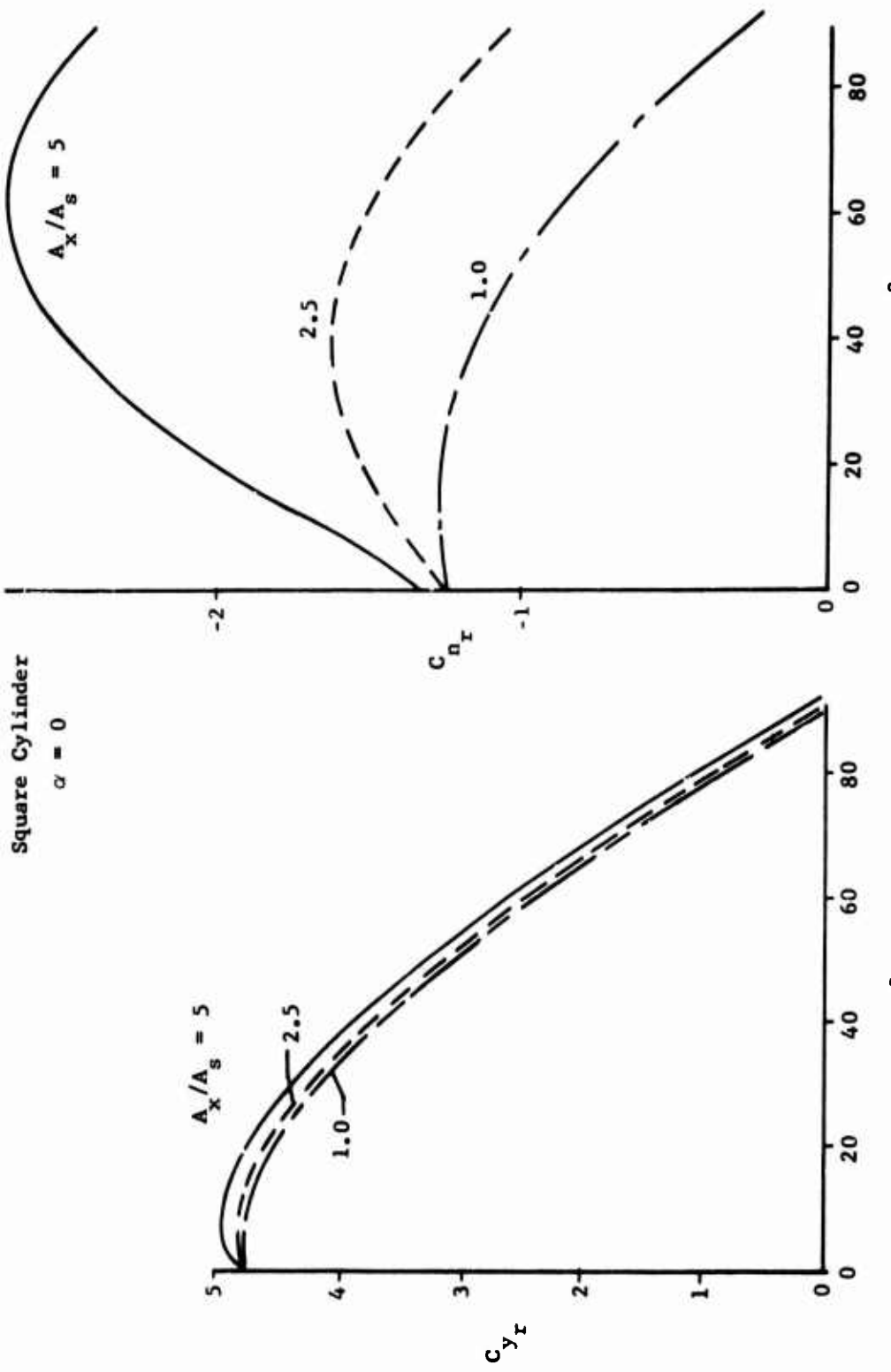


Figure 72. C_{y_r} and C_{n_r} vs β .

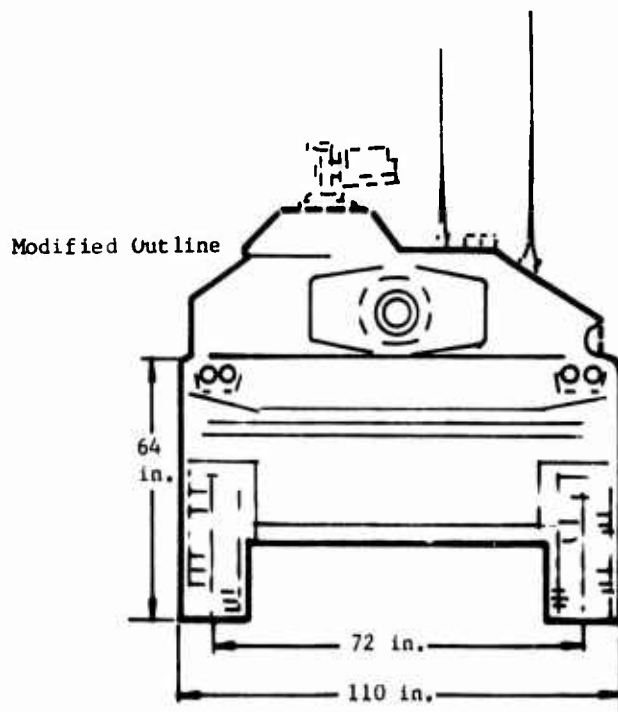
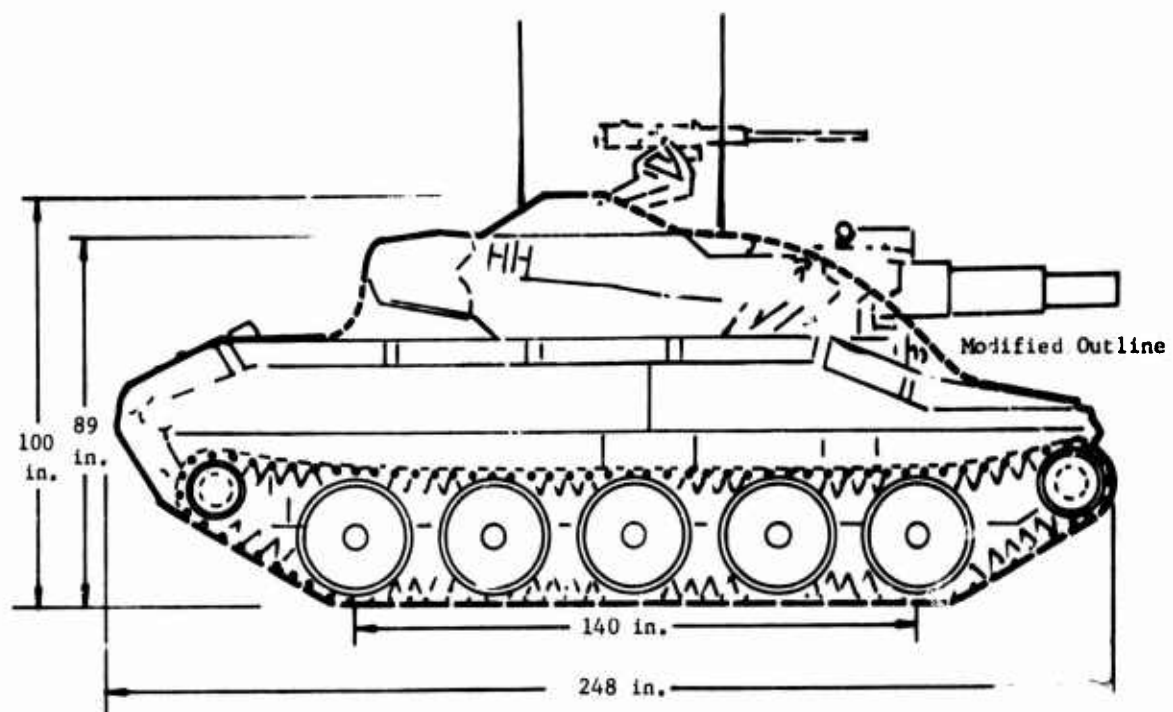


Figure 73. Armored Reconnaissance/Airborne Assault Vehicle, M-551.

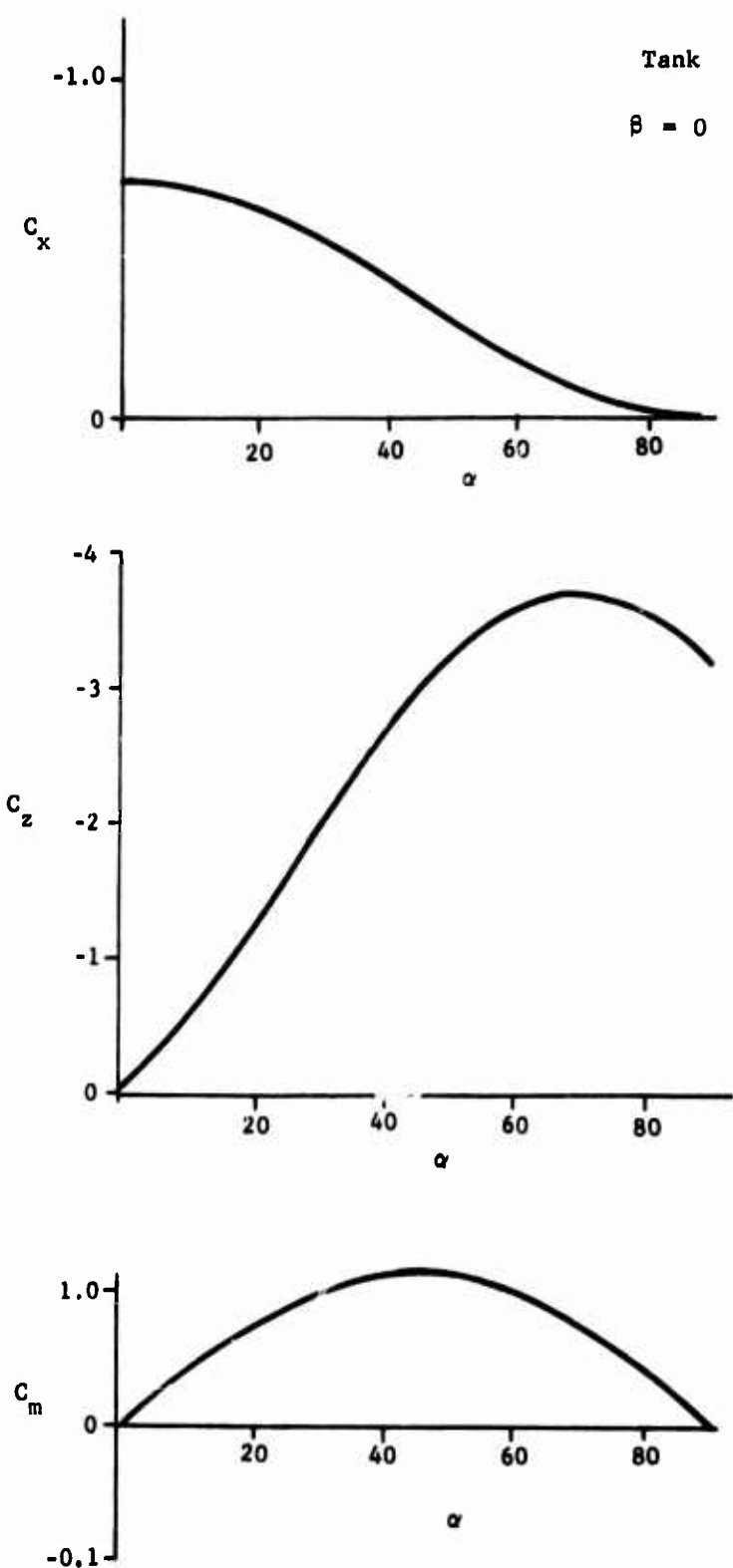


Figure 74. C_x , C_z , and C_m vs α .

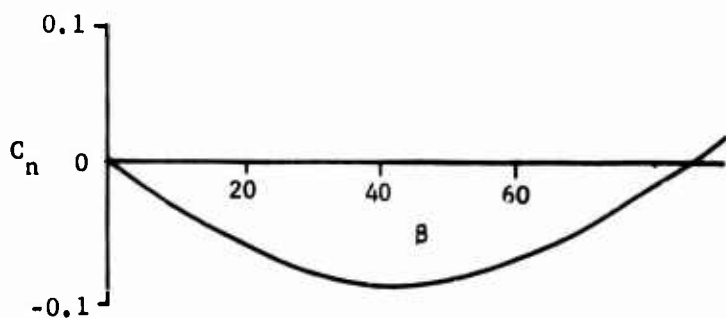
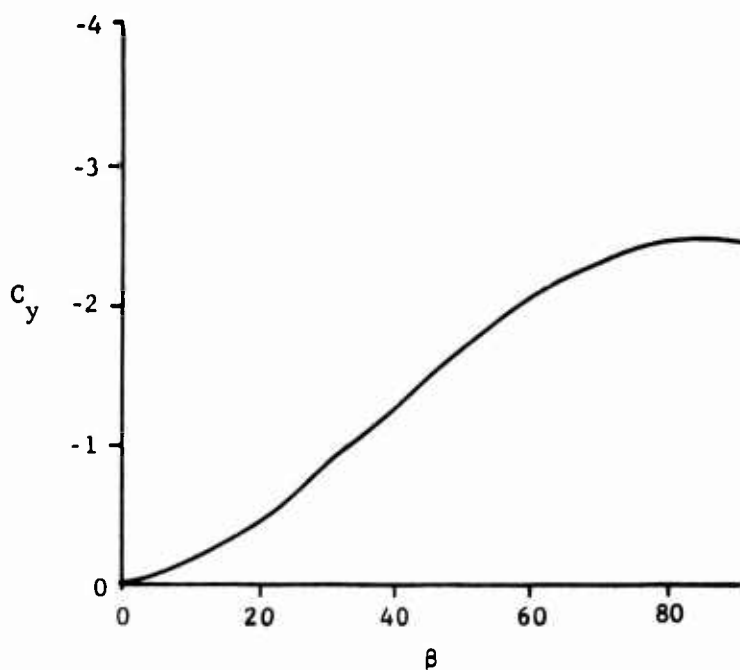
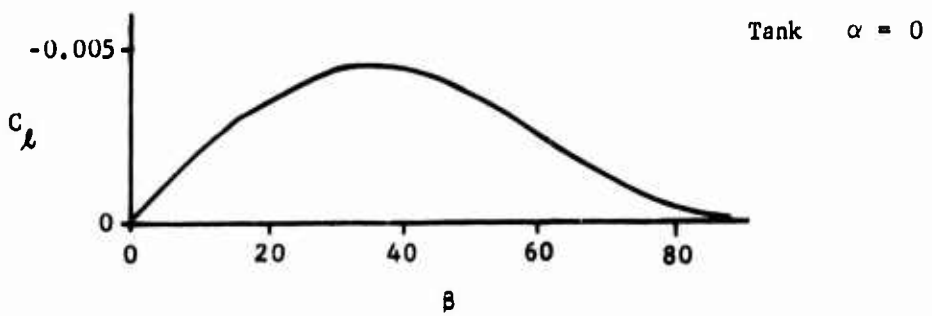
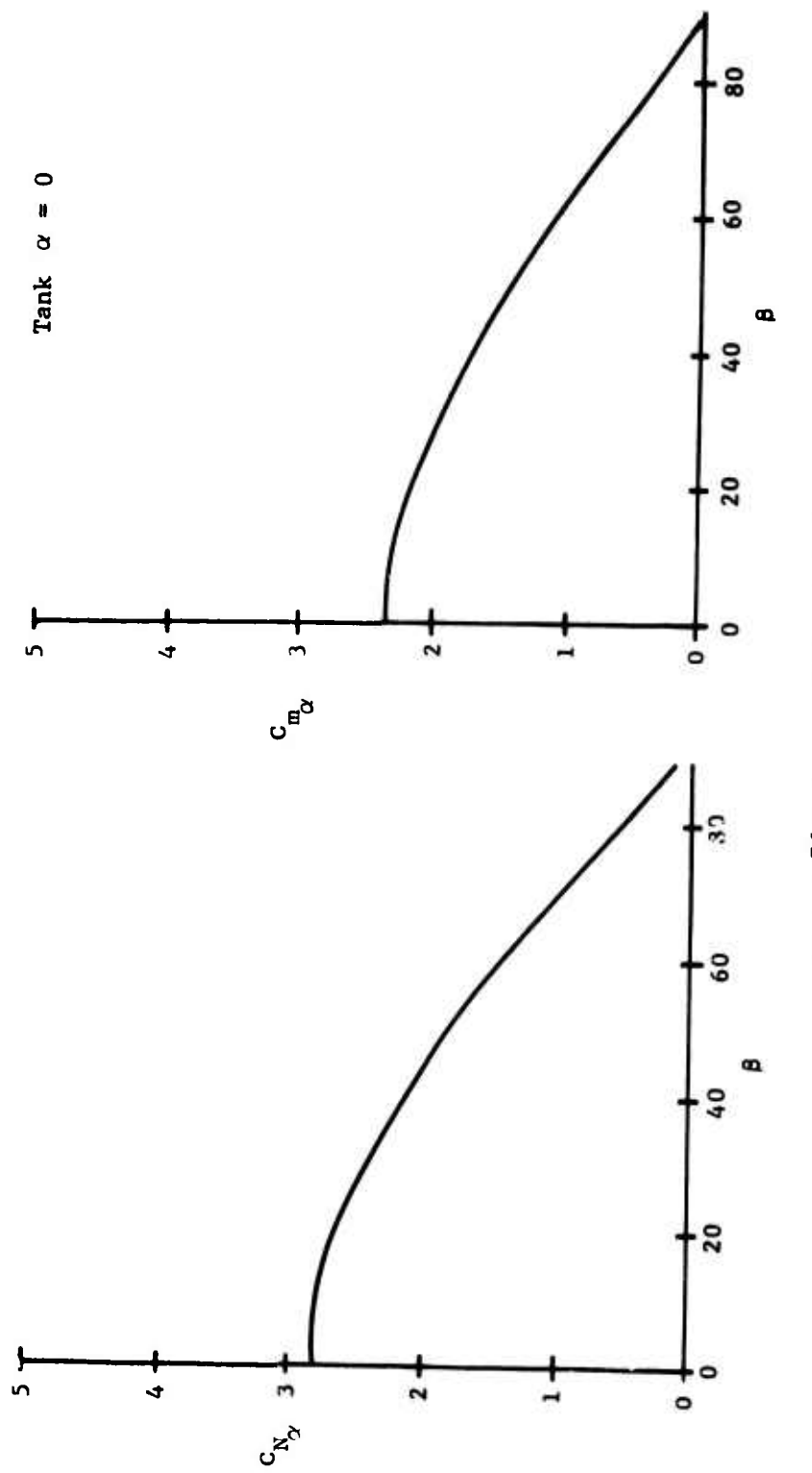


Figure 75. C_l , C_y , and C_n vs θ .



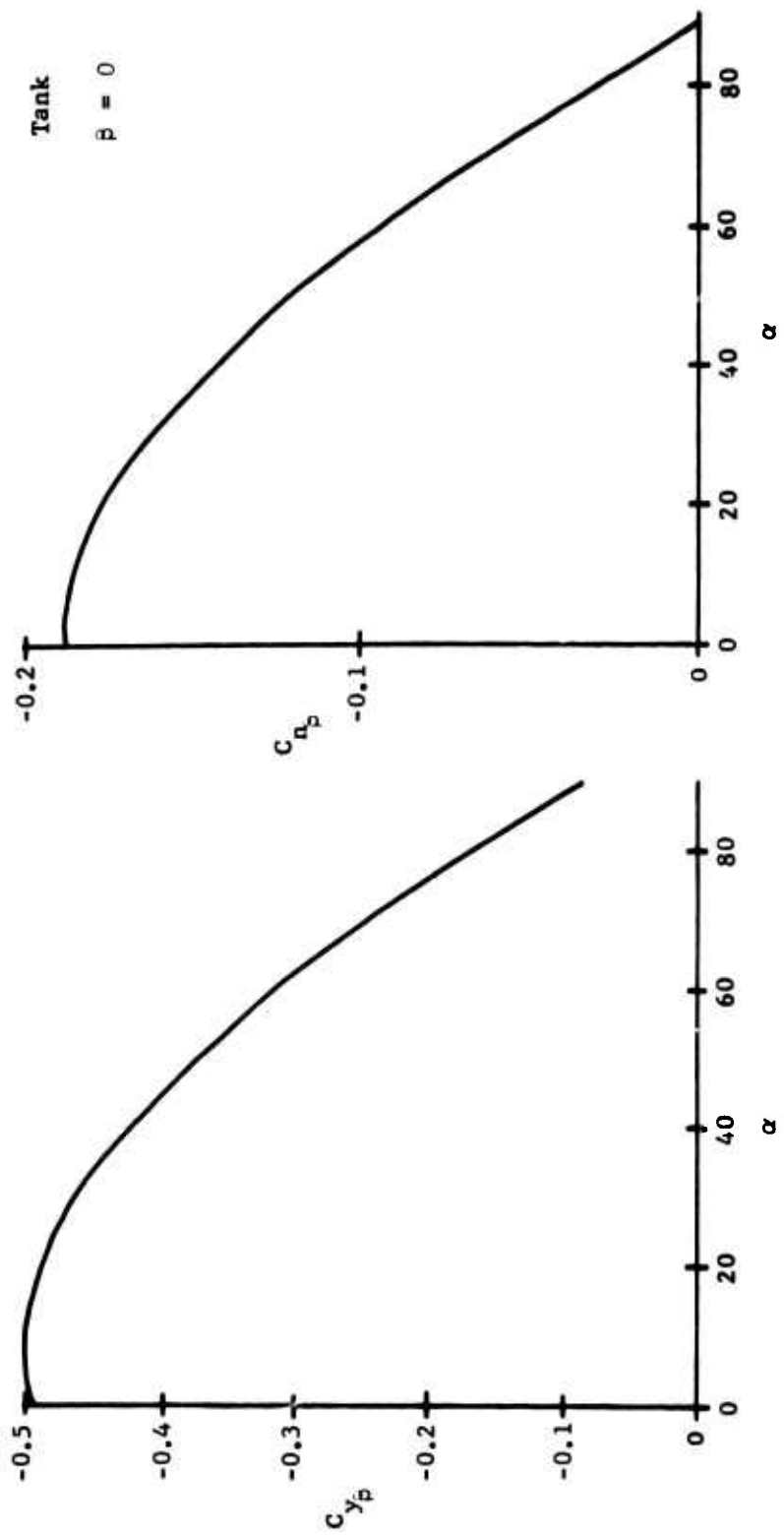


Figure 77. C_{y_p} and C_{n_p} vs α .

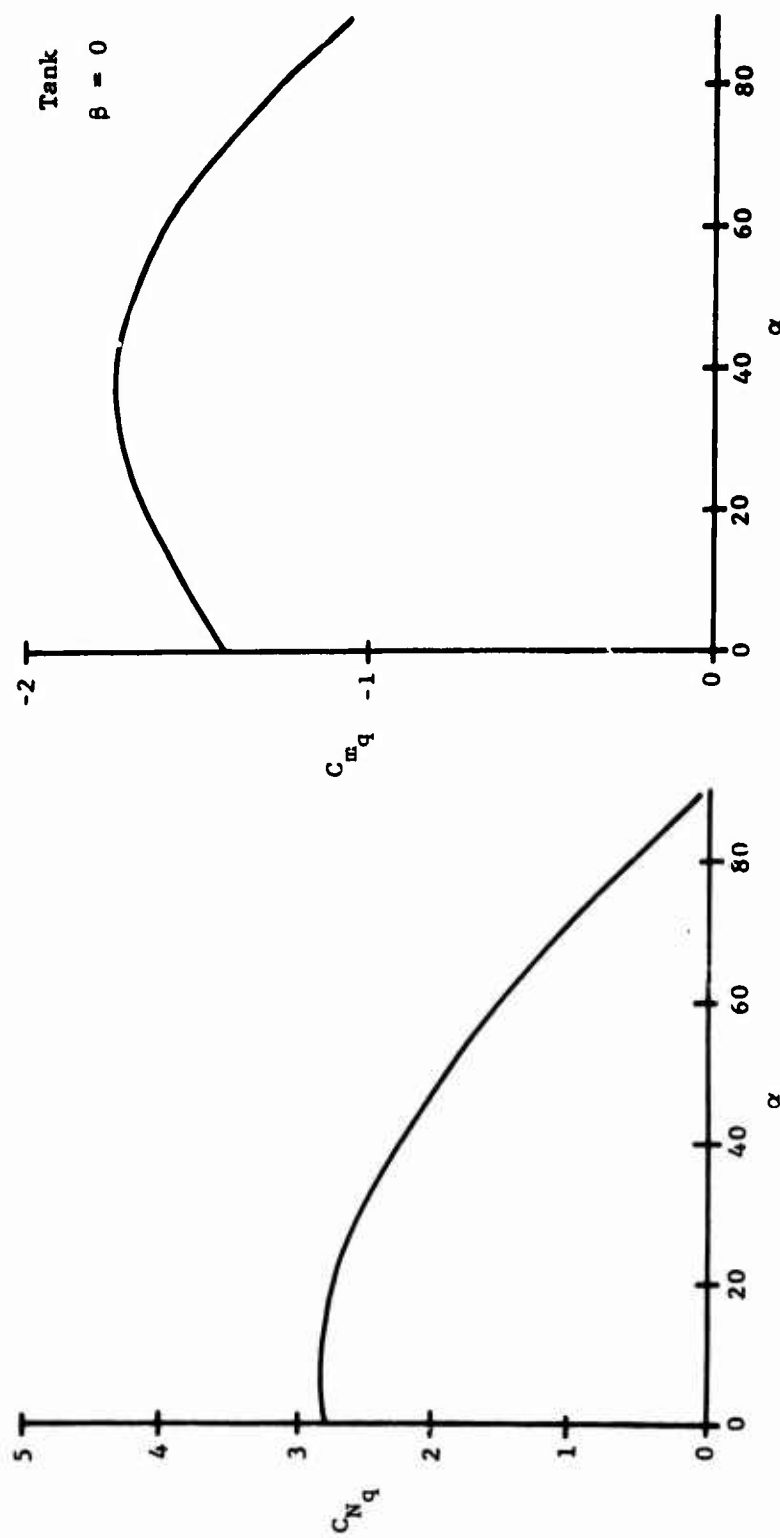


Figure 78. C_{Nq} and C_{mq} vs α .

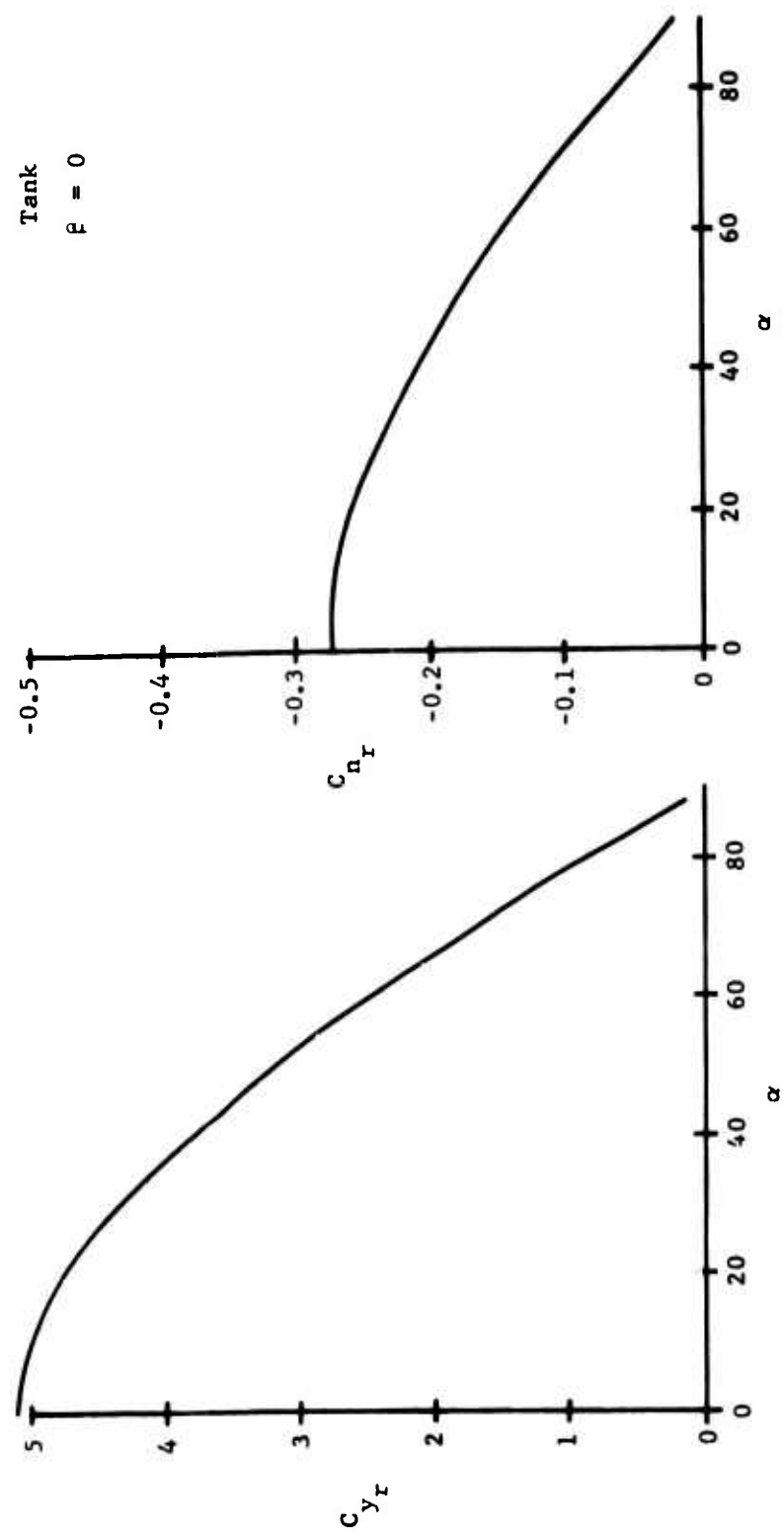
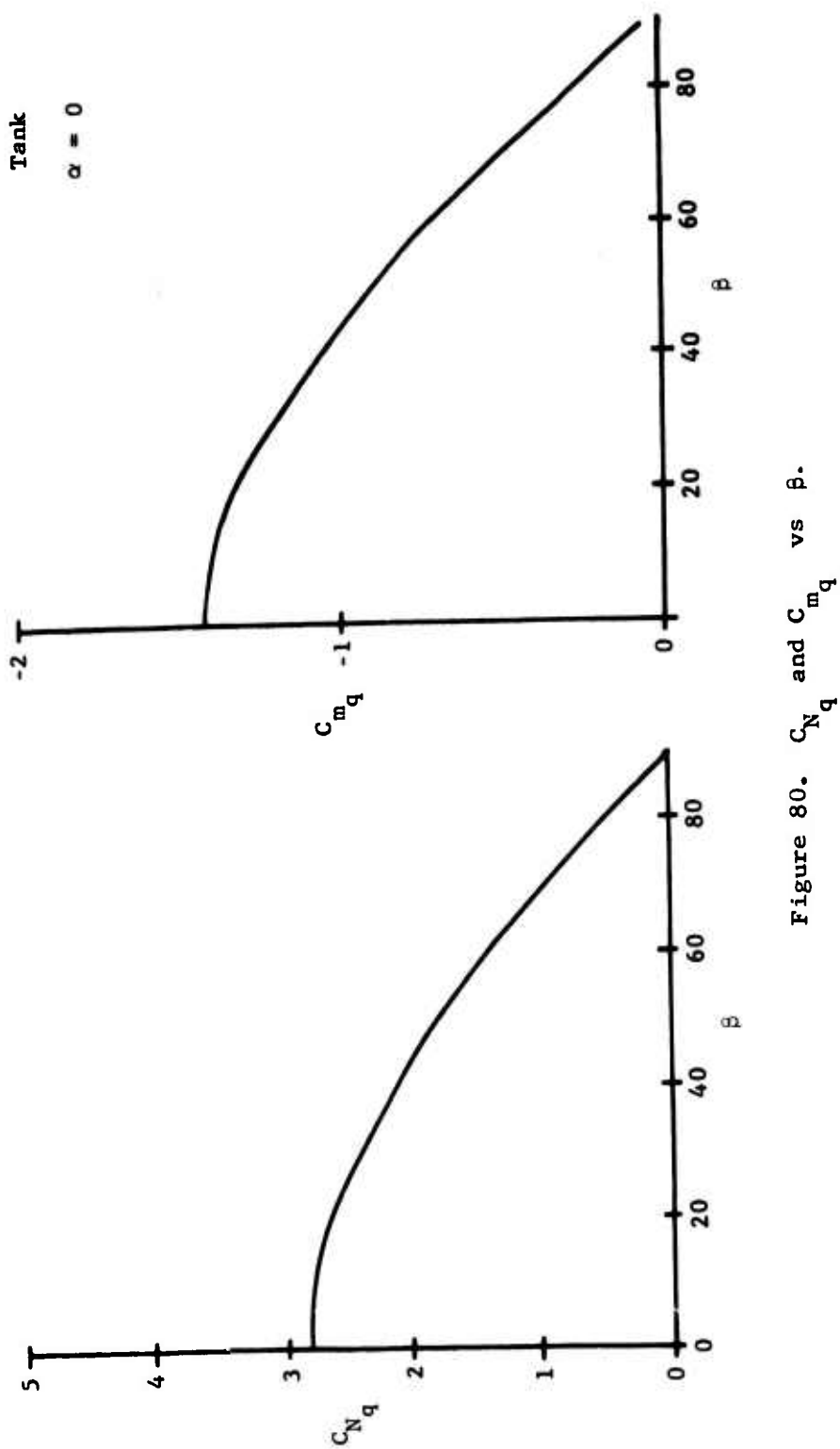


Figure 79. C_{y_r} and C_{n_r} vs α .



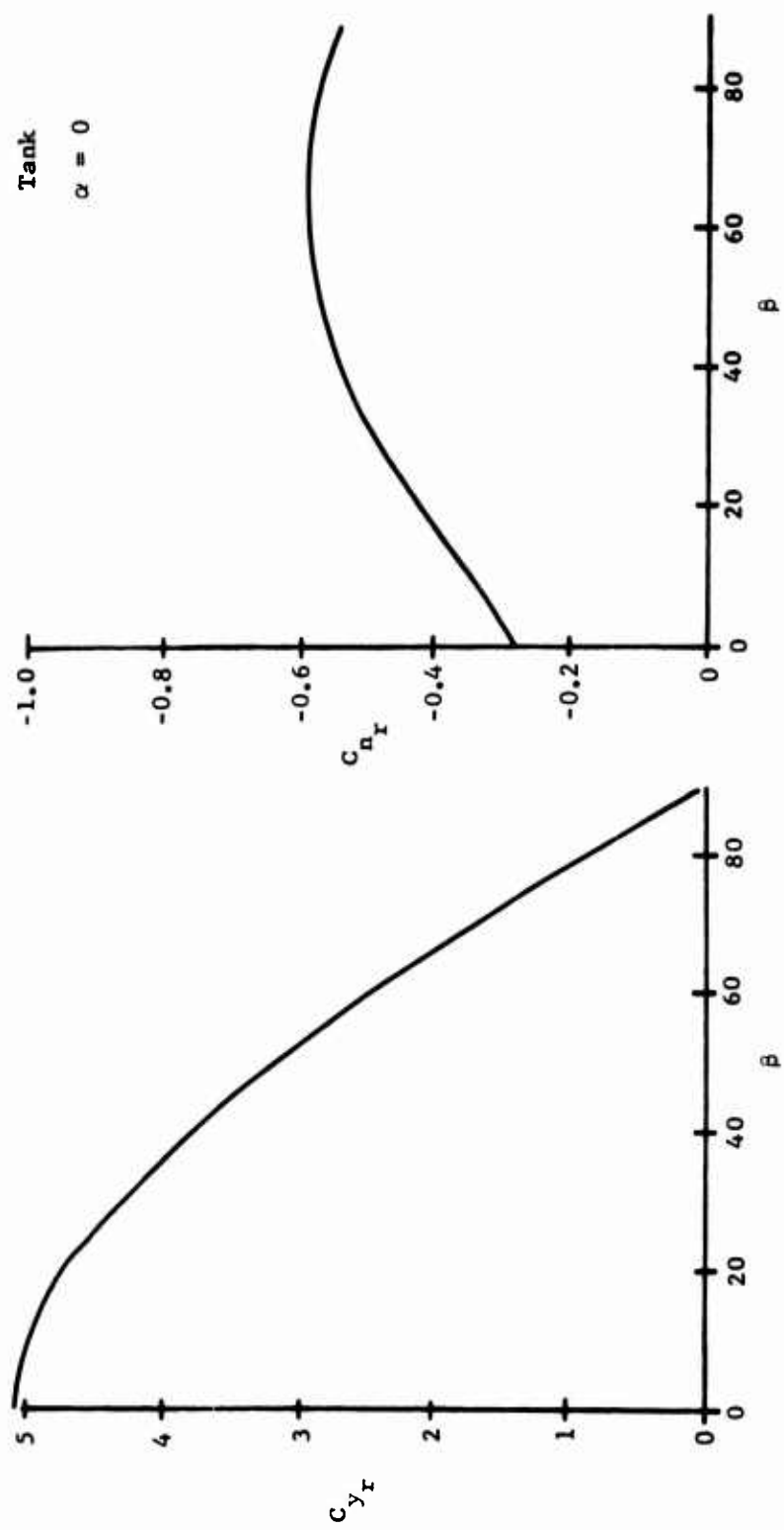


Figure 81. C_{y_r} and C_{n_r} vs β .

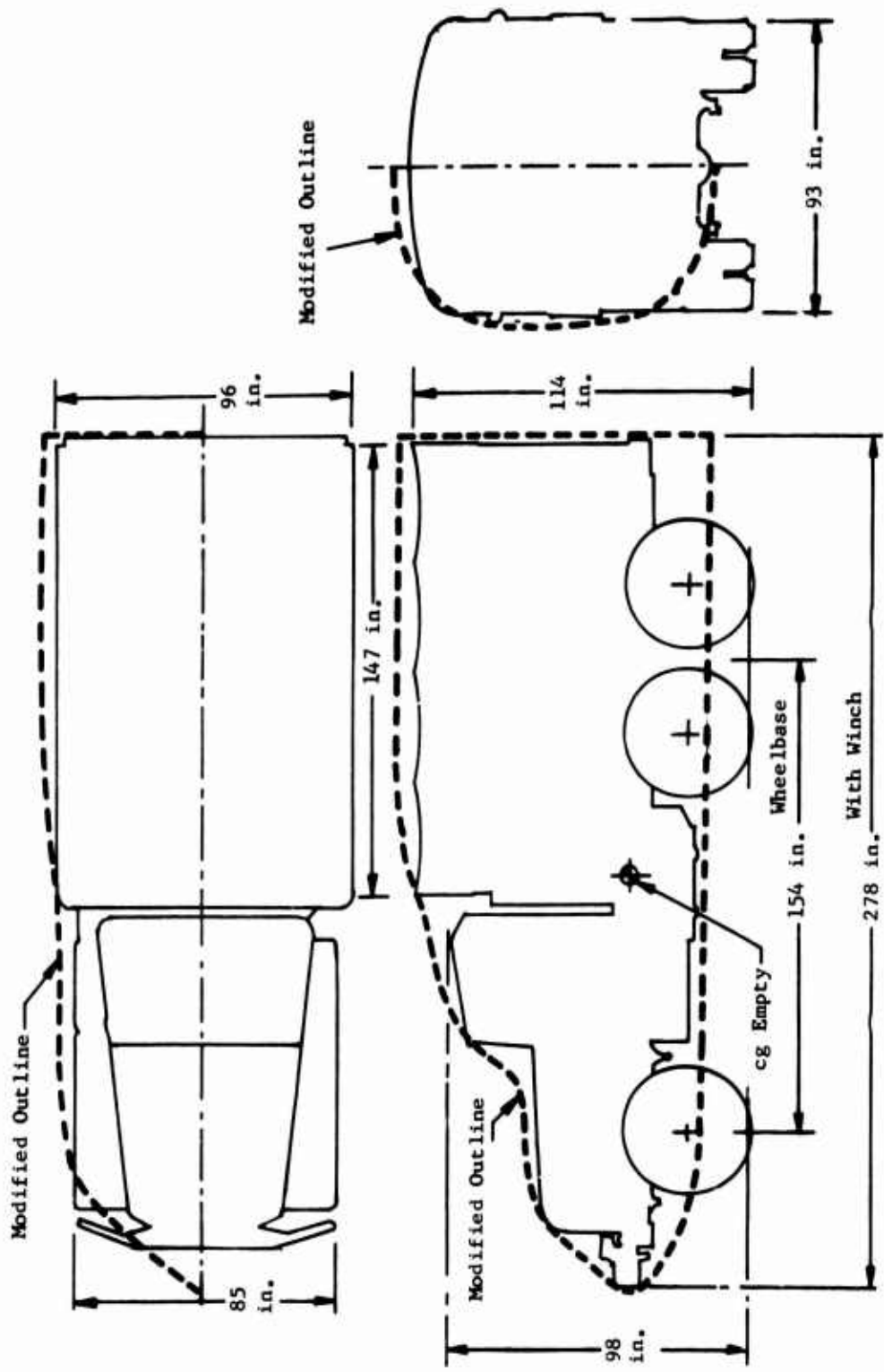


Figure 82. Truck, Cargo -- General Outline as Modified for Use in Computer Program.

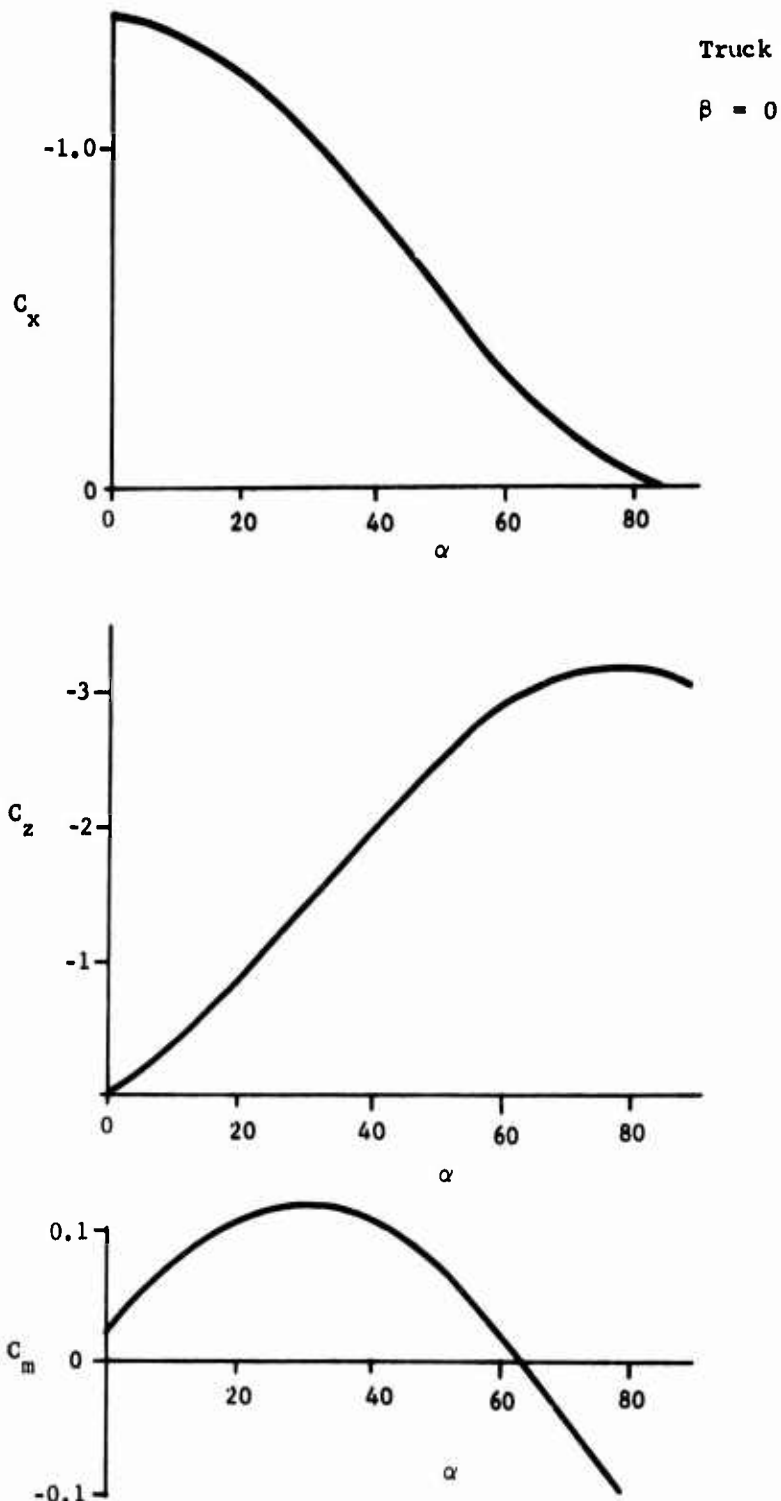


Figure 83. C_x , C_z , and C_m vs α .

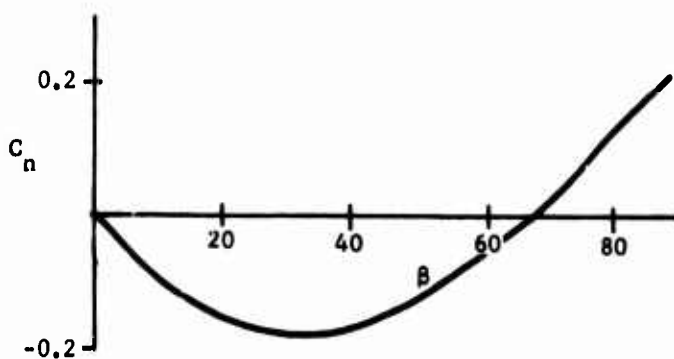
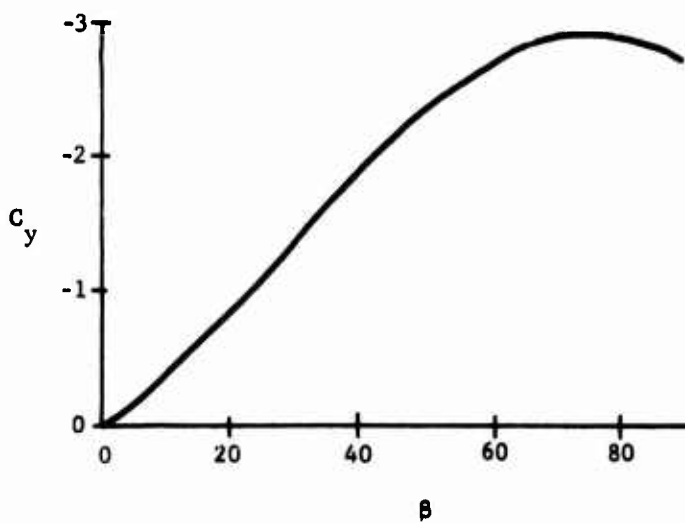
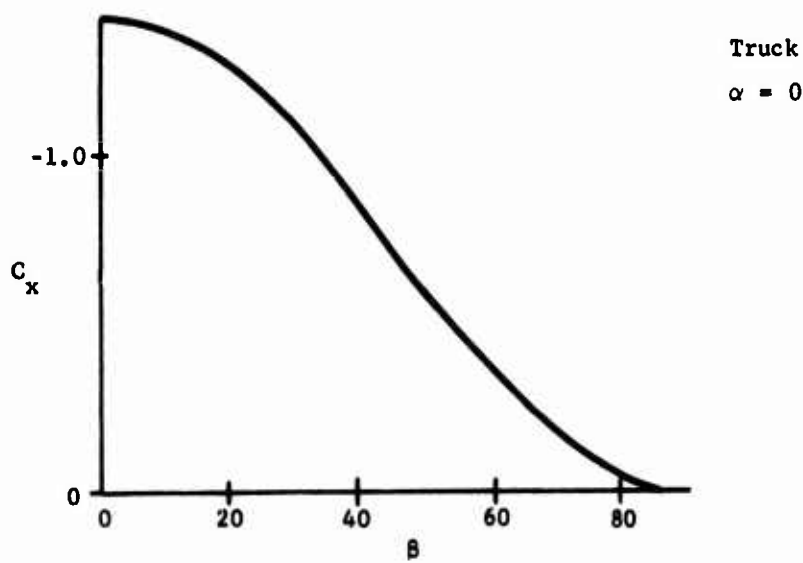


Figure 84. C_x , C_y , and C_n vs β .

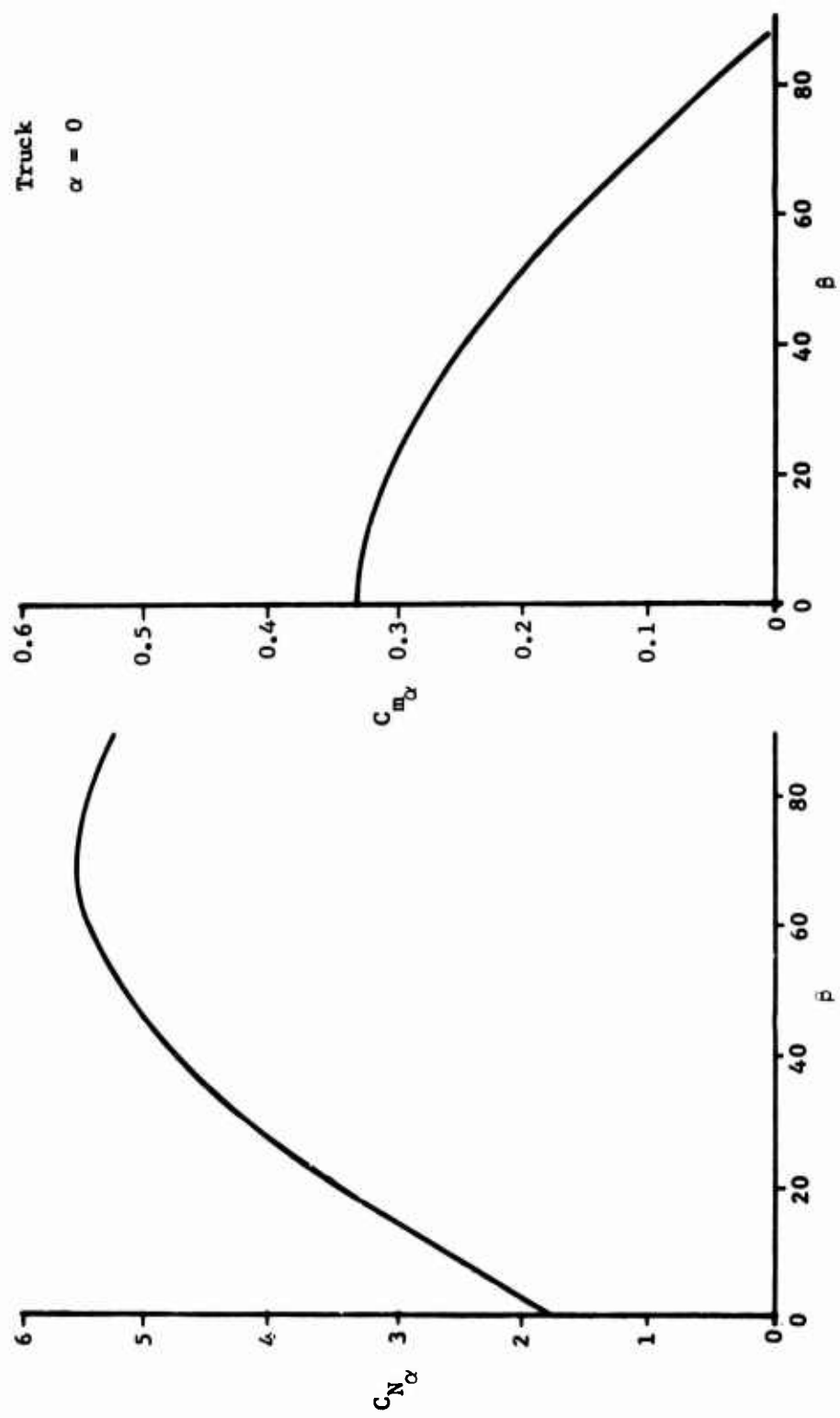


Figure 85. $C_{N\alpha}$ and $C_{m\alpha}$ vs β .

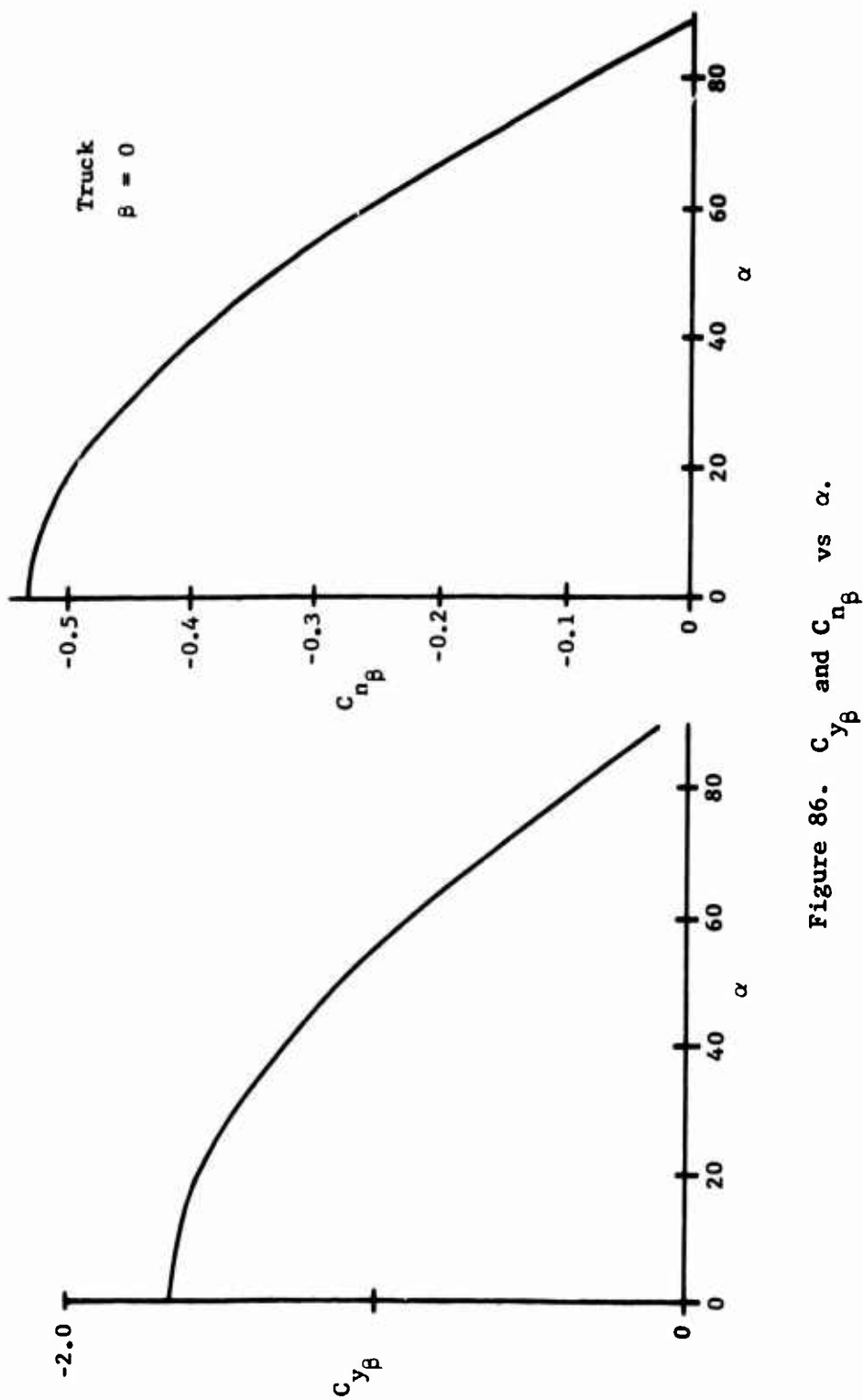


Figure 86. $C_{n\beta}$ and $C_{y\beta}$ vs α .

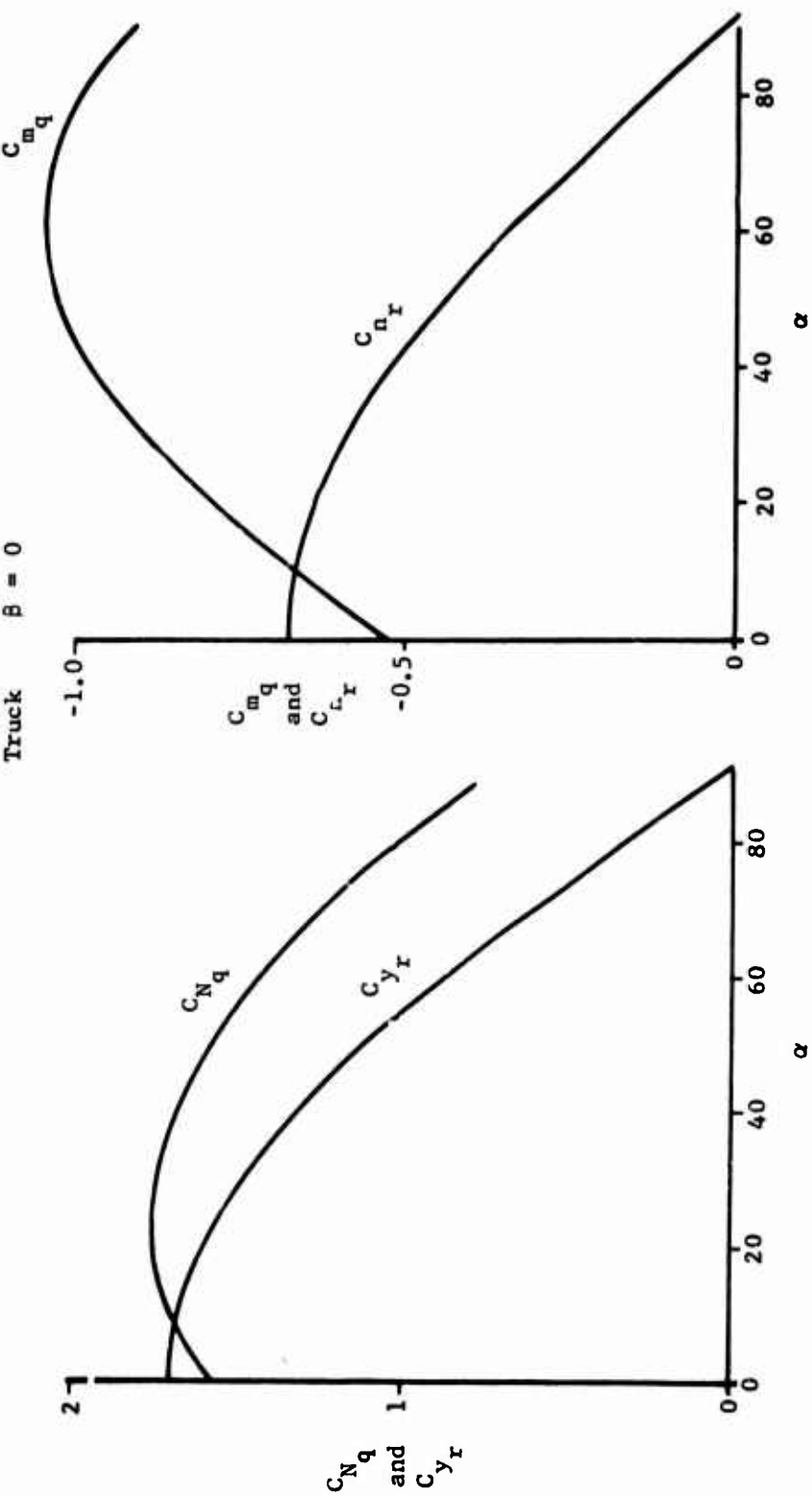


Figure 87. C_{N_q} , C_{y_r} , C_{m_q} , and C_{n_r} vs α .

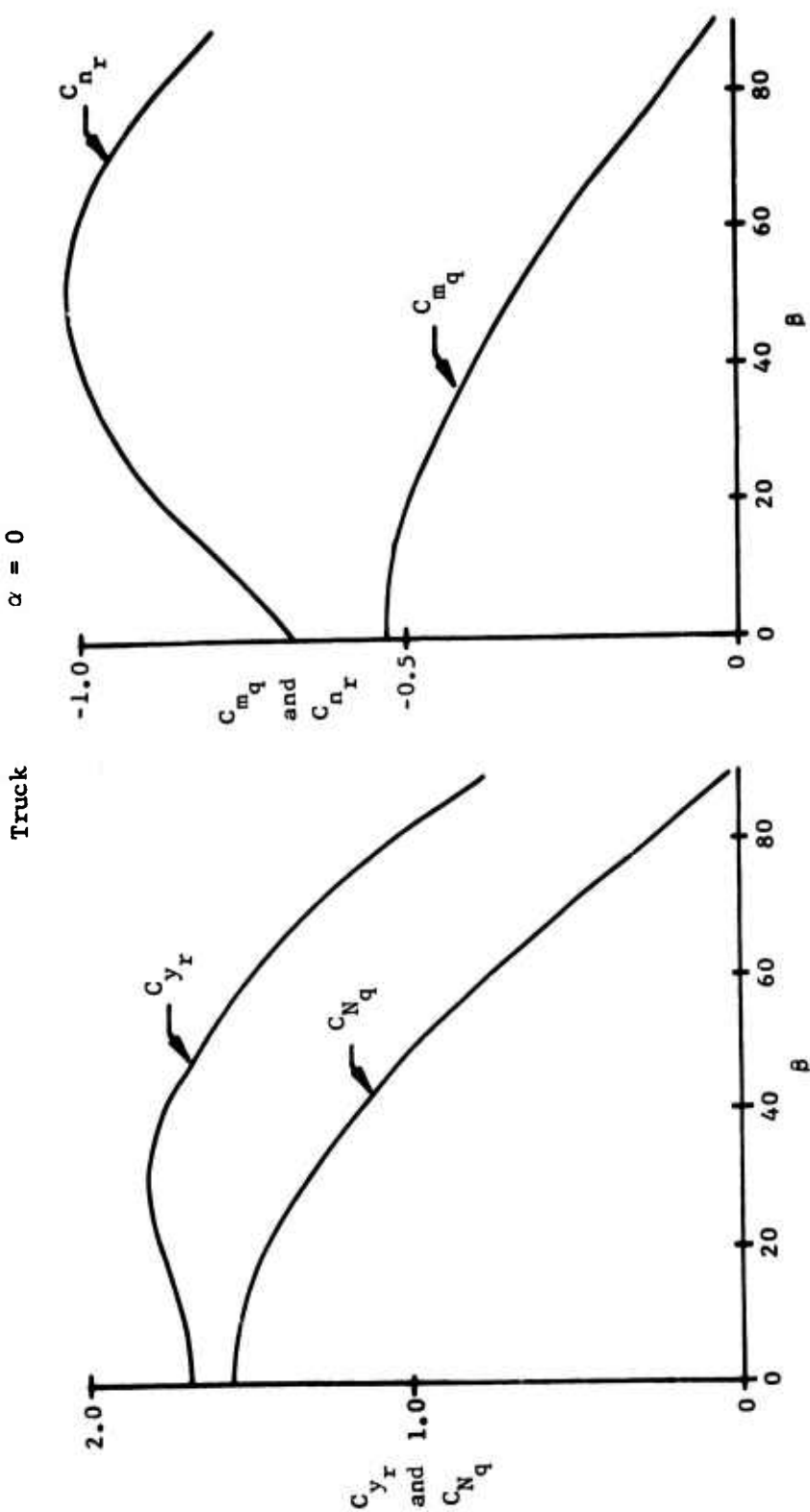


Figure 88. C_{Nq} , C_{yr} , C_{mq} , and C_{nr} vs β .

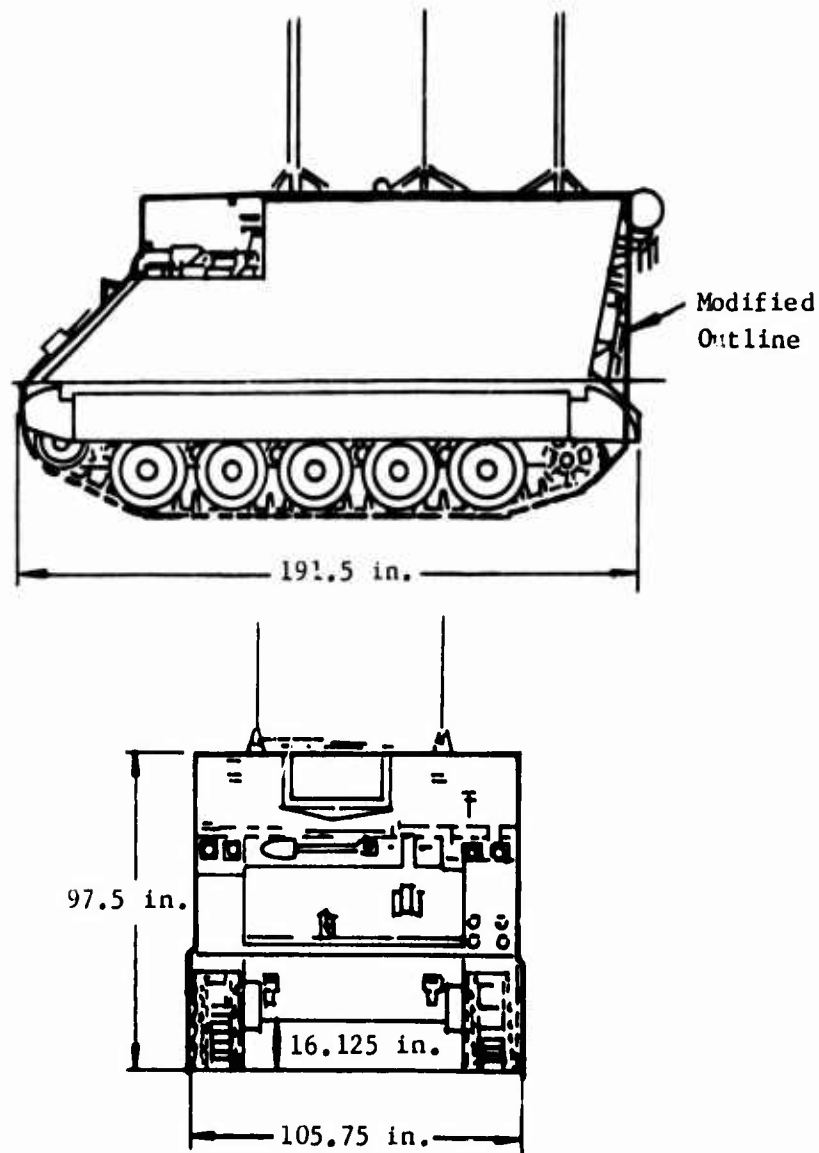


Figure 89. Command Post Carrier.

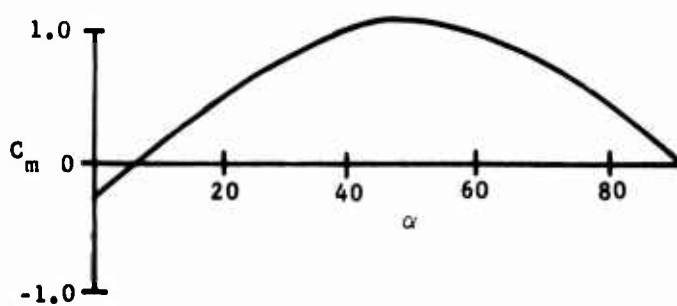
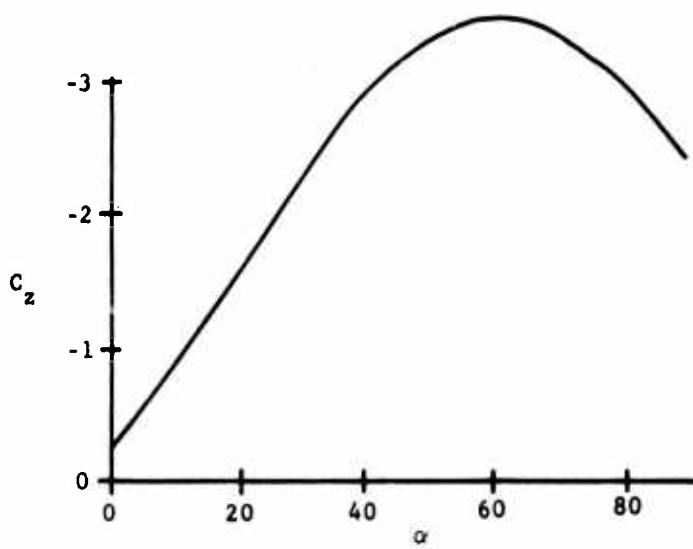
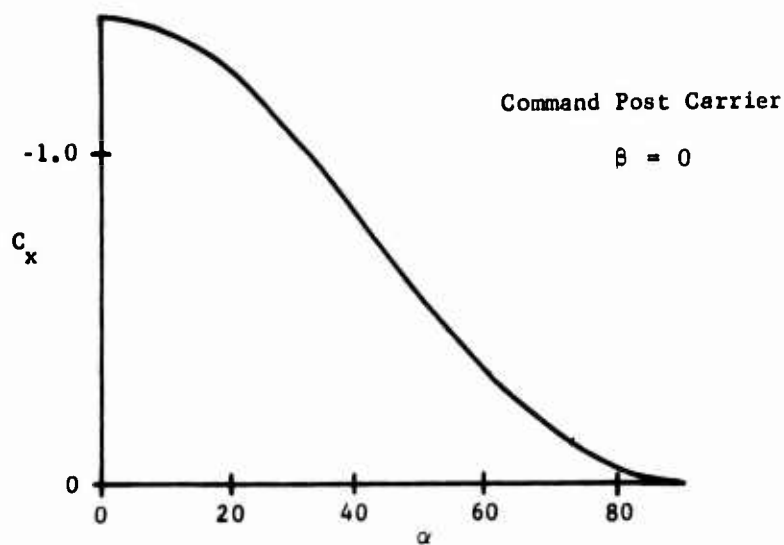


Figure 90. C_x , C_z , and C_m vs α .

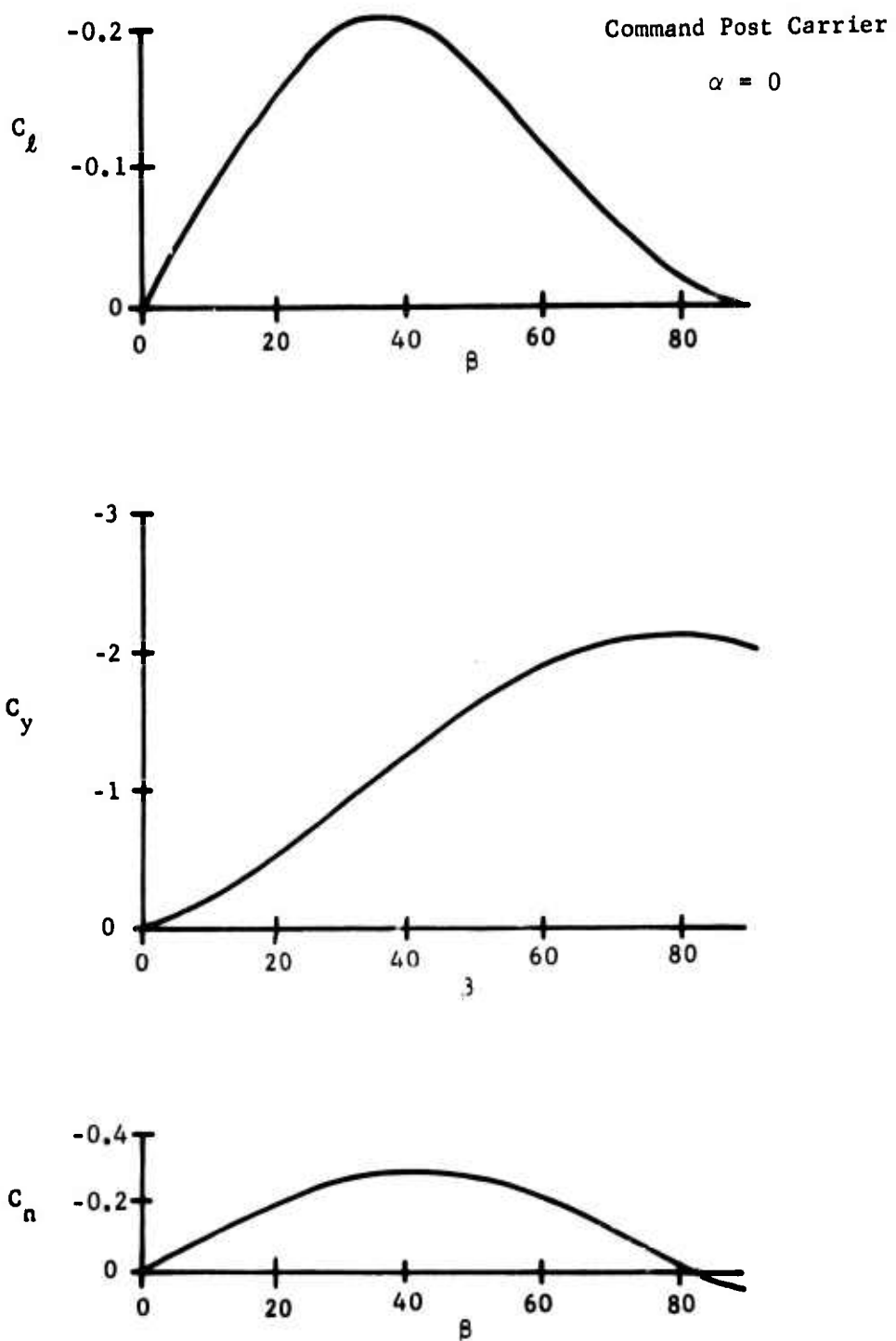


Figure 91. C_l , C_y , and C_n vs β .

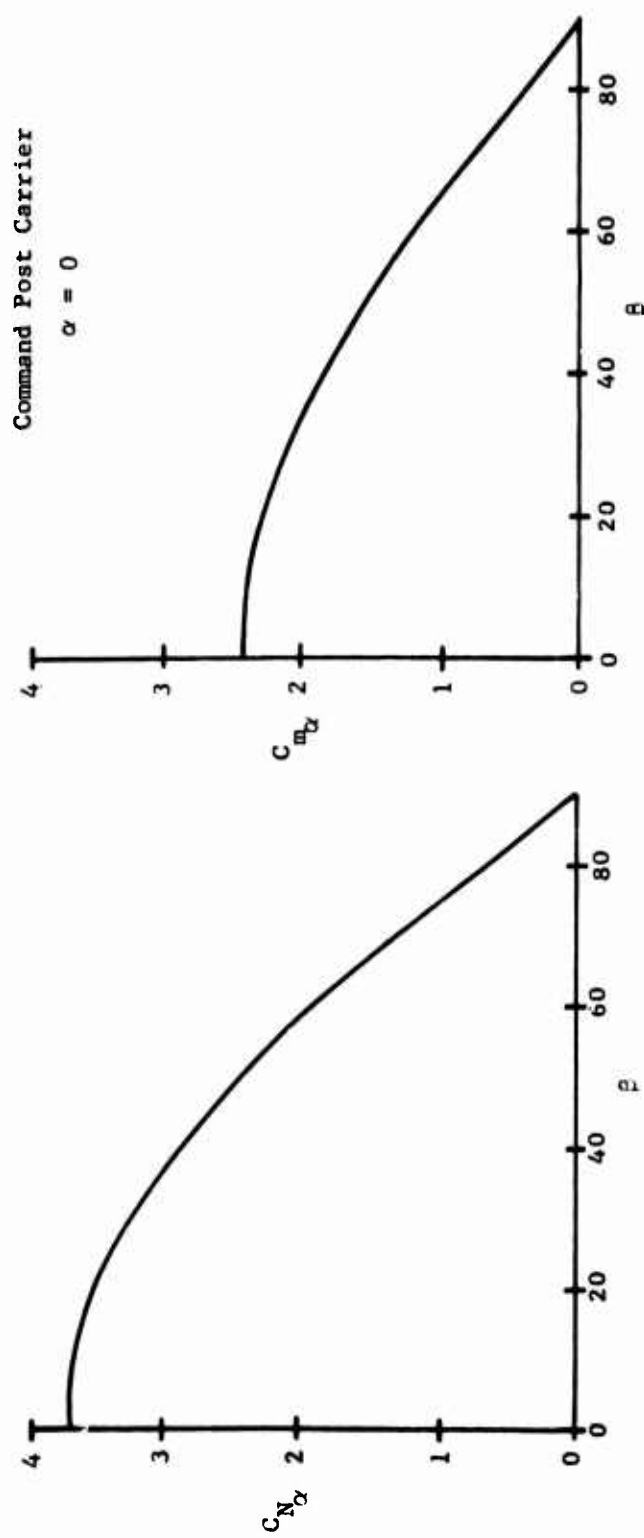


Figure 92. $C_{N\alpha}$ and $C_{m\alpha}$ vs β .

Command Post Carrier

$$\beta = 0$$

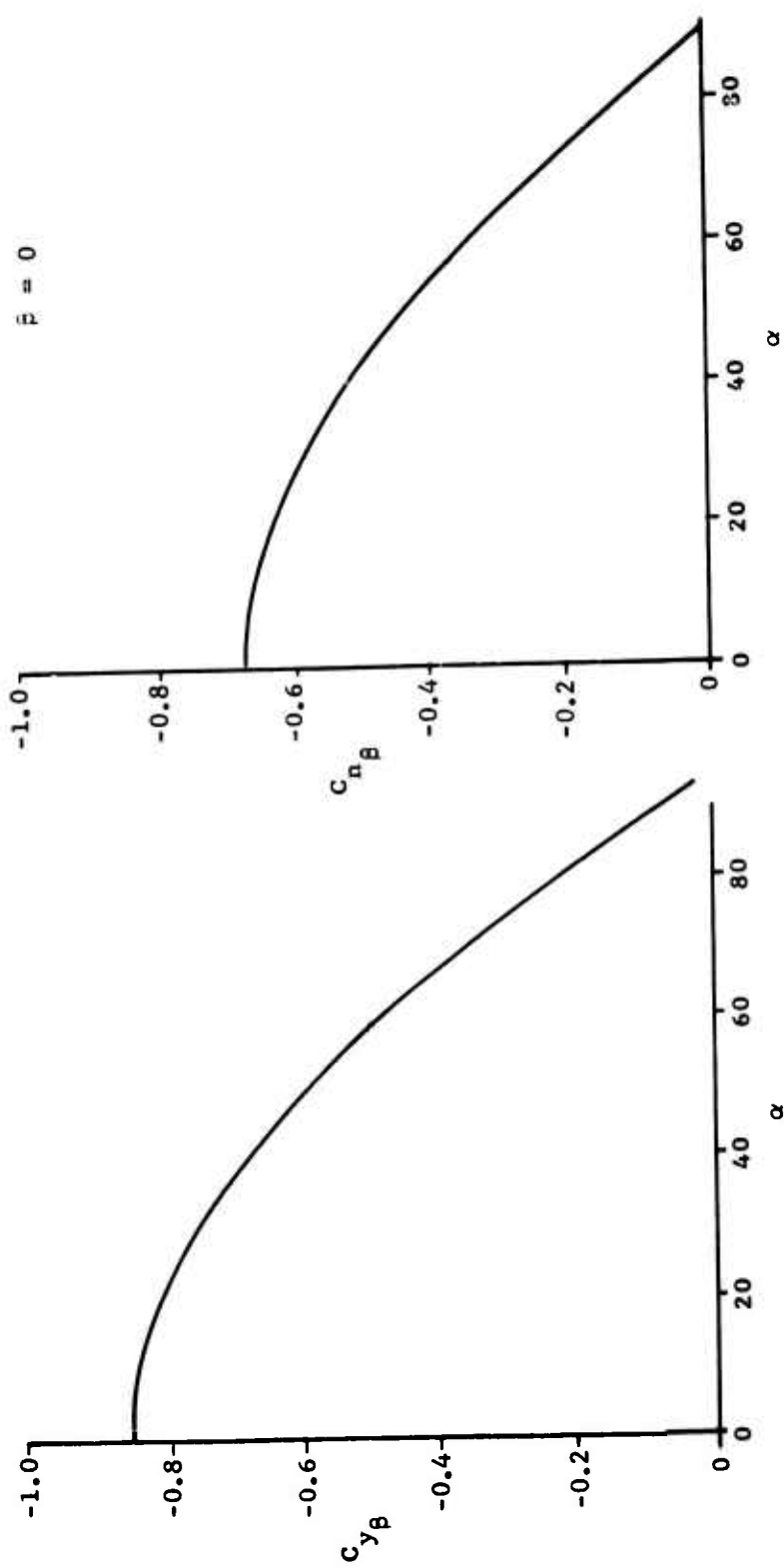


Figure 93. C_{y_B} and C_{n_B} vs α .

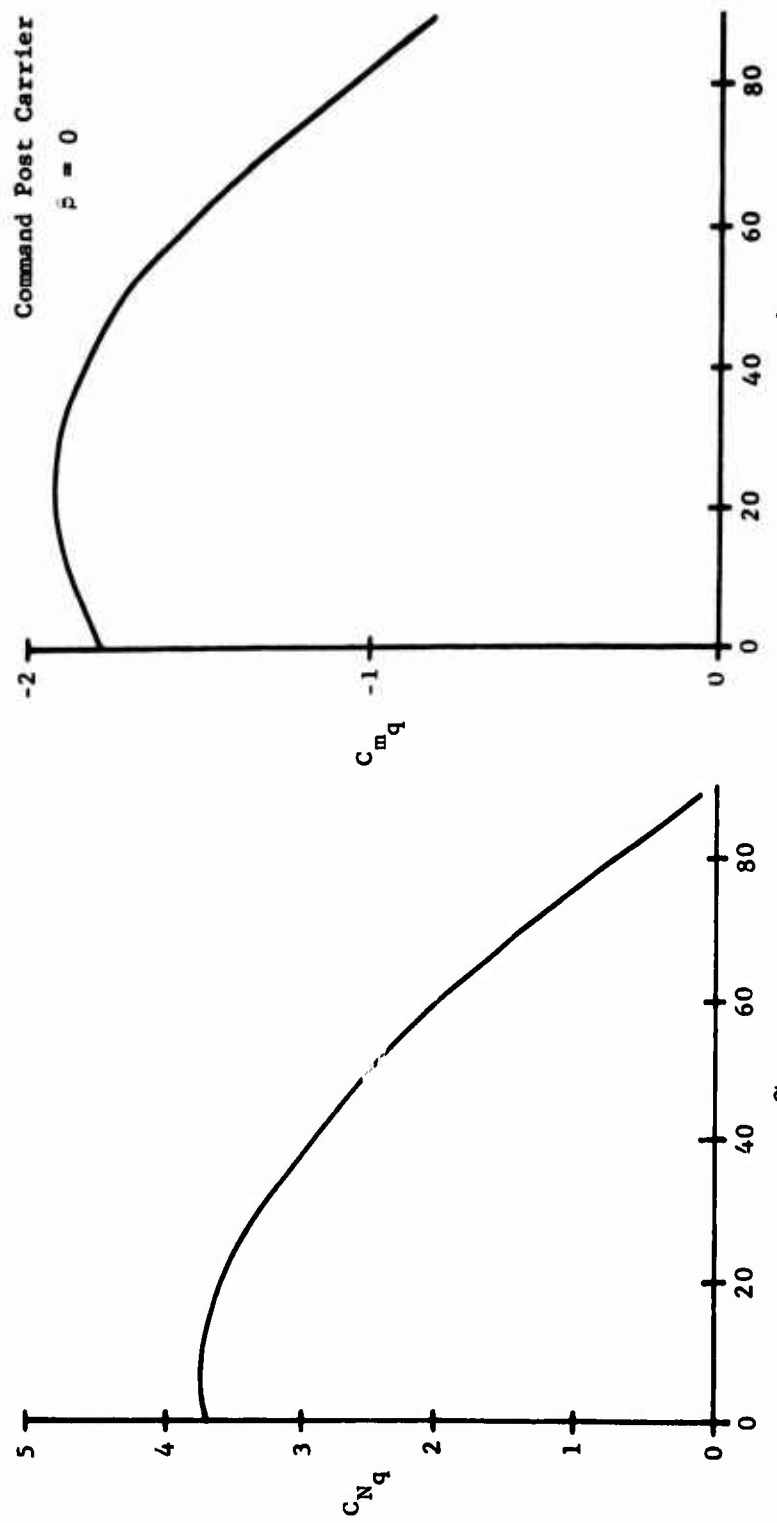


Figure 94. C_{N_q} and C_{m_q} vs α .

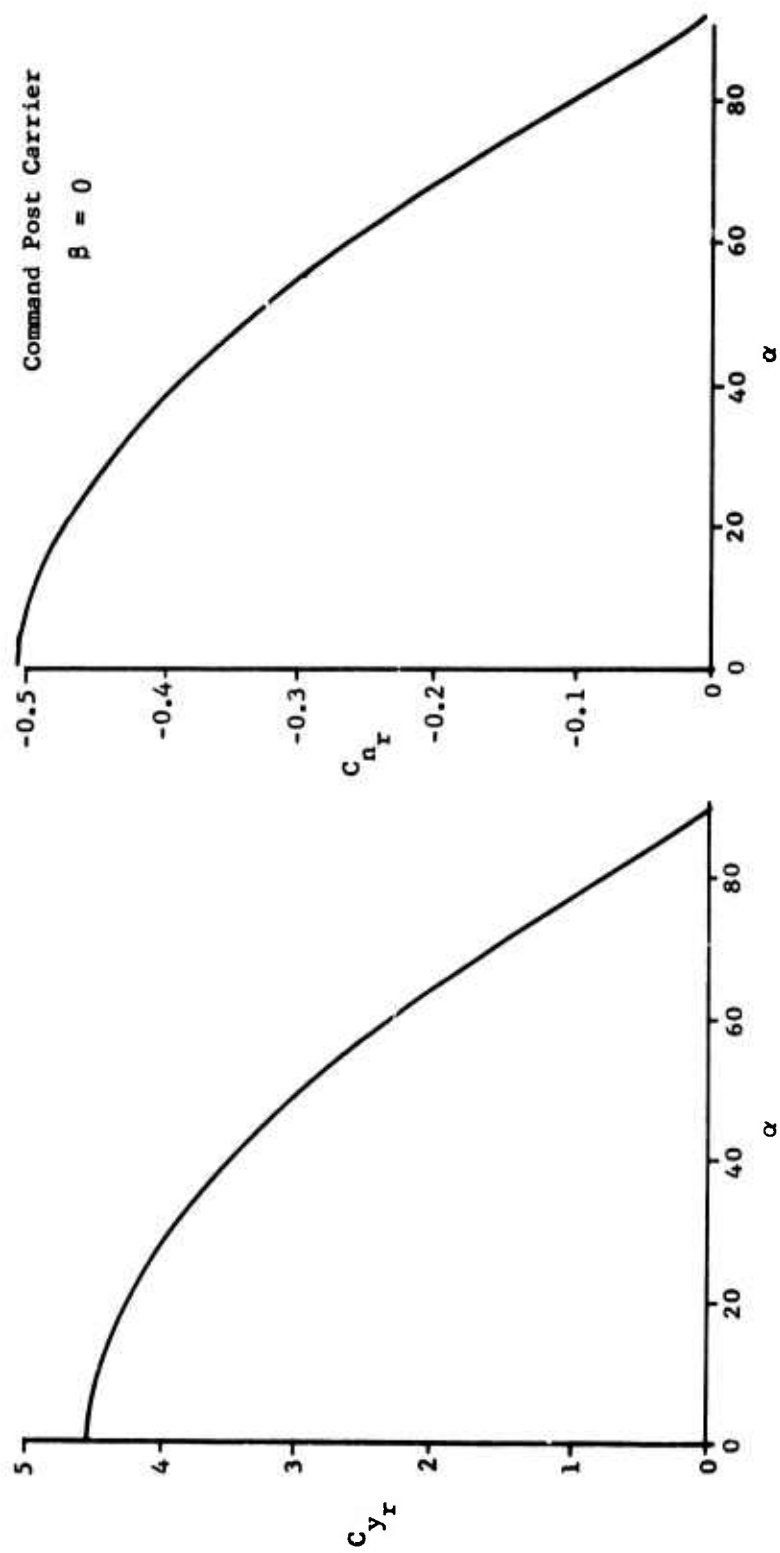


Figure 95. C_{y_r} and C_{n_r} vs α .

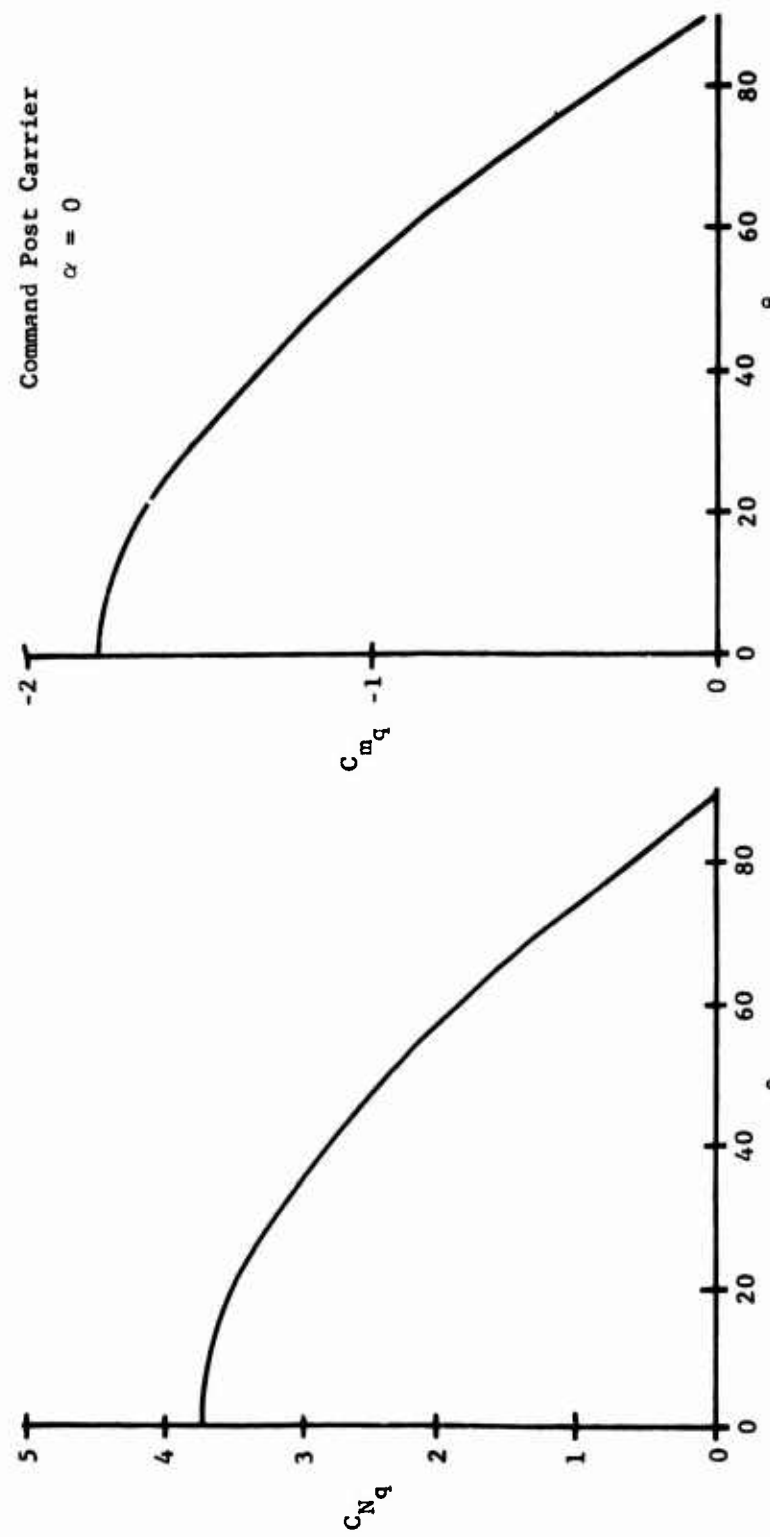


Figure 96. C_{N_q} and C_{m_q} vs β .

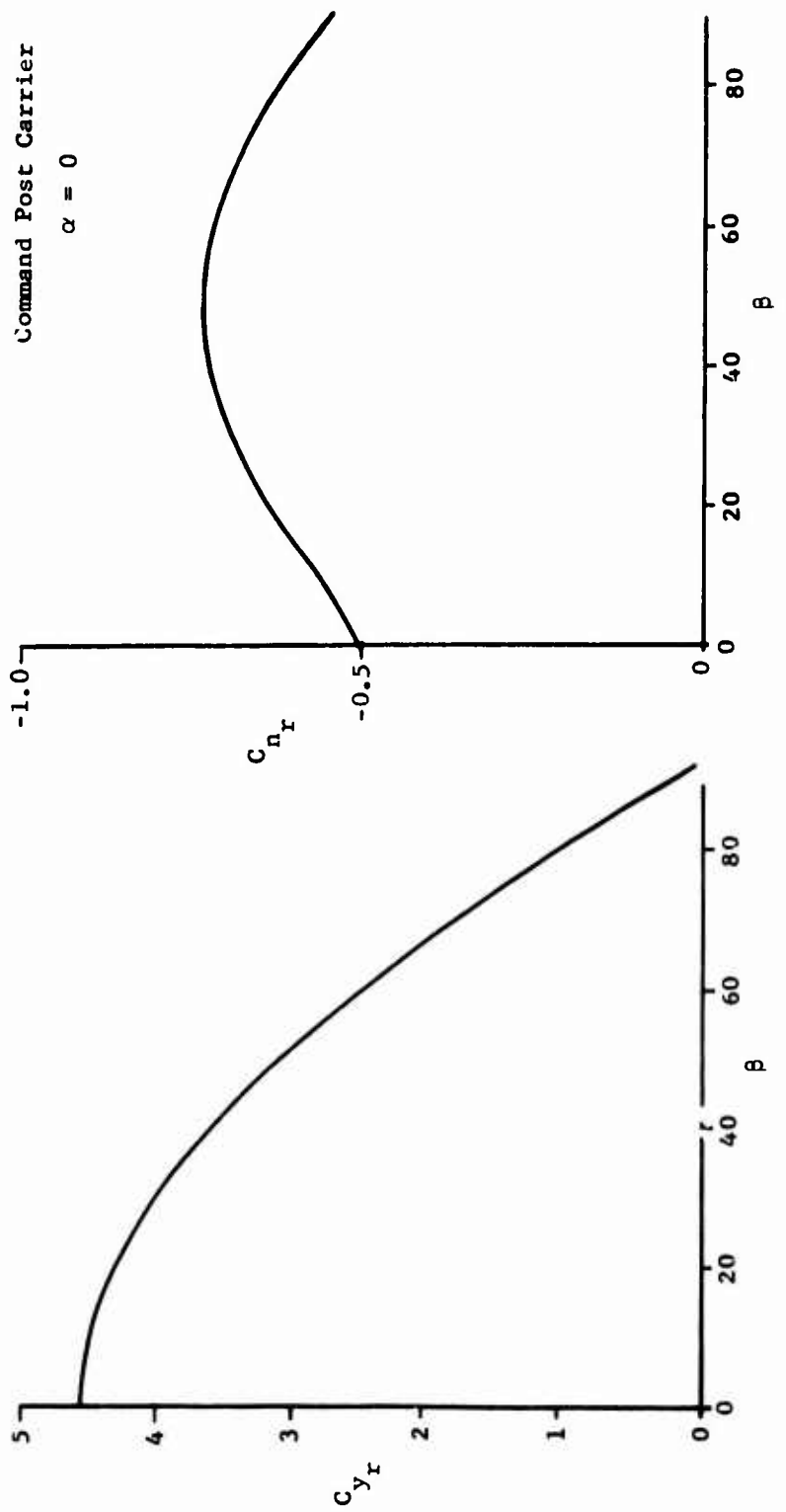


Figure 97. C_{y_r} and C_{n_r} vs β .

APPENDIX III

HELICOPTER FLIGHT SIMULATION

This appendix presents the detailed results of the helicopter flight simulation program. The following tables summarize the longitudinal, lateral, and directional runs depicted in the charts, Figures 98 through 115.

TABLE XXXI. VALUES PER LINE (LONGITUDINAL CASES)

Channel	Parameter	Value/Line
1	δ	0.1 inch
2	$\ddot{\theta}$	2.0 deg/sec ²
3	$\dot{\theta}$	0.5 deg/sec
4	θ	2.0 deg
5	\dot{U}	1.0 ft/sec ²
6	U	1.0 ft/sec
7	\dot{W}	1.0 ft/sec ²
8	W	5.0 ft/sec

All channels positive upward

Longitudinal Cases:

Figure	Run Number	Flight Speed (knots)	Longitudinal Control Inputs
98	62	50	1-inch pulse
99	57	50	1-inch step
100	48	100	1-inch pulse
101	53	100	1-inch step
102	68	150	1/2-inch pulse
103	72	150	1/2-inch step

TABLE XXXII. VALUES PER LINE (LATERAL AND DIRECTIONAL)

Channel	Parameter	Value/Line
1	δ_{LAT}	0.1 inch
2	δ_{RUD}	0.1 inch
3	$\dot{\psi}$	1.2 deg/sec ²
4	$\dot{\phi}$	1.0 deg/sec
5	$\dot{\psi}$	1.0 deg
6	$\ddot{\psi}$	1.0 deg/sec ²
7	$\dot{\psi}$	1.0 deg/sec
8	ψ	1.0 deg

All channels positive upward

Lateral Cases:

<u>Figure</u>	<u>Run Number</u>	<u>Flight Speeds</u>	<u>Lateral Control Inputs</u>
104	96	50	1-inch pulse
105	104	50	1-inch step
106	94	100	1-inch pulse
107	106	100	1-inch step
108	100	150	1/2-inch pulse
109	102	150	1/2-inch step

Directional Cases:

<u>Figure</u>	<u>Run Number</u>	<u>Flight Speeds</u>	<u>Rudder Control Inputs</u>
110	97	50	1-inch pulse
111	105	50	1-inch step
112	95	100	1-inch pulse
113	107	100	1-inch step
114	101	150	1/2-inch pulse
115	103	150	1/2-inch step

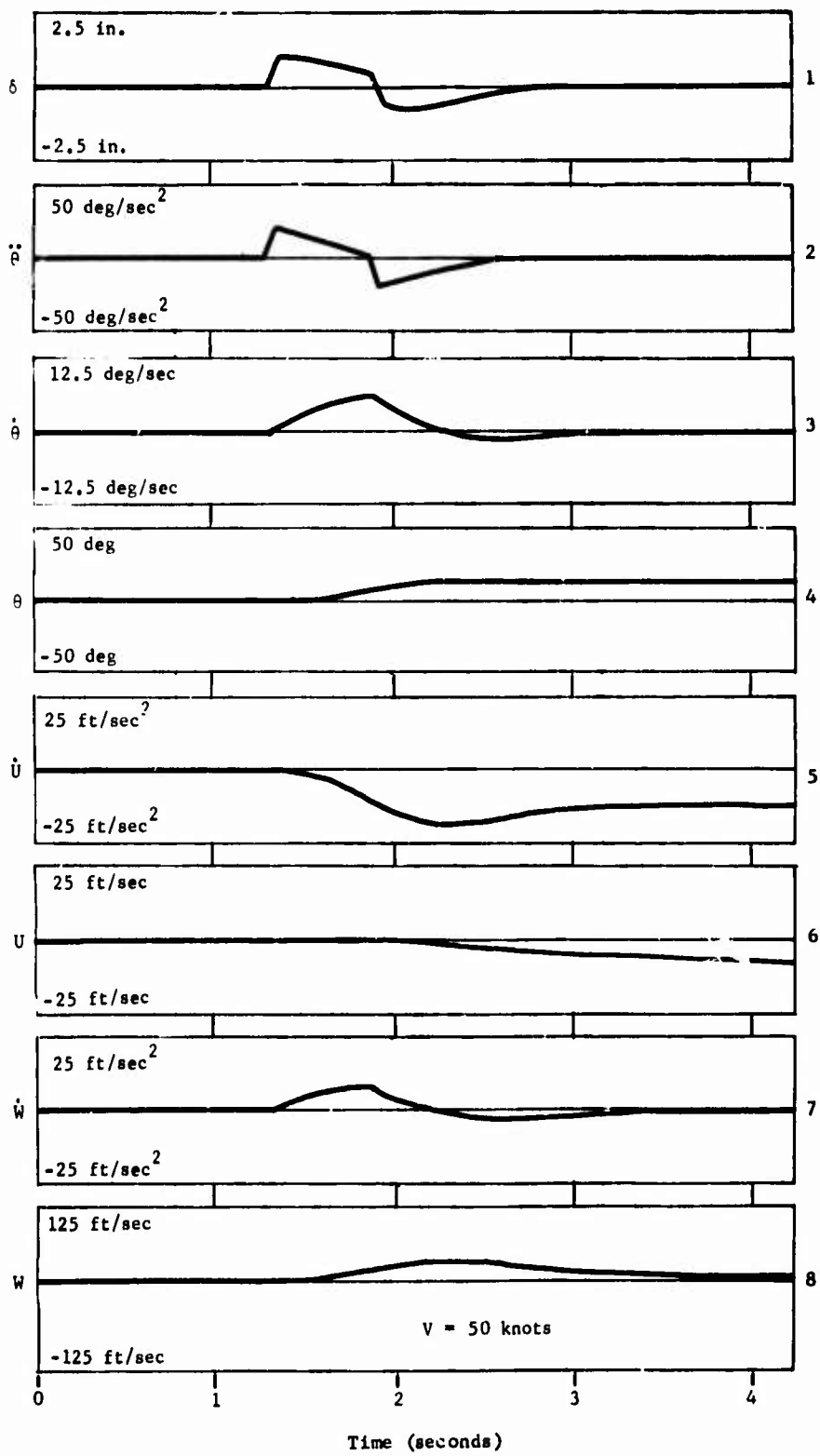


Figure 98. Helicopter Flight Simulation -- Run 62.

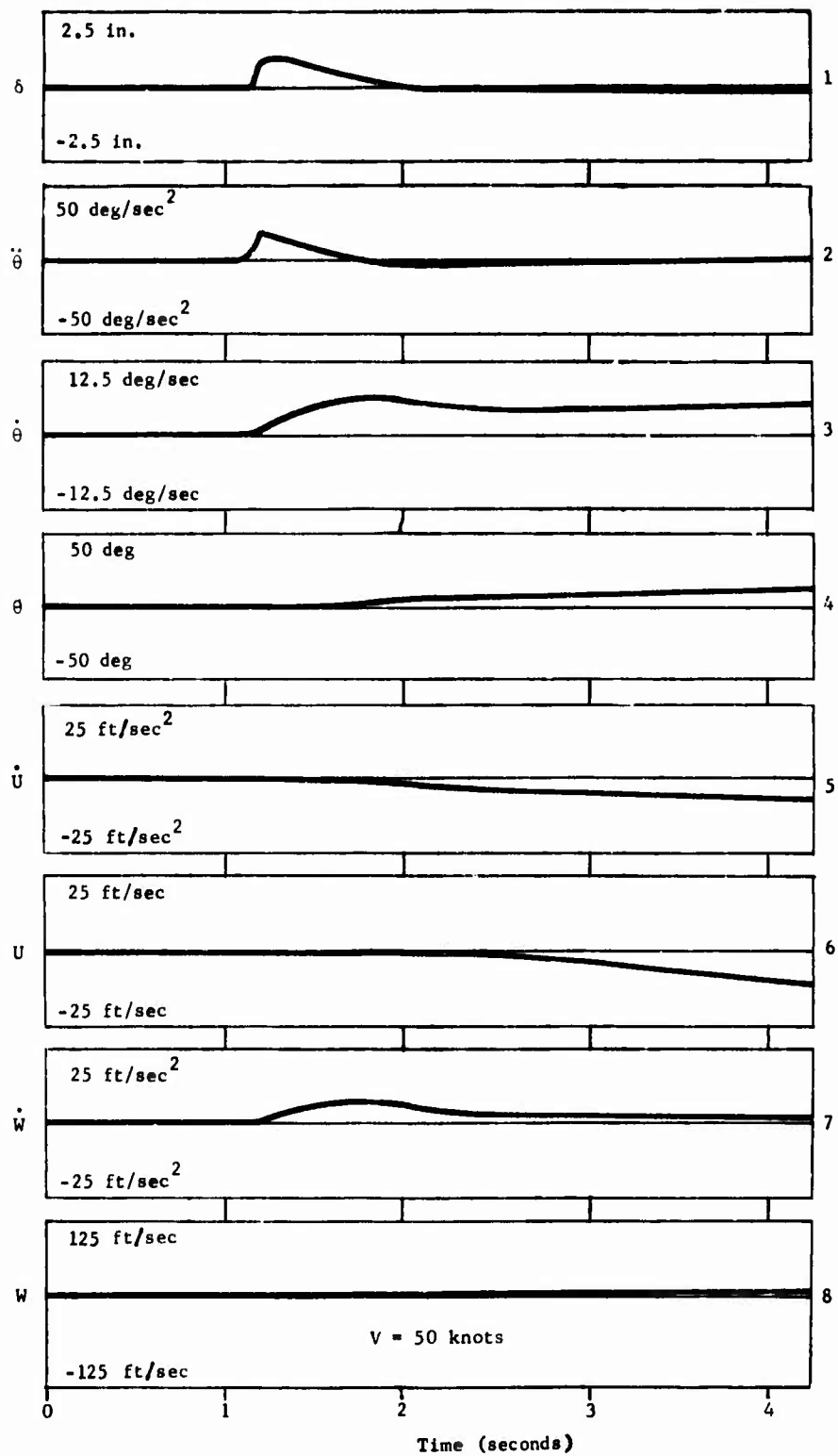


Figure 99. Helicopter Flight Simulation -- Run 57.

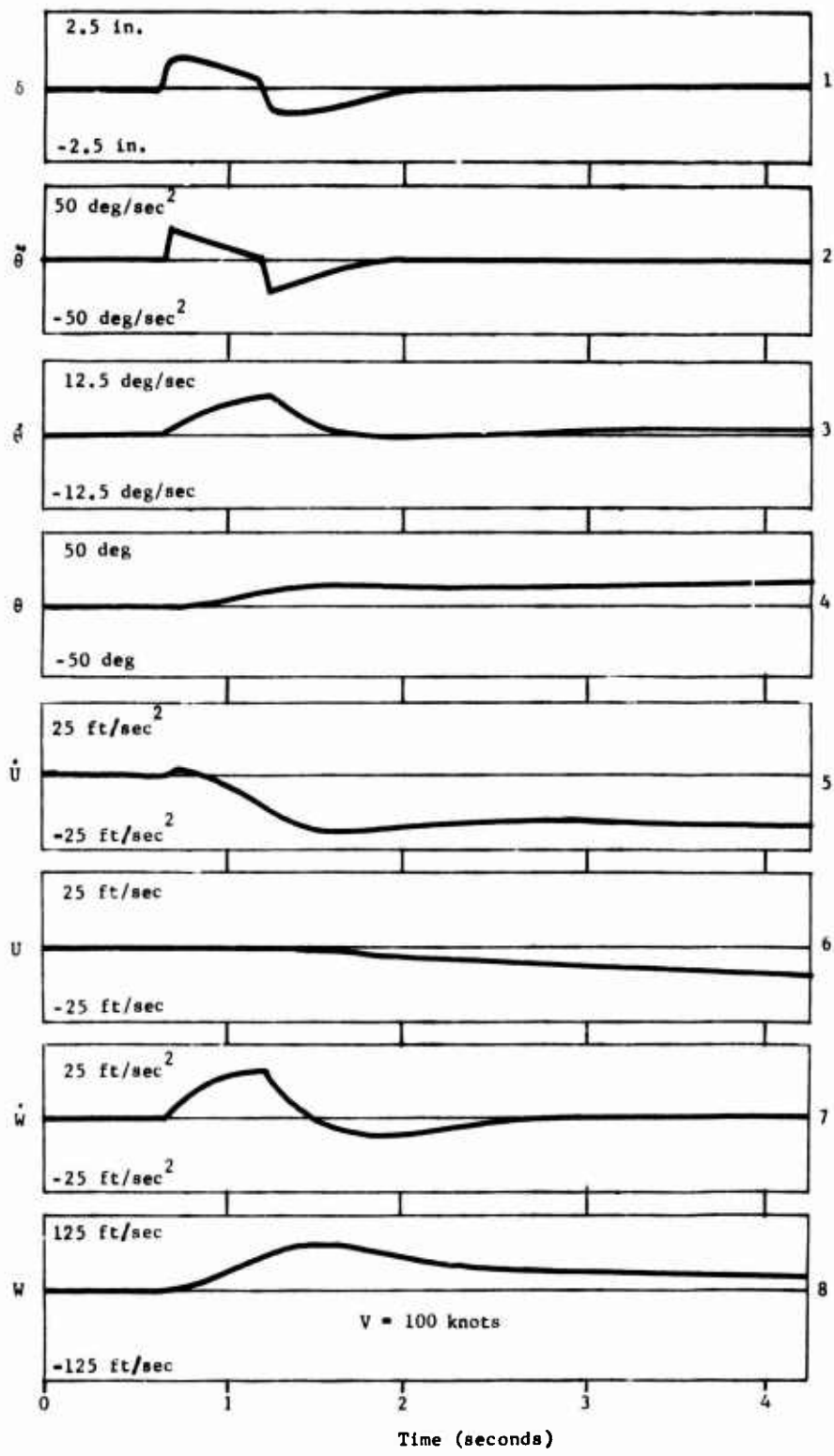


Figure 100. Helicopter Flight Simulation -- Run 48.

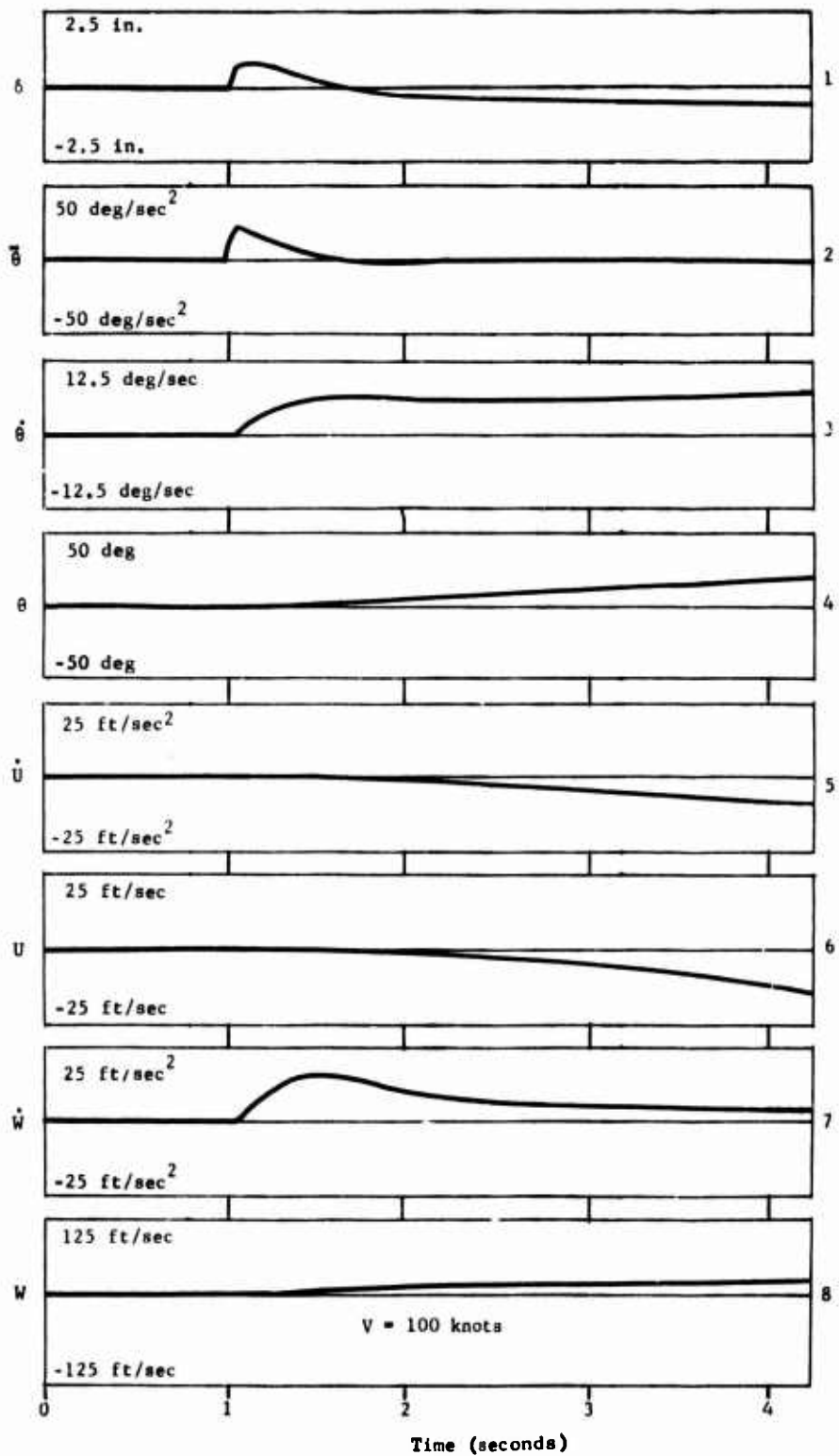


Figure 101. Helicopter Flight Simulation -- Run 53.

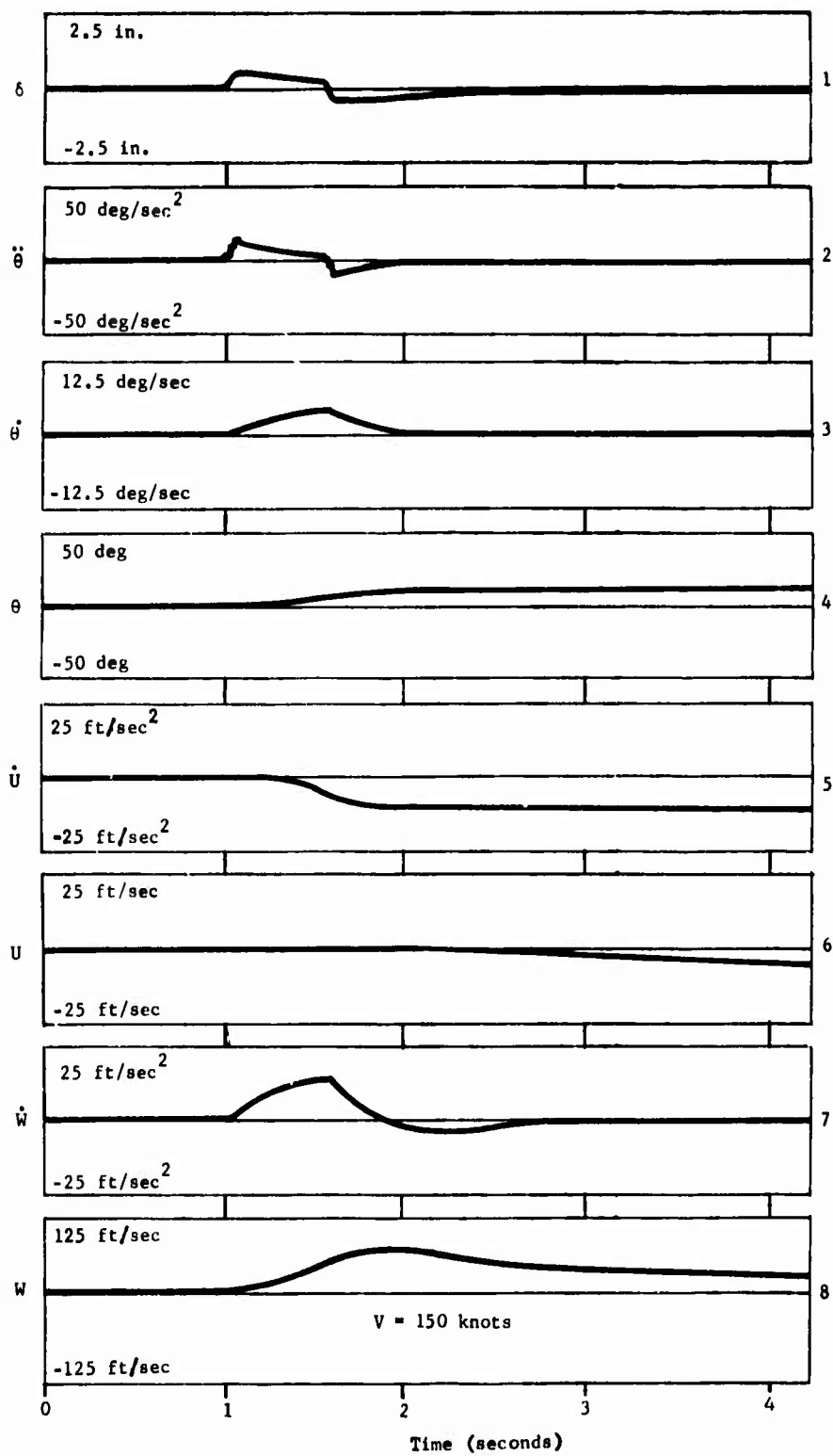


Figure 102. Helicopter Flight Simulation -- Run 68.

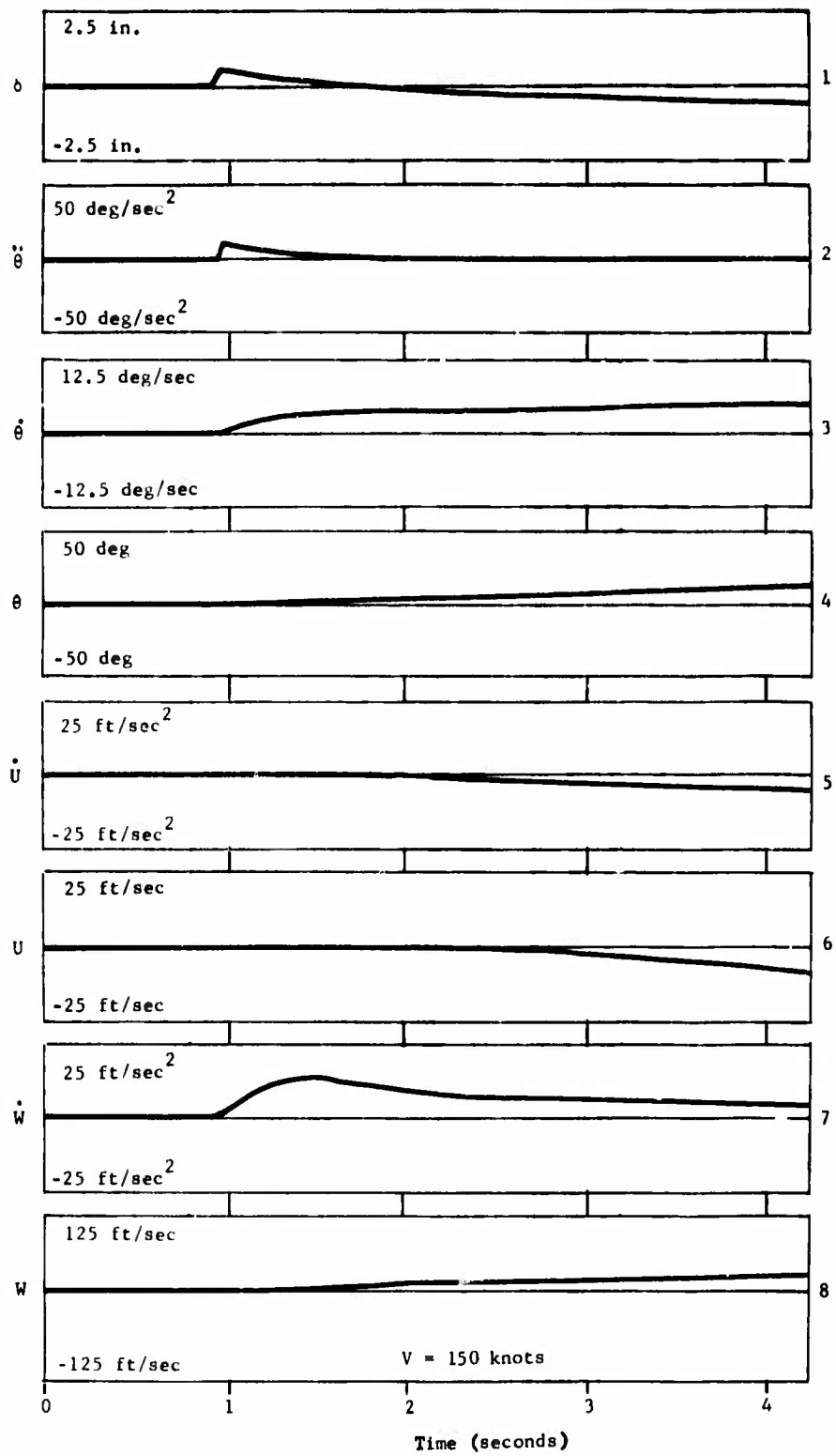


Figure 103. Helicopter Flight Simulation -- Run 72.

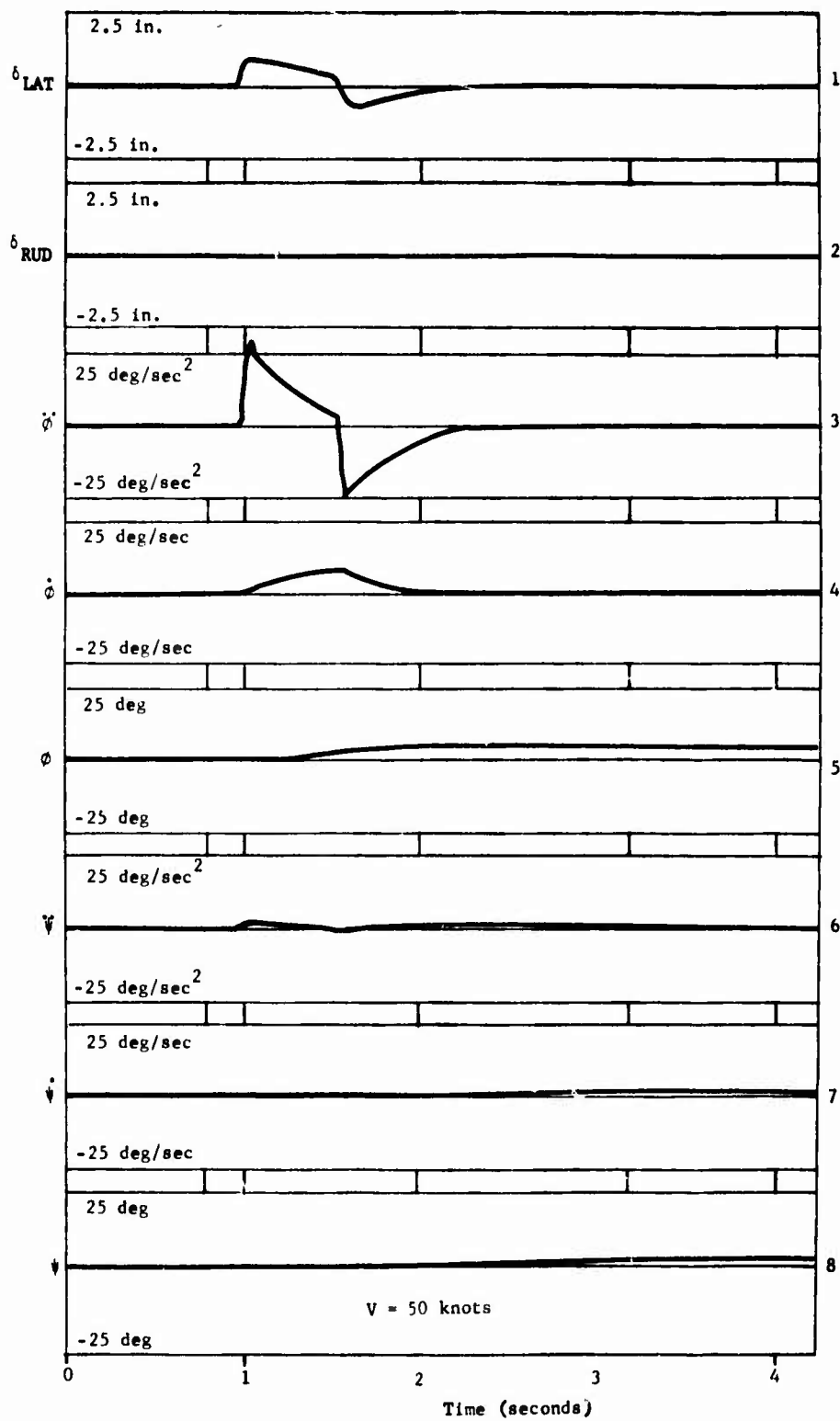


Figure 104. Helicopter Flight Simulation -- Run 96.

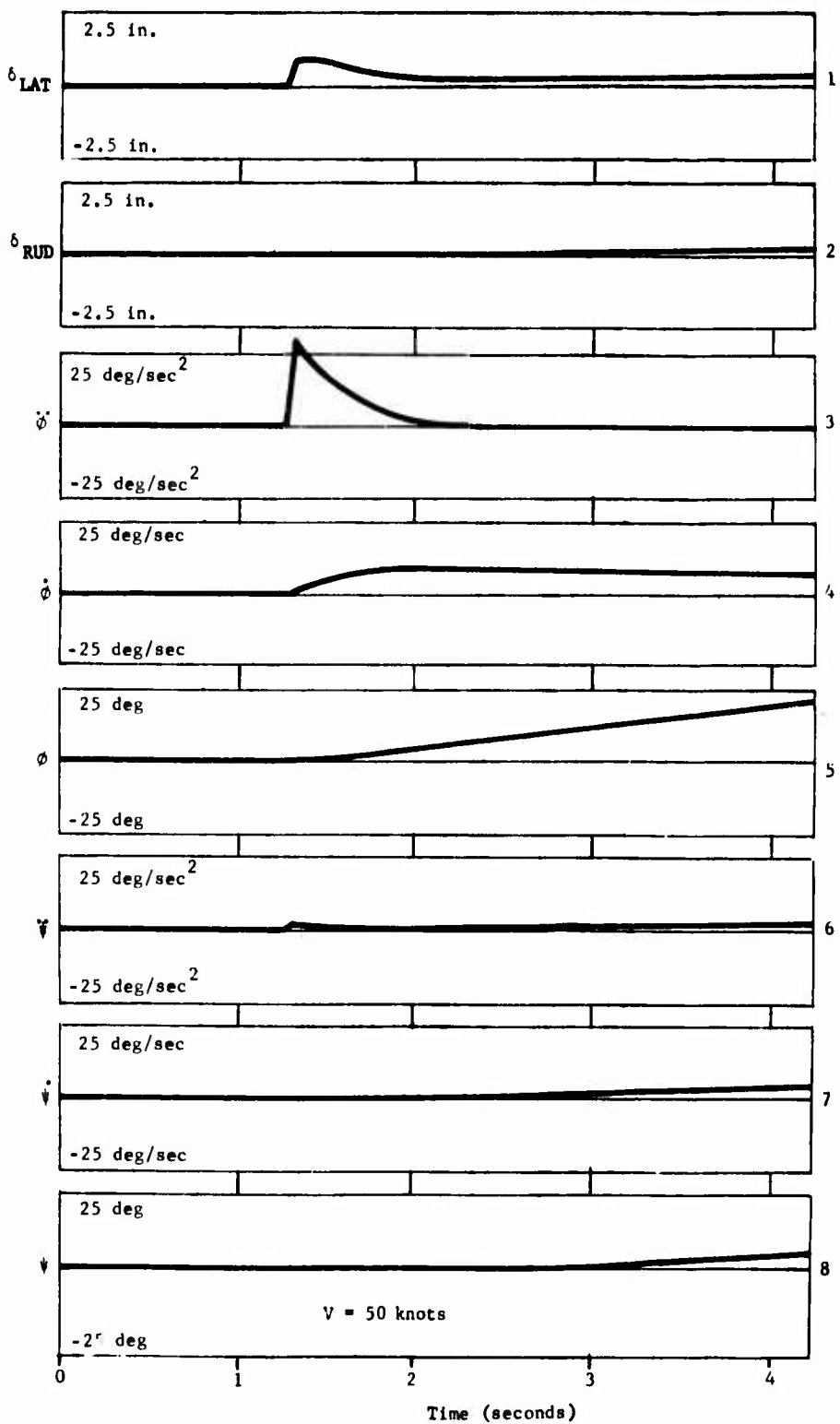


Figure 105. Helicopter Flight Simulation -- Run 104.

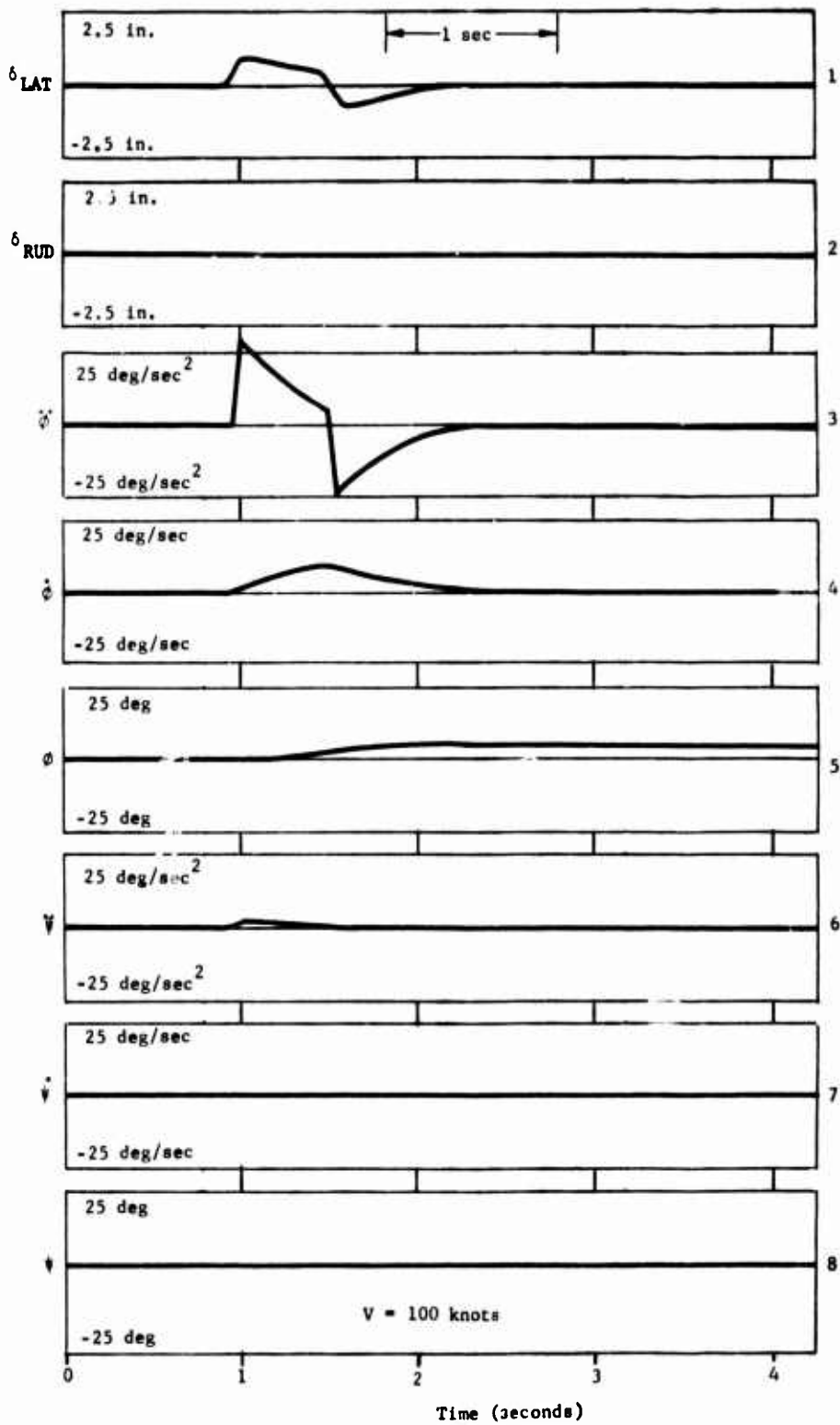


Figure 106. Helicopter Flight Simulation -- Run 94.

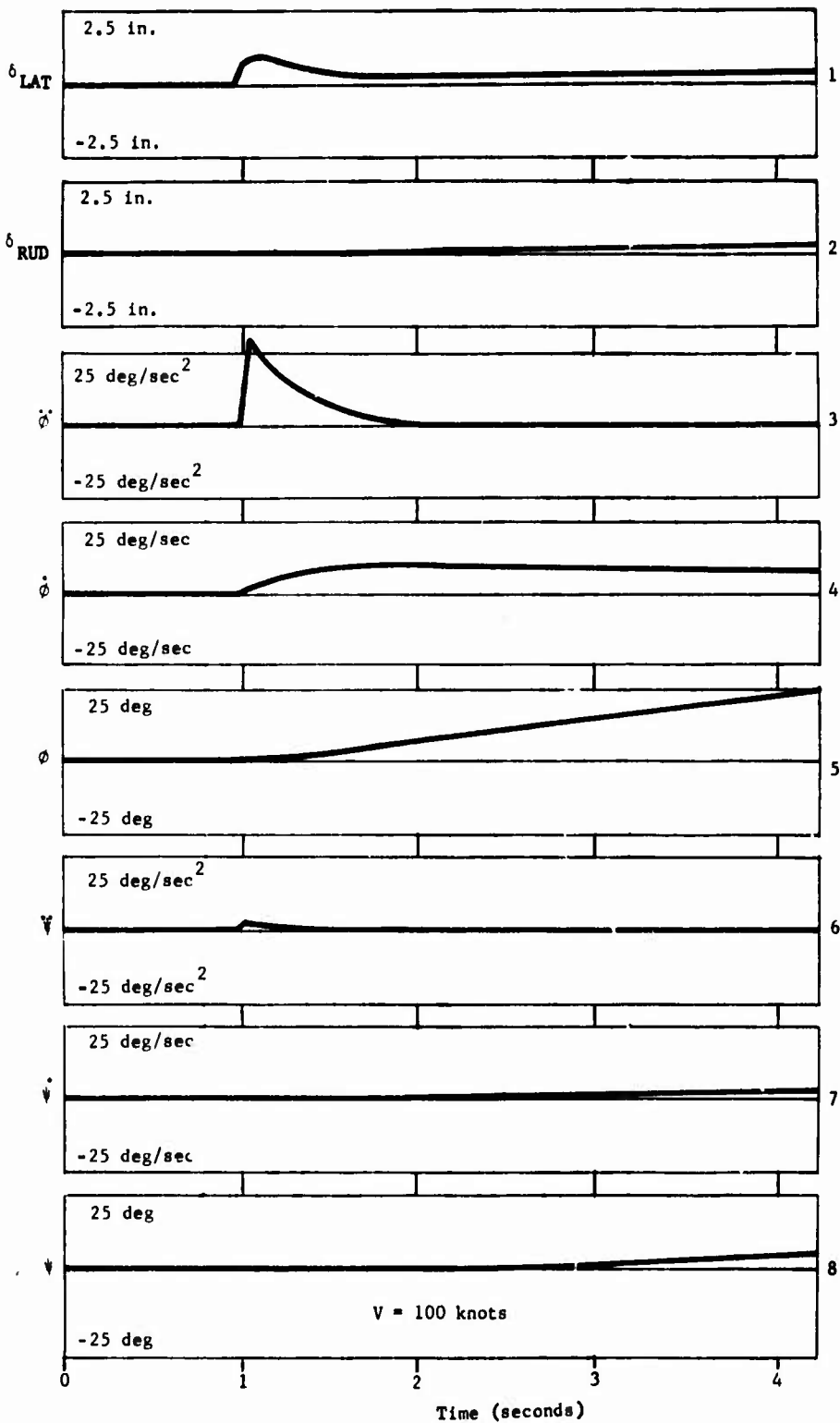


Figure 107. Helicopter Flight Simulation -- Run 106.

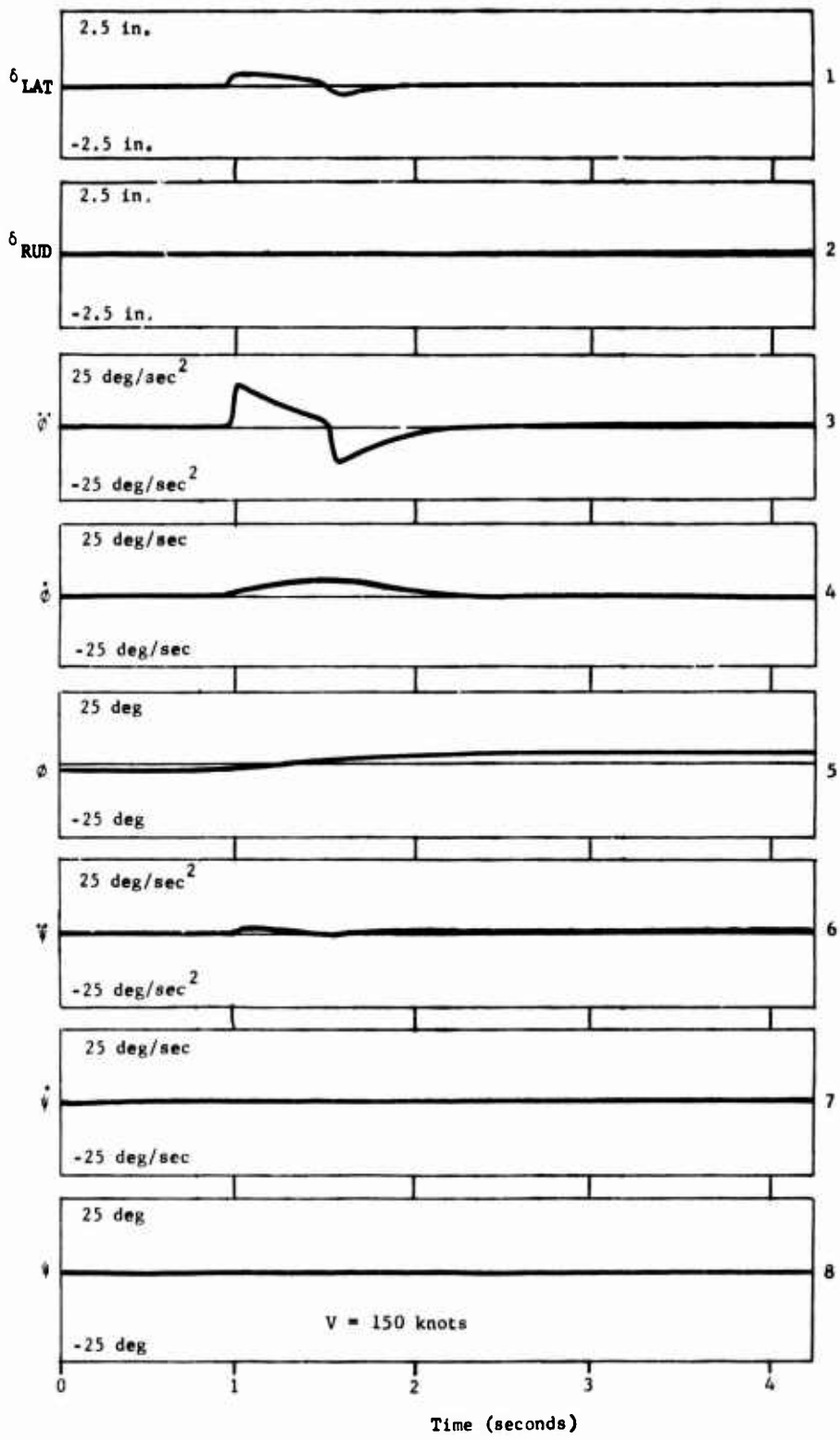


Figure 108. Helicopter Flight Simulation -- Run 100.

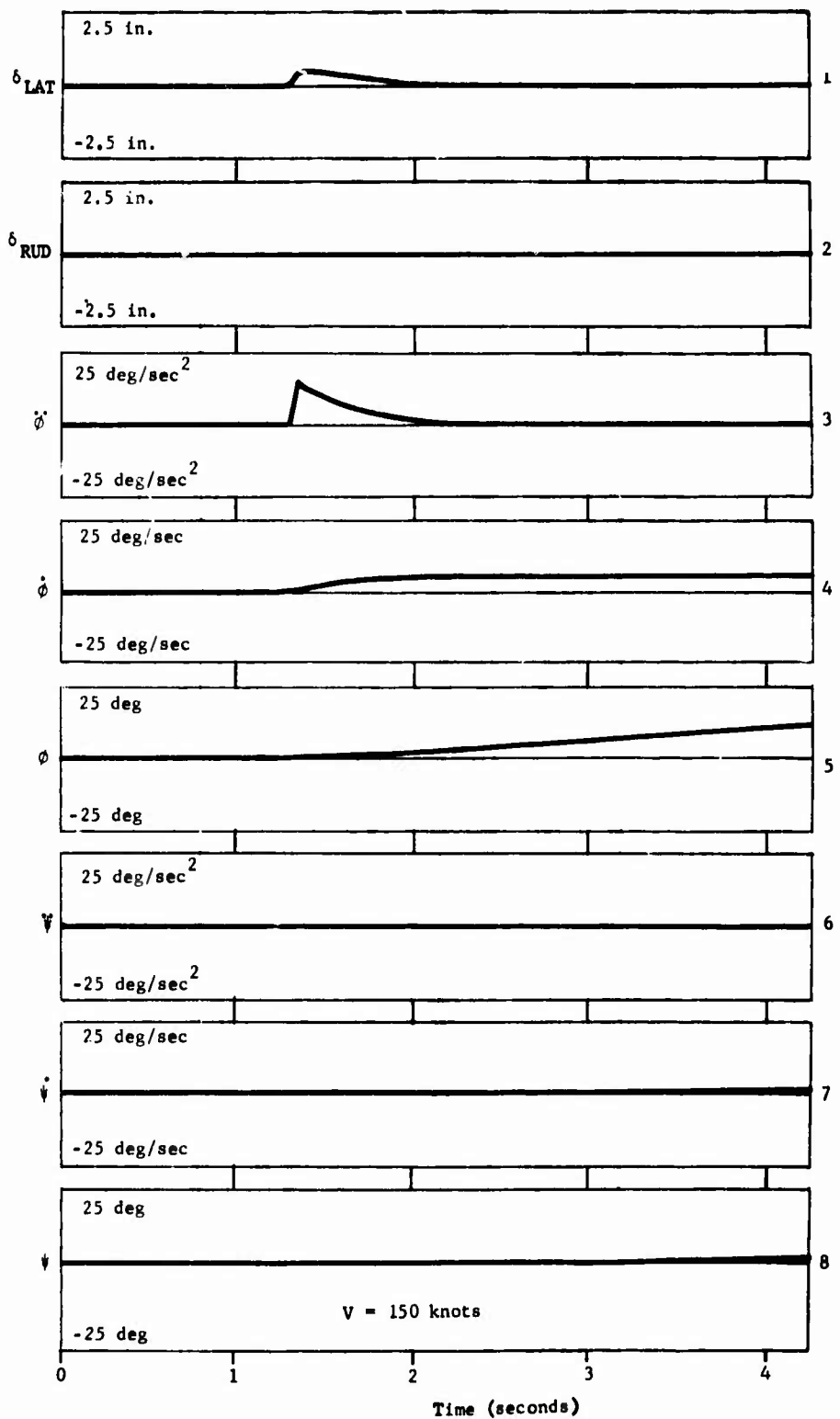


Figure 109. Helicopter Flight Simulation -- Run 102.

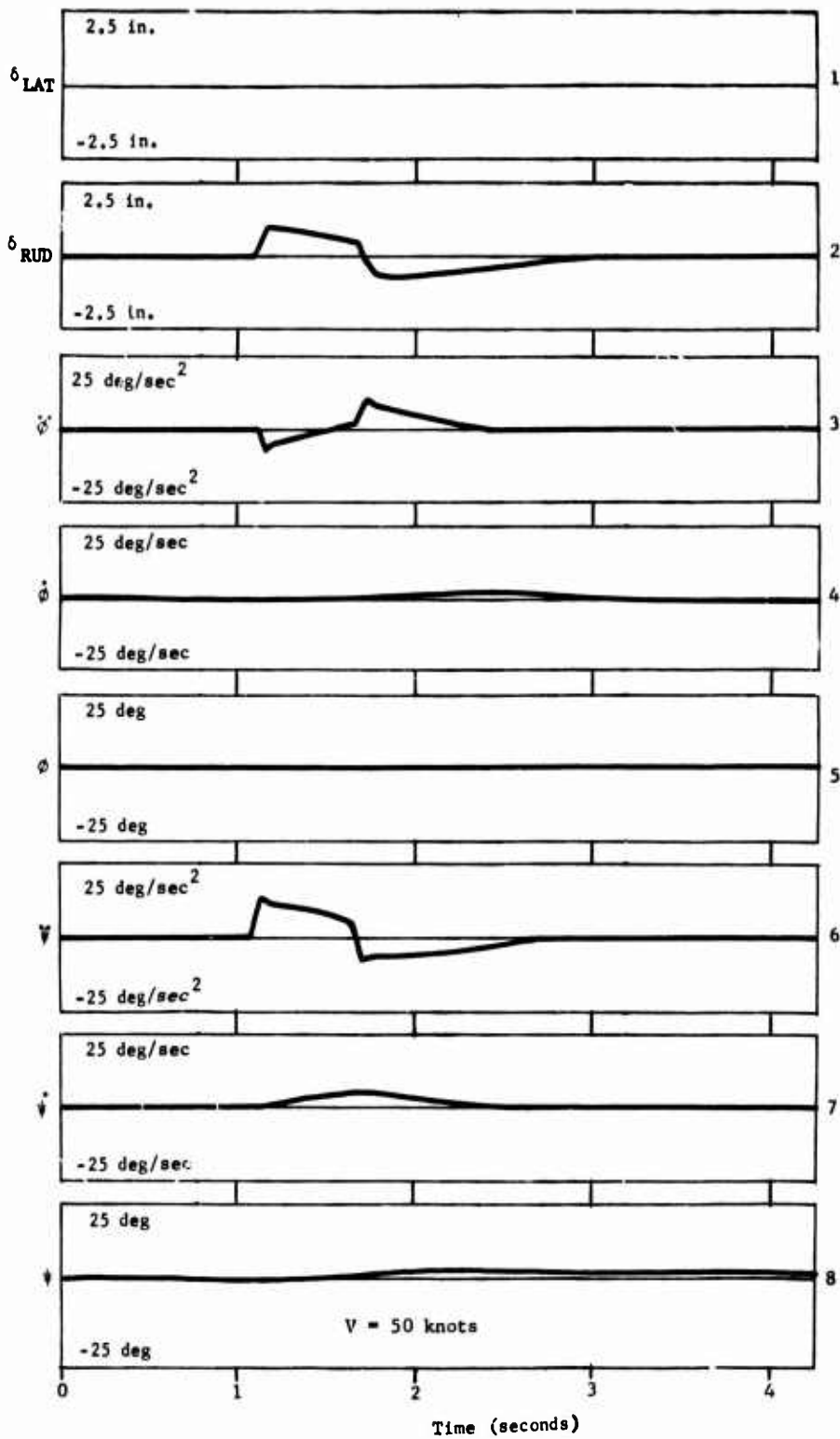


Figure 110. Helicopter Flight Simulation -- Run 97.

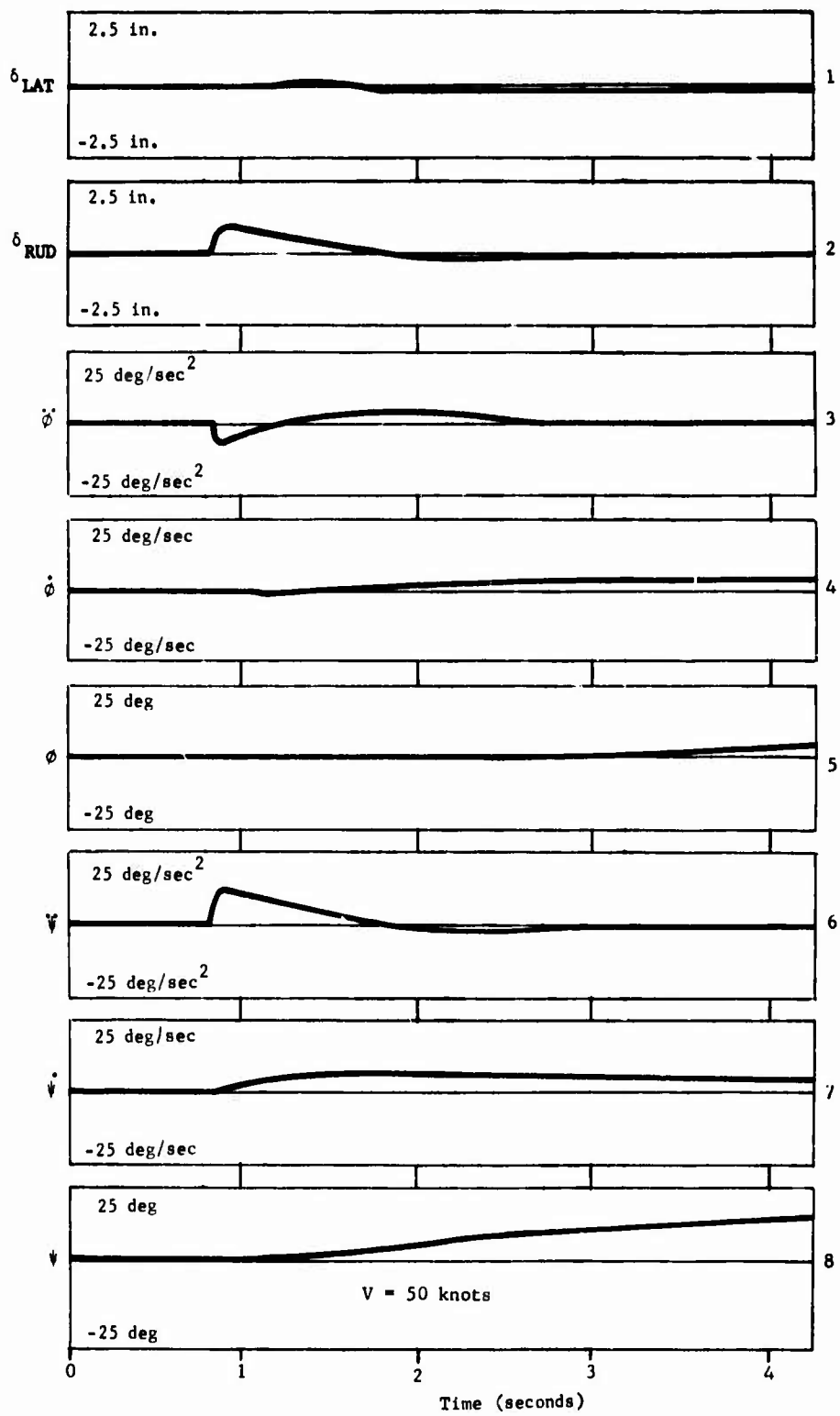


Figure 111. Helicopter Flight Simulation -- Run 105.

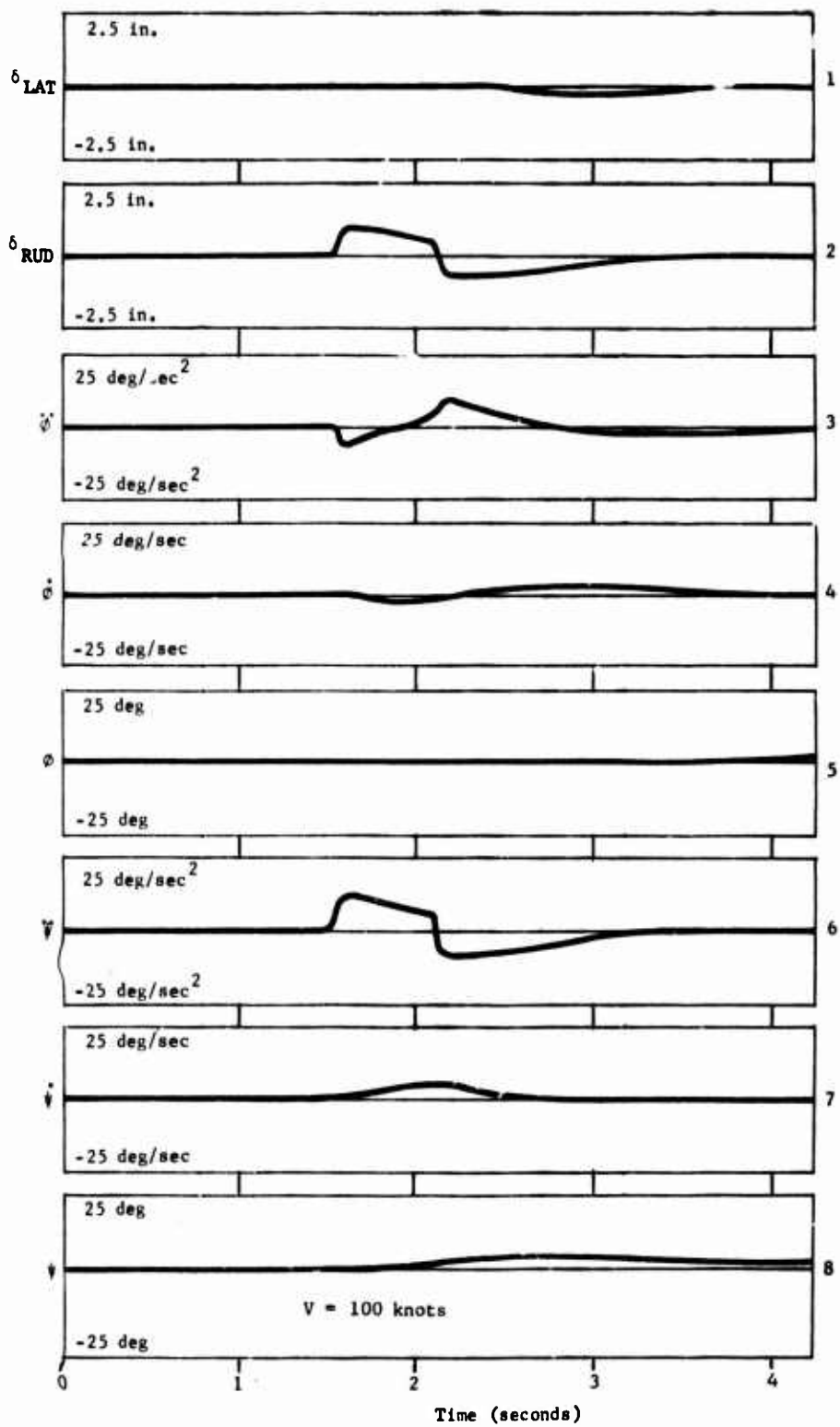


Figure 112. Helicopter Flight Simulation -- Run 95.

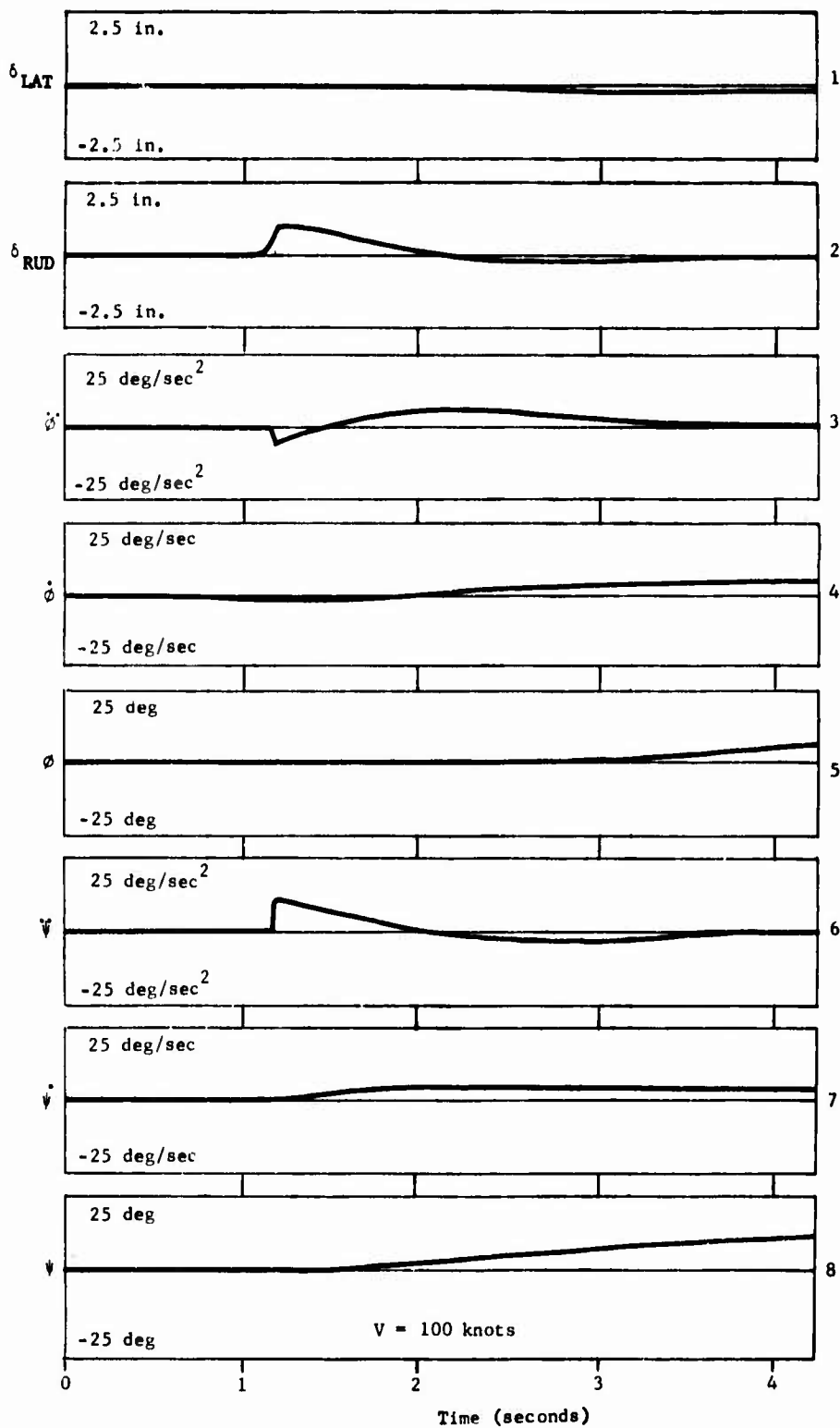


Figure 113. Helicopter Flight Simulation -- Run 107.

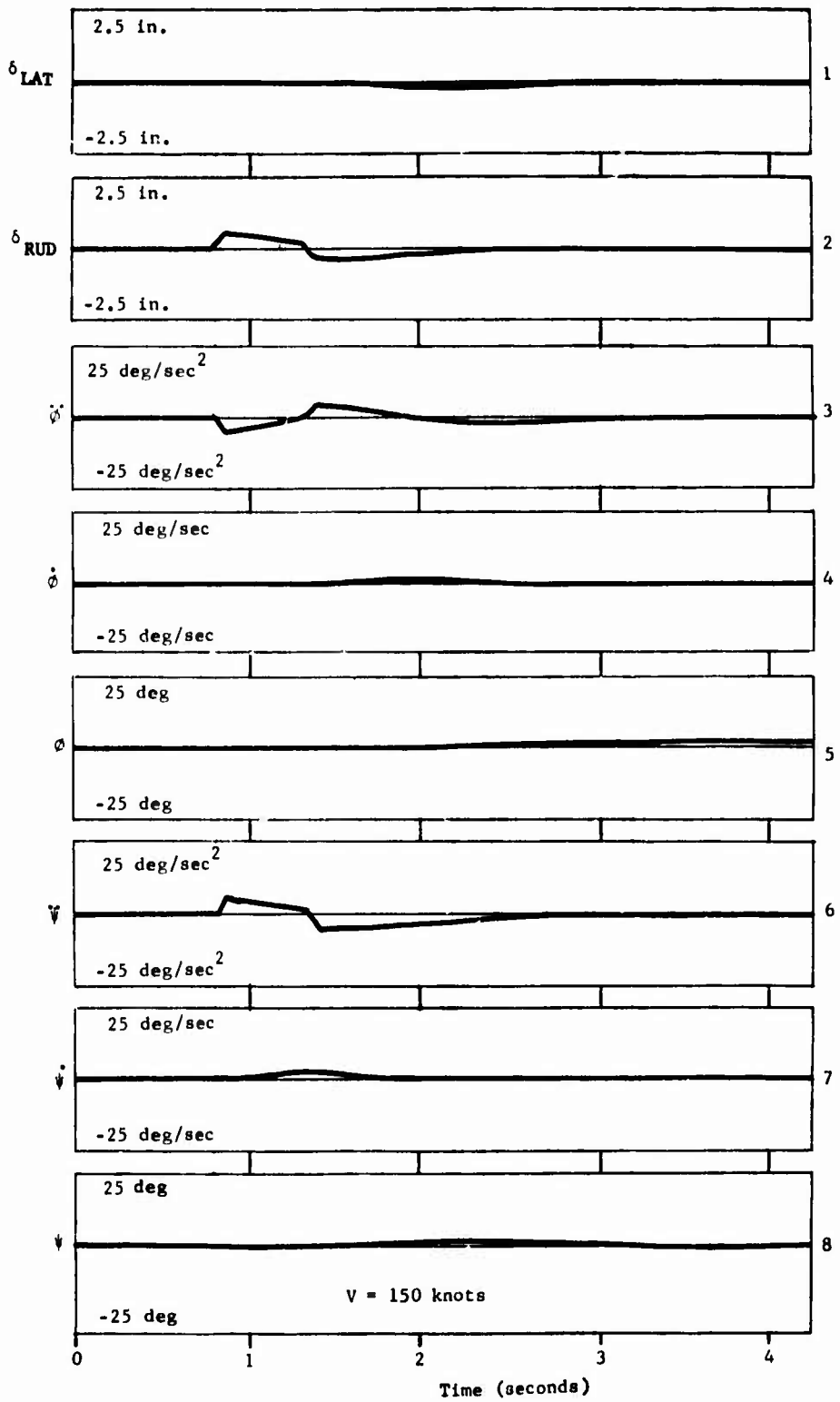


Figure 114. Helicopter Flight Simulation -- Run 101.

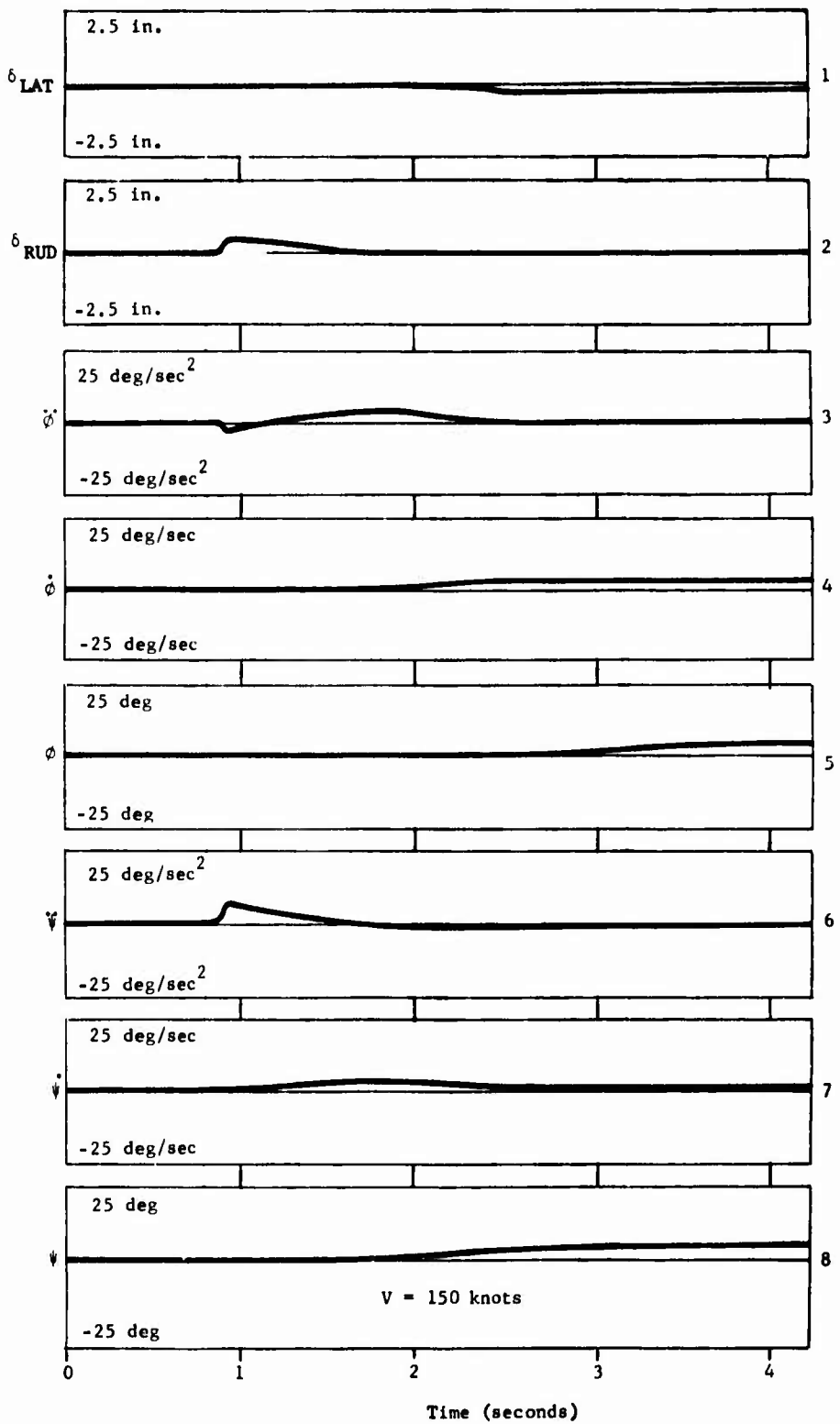


Figure 115. Helicopter Flight Simulation -- Run 103.

DISTRIBUTION

Director of Defense Research & Engineering	1
Assistant Secretary of the Army (R&D)	1
Assistant Chief of Staff for Force Development, DA	2
Deputy Chief of Staff for Logistics, DA	1
Deputy Chief of Staff for Personnel, DA	1
United States Army, Pacific	1
Chief of Research & Development, DA	2
Army Materiel Command	6
Army Aviation Systems Command	10
Hq, Army Air Mobility Research & Development Laboratory	2
Systems Research Integration Office, AMRDL	1
Ames Directorate, Army Air Mobility R&D Laboratory	1
Eustis Directorate, Army Air Mobility R&D Laboratory	28
Langley Directorate, Army Air Mobility R&D Laboratory	2
Lewis Directorate, Army Air Mobility R&D Laboratory	2
Army Aviation Systems Test Activity	2
Army R&D Group (Europe)	2
Army Scientific & Technical Information Team (Europe)	1
Army Advanced Materiel Concepts Agency	2
Army Aeromedical Research Laboratory	3
Harry Diamond Laboratories	1
Army Coating & Chemical Laboratory	1
Army Human Engineering Laboratories	3
Army Natick Laboratories	3
Army Ballistic Research Laboratory	1
Army Fuels & Lubricants Laboratory	1
Army Research Office	1
Army Materials & Mechanics Research Center	3
Army Test & Evaluation Command	1
Army Materiel Systems Analysis Agency	1
Army Electronics Command	2
Army Missile Command	2
USACDC Experimentation Command	1
USACDC Aviation Agency	3
USACDC Transportation Agency	1
Army Medical R&D Command	1
Army Tank-Automotive Command	1
Edgewood Arsenal	1
Frankford Arsenal	1
Army Command & General Staff College	1
Army Aviation Test Board	2
Army Arctic Test Center	1
Army Aviation Human Research Unit	1
Army Agency for Aviation Safety	2
Army Field Office, AFSC	1
Air Force Armament Development & Test Center	1
Aerospace Medical Research Laboratory	2
Air Force Aero Propulsion Laboratory	1
Air Force School of Aerospace Medicine	1

Air Force Institute of Technology	1
Air Force Materials Laboratory	2
Air Force Flight Dynamics Laboratory	4
Aeronautical Systems Division, AFSC	2
Naval Air Systems Command	12
Chief of Naval Research	3
Naval Research Laboratory	1
Naval Safety Center	1
Naval Air Rework Facility	1
Naval Air Test Center, Patuxent River	1
Naval Air Development Center	7
Naval Air Propulsion Test Center	1
Naval Air Station, Lakehurst	1
Naval Weapons Center	1
Naval Weapons Laboratory	1
Naval Ship Research & Development Center	3
Marine Corps Development & Education Command	1
Marine Corps Liaison Officer, Army Transportation School	1
U.S. Coast Guard	1
Transportation Systems Center	2
NASA Headquarters	1
Ames Research Center, NASA	6
Langley Research Center, NASA	2
Lewis Research Center, NASA	2
Manned Spacecraft Center, NASA	1
Marshall Space Flight Center, NASA	1
Scientific & Technical Information Facility, NASA	2
National Aviation Facilities Experimental Center, FAA	2
Department of Transportation Library	1
Eastern Region Library, FAA	1
Federal Aviation Administration, Washington	5
Civil Aeromedical Institute, FAA	2
Bureau of Aviation Safety, National Transportation Safety Board	3
National Bureau of Standards	1
Government Printing Office	1
Defense Documentation Center	12